Theoretical Study of the Earthquake Response of a Coal Handling Elevator Supporting Structure

Prepared by

T.Y. Yang, Robert C. Morehead, and J.L. Bogdanoff
School of Aeronautics and Astronautics
Purdue University
West Lafayette, Indiana

Submitted to

The National Science Foundation

April 30, 1978

50272-101

REPORT DOCUMENTATION PAGE	1. REPORT NO. NSF/RA-780528	2.	3. Recipient's Accession No. PB292536

4. Title and Subtitle
Theoretical Study of the Earthquake Response of a Coal Handling Elevator Supporting Structure

5. Report Date
April 30, 1978

6.

7. Author(s)
T.Y. Yang, R.C. Morehead, J.L. Bogdanoff

8. Performing Organization Rept. No.

9. Performing Organization Name and Address
Purdue University
School of Aeronautics and Astronautics
West Lafayette, Indiana 47907

10. Project/Task/Work Unit No.

11. Contract(C) or Grant(G) No.
(C)
(G) ENV7401575

12. Sponsoring Organization Name and Address
Applied Science and Research Applications (ASRA)
National Science Foundation
1800 G Street, N.W.
Washington, D.C. 20550

13. Type of Report & Period Covered

14.

15. Supplementary Notes

16. Abstract (Limit: 200 words)

This report is concerned with determining the seismic response of a supporting structure for two handling elevators at a TVA steam power generating plant in Paradise, Kentucky. It describes the dynamic behavior of the system, modeling, frequencies and mode shapes, a 3-dimensional plotting program, a response spectrum analysis, an earthquake time-history response analysis, and discusses results based on two types of graphical presentation. The 3-dimensional plotting program has the capabilities of displaying either the basic structural model or of superimposing a deformed structural configuration, such as mode shape, upon the original undeformed configuration. Illustrations include descriptions of a general 3-dimensional beam finite element and a general quadrilateral plate finite element in a 3-dimensional space, a basic structural model, vibrational modes, yield and buckling ratios, Z-displacement time-histories, axial stress time-histories, and bending moment time-histories.

17. Document Analysis a. Descriptors

Steam electric power generation elevators
Vibration testing
Earthquake resistant structures
Time studies
Numerical analysis
Models
Axial stress
Bending moments
Kentucky
Earthquakes

b. Identifiers/Open-Ended Terms

Z-displacement

c. COSATI Field/Group

18. Availability Statement	19. Security Class (This Report)	21. No. of Pages
NTIS		164
	20. Security Class (This Page)	22. Price PC A08 MF A01

(See ANSI-Z39.18) *See Instructions on Reverse*

OPTIONAL FORM 272 (4-77)
(Formerly NTIS-35)
Department of Commerce

Theoretical Study of the Earthquake Response of a Coal Handling Elevator Supporting Structure

Prepared by

T.Y. Yang, Robert C. Morehead, and J.L. Bogdanoff
School of Aeronautics and Astronautics
Purdue University
West Lafayette, Indiana

Submitted to

The National Science Foundation

April 30, 1978

Introduction

This study is concerned with determining the seismic response of the supporting structure for coal handling elevators No. 28 and No. 29 at TVA's steam power generating plant in Paradise, Kentucky. These elevators feed live piles No. 3 and No. 4, respectively.

The supporting structure for the coal conveyors is a complex three-dimensional system. An adequate model for analyzing the dynamic behavior of the system, required the use of over 1000 three-dimensional truss, beam, and plate finite elements and approximately 100 lumped masses. The assembled system has 714 degrees of freedom.

The analysis has the following objectives:

a) Determine the basic dynamic properties of the system, i.e., the natural frequencies and their corresponding normal modes.

b) Perform a response spectrum analysis to determine the necessary number of modes to be included in an earthquake time-history response analysis and to provide a means of checking the time-history calculations.

c) Determine the response of the coal handling equipment to the North-South component of the El Centro, 1940, earthquake using the mode superposition technique and investigate the effect of viscous damping on the response.

d) Identify the vulnerable members of the structure.

e) Utilize computer graphics techniques for data checking, displaying results, and as a medium for gaining insight into the nature of the structure's dynamic behavior.

The free vibration analysis, the earthquake response spectrum analysis, and the earthquake time-history response analysis, were carried out with an

existing structural analysis program, SAP IV. To enhance the entire analysis process, a three-dimensional perspective projection plotting program was developed. This program has the capabilities of displaying either the basic structural model or of superimposing a deformed structural configuration, such as a mode shape, upon the original undeformed configuration. A number of other programs were required to further analyze and display the results.

Description of the System

The supporting structure for elevators No. 28 and No. 29 is 517.2 feet long and 111.3 feet high. The structure's side view, shown in Fig. 1, consists of two separate truss systems corresponding to the two elevators. The lower one will be referred to as truss system 1 and the upper one will be referred to as truss system 2. Elevator No. 28 (system 1) feeds live pile No. 3 or alternatively, it feeds elevator No. 29 (system 2) which feeds live pile No. 4.

The lower end of truss system 1 is bolted to a concrete foundation so that it is restrained from any displacements. The upper end of truss system 1 rests on truss system 2 at four joints with roller conditions. Intermediate support for truss system 1 is provided by two bents. These bents are connected to the truss by joints with hinged conditions and anchored at the based with nearly fixed conditions to concrete footings.

Truss system 2 has a nonuniform cross-section and is supported by a tower at its lower end and a bent in the center. The tower and the bents are connected to the truss by joints with hinged conditions and anchored to concrete footings with nearly fixed conditions at the base. The outer end of truss system 2 is entirely free.

The structure also has several secondary components of concern. There is a three inch thick cement walkway beneath the elevators. The combined weight of the coal and elevators can be over 100,000 pounds and must be taken into account. In truss system 2, there are two machinery rooms containing drive motors and auxiliary equipment. Also in truss system 2 there are a considerable number of secondary structural members which serve to support the machinery rooms, the elevator, and the walkway in this section. Feeding the coal to each live pile, there is an 80 foot telescopic chute.

Finite Elements

Two types of finite elements are used. One type is the three-dimensional beam finite element with three displacement and three rotational degrees of freedom at each nodal point. The truss bar finite element, without the rotational degrees of freedom at the nodes, is a special case of the beam element. The other type is a three-dimensional quadrilateral plate finite element.

i The three-dimensional beam finite element

The three-dimensional beam finite element is described in Fig. 2. The element is assumed to have six degrees of freedom at each nodal point: three displacements $\bar{u}$, $\bar{v}$, and $\bar{w}$ in the local $\bar{x}$, $\bar{y}$, and $\bar{z}$ directions, respectively; and three rotations $\theta_{\bar{x}}$, $\theta_{\bar{y}}$, and $\theta_{\bar{z}}$ about $\bar{x}$, $\bar{y}$, and $\bar{z}$, respectively. Corresponding to the six nodal degrees of freedom, there are three forces $F_{\bar{x}}$, $F_{\bar{y}}$, $F_{\bar{z}}$, one twisting moment $M_{\bar{x}}$, and two bending moments $M_{\bar{y}}$, $M_{\bar{z}}$, respectively.

The element formulation is derived in the form that the 12 nodal forces are related to the 12 nodal displacements (in local coordinates) by the stiffness and mass matrices.

$$\underset{12x1}{\{\bar{F}\}} = \underset{12x12}{[\bar{k}]}\ \underset{12x1}{\{\bar{q}\}} - \omega^2\ \underset{12x12}{[\bar{m}]}\ \underset{12x1}{\{\bar{q}\}} \qquad (1)$$

where the stiffness matrix is shown in Table 1. In Table 1, the terms EA, EI, and GJ are defined as the axial, bending, and torsional rigidities, respectively and L is the length of the element. The stiffness matrix can be derived either by the stress-strain equilibrium method or by the minimum strain energy method. The mass matrix $[\bar{m}]$ is formulated on the basis of lumped masses. The rotatory inertia is neglected. There

Table 1. The stiffness matrix $[\bar{k}]$ for a local 3-D beam finite element.

$$
\begin{bmatrix}
\frac{AE}{L} & & & & & & & & & & & \\
0 & \frac{12EI_{\bar{y}}}{L^3} & & & & & & & & & & \\
0 & 0 & \frac{12EI_{\bar{z}}}{L^3} & & & & & & & & & \\
0 & 0 & 0 & \frac{GJ}{L} & & & & & & & & \\
0 & -\frac{6EI_{\bar{y}}}{L^2} & 0 & 0 & \frac{4EI_{\bar{y}}}{L} & & & & & & & \\
0 & 0 & \frac{6EI_{\bar{z}}}{L^2} & 0 & 0 & \frac{4EI_{\bar{z}}}{L} & & & & & & \\
-\frac{AE}{L} & 0 & 0 & 0 & 0 & 0 & \frac{AE}{L} & & & & & \\
0 & -\frac{12EI_{\bar{y}}}{L^3} & 0 & 0 & \frac{6EI_{\bar{y}}}{L^2} & 0 & 0 & \frac{12EI_{\bar{y}}}{L^3} & & & & \\
0 & 0 & -\frac{12EI_{\bar{z}}}{L^3} & 0 & 0 & -\frac{6EI_{\bar{z}}}{L^2} & 0 & 0 & \frac{12EI_{\bar{z}}}{L^3} & & & \\
0 & 0 & 0 & -\frac{GJ}{L} & 0 & 0 & 0 & 0 & 0 & \frac{GJ}{L} & & \\
0 & -\frac{6EI_{\bar{y}}}{L^2} & 0 & 0 & \frac{2EI_{\bar{y}}}{L} & 0 & 0 & \frac{6EI_{\bar{y}}}{L^2} & 0 & 0 & \frac{4EI_{\bar{y}}}{L} & \\
0 & 0 & \frac{6EI_{\bar{z}}}{L^2} & 0 & 0 & \frac{2EI_{\bar{z}}}{L} & 0 & 0 & -\frac{6EI_{\bar{z}}}{L^2} & 0 & 0 & \frac{4EI_{\bar{z}}}{L}
\end{bmatrix}
$$

are only six nonzero terms on the diagonal of the mass matrix, which correspond to the $\bar{u}$, $\bar{v}$, $\bar{w}$ displacements at both nodal points. These terms are all in the same form of $\rho AL/2$ which is half of the mass of the finite element.

Before the assemblage of each individual element, the equations of motion (1) for each element must be transformed from the local coordinates ($\bar{x}$, $\bar{y}$, $\bar{z}$) to the global coordinates (x, y, z) by using the nine direction cosines defined as follows.

$$\begin{cases} \lambda_i = \cos\theta_{xi} \\ \mu_i = \cos\theta_{yi} \\ \nu_i = \cos\theta_{zi} \end{cases} \qquad i = \bar{x}, \bar{y}, \text{ and } \bar{z} \tag{2}$$

The equations of motion with reference to the global coordinates are in the form

$$\underset{12x1}{\{F\}} = \underset{12x12}{[T]^T} \left[\underset{12x12}{[\bar{k}]} - \omega^2 \underset{12x12}{[\bar{m}]} \right] \underset{12x12}{[T]} \underset{12x1}{\{q\}} \tag{3}$$

where the coordinate transformation matrix is defined as

$$[T] = \begin{bmatrix} \Lambda & & & \\ & \Lambda & & \\ & & \Lambda & \\ & & & \Lambda \end{bmatrix} \tag{4}$$

with

$$[\Lambda] = \begin{bmatrix} \lambda_{\bar{x}} & \mu_{\bar{x}} & \nu_{\bar{x}} \\ \lambda_{\bar{y}} & \mu_{\bar{y}} & \nu_{\bar{y}} \\ \lambda_{\bar{z}} & \mu_{\bar{z}} & \nu_{\bar{z}} \end{bmatrix} . \tag{5}$$

In the assemblage of such finite elements, the hinged joint conditions can be achieved by neglecting the compatibility requirement for the three rotational degrees of freedom. This is done by eliminating such unwanted degrees of freedom at the element level.

Since the stiffness and mass matrices are in the form of a band matrix only the bands are stored in the computer for the calculation of frequencies and mode shapes. The bands are stored in blocks and are solved by a subspace iterative procedure. A careful numbering of the joints of the structural model can minimize the bandwidth and result in saving computing time. For the 12 degree of freedom element, the bandwidth is calculated by the formula

$$\text{Bandwidth} = 2(6n + 5) + 1 \qquad (6)$$

where n is the maximum numerical difference between any pair of connected nodal point numbers.

ii The three-dimensional orthotropic quadrilateral plate finite element

The three-dimensional orthortopic quadrilateral plate element is shown in Fig. 3. This element has five degrees of freedom at each corner nodal point: three displacement degrees of freedom $\bar{u}$, $\bar{v}$, and $\bar{w}$ in the Cartesian local coordinate directions $\bar{x}$, $\bar{y}$, and $\bar{z}$, respectively; and two slope degrees of freedom about the $\bar{x}$ and $\bar{y}$ axes, respectively. For reasons of computational efficiency, the quadrilateral element is composed of four triangular elements. The four triangles share a common central nodal point which is located at the average of the coordinates of the four corner nodal points. The five degrees of freedom at this central nodal point are eliminated at the elemental level prior to assemblage, thus the quadrilateral element effectively has a total of 20 degrees of freedom, five per

nodal point.

The membrane stiffness of each sub-triangular element is represented by the constant strain based on linear displacement functions in both $\bar{u}$ and $\bar{v}$ [Ref. 1]. The flexural stiffness of each sub-triangular element is represented by the fully compatible HCT element based on the cubic displacement functions in $\bar{w}$ [Ref. 2]. The orthotropic material property is included in the formulations for both the membrane and flexural stiffness matrices. The mass matrix of the quadrilateral element is formulated on the basis of lumped masses. The formulation, with reference to the local coordinates $\bar{x}$, $\bar{y}$, and $\bar{z}$, is given in the following symbolic form

$$\underset{20\times1}{\{\bar{F}\}} = \left[\underset{20\times20}{[\bar{k}]} - \omega^2 \underset{20\times20}{[\bar{m}]}\right] \underset{20\times1}{\{\bar{q}\}} \qquad (7)$$

where $\{\bar{F}\}$ and $\{\bar{q}\}$ are vectors of nodal forces and displacements, respectively; [k] and [m] are the element stiffness and mass matrices, respectively; the "bar" represents local coordinates.

Through a congruent coordinate transformation technique, the element formulation (7) in local coordinates is transformed into the formulation in global coordinates,

$$\underset{24\times1}{\{F\}} = \left[\underset{24\times20}{[T]^T} \underset{20\times20}{[k]} \underset{20\times24}{[T]} - \omega^2 \underset{24\times20}{[T]^T} \underset{20\times20}{[m]} \underset{20\times24}{[T]}\right] \underset{24\times1}{\{q\}} \qquad (8)$$

where the matrix [T] is the coordinate transformation matrix. This coordinate transformation generates six degrees of freedom at each nodal point: three displacement degrees of freedom u, v, and w in the global coordinate directions, x, y, and z, respectively; and three rotational degrees of freedom θ_x, θ_y, and θ_z about the x, y, and z axes, respectively.

Modeling

The supporting structure for the coal conveyors is a complex three-dimensional system requiring the use of three types of finite elements and the inclusion of additional lumped masses in order to construct an adequate model for a dynamic analysis. The finite elements used were three-dimensional truss bar, beam, and orthotropic quadrilateral plate elements.

The structure is of truss type with many cross bracing members. The conditions of the joints were designed as hinged. Beam elements assume rigid joints and truss elements (beam elements without the rotational degrees of freedom) assume hinged joints. In this study, the 49 bays of the structure were modeled using 956 truss elements. It is felt that for structures of this type, the lower natural frequencies and mode shapes obtained by assuming either hinged joints or rigid joints will not differ by much.

The bents and the tower, which support the truss structures, are designed to have bending and torsional rigidities. A total of 81 beam elements were used to model the bents and the tower. The basic structural model is shown in Figure 4 and the nodal point numbers are shown in Figure 5.

The structure has a number of secondary components which have a significant effect on the dynamic response of the system. As indicated earlier, the weight of the elevators when loaded with coal is significant. The geometry of the elevators indicate that they would add little to the overall stiffness of the structure. Therefore, the mass of the elevators when loaded with coal was estimated and this effect was modeled by distributing the mass throughout the structure as lumped masses at the appropriate nodal points. Also included as lumped masses were the two drive

motors located in the upper section of the structure and the two telescopic chutes which feed the live piles.

In truss system 2, there are a great number of secondary, internal structural elements. The secondary elements which were judged to make a significant contribution to the overall stiffness of the structure, were included as additional truss elements. The mass of the internal elements of this system, which were judged to provide mainly internal support and contribute little to the overall structural stiffness, was included in the model as lumped masses.

Beneath the elevators is a 3 inch thick reinforced concrete walkway. The concrete was assumed to be orthotropic and was modeled with 34 quadrilateral plate finite elements.

The complete model of the structure has 232 joints, over 1000 finite elements and about 100 lumped masses. The assembled system results in 714 equations and has a bandwidth of 126.

Frequencies and Mode Shapes

The first step of a seismic analysis is the determination of the basic dynamic properties of the system, i.e., the natural frequencies and the corresponding mode shapes. The equation of dynamic equilibrium of an undamped structure in free vibration may be written in matrix form as follows:

$$[M]\{\ddot{u}\} + [K]\{u\} = \{0\} \tag{9}$$

in which

$[M]$ = mass matrix

$[K]$ = stiffness matrix

$\{u\}$ = displacement vector

$\{\ddot{u}\}$ = acceleration vector

In free vibration of undamped systems, the motion is simple harmonic in form, i.e., the displacements in any mode "n" may be expressed

$$\{u\} = \{\phi_n\} \sin \omega_n t \tag{10}$$

where ω_n is the circular frequency. Differentiating eq.10 twice gives the accelerations

$$\{\ddot{u}\} = -\{\phi_n\} \omega_n^2 \sin \omega_n t \tag{11}$$

Substituting eqs. 10 and 11 into eq. 9 yields

$$- \omega_n^2 [M]\{\phi_n\} + [K]\{\phi_n\} = \{0\}$$

or

$$\left[[K] - \omega_n^2[M]\right]\{\phi_n\} = \{0\} \tag{12}$$

Eq. 12 is a form of characteristic equation of which the roots, ω_n^2, (eigenvalues) define the frequencies of vibration of the structure. Corresponding to each root is a characteristic mode shape (eigenvector), ϕ_n.

Theoretically, one could find a number of frequencies and mode shapes equal to the number of degrees of freedom of the system. In practice, it has been observed that the lower modes dominate the structural response. The solution of eq. 12 for the first 25 frequencies was obtained in SAP IV, the structural analysis program used in the study, by the subspace iteration technique. Subspace iteration is a technique whereby the number of equations, in this case 714, is reduced to only the number of frequencies being sought. This reduced set of equations, or subspace, is then iterated until the desired solution is converged upon. The results for the first 25 frequencies are shown in Table 2.

Table 2. The results of the vibrational frequency analysis

Mode No.	Frequency(Hz)	Period (Sec)
1	.440	2.274
2	.576	1.737
3	.716	1.396
4	.775	1.290
5	1.059	.945
6	1.268	.789
7	1.299	.770
8	1.354	.738
9	1.503	.665
10	1.557	.642
11	1.612	.620
12	1.709	.585
13	1.794	.557
14	1.897	.527
15	2.079	.481
16	2.393	.418
17	2.684	.373
18	2.831	.353
19	2.997	.334
20	3.031	.330
21	3.190	.313
22	3.228	.310
23	3.231	.309
24	3.264	.306
25	3.290	.304

Three-Dimensional Plotting Program

In order to display the basic structural model and the mode shapes calculated, a three-dimensional plotting program was developed. The program has the ability to superimpose a mode shape, or deformed structural configuration, on top of the original structure. For each mode, the program creates two plots which show the structure at opposite extremes of its vibrational cycle. This is accomplished by scaling the eigenvectors with appropriate constants. These plots allow one to see clearly and with full three-dimensional detail, the results of the analysis. These plots have been a great aid in gaining a physical insight into the nature of the structural dynamic response. The first 15 mode shapes are displayed in Figs. 6-20, respectively. The three-dimensional plotting program also proved to be valuable in checking the basic input data. One could see, almost at a glance, whether or not the nodal points and finite elements had been correctly defined.

The three-dimensional plotting program forms a perspective projection of the object to be displayed. The field of view of the eye is modeled as a pyramid and points falling within the viewing pyramid will be projected onto a display plane to create a two-dimensional image (see diagram below).

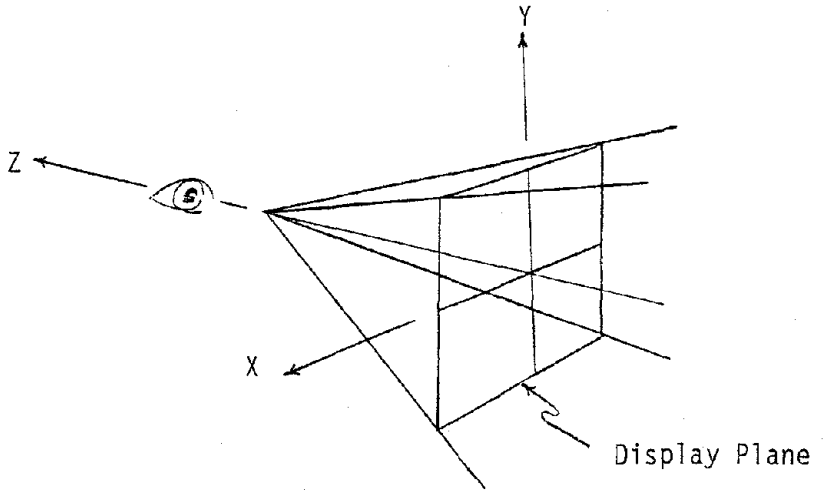

The heart of the plotting program is the calculation of the two-dimensional perspective projection. Because the field of view of the eye is modeled as a four sided pyramid, points can be projected onto the display plane by using similar triangle relationships. A general point (x,y,z) in three-dimensional space will have its projected point (x_D, y_D) calculated by the scheme illustrated below.

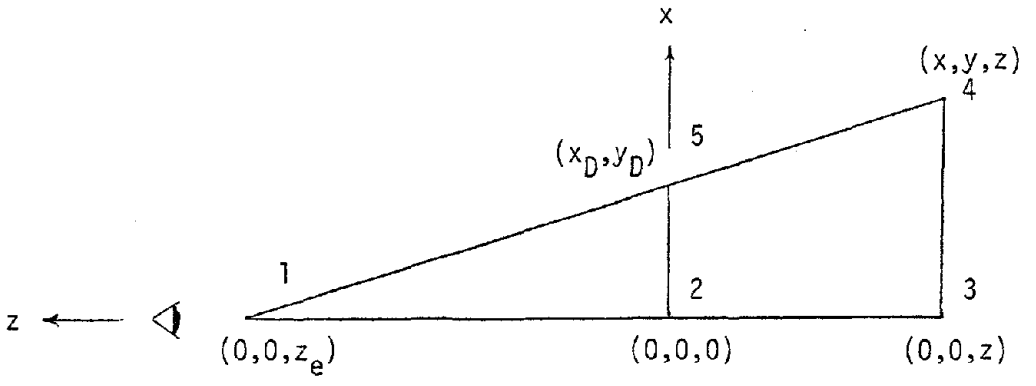

There are two similar triangles Δ 1 2 5 ~ Δ 1 3 4

$$\therefore \quad \frac{x_D}{z_e} = \frac{x}{z_e - z}$$

or

$$x_D = \frac{xz_e}{z_e - z} \tag{13}$$

Similarly

$$y_D = \frac{yz_e}{z_e - z} \tag{14}$$

Each of the 232 joints in the structural model has its projection calculated by means of eqs. 13 and 14. The two-dimensional image can then be displayed as a hard-copy plot or viewed on a CRT screen. In addition to the perspective transformation, there are a number of additional complex auxiliary functions

which must be carried out in order to create a two-dimensional display. The basic flow chart of the program, which outlines the steps necessary to create a two-dimensional projection, is given below.

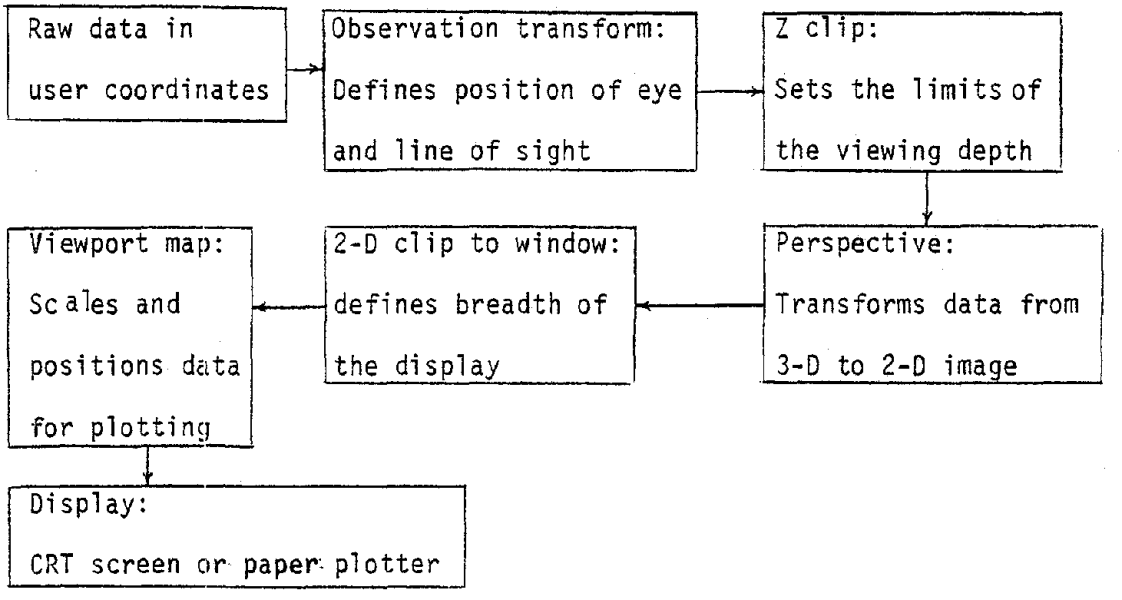

Response Spectrum Analysis

While it is generally true that the lower modes dominate the dynamic structural response, there is the question of exactly how many modes make a significant contribution in a given analysis. In this study, the structure's response to strong-motion earthquakes is investigated. The North-South component of the El Centro, 1940 earthquake was chosen since this is one of the strongest earthquakes for which reliable data has been recorded. The acceleration time-history of the El Centro earthquake is shown in Fig. 21. Also, the spectrum of this earthquake displays a typical pattern seen in many earthquakes [Ref. 4]. The simulated earthquake will be applied in the z-direction (see Fig. 4). This direction is perpendicular to the major axis of the structure which makes it the structure's most vulnerable direction.

Performing a response spectrum analysis enables one to see what the maximum response of each mode considered will be. It also allows one to form a picture of the overall pattern of modal responses. Therefore, a response spectrum analysis was carried out to determine the number of modes which should be included in the earthquake time-history analysis in order to be reasonably sure of including all significant responses. A response spectrum analysis also gives an estimate of the maximum displacements and stresses, which provides a check for the values calculated in the time-history analysis.

The response of each mode of vibration to a given earthquake excitation may be calculated by means of the Duhamel integral equation:

$$Y_n(t) = \frac{R_n}{M_n \omega_n} \int_0^t \ddot{u}_g(\tau)\, e^{-\lambda_n \omega_n (t-\tau)} \sin \omega_n (t-\tau) d\tau \qquad (15)$$

in which

$Y_n(t)$ = response of the n^{th} mode of vibration

R_n = earthquake participation factor = $\sum_i M_i \phi_{in}$

M_i = mass at node "i"

ϕ_{in} = displacement at node "i" in the n^{th} mode

M_n = generalized mass = $\sum_i M_i \phi_{in}^2$

$\ddot{u}_g(\tau)$ = earthquake ground acceleration time-history

λ_n = ratio of damping to its critical value

In each symbol, the subscript "n" refers to the n^{th} mode of vibration. It may be seen in eq. 15 that the response of the n^{th} vibration mode, $Y_n(t)$, depends directly upon the magnitude of the integral. This integral has the dimensions of velocity and the point where it achieves its maximum absolute value is designated as the spectral velocity, S_{V_n}.

$$S_{V_n} = \left| \int_o^t \ddot{u}_g(\tau)\, e^{-\lambda_n \omega_n (t-\tau)} \sin \omega_n (t-\tau) d\tau \right|_{max} \tag{16}$$

Therefore the maximum response of the n^{th} mode equals:

$$Y_{n_{max}} = \frac{R_n}{M_n \omega_n} S_{V_n} \tag{17}$$

Since the maximum response of each mode occurs at a different time, these maxima cannot be simply superposed to give the maximum total response. Clough [Ref. 3] has suggested two ways to obtain an estimate of the total response. The method which shows the greatest agreement with true values is the root-mean-square approximation. From probability considerations, it has been shown that the most probable value of any earthquake response quantity is given by the square root of the sum of the squares of the corresponding modal maxima. The maximum displacements at each node in each

mode are obtained from

$$\{u_{in}\}_{max} = \{\phi_{in}\}Y_{n_{max}} \tag{18}$$

The RMS approximation of the total maxima is then obtained by taking the square root of the sum of the squares of the modal maxima. For example, at node "i"

$$u_{i_{max}} = \sqrt{u_{i1}^2 + u_{i2}^2 + u_{i3}^2 + \ldots + U_{i25}^2} \tag{19}$$

The results of eq. 19 provide a check on the results obtained in the time-history analysis.

An examination of eq. 17, the individual modal maxima (calculated by eq. 18), and the eigenvector associated with each mode, enables one to make a good judgement as to which modes will make a significant contribution to and should be included in a time-history analysis. In eq. 17, one sees the factor

$$\frac{R_n}{M_n} = \text{modal participation factor} \tag{20}$$

The modal participation factor is a function of the mass distribution of the system and the mode shape. Its magnitude gives an indication of the significance of a given mode to the total response. In general, above a certain mode, a trend or pattern of decreasing modal participation factors will be observed; indicating decreasing significance of these higher modes. The modal participation factors for the first 25 modes are given in Table 3. An examination of these factors suggests that 15 modes should be included to obtain good results in a time-history analysis. To determine whether any of the higher modes make a significant contribution, the individual

Table 3 Modal Participation Factors

Mode No.	x-direction	y-direction	z-direction
1	-9.91E-07	5.96E-08	-3.72E+01
2	1.02E+02	-1.70E+00	-2.85E-07
3	4.12E-07	-3.84E-06	-8.54E+01
4	5.74E+01	-3.90E+01	1.70E-05
5	1.01E-05	-7.76E-06	-7.83E+01
6	-2.40E+01	8.63E+00	2.75E-06
7	1.49E-06	-2.15E-06	-1.85E+01
8	-6.52E-06	1.74E-05	-2.02E+01
9	-7.37E+00	-8.28E+01	-3.66E-06
10	-3.22E+01	-2.85E+01	-2.07E-06
11	8.26E-06	1.25E-05	-1.32E+01
12	6.46E+01	-1.07E+01	-1.02E-07
13	-8.22E-07	-1.52E-06	-1.34E+01
14	-2.70E-06	-3.22E-06	4.29E+01
15	1.59E+01	6.49E+01	-1.05E-08
16	7.13E-06	4.75E-06	-2.01E+01
17	-6.54E-06	3.14E-05	1.11E+00
18	-2.20E-04	2.24E-04	1.49E+01
19	1.34E+01	-5.04E+00	2.13E-04
20	3.19E-04	-1.05E-03	-4.19E+00
21	-7.20E+00	-2.31E+00	1.28E-03
22	-1.05E+01	-4.12E+00	3.64E-03
23	-5.26E-03	5.76E-03	-4.89E+00
24	-7.43E-04	7.45E-03	-3.13E+00
25	3.09E-04	-5.76E-02	1.33E+01

modal maxima can be examined at the relevant points as indicated by the mode shapes. Individual modal maxima from selected nodal points are given in Table 4. See Fig. 5 for key to nodal points. The z-displacement maxima are shown since this is the direction in which the earthquake will be applied. The individual modal maxima support the evidence of the modal participation factors that the modes below mode 15 dominate the structural response for an earthquake applied in the z-direction. In particular, modes 1, 3, 5, 7, 8, 11, 13, and 14 are the dominant modes. It was concluded that the use of 15 modes in the El Centro earthquake time-history response analysis, would yield good results.

Table 4. Individual modal maximum Z - displacements (IN) and RMS approximation of maximum nodal displacement.

Mode No.	Node 27	Node 63	Node 101	Node 169	Node 197	Node 231
1	4.23E-03	-3.26E-02	-1.94E-01	1.23E+00	-4.83E-02	-1.41E+01
2	4.97E-12	9.07E-12	1.03E-11	-7.99E-11	-4.96E-11	4.38E-13
3	-3.38E-02	3.10E-01	1.52E+00	-6.32E+00	-8.30E+00	-2.73E+00
4	1.27E-10	4.21E-10	-3.97E-11	3.93E-10	4.01E-09	6.54E-12
5	-2.22E-01	-8.65E+00	-1.64E+01	-1.53E+00	-8.14E-01	-2.01E-01
6	4.64E-10	-1.10E-09	1.42E-09	-5.17E-10	-2.11E-10	-6.89E-13
7	4.04E-02	1.72E-01	1.06E-02	7.73E-01	1.61E+00	9.69E-01
8	-5.57E-01	-1.88E+00	7.84E-01	2.88E-01	-3.15E-03	8.57E-02
9	-1.05E-09	6.95E-10	-1.83E-10	-1.32E-09	-1.29E-09	-8.12E-12
10	1.30E-09	-3.49E-10	-6.67E-10	-5.29E-10	-4.23E-10	-2.60E-12
11	-2.02E-01	-1.94E-01	2.09E-01	-1.03E+00	3.99E-01	6.46E-02
12	4.09E-11	-1.53E-11	1.91E-11	7.70E-12	-5.87E-12	-7.36E-14
13	1.08E-01	1.39E-02	-7.61E-02	-3.80E-01	-6.21E-01	2.54E+00
14	7.59E+00	-1.11E+00	4.83E-01	-5.83E-01	2.31E-01	-3.96E-01
15	1.58E-12	4.26E-12	1.04E-12	2.96E-13	8.97E-14	-6.61E-16
16	3.84E-01	-2.52E-01	3.48E-01	8.01E-02	2.66E-01	2.16E-02
17	-1.32E-02	9.30E-03	3.79E-03	1.65E-02	-8.69E-03	4.53E-01
18	2.08E-01	-2.91E-02	1.89E-01	4.26E-01	-5.98E-01	4.56E-01
19	4.62E-09	2.95E-09	-8.46E-09	4.43E-08	-1.42E-08	7.09E-10
20	2.91E-02	7.08E-02	1.84E-01	-2.67E-02	3.31E-02	-2.62E-02
21	1.68E-08	-1.94E-08	-1.83E-08	9.22E-08	-1.43E-07	2.06E-08
22	4.14E-08	-9.57E-08	1.82E-07	2.31E-07	-5.99E-08	6.51E-08
23	1.20E-03	1.22E-02	3.51E-02	1.74E-02	-3.07E-02	1.64E-02
24	5.77E-03	9.70E-03	1.75E-02	4.39E-03	-1.16E-02	3.91E-03
25	-1.55E-01	-1.55E-01	-2.68E-01	-8.67E-02	3.08E-01	-1.05E-01
RMS	7.63E+00	8.94E+00	1.65E+01	6.08E+00	8.56E+01	1.46E+01
Max % of RMS above mode 15	5.0	2.8	2.1	6.3	7.0	3.1

Earthquake Time-history Response Analysis by Mode Superposition

It was seen in eq. 15 that the response of each mode to the El Centro earthquake can be calculated independently. Since the modal responses are independent of each other, the total response of the structure at any time "t" may be obtained by superposing the individual modal response effects at that time. In matrix form, this superposition may be expressed:

$$\{u_i(t)\} = [\phi_{in}]\{y_n(t)\} \qquad (21)$$

in which

$\{u_i(t)\}$ = displacement at node "i" at time "t"

$[\phi_{in}]$ = matrix of vibration mode shapes, arranged by columns

$\{y_n(t)\}$ = vector of modal responses at time "t"

The distribution of internal axial force, shearing forces, and bending moments at time "t" may be obtained by substituting the displacements and rotations obtained in eq. 21 into the element stiffness matrix equations. For truss elements, there are no rotational degrees of freedom and only axial forces can be computed.

The purpose of the earthquake time-history response analysis is to identify the vulnerable members of the structure and to see what failures the structure would sustain if it were subjected to such a strong-motion earthquake. This can be accomplished by examining the nodal point displacements and the element stresses and moments.

Results and Discussion

The analysis of a complex system results in a large amount of data. In order to visualize the results obtained in this study, two types of graphical presentation were utilized. The El Centro earthquake accelerations were input in 1500 time steps, .02 seconds apart. The program, SAP IV, calculates the resulting nodal point displacements, element stresses, and bending moments for the 30 second duration of the earthquake at each increment of .02 seconds. The results of the calculations were saved every fourth step, i.e., every .08 seconds for 30 seconds. This gives 374 results for each quantity of interest. To obtain the overall picture, programs were written that search through the generated data to find the maximum response of each variable. The stress maxima were then used to calculate buckling and yield ratios for the 778 members of the basic structural model. These ratios are presented in a series of nine graphs which show the maximum axial stress response of the entire structure. In order to see how the structure responded to the earthquake as a function of time, crucial nodal points and elements were selected in each region of the structure and their corresponding time-histories of nodal point displacements, element axial stresses, and bending moments were plotted. Nodal point displacement time-histories and element axial stress time-histories were each plotted for 8 crucial points; selected to span the structure and give an overview of the structure's response. Bending moment time-histories were plotted at 5 points; one at the base of each of the 3 bents and two at the base of the tower.

It has been observed that even small amounts of damping will reduce the structural response sharply [Ref. 4]. The actual damping in the structure is not known, but it is felt that the fraction of critical damping, for structures such as the one being investigated, may fall somewhere between 1

and 5 percent. The analysis was repeated for fractions of critical damping equal to 1 and 5 percent in order to see the effect of viscous damping. It was assumed that all modes have the same viscous damping coefficient.

Using the results of the response spectrum analysis, it is possible to calculate an estimate of the axial stress in each element. These axial stresses can then be used to calculate the yield and buckling ratios. The response spectrum results can be used for comparison and as a check on the time-history axial stress calculations for the case of zero damping.

Yield and Buckling Ratios

The maximum tensile and compressive stresses engendered in a structural member can be conveniently characterized as to damage producing potential, by calculating yield and buckling ratios respectively. The yield strength for the steel in this structure was taken to be 36000 PSI. The buckling stress, σ_{cr}, was calculated by

$\sigma_{cr} = \pi^2 EI/AL^2$ (both ends pinned)

$\sigma_{cr} = 4\pi^2 EI/AL^2$ (both ends fixed)

$\sigma_{cr} = 20.19\ EI/AL^2$ (one end pinned, one end fixed)

in which

E = modulus of elasticity

I = moment of inertia in the member's weak direction

A = cross-sectional area

L = length of the member

The yield and buckling ratios for each member were then calculated as

$$\text{Yield Ratio} = \frac{\text{Max Tensile Stress}}{36000.}$$

$$\text{Buckling Ratio} = \frac{\text{Max Compressive Stress}}{\sigma_{cr}}$$

For columns with bending moments, the axial stress and bending stresses are superimposed to obtain the maximum tensile and compressive stresses. These ratios were calculated for every structural member for each of the 3 fractions of critical damping considered. The components of the structure were separated into a series of nine views. The yield and buckling ratios for each member were then plotted adjacent to each member (see Figs. 22-57). The yield ratios are shown as positive numbers and the buckling ratios are shown as negative numbers. Yield ratios greater than +1.00 or buckling ratios less than -1.00 imply that the corresponding structural member would suffer permanent damage from the earthquake. It is noted that the ratios which are shown as "zero" actually mean either $0 \leq$ YIELD RATIO $< .01$, or $-.01 <$ BUCKLING RATIO ≤ 0. The corners of each section of the structure are marked with their corresponding nodal point numbers so that the section's location on the structure can be easily determined (see Figs. 4 and 5).

Also shown in Figs. 22-57 are yield and buckling ratios which were calculated from results of the response spectrum analysis. SAP IV calculates, as part of the results of the response spectrum analysis, the maximum modal displacements at each nodal point. These displacement maxima enable one to calculate the maximum modal axial stresses in each element using

$$\sigma_n = \frac{E\Delta L}{L}$$

in which

σ_n = maximum element axial stress in mode "n"

E = modulus of elasticity

ΔL = change in element length

L = original element length

The total axial stress in an element can then be estimated by taking a root-mean-square approximation of the modal maximum stresses.

$$\tilde{\sigma} = \sqrt{\sigma_1^2 + \sigma_2^2 + \cdots + \sigma_{15}^2}$$

This estimate provides a check on the time-history response values for the undamped case. The response spectrum estimate gives only a single value which means one must assume the tensile and compressive stresses in each element have the same magnitude. Based on the time-history results, where the maximum tensile and compressive stresses can be obtained separately, this is a reasonable assumption for most elements.

The individual modal maximum stresses can be examined to determine which modes dominate the response at different points on the structure. The results, for the modal maximum stresses in some selected elements which span the structure, are given in Table 5. An examination of this table indicates that modes 1, 3, 7, 11, and 13 are the predominant modes in truss system 1 and that modes 3, 5, 8, and 14 are the predominant modes in truss system 2.

An examination of Figs. 22-57 shows that the stresses calculated from the response spectrum analysis generally indicate the correct pattern of element responses. Some of the estimates differ from the time-history values by 30 to 40 percent, however. This indicates that the response spectrum analysis is useful for predicting trends and for obtaining approximate estimates, but that the results should be used cautiously if one wishes to make predictions.

There are several trends and conclusions that can be drawn from the yield and buckling ratio data. The effect of viscous damping is to sharply reduce the response. While the maximum responses were reduced over 50% for fraction of critical damping equal to .05, the structure would still sustain permanent damage under the action of such a strong earthquake. Buckling of the structural members would be more of a problem than yielding. The cross-

TABLE 5

Individual modal maximum element stresses (PSI) and RMS approximation of maximum element stresses

Mode No.	Element 74	Element 209	Element 349	Element 564	Element 619	Element 727
1	4.460E+01	2.752E+02	2.134E+03	1.154E+04	1.994E+04	2.024E+03
2	2.410E-05	1.933E-05	1.819E-05	7.398E-05	2.105E-04	6.848E-05
3	4.927E+02	1.826E+03	1.310E+04	2.853E+04	4.789E+04	1.410E+04
4	9.081E-04	6.005E-04	9.446E-04	2.014E-03	7.313E-04	7.718E-03
5	1.474E+04	1.447E+04	7.171E+04	5.116E+03	4.723E+03	1.374E+03
6	9.967E-04	4.582E-04	1.621E-03	4.162E-04	7.695E-04	4.938E-04
7	1.777E+02	1.171E+03	8.071E+02	1.068E+04	6.992E+03	1.509E+04
8	1.509E+03	1.371E+04	1.064E+04	6.897E+02	1.817E+03	1.890E+02
9	1.083E-03	3.690E-04	1.932E-04	5.965E-04	1.704E-03	1.152E-03
10	1.581E-03	1.883E-04	4.349E-04	9.070E-05	6.033E-04	4.191E-04
11	7.958E+02	1.630E+03	2.899E+03	5.051E+03	1.212E+03	7.179E+03
12	6.116E-05	8.424E-05	2.171E-05	1.537E-06	1.476E-05	4.669E-06
13	7.788E+02	7.303E+01	1.997E+02	7.584E+03	6.334E+03	2.065E+04
14	6.779E+04	3.350E+04	2.068E+04	6.591E+03	9.532E+03	4.048E+03
15	1.023E-06	1.364E-06	4.548E-07	0.	4.399E-06	1.401E-06
RMS	6.940E+04	3.907E+04	7.661E+04	3.485E+04	5.384E+04	3.044E+04

bracing members in particular, would suffer the heaviest damage. The worst results are seen in the bents and tower especially in bent 2. Truss system 2 shows the next worst results with truss system 1 showing the least damage. The time-history and response spectrum results are summarized in Table 6.

Time-History Plots at Crucial Points

While it is impractical to present the time-history of every quantity of interest, selecting crucial points and elements in each portion of the structure will allow one to form an overview of the structures time-history response to the El Centro earthquake. At each fraction of critical damping, 0., .01, .05, the time histories of 8 nodal point z-displacements, 8 element axial stresses, and 5 bending moments were plotted. For each type of plot, a key identifying the points or elements considered is provided. The key for the nodal point z-displacements is given in Fig. 58. The horizontal z-displacements are shown since the earthquake was applied in the z-direction and these are the maximum displacement at each point. The key for the element axial stress time-histories is given in Fig. 83 and the key for the bending moment time-histories is given in Fig. 108.

These plots reveal several new characteristics of the structural response and reinforce the observations in the previous section. The sharp reduction in the magnitude of the responses as the viscous damping is increased is easily seen. There is also a trend for the maximum responses to occur earlier in the earthquake as the viscous damping is increased. As noted in the previous section, truss system 2 is dominated by the lower modes and truss system 1 is dominated by the higher modes. This effect is seen in a gradually decreasing frequency of response as one examines the time-history curves from the lower end of the structure to the upper end.

TABLE 6 Summary of time-history and response spectrum results

	No. Exceeding Yield Stress	No. Exceeding Buckling Stress	Max Tensile Stress (PSI)	Max Compressive Stress (PSI)	% Reduction
Time-History ξ = 0*.					
Main structure	137	302	88107	- 88107	-
Bents and Tower	44	22	268350	-269612	-
Response Spectrum ξ = 0.					
Main Structure	109	289	105079	-105079	-
Bents and Tower	43	18	268935	-268935	-
Time-History ξ = .01					
Main Structure	53	223	69230	- 69231	21.4
Bents and Tower	26	14	211676	-210841	21.8
Time-History ξ = .05					
Main Structure	7	133	41370	- 41369	53.0
Bents and Tower	17	12	129637	-129034	52.1

* ξ = Fraction of Critical Damping

There are 697 elements in the main structure.

There are 81 elements in the bents and tower.

References

[1] Turner, M. J., et al., "Stiffness and Deflection Analysis of Complex Structures," Journal of Aeronautical Sciences, Vol. 23, No. 9, Sept. 1956, pp. 805-823.

[2] Clough, R. W. and Tocher, J. L., "Finite Element Stiffness Matrices for the Analysis of Plate Bending," Proceedings of the Conference on Matrix Methods in Structural Mechanics, Air Force Flight Dynamics Lab. Report TR-66-80., Dayton, Ohio, Oct. 1965.

[3] Clough, R. W., "Earthquake Analysis by Response Spectrum Superposition," Bulletin of the Seismological Society of America, Vol. 52, No. 3, July, 1962, pp. 647-660.

[4] Housner, G. W., Martel, R. R., and Alford, J. L, "Spectrum Analysis of Strong Motion Earthquakes," Bulletin of the Seismological Society of America, Vol. 43, No. 2, April, 1953, pp. 97-119.

[5] Newman, W. M., and Sproull, R. F., Principles of Interactive Computer Graphics, McGraw-Hill, 1973.

[6] Clough, R. W., and Penzien, J., Dynamics of Structures, McGraw-Hill, 1975.

List of Figures

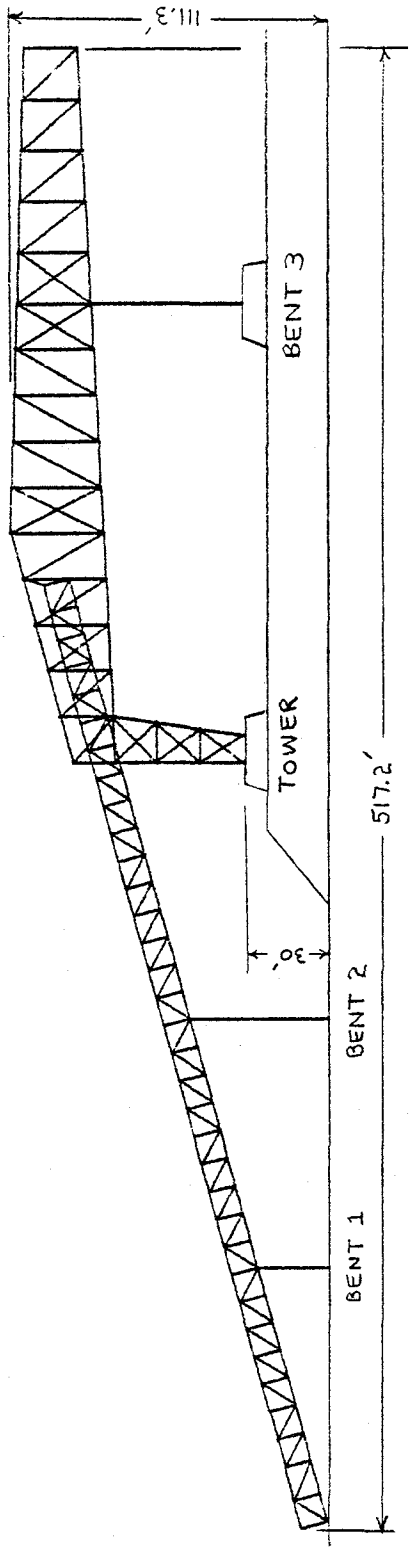

Figure 1

Side view of supporting structure for conveyors No. 28 and No. 29.

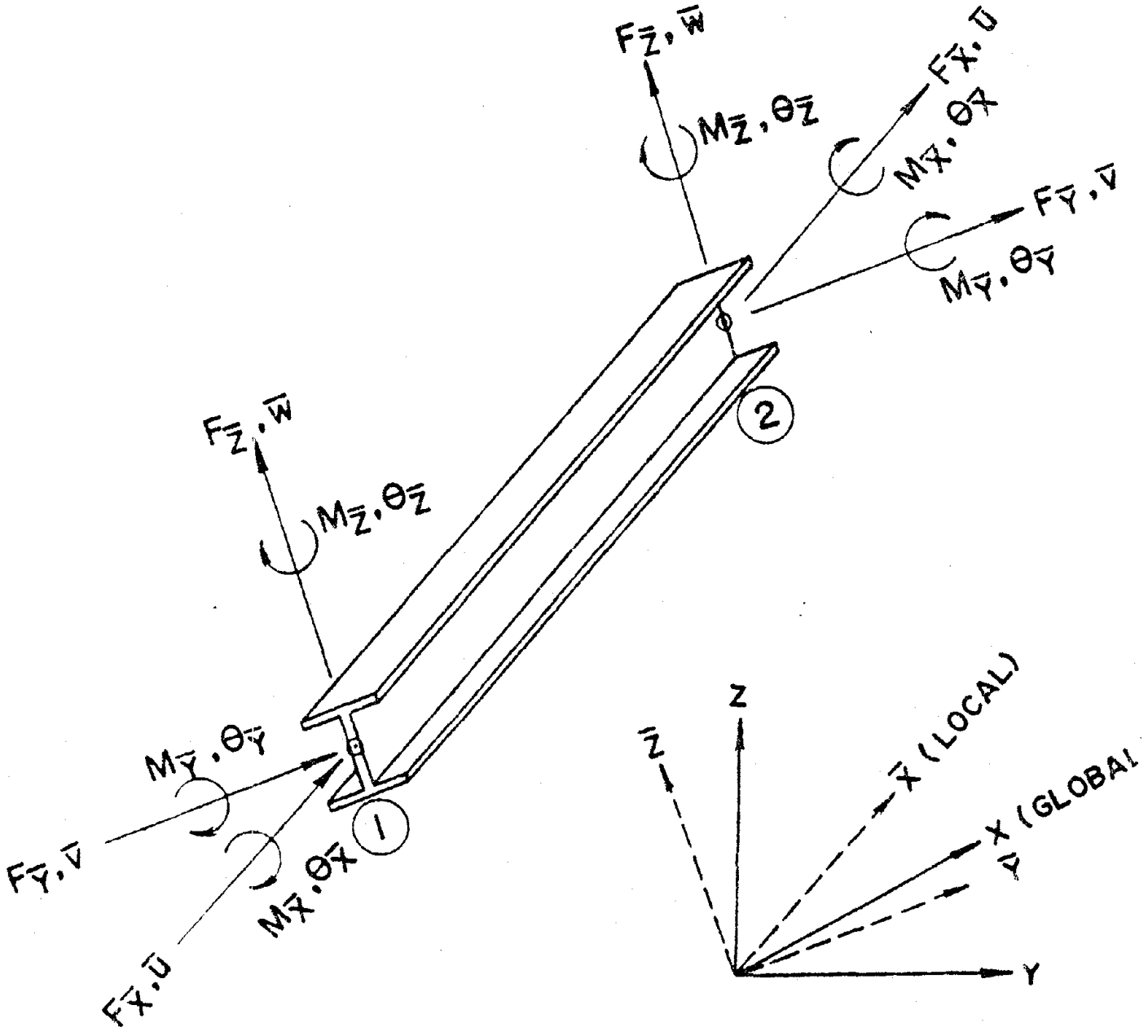

Figure 2

Description of a general three-dimensional beam finite element.

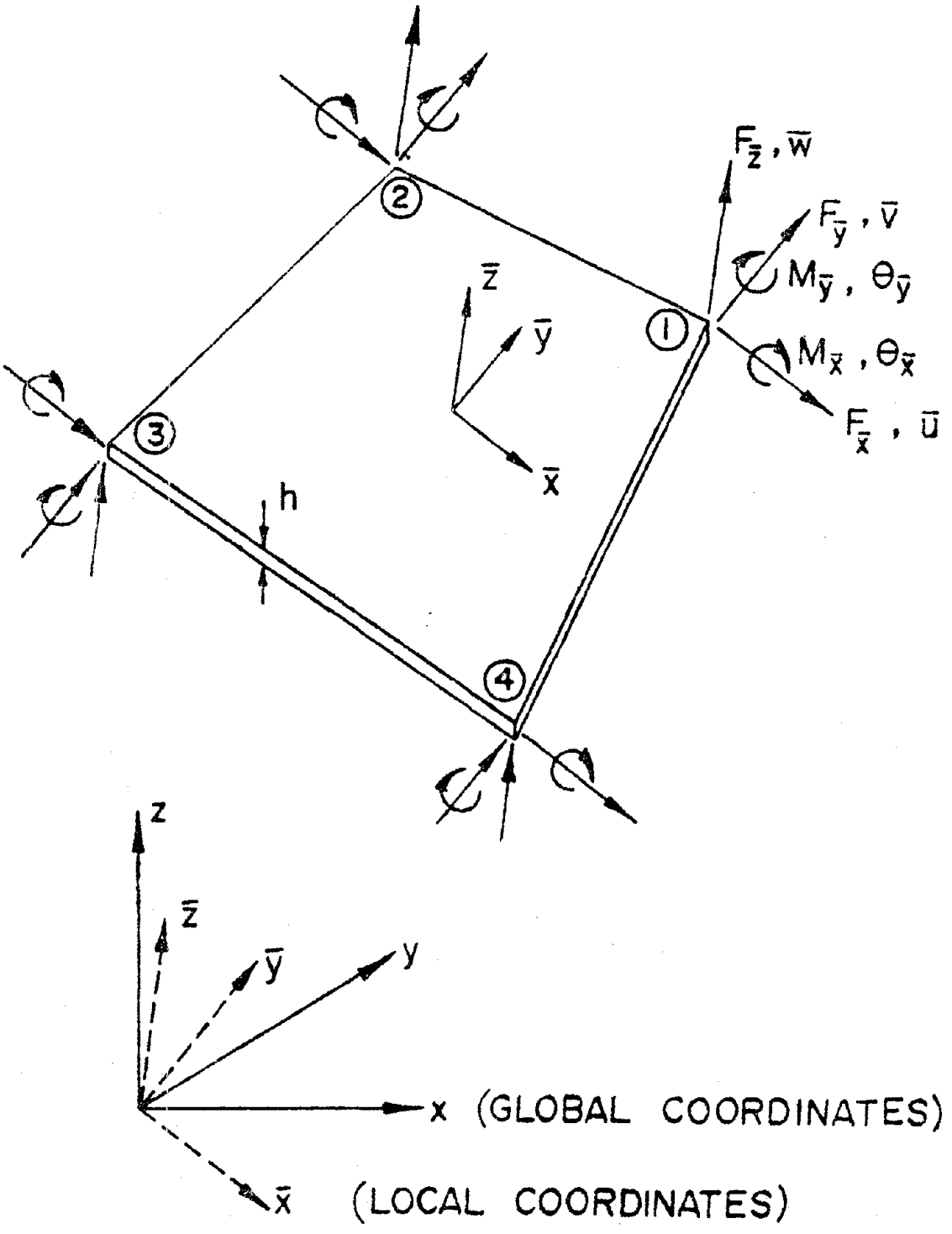

Figure 3

Description of a general quadrilateral plate finite element in the three-dimensional space.

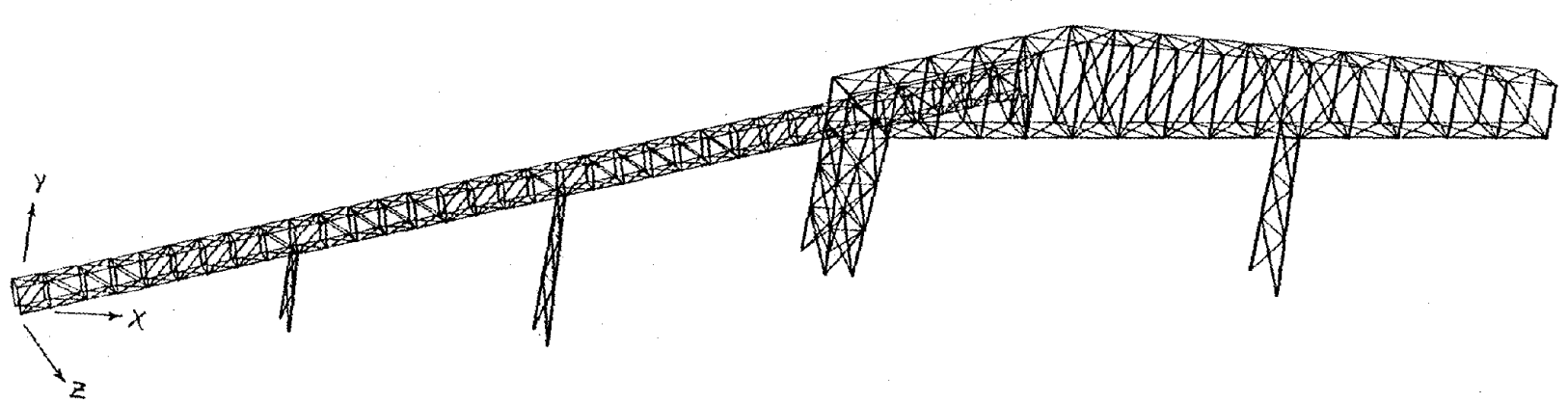

Figure 4
Basic structural model

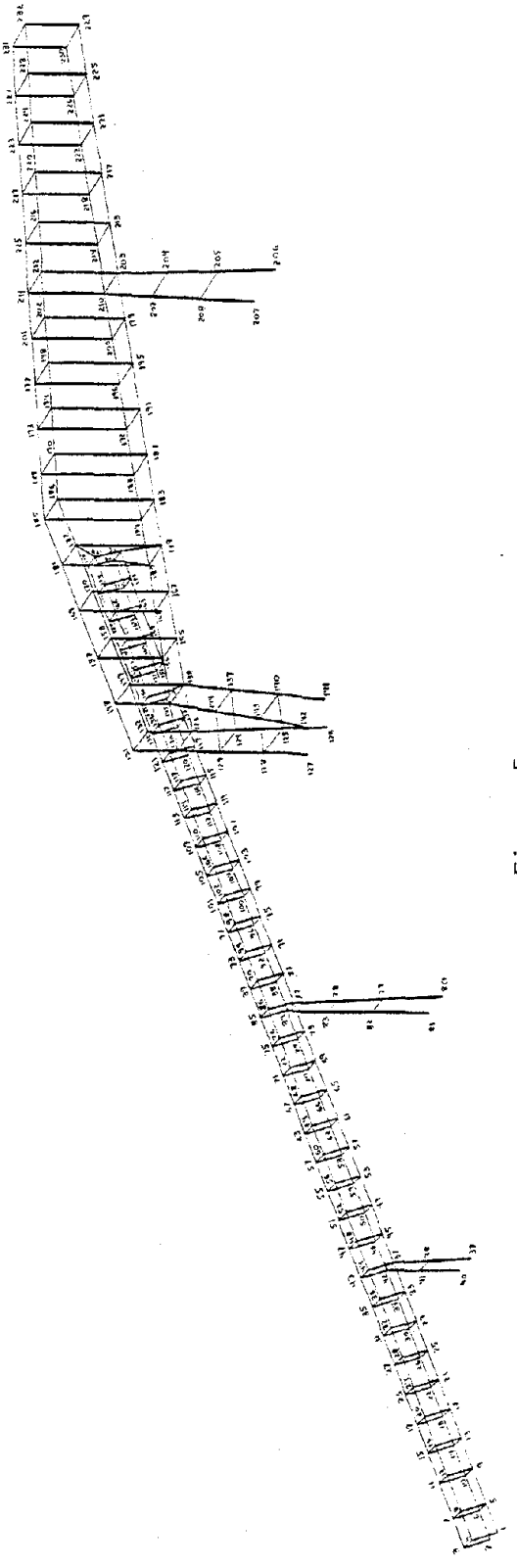

Figure 5

Structural skeleton showing nodal point numbers

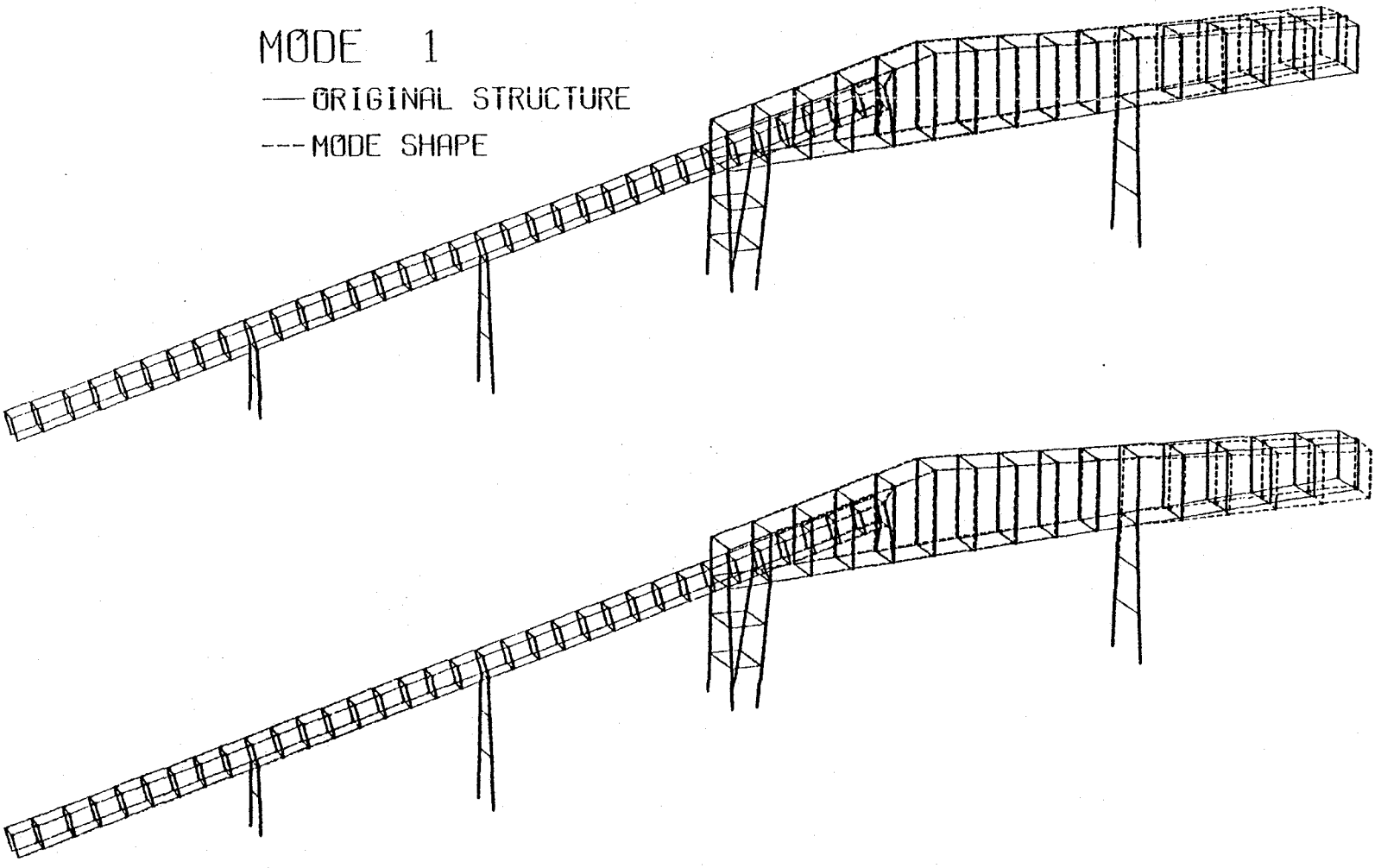

Figure 6

First vibrational mode, Frequency = .440 Hz.

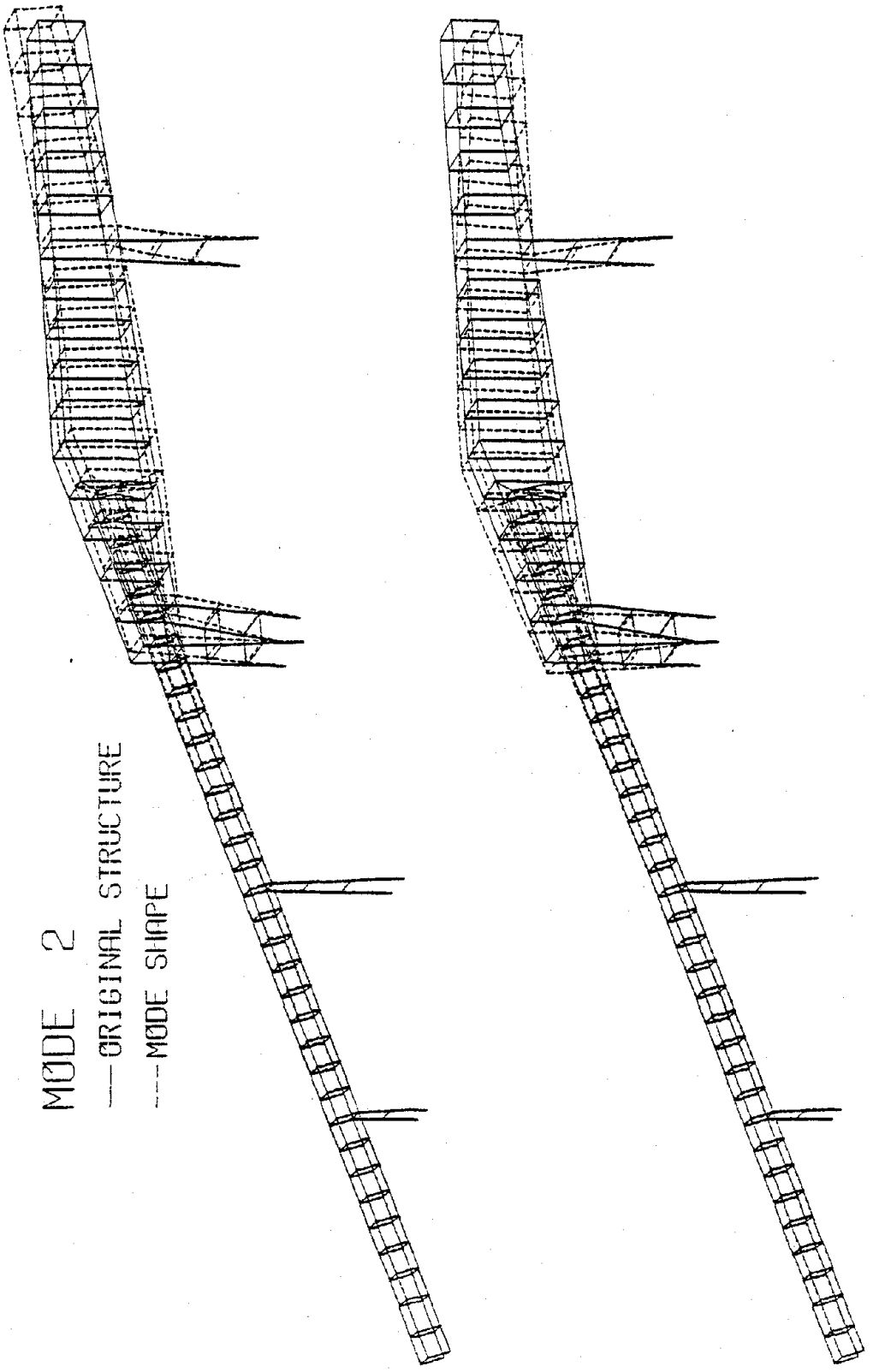

Figure 7

Second vibrational mode, Frequency = .576 Hz.

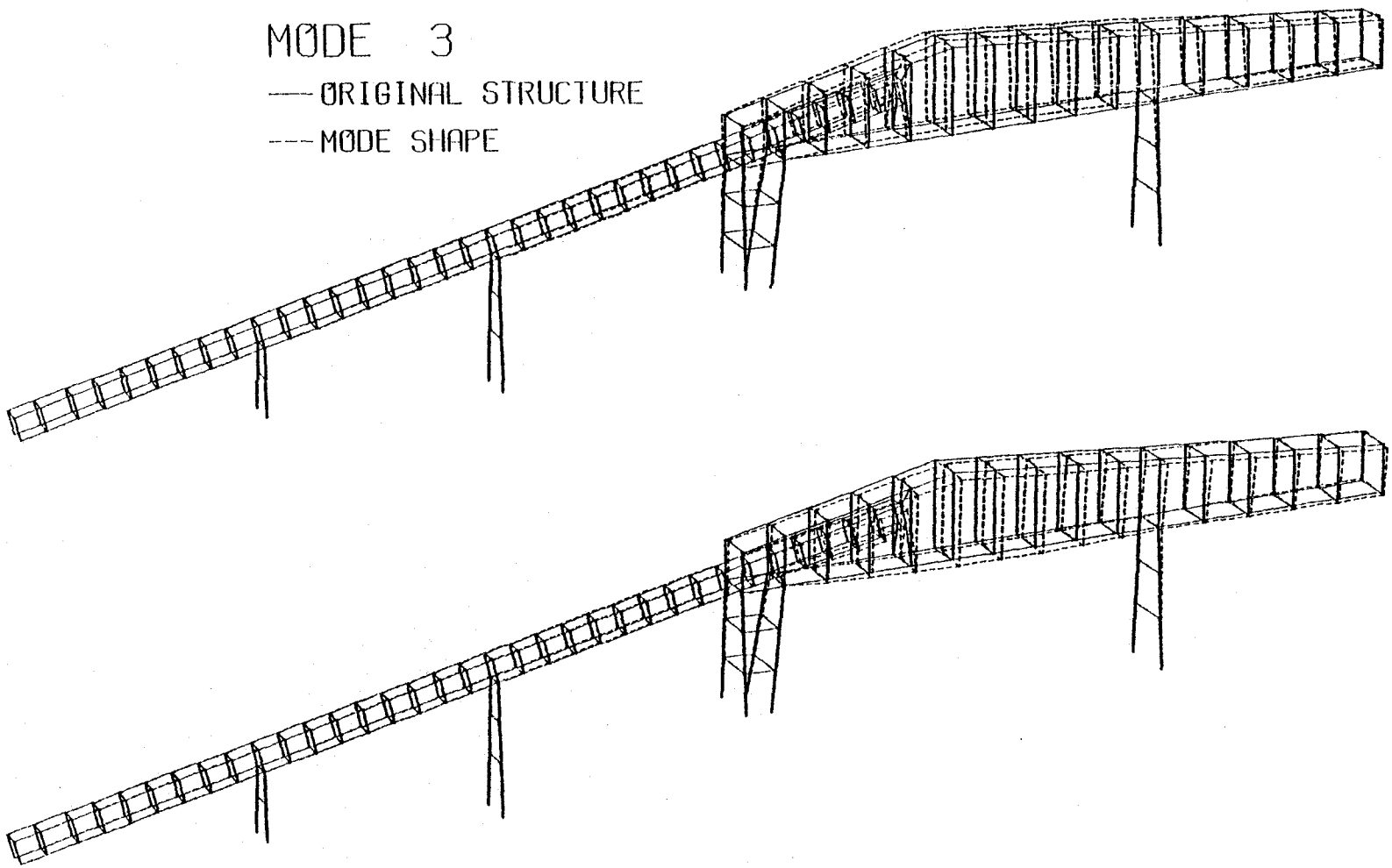

Figure 8

Third vibrational mode, Frequency = .716 Hz.

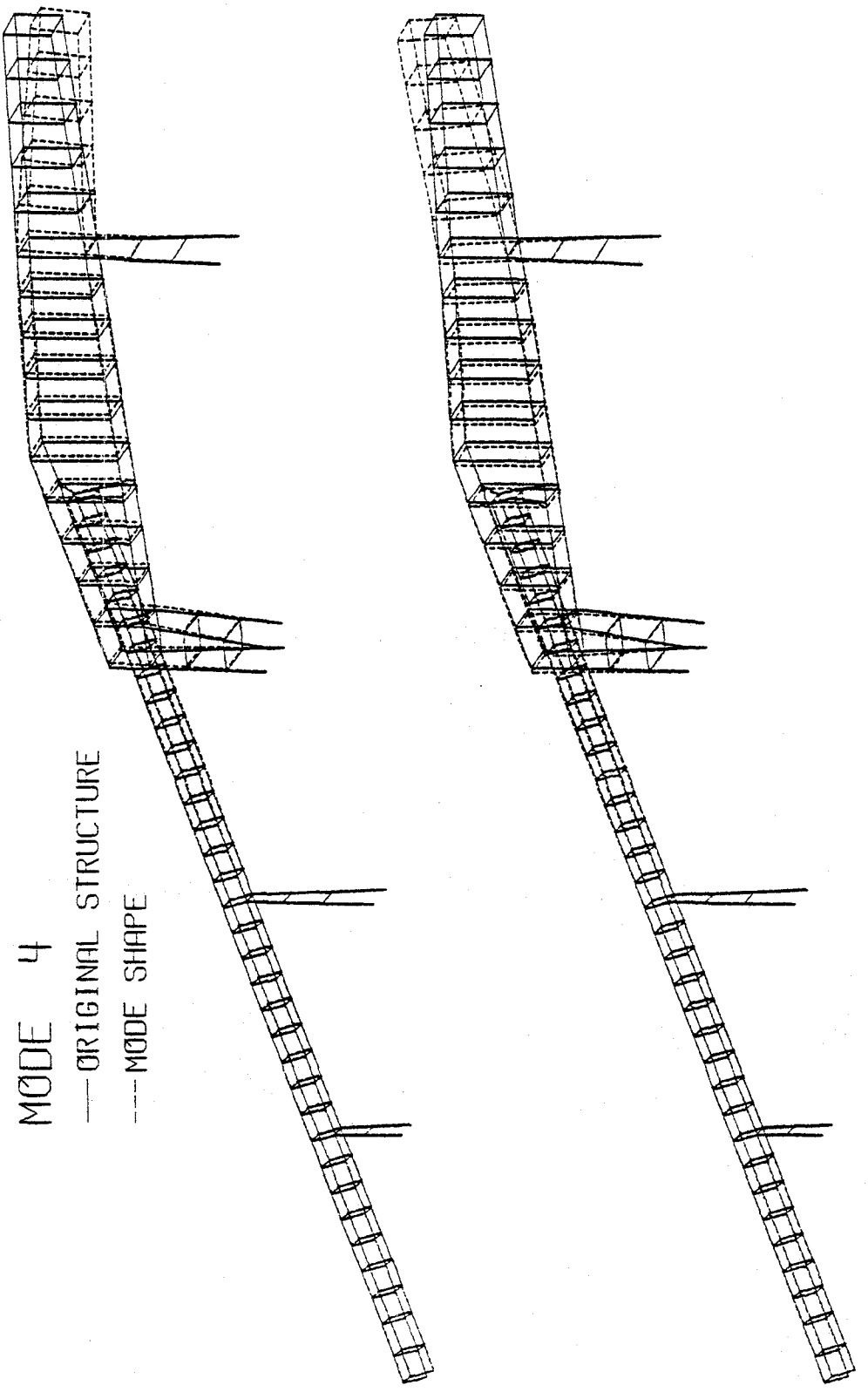

Figure 9

Fourth vibrational mode, Frequency = .775 Hz.

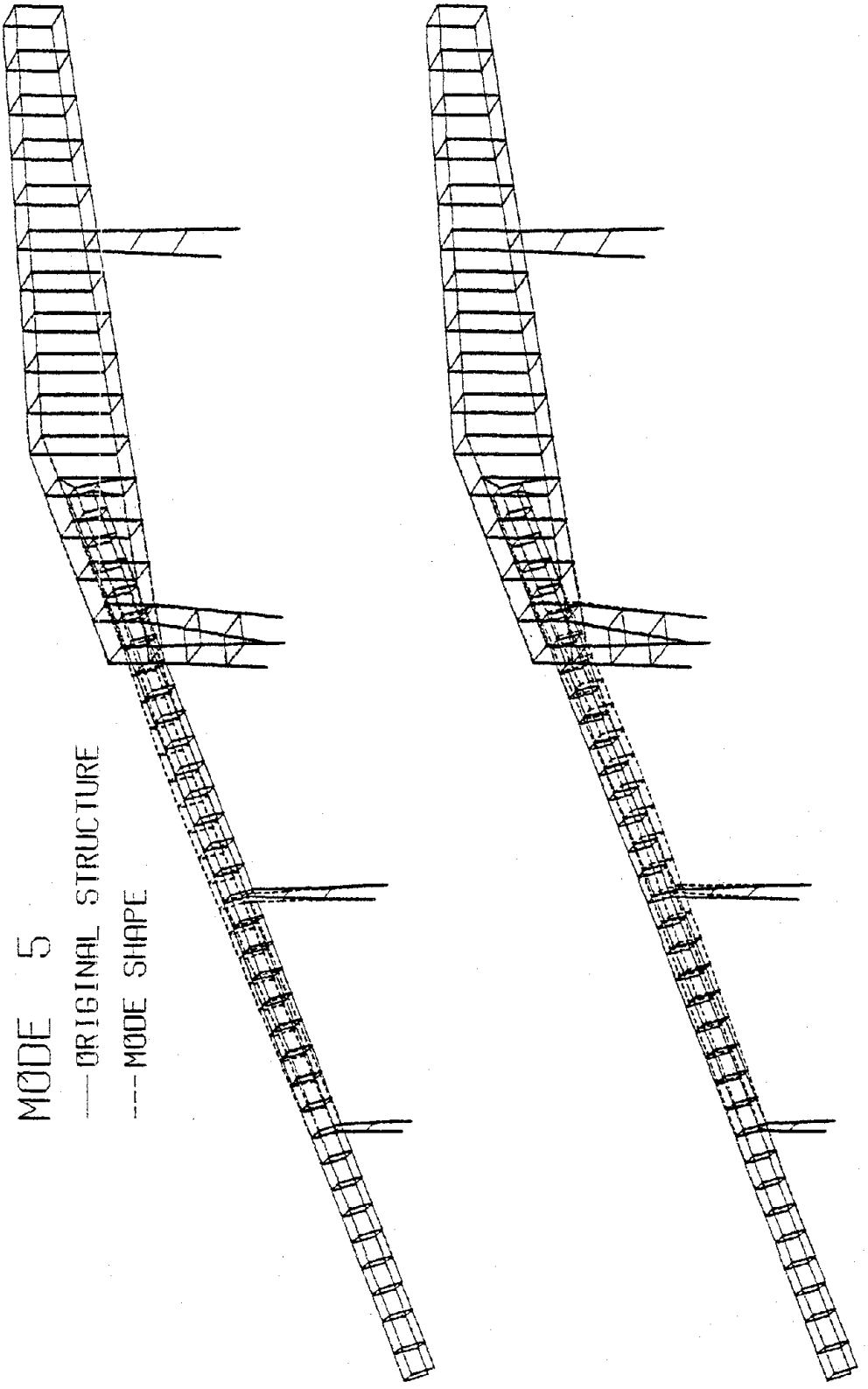

Figure 10

Fifth vibrational mode, Frequency = 1.059 Hz.

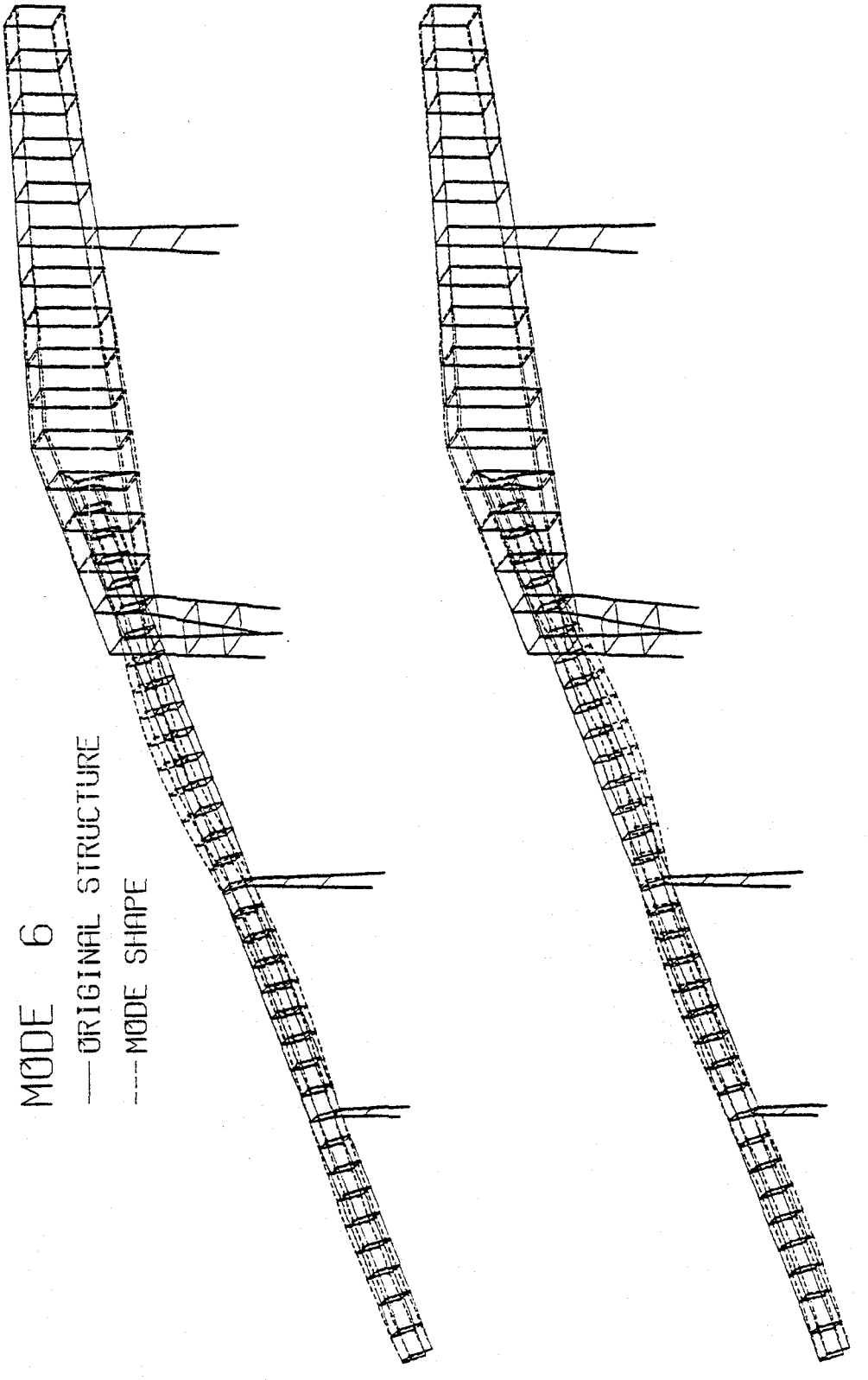

Figure 11

Sixth vibrational mode, Frequency = 1.268 Hz.

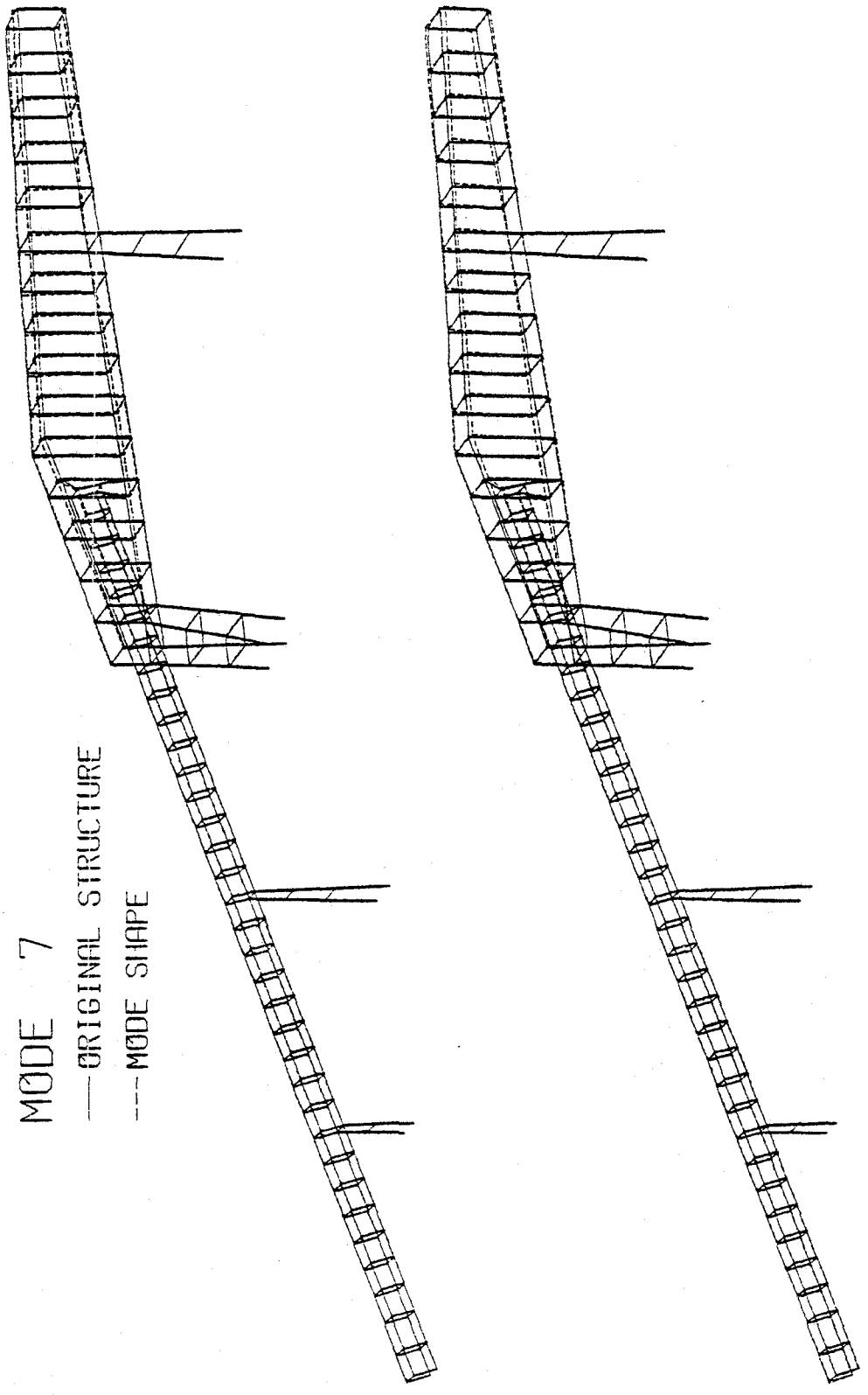

Figure 12

Seventh vibrational mode, Frequency = 1.299 Hz.

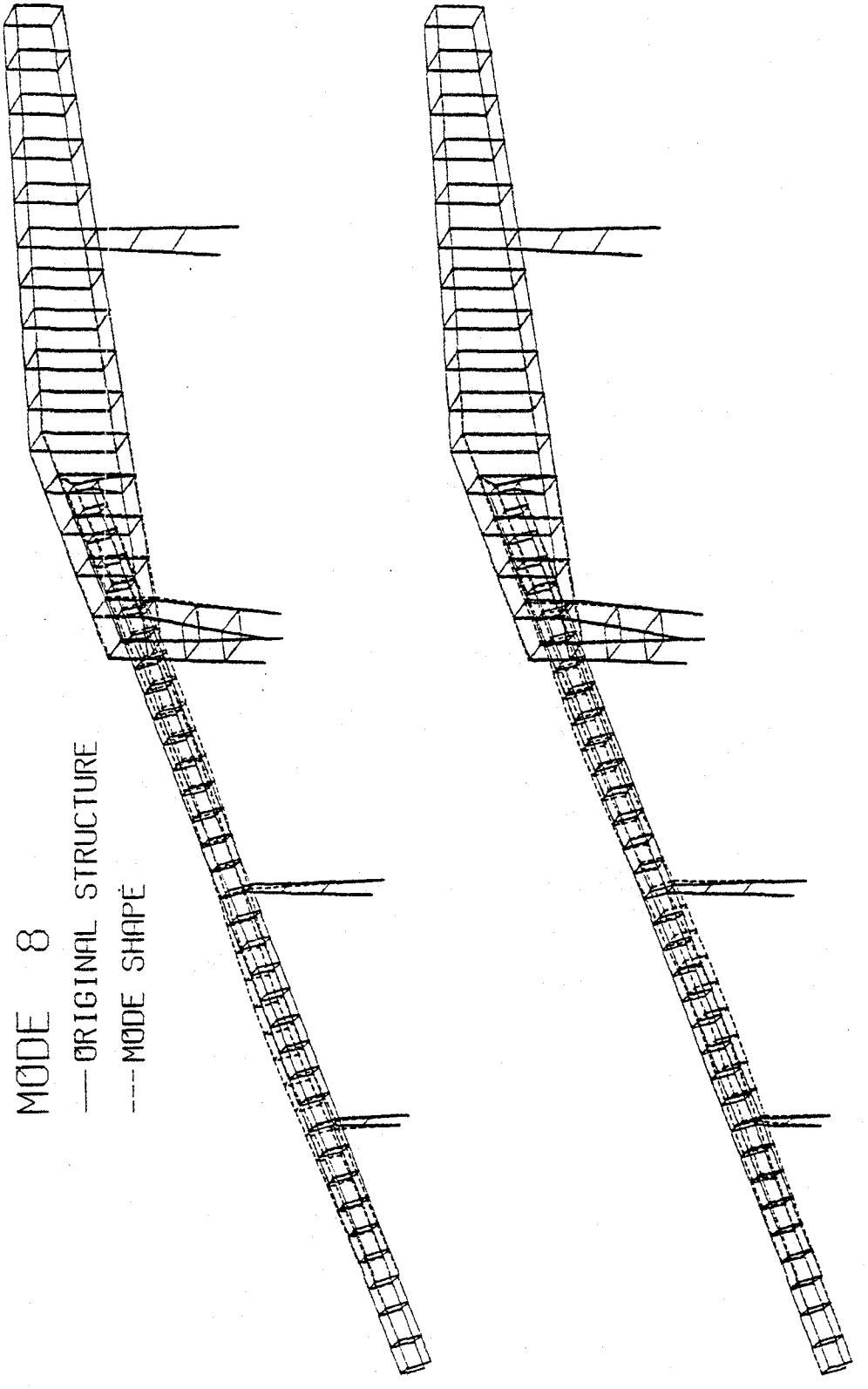

Figure 13

Eighth vibrational mode, Frequency = 1.354 Hz.

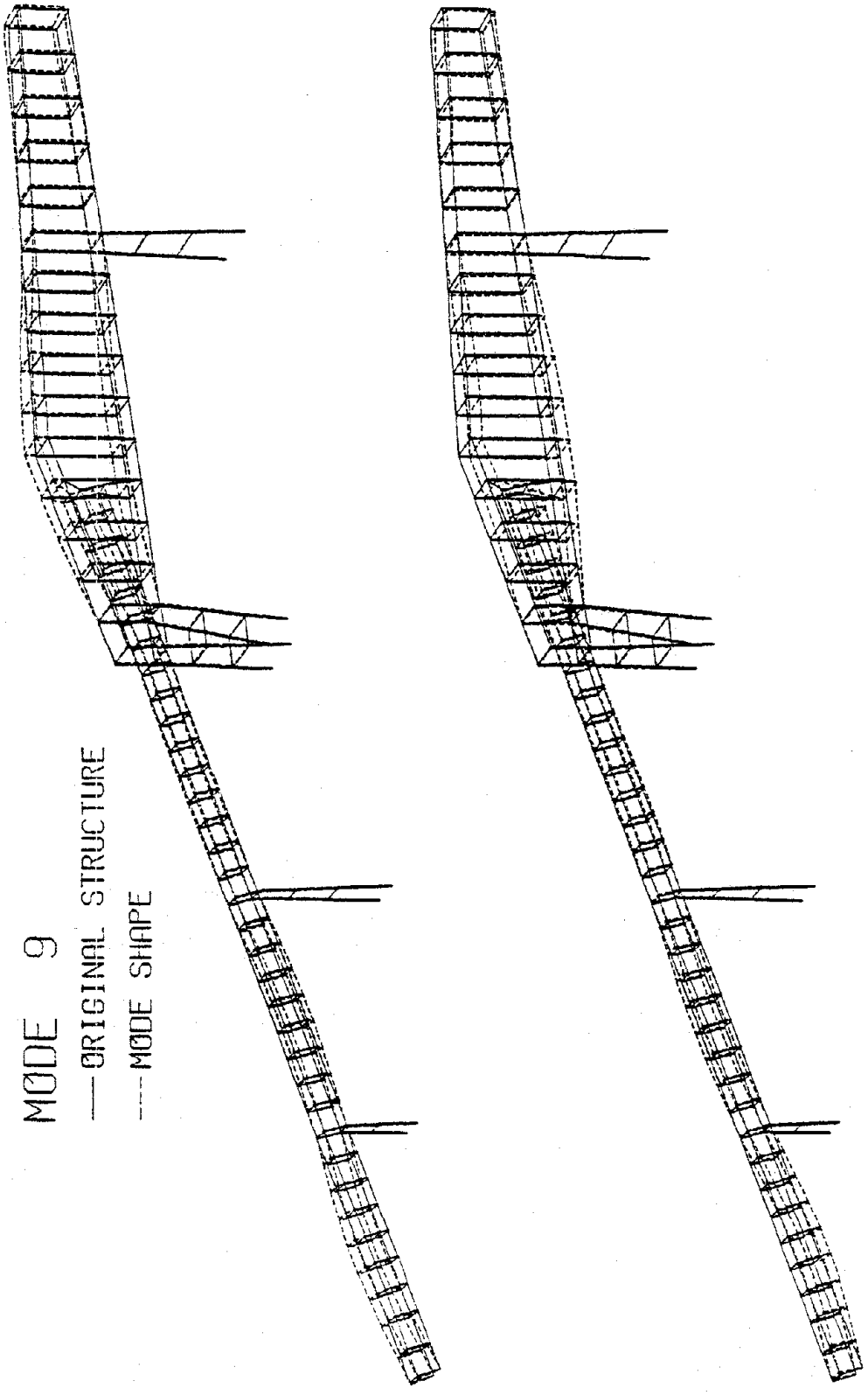

Figure 14

Ninth vibrational mode, Frequency = 1.503 Hz.

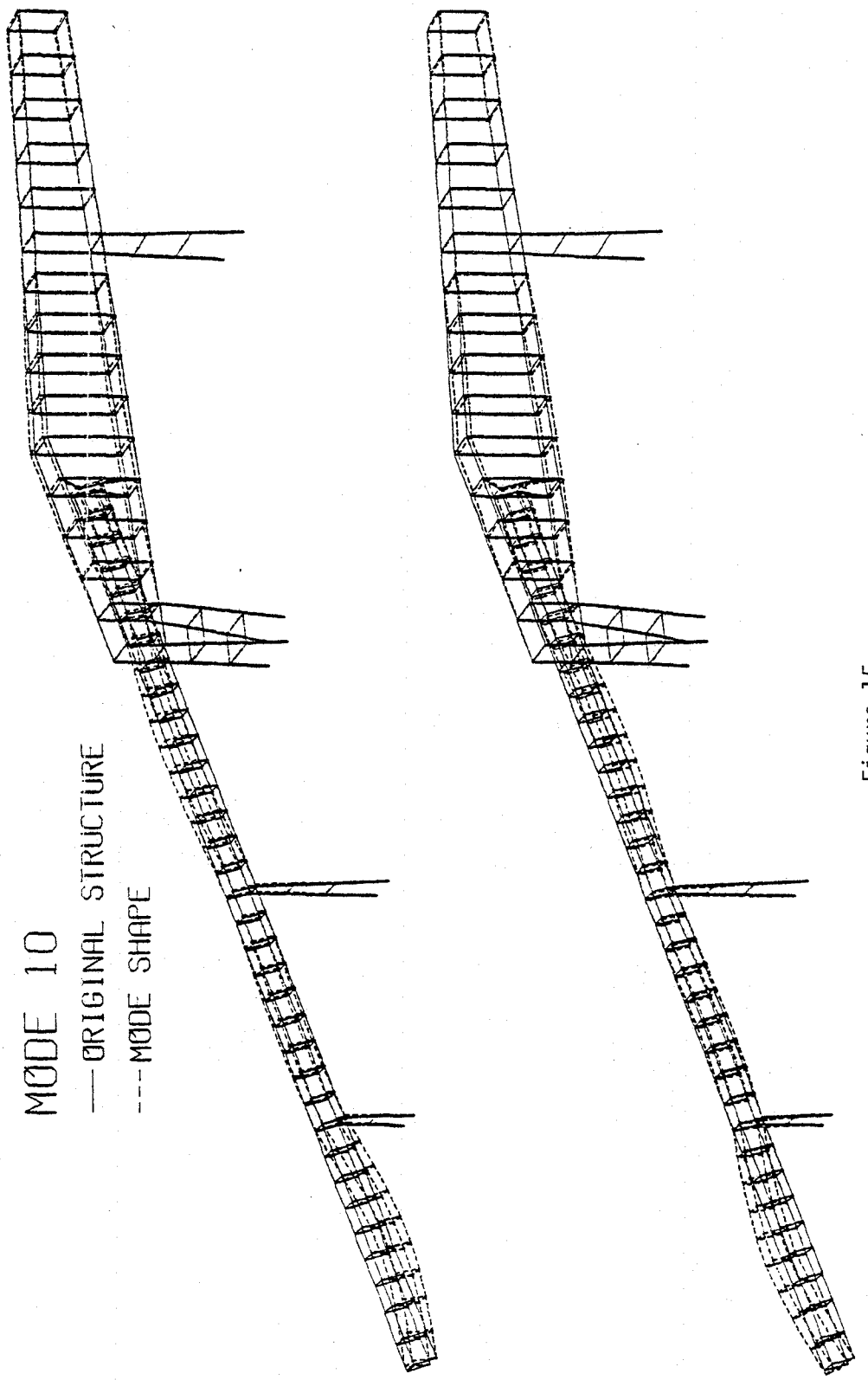

Figure 15

Tenth vibrational mode, Frequency = 1.557 Hz.

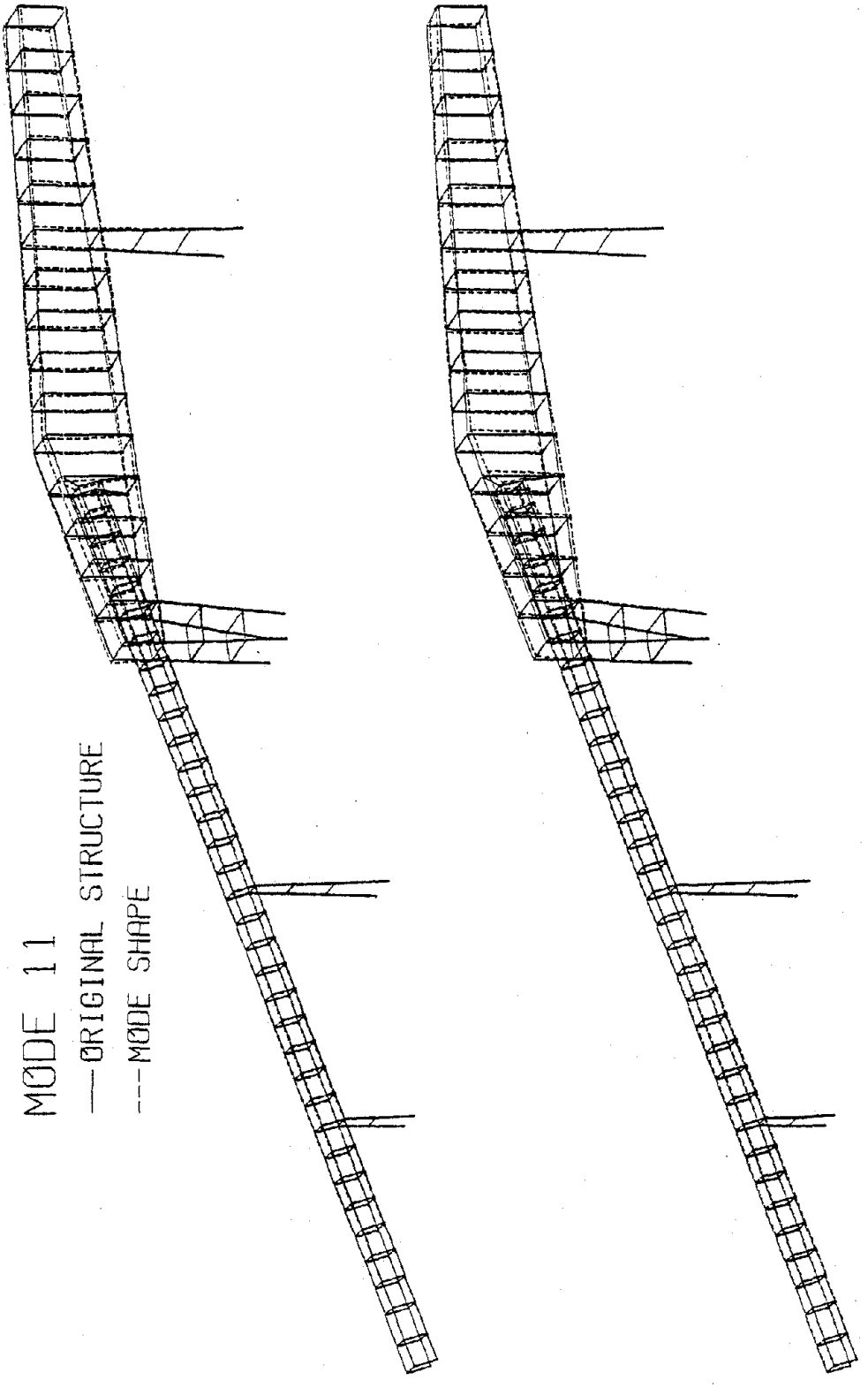

Figure 16

Eleventh vibrational mode, Frequency = 1.612 Hz.

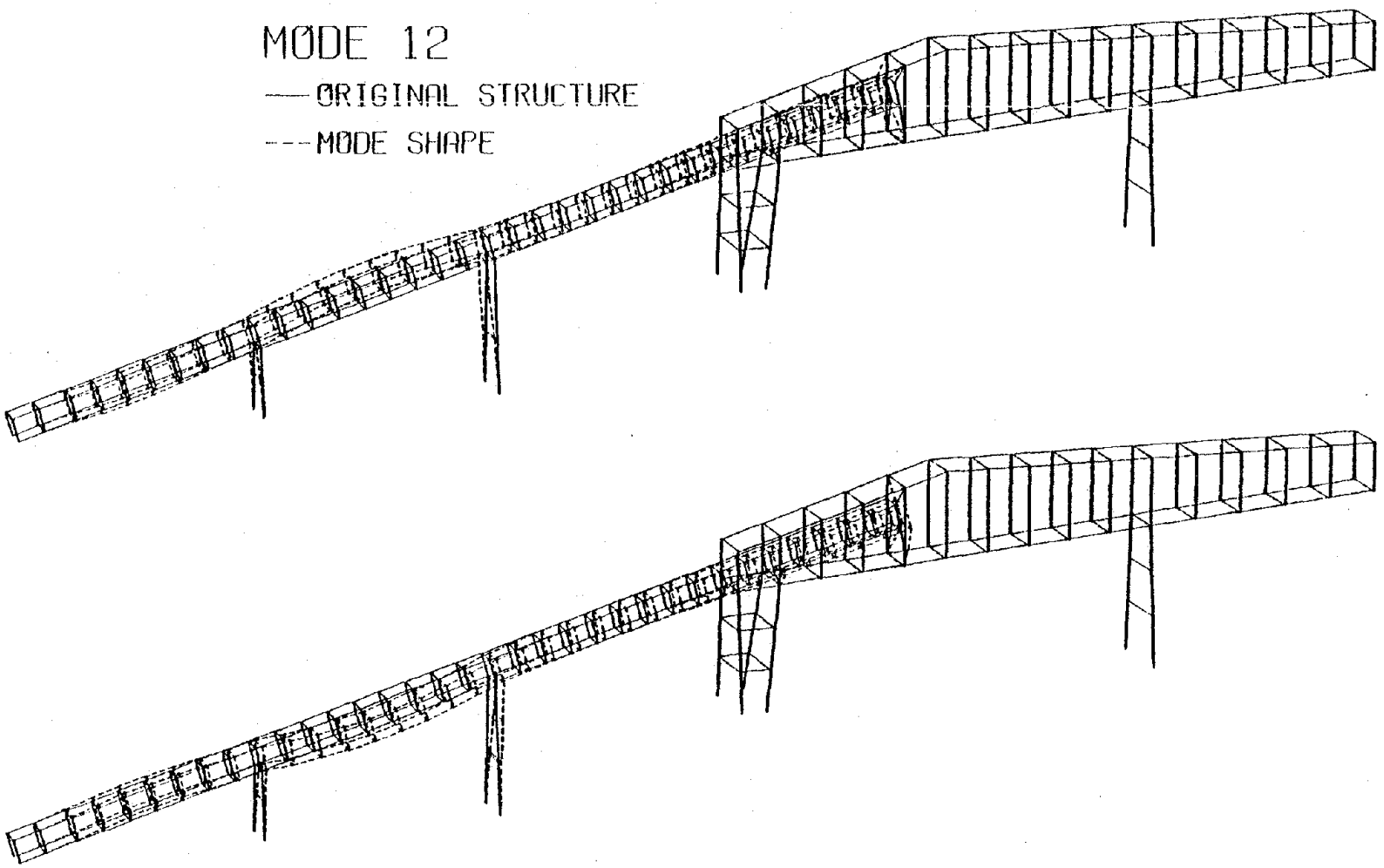

Figure 17

Twelfth vibrational mode, Frequency = 1.709 Hz.

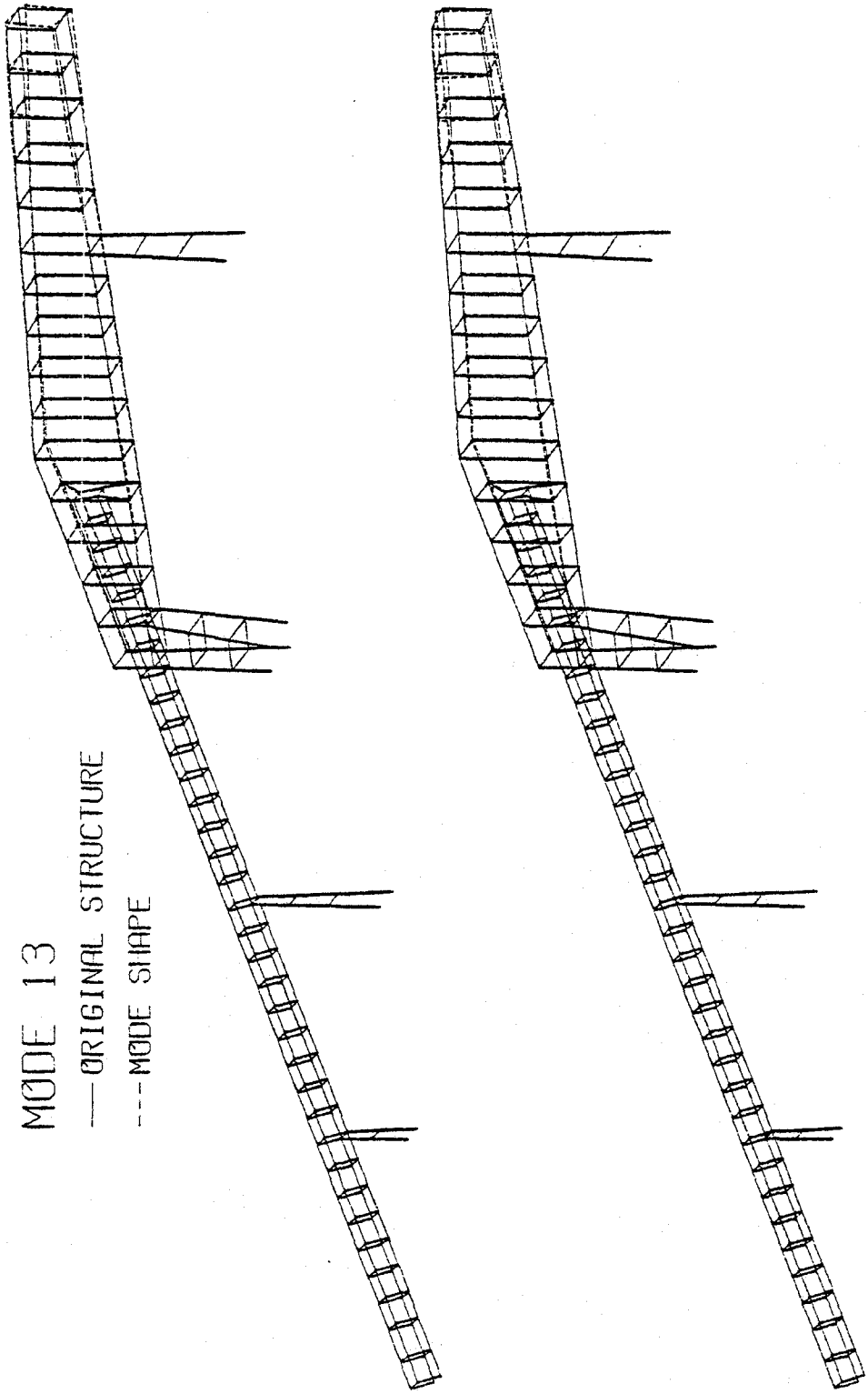

Figure 18

Thirteenth vibrational mode, Frequency = 1.794 Hz.

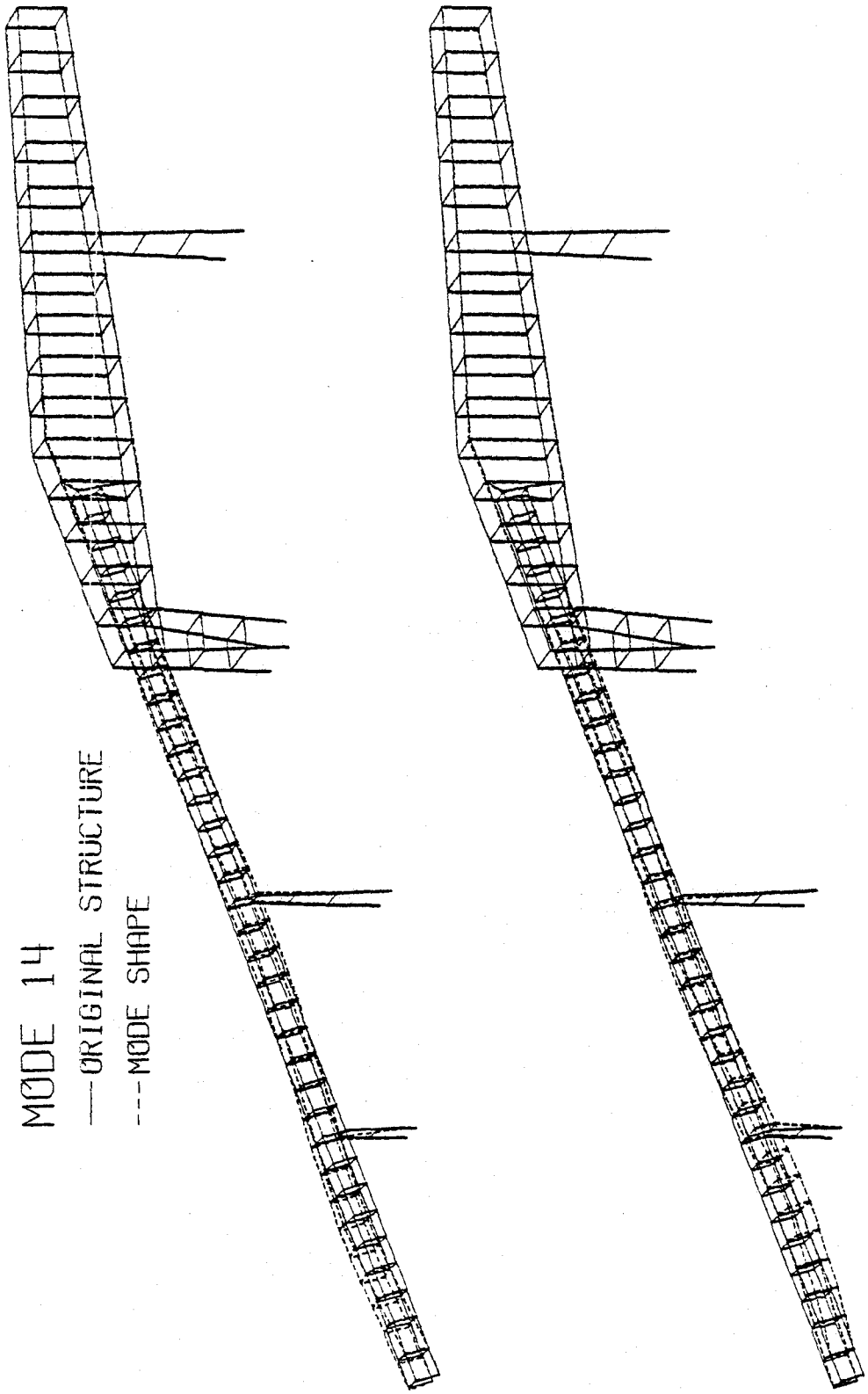

Figure 19

Fourteenth vibrational mode, Frequency = 1.897 Hz.

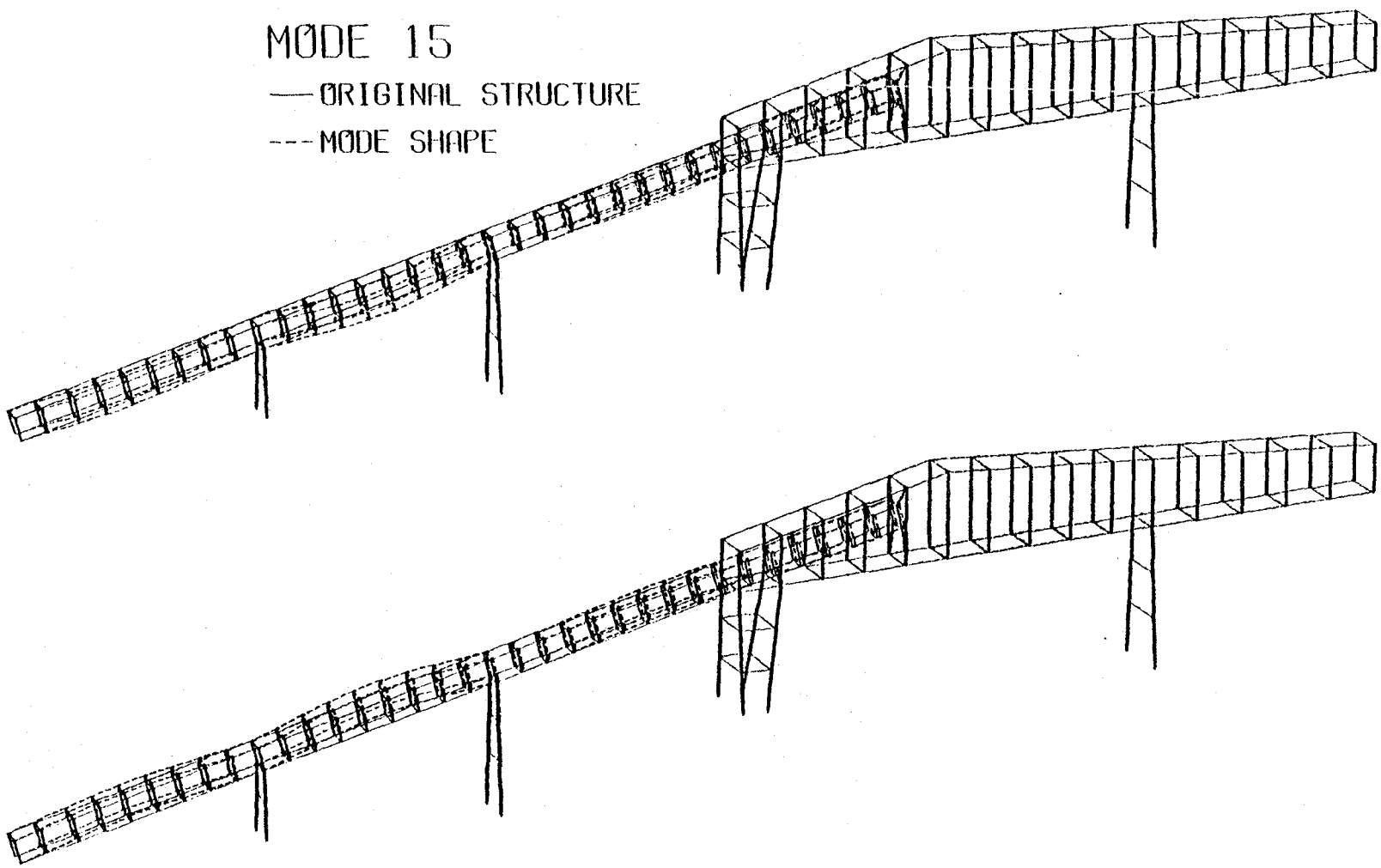

Figure 20

Fifteenth vibrational mode, Frequency = 2.079 Hz.

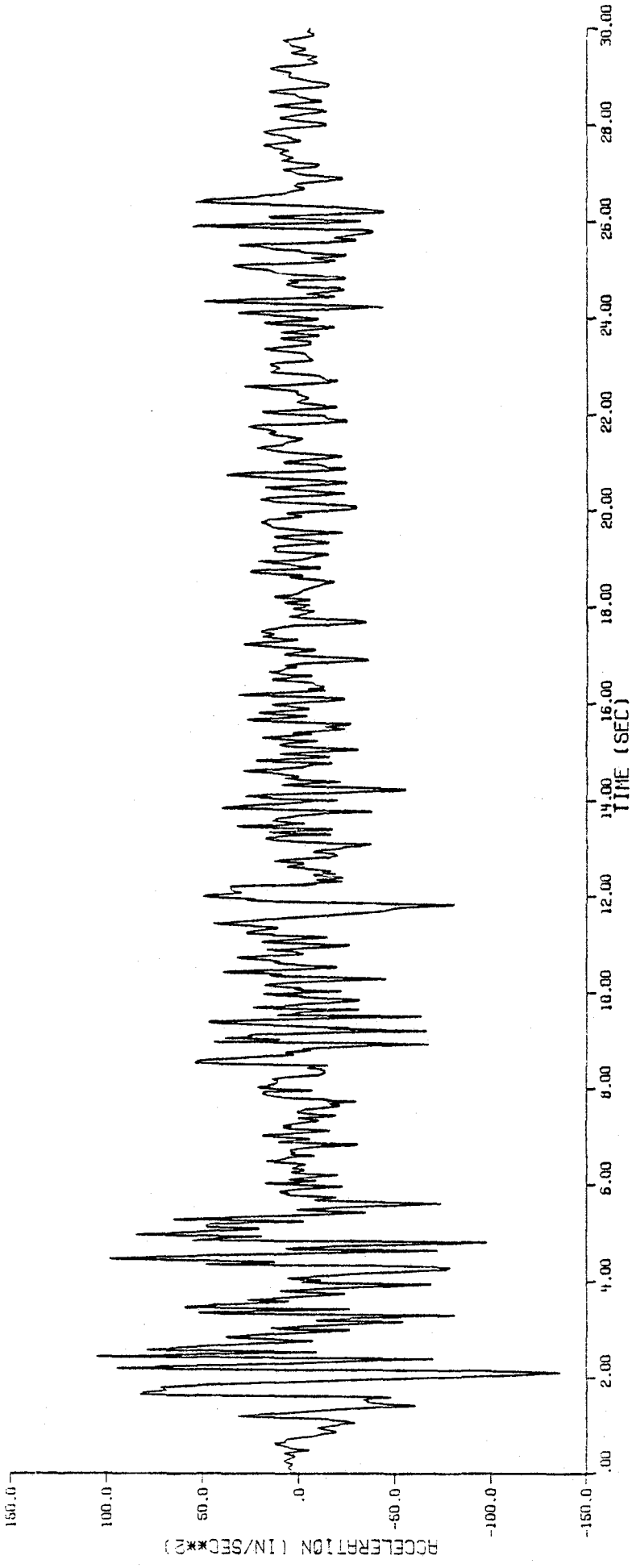

Figure 21

The North-South acceleration time-history of the 1940 El Centro earthquake.

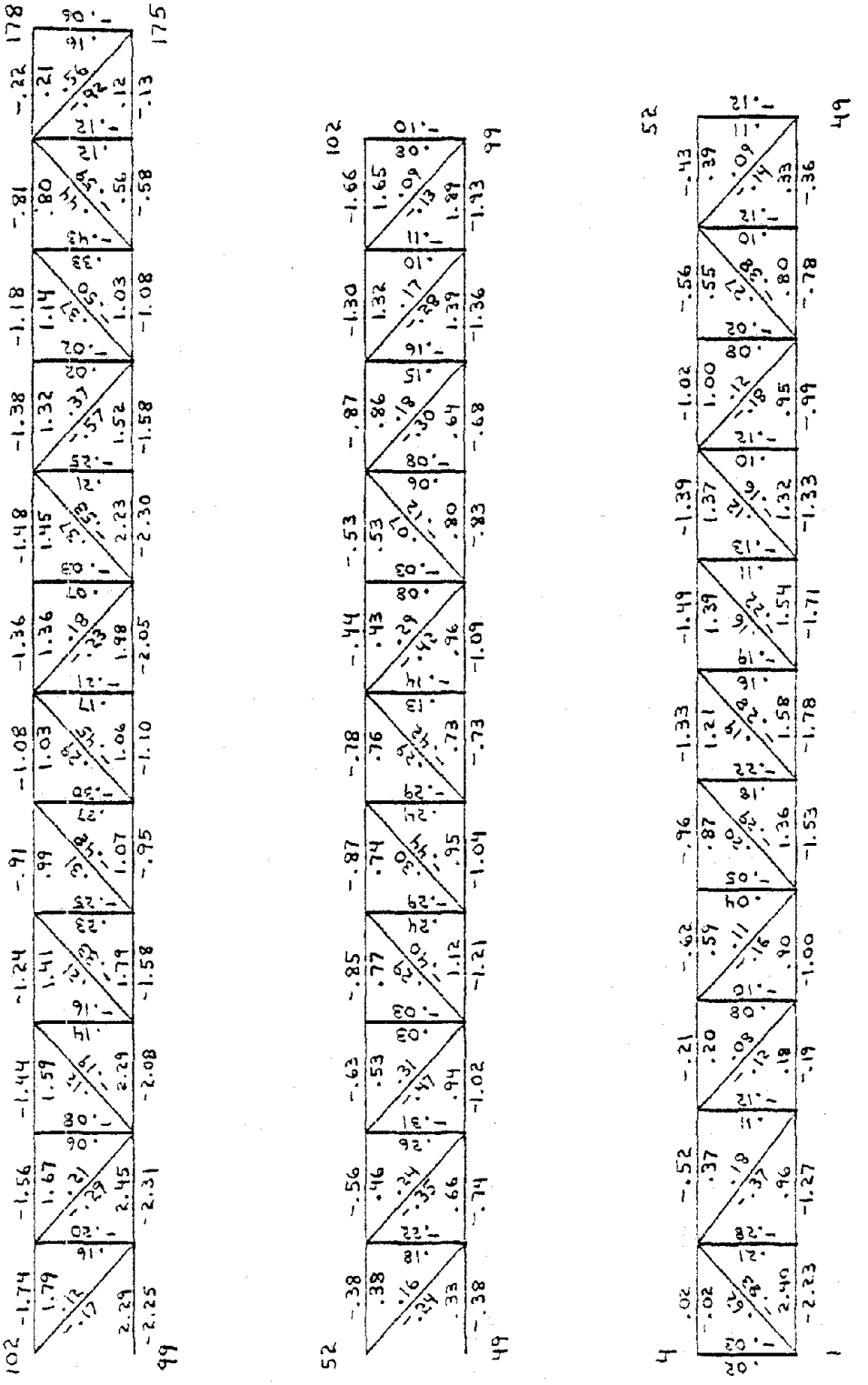

Figure 22

Buckling and yield ratios, truss system 1: front view, undamped.

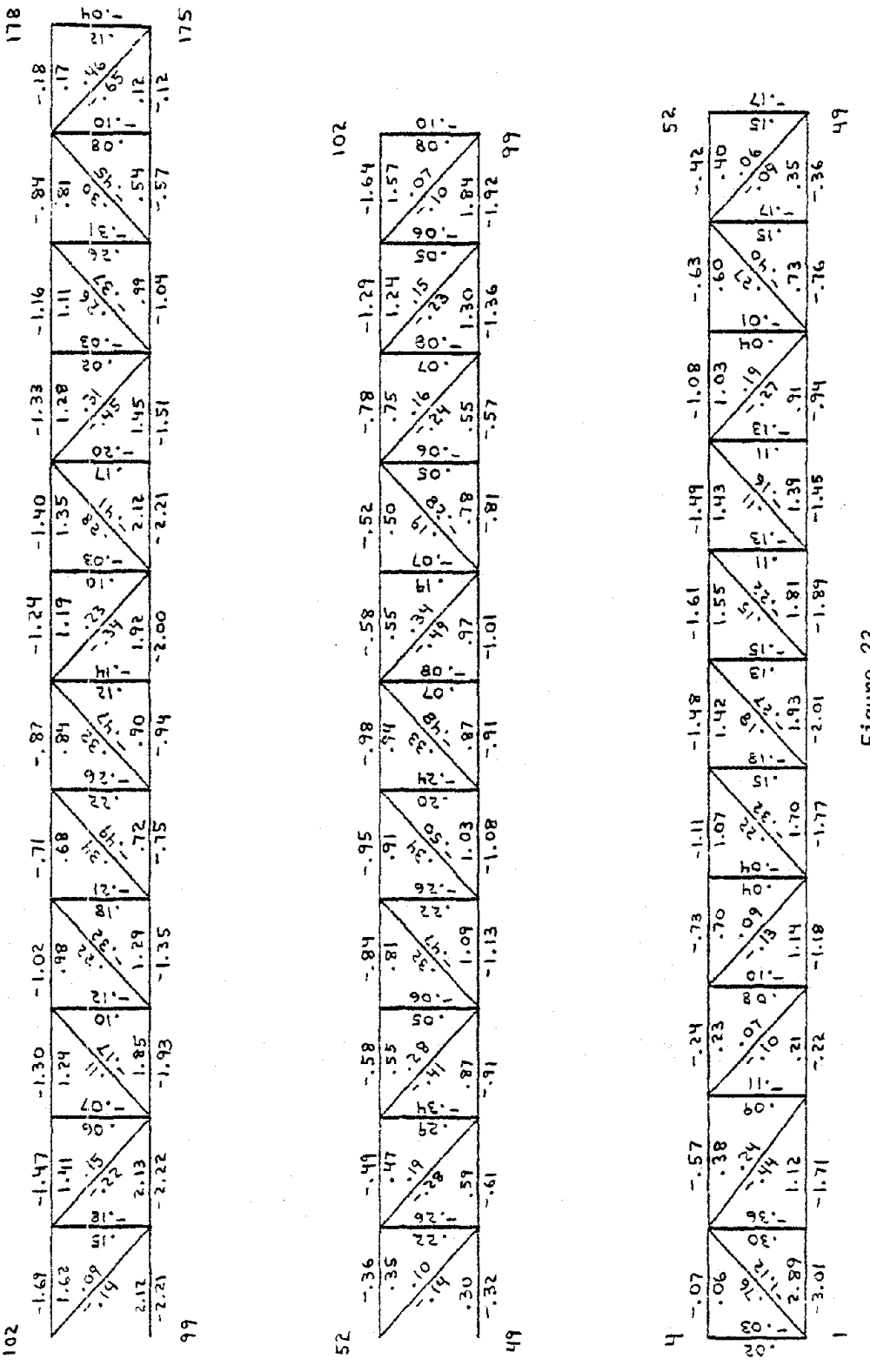

Figure 23

Buckling and yield ratios from the response spectrum analysis, truss system 1: front view, undamped.

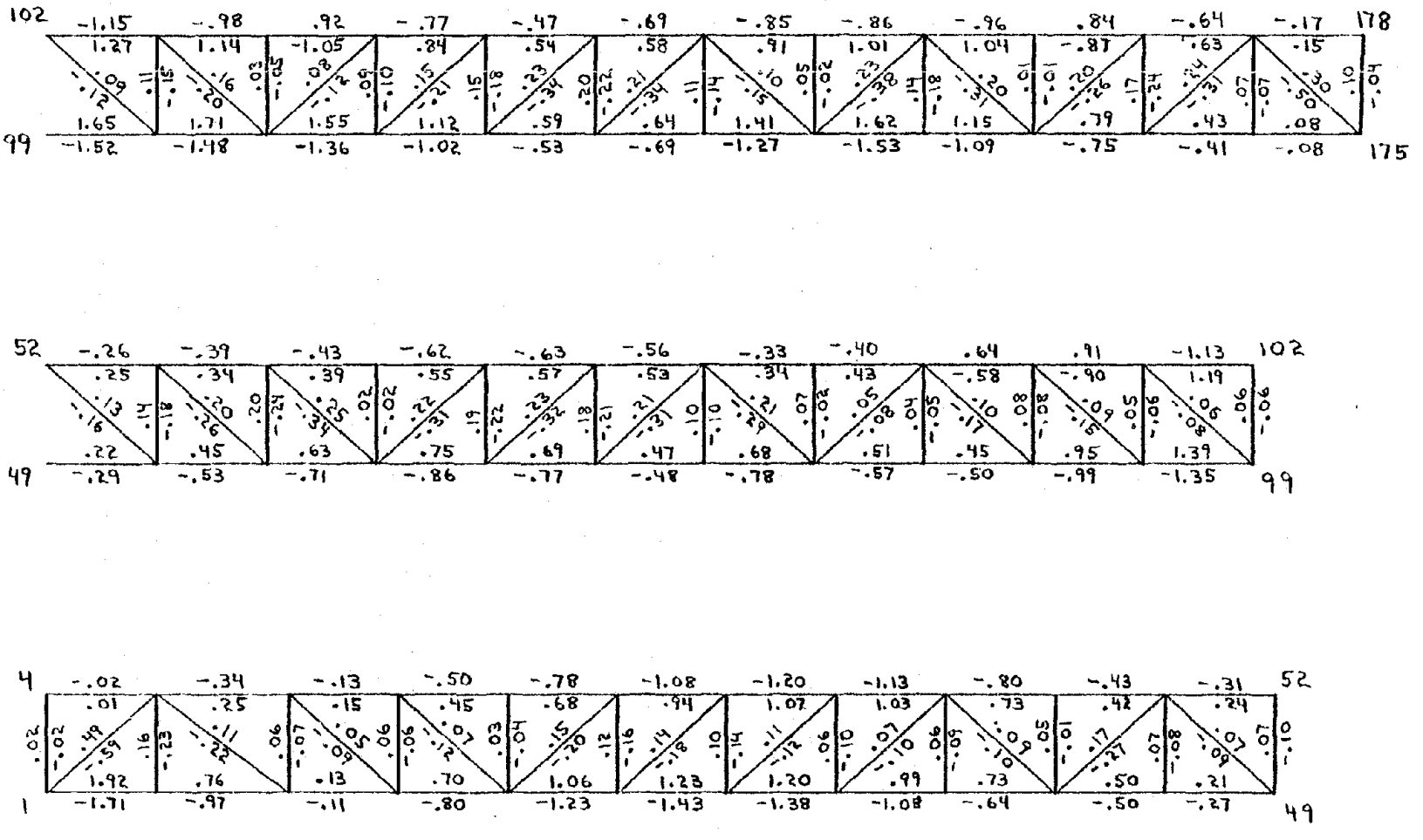

Figure 24

Buckling and yield ratios, truss system 1: front view, fraction of critical damping = .01.

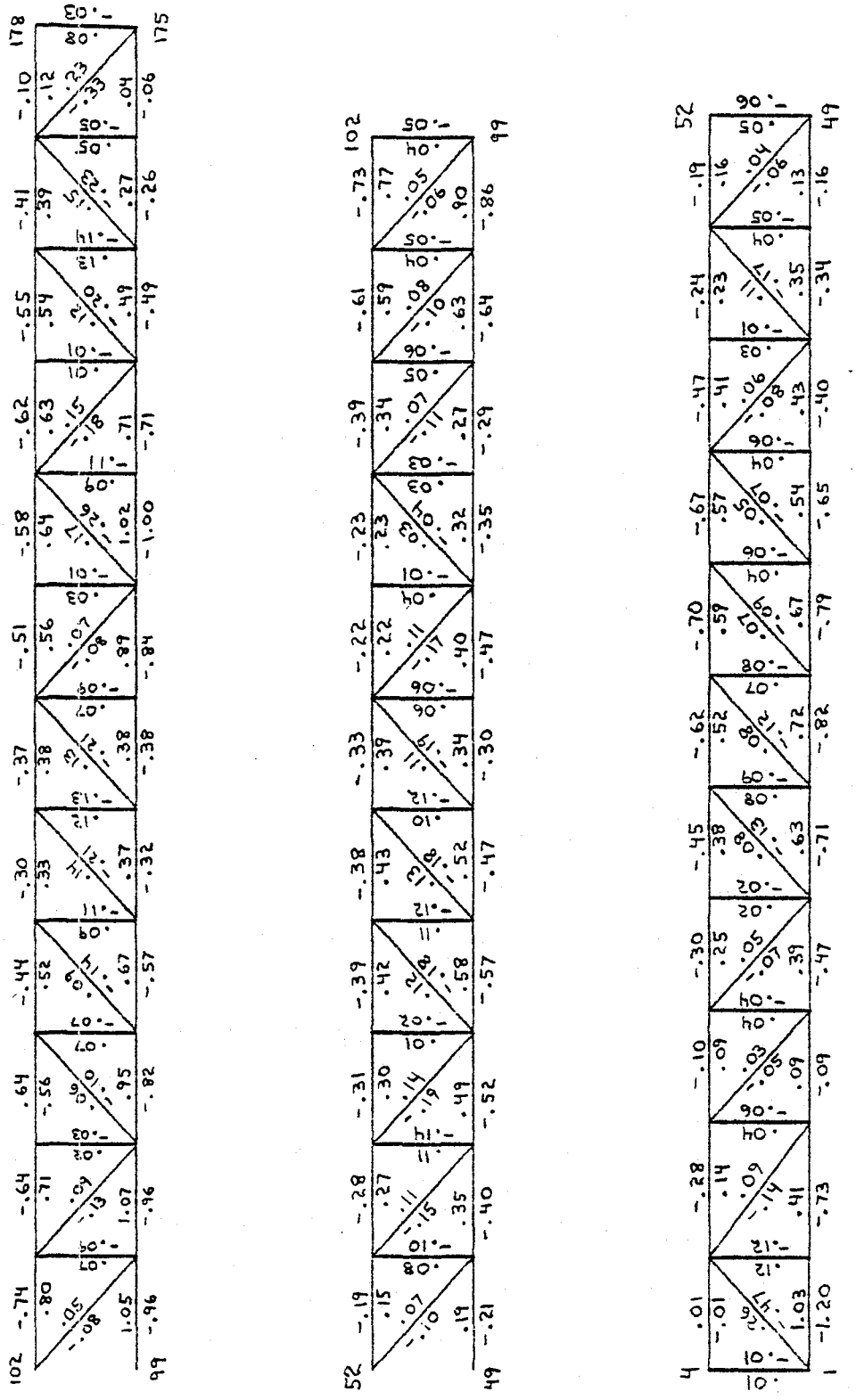

Figure 25

Buckling and yield ratios, truss system 1: front view, fraction of critical damping = .05.

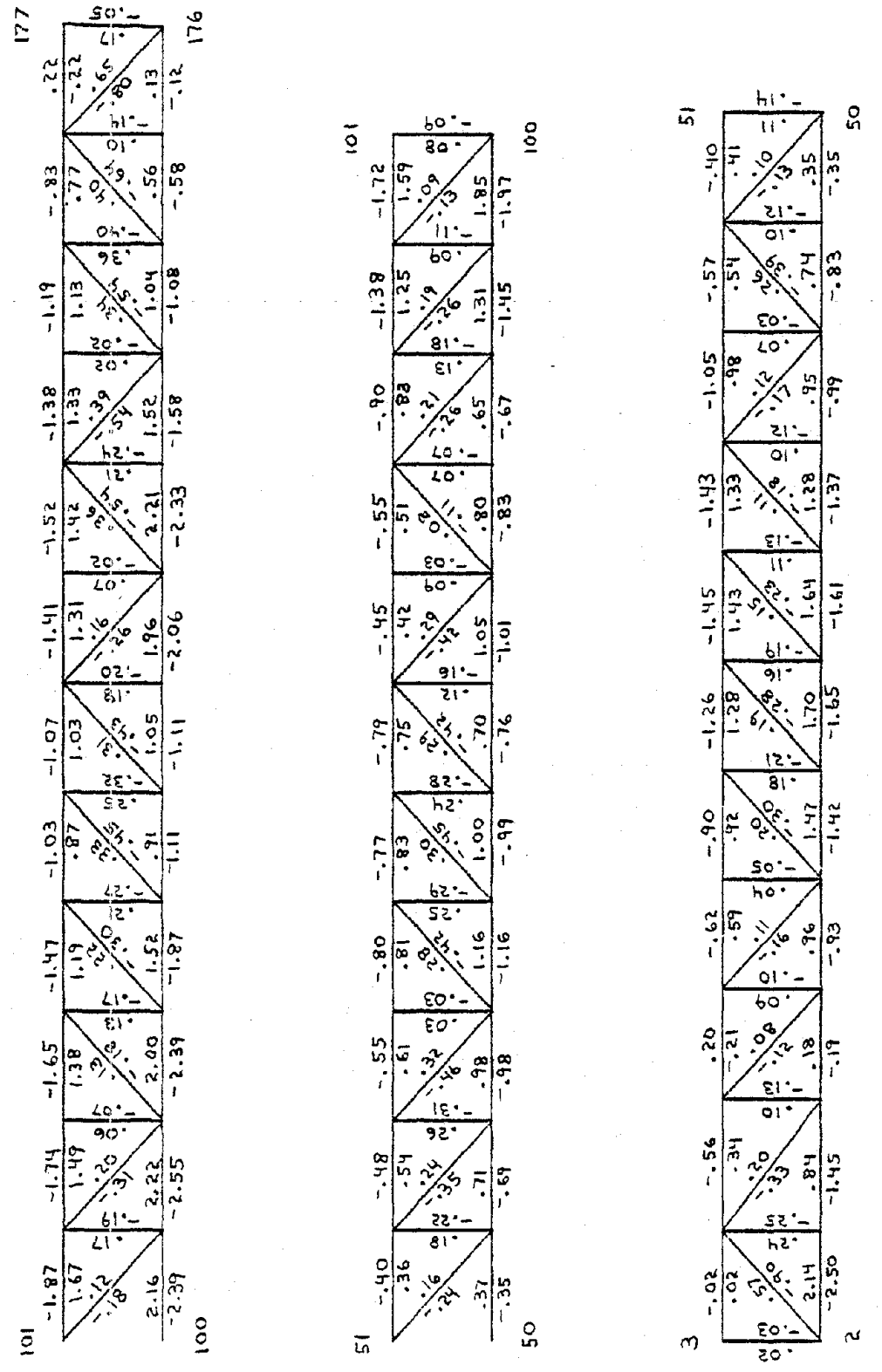

Figure 26

Buckling and yield ratios, truss system 1: back view, undamped.

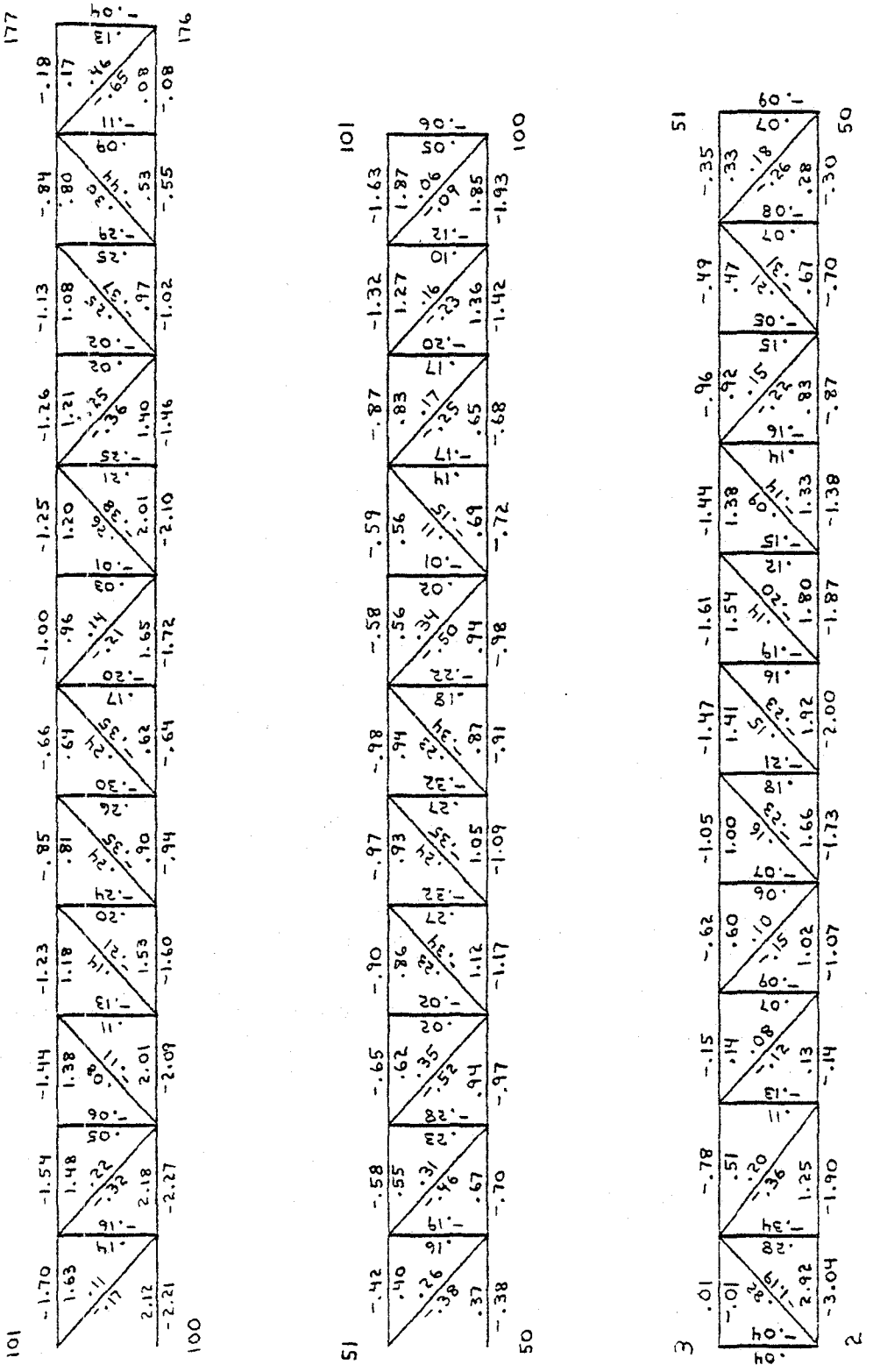

Figure 27

Buckling and yield ratios from the response spectrum analysis, truss system 1: back view, undamped.

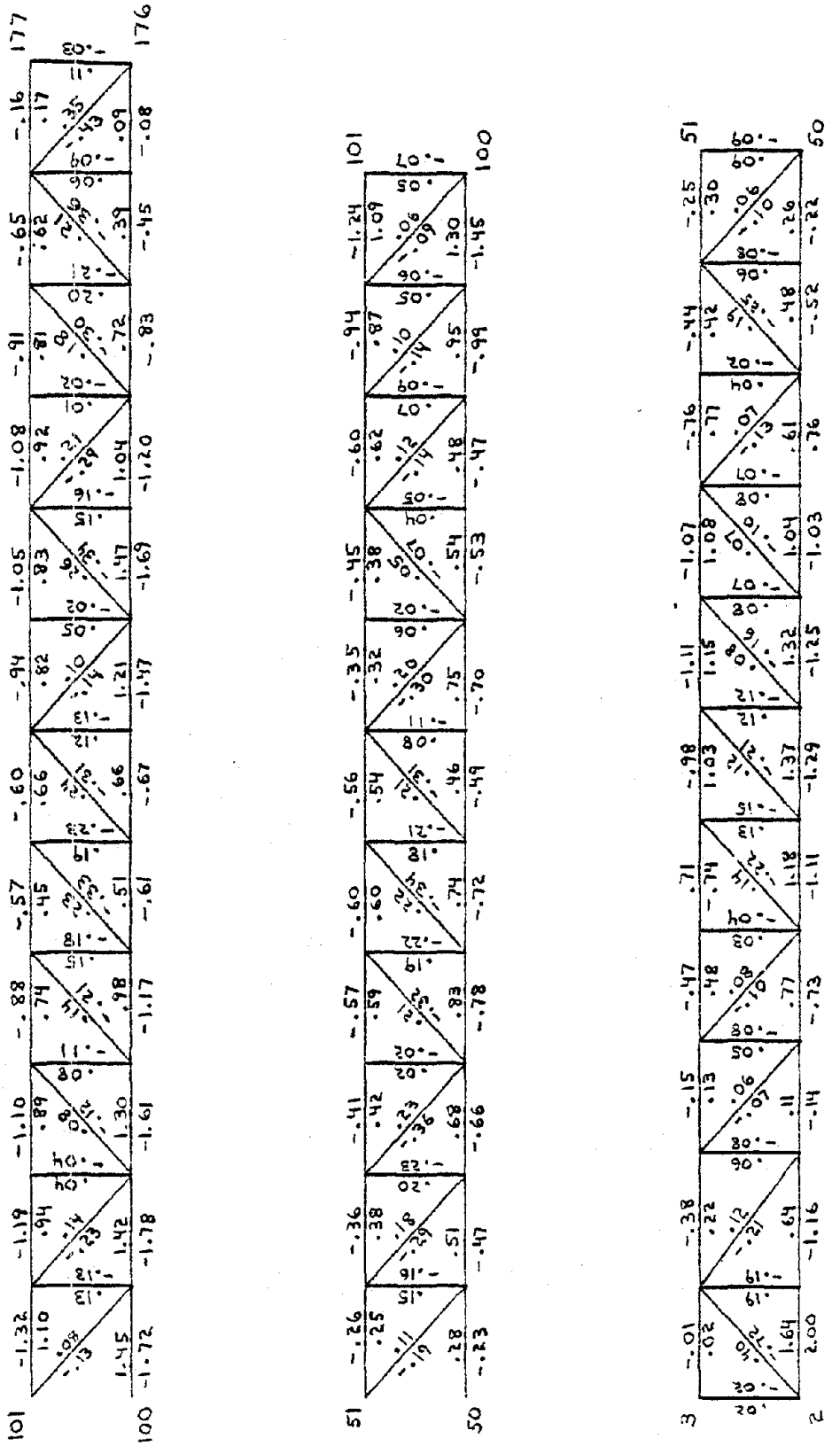

Figure 28

Buckling and yield ratios, truss system 1: back view, fraction of critical damping = .01.

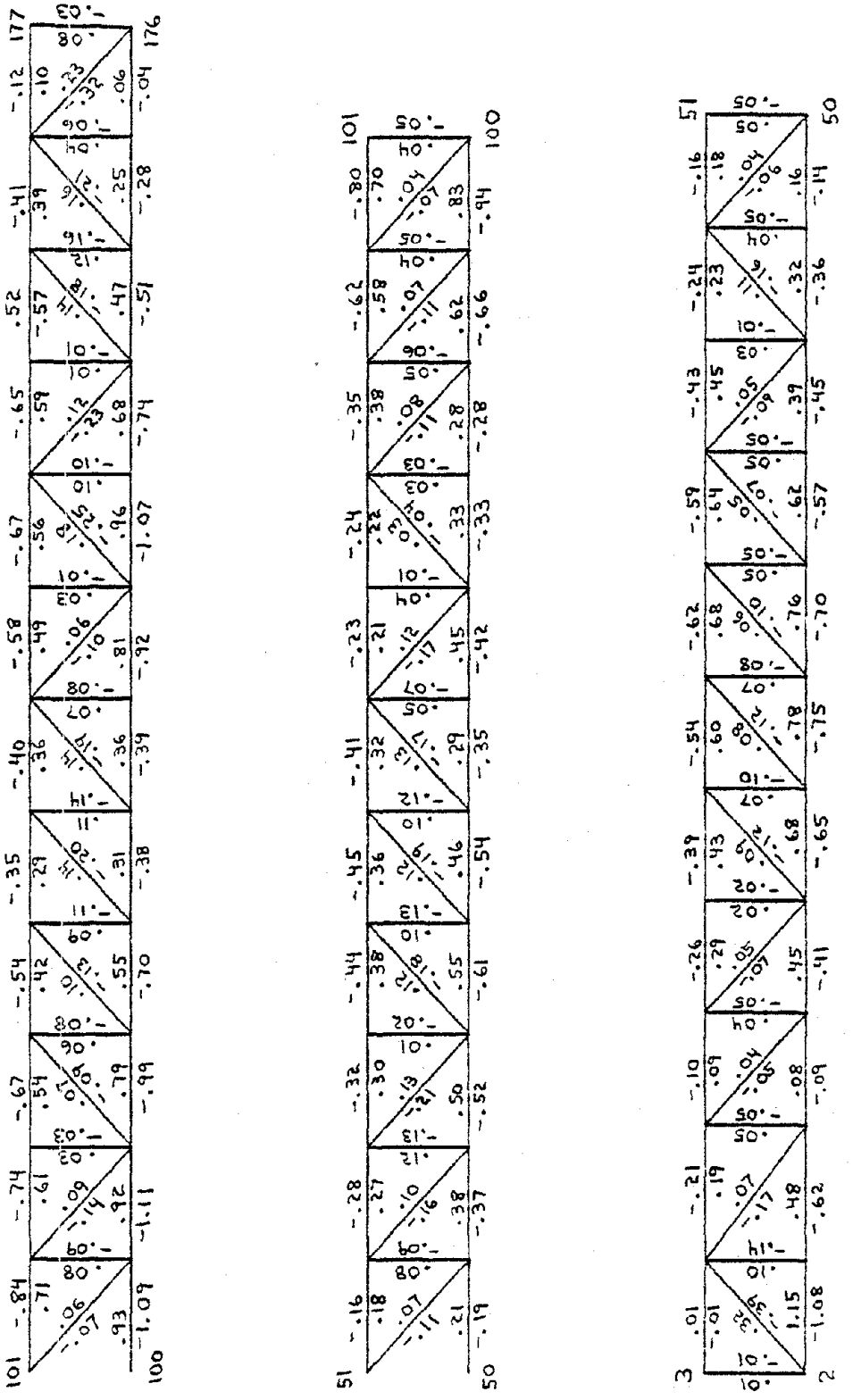

Figure 29

Buckling and yield ratios, truss system 1: back view, fraction of critical damping = .05.

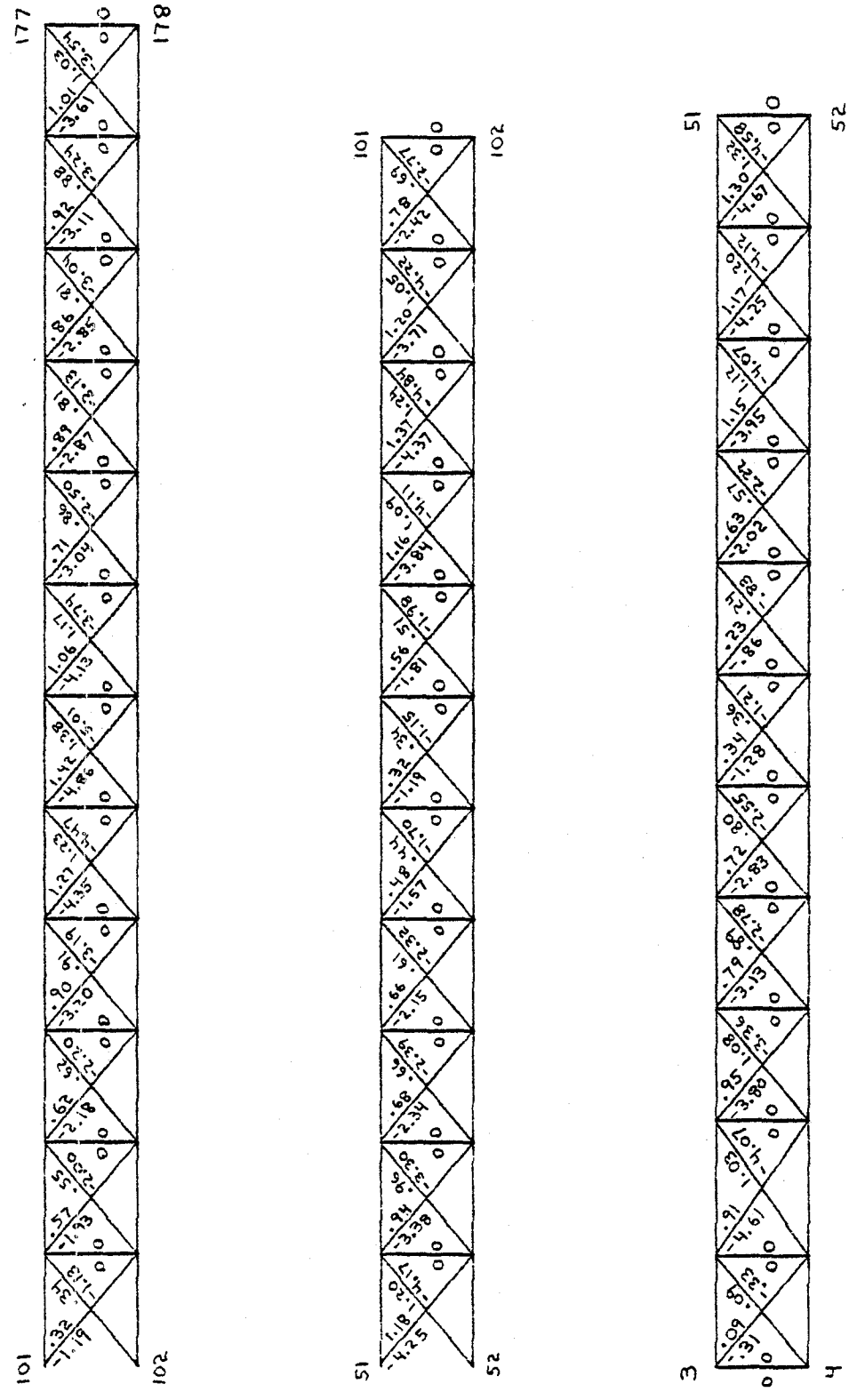

Figure 30

Buckling and yield ratios, truss system 1: roof view, undamped.

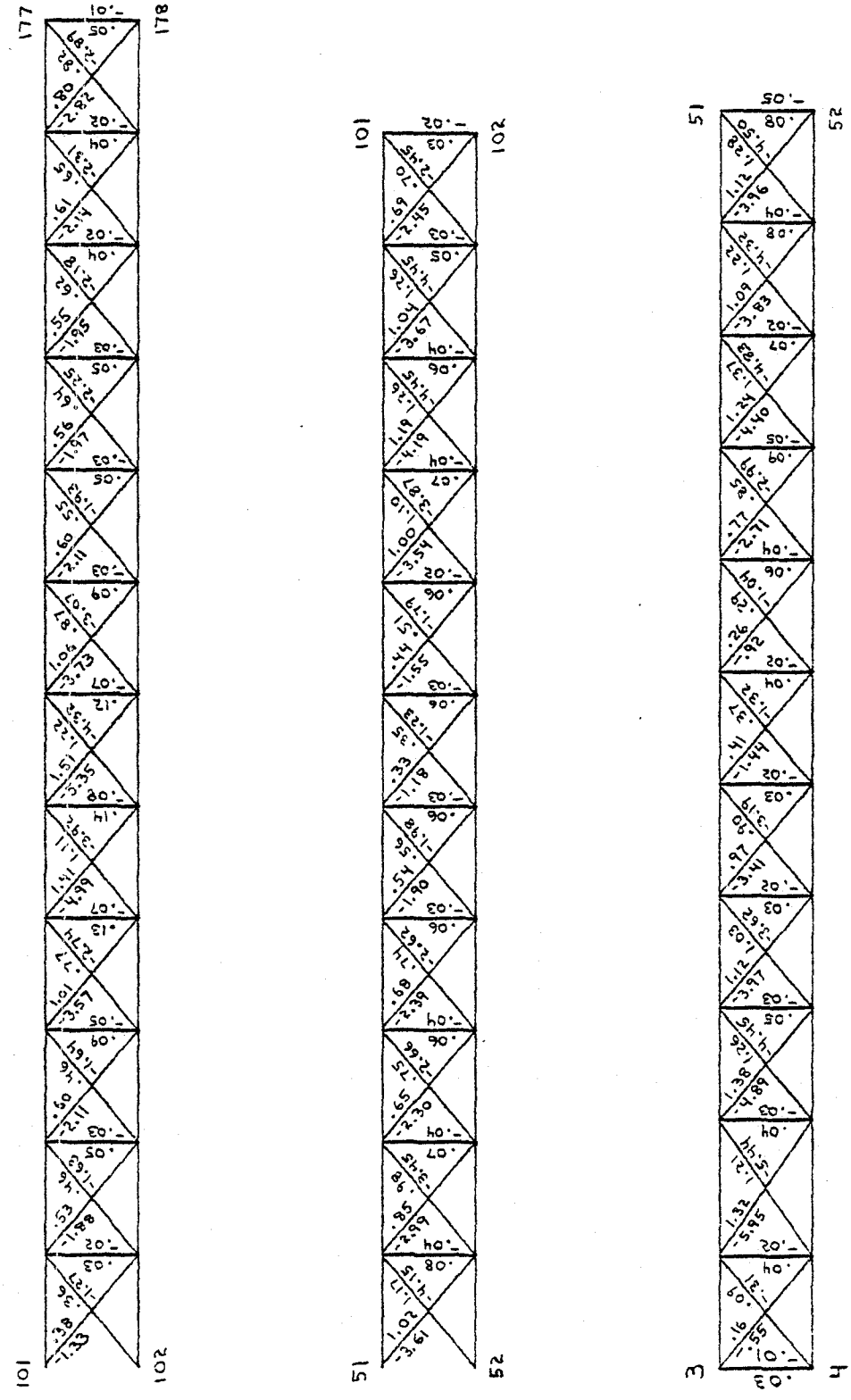

Figure 31

Buckling and yield ratios from the response spectrum analysis, truss system 1: roof view, undamped.

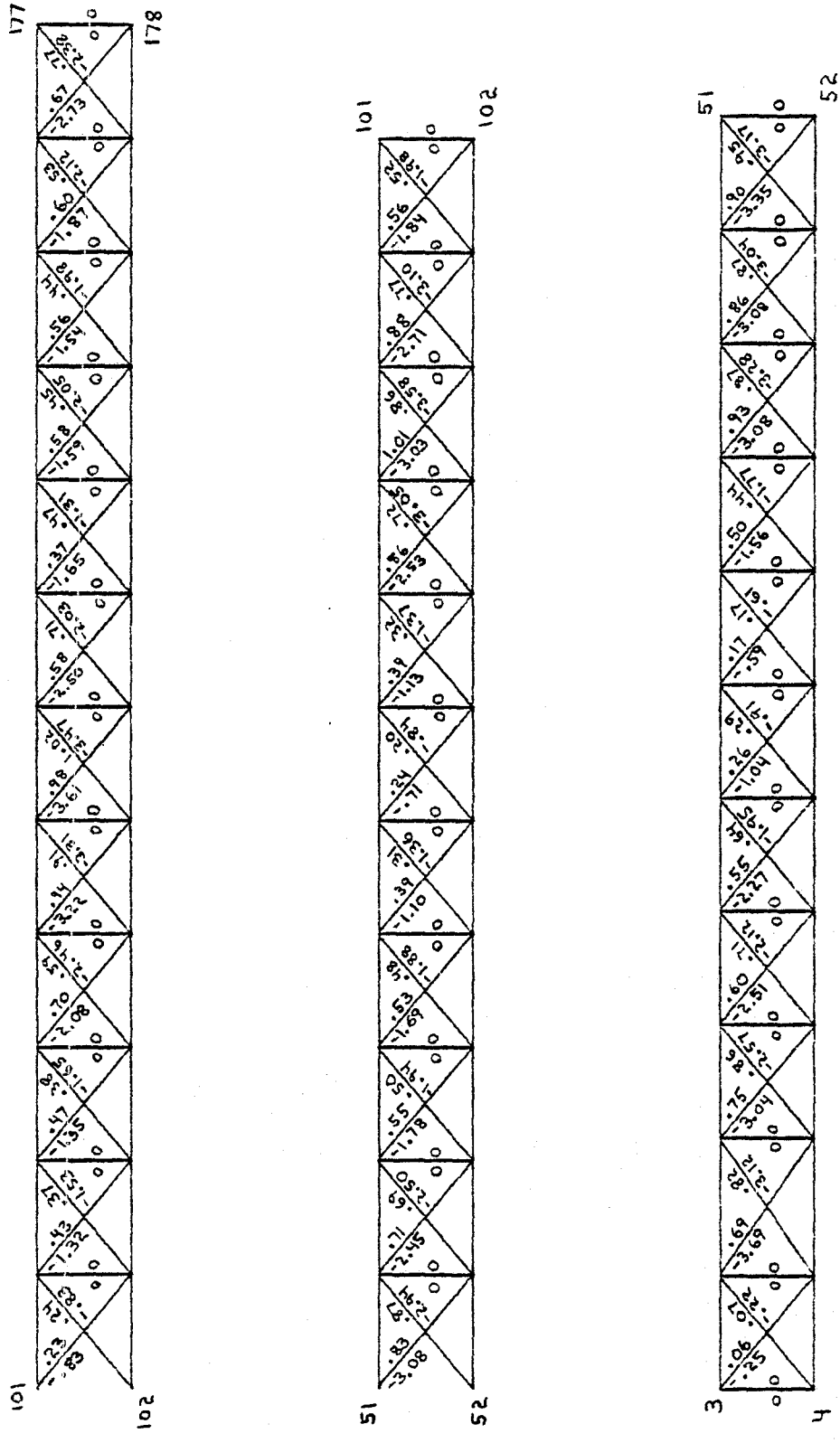

Figure 32

Buckling and yield ratios, truss system 1: roof view, fraction of critical damping = .01.

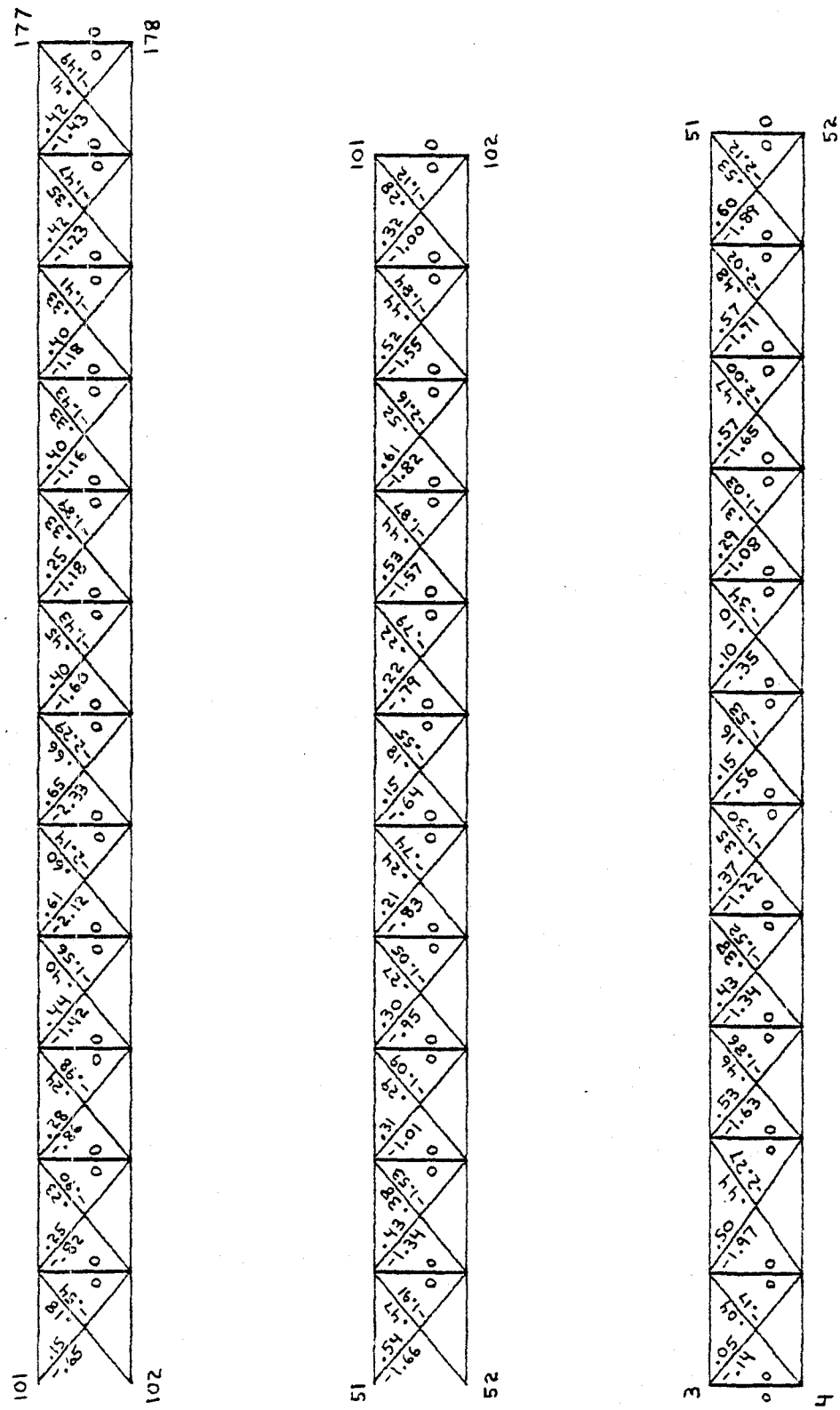

Figure 33

Buckling and yield ratios, truss system 1: roof view, fraction of critical damping = .05.

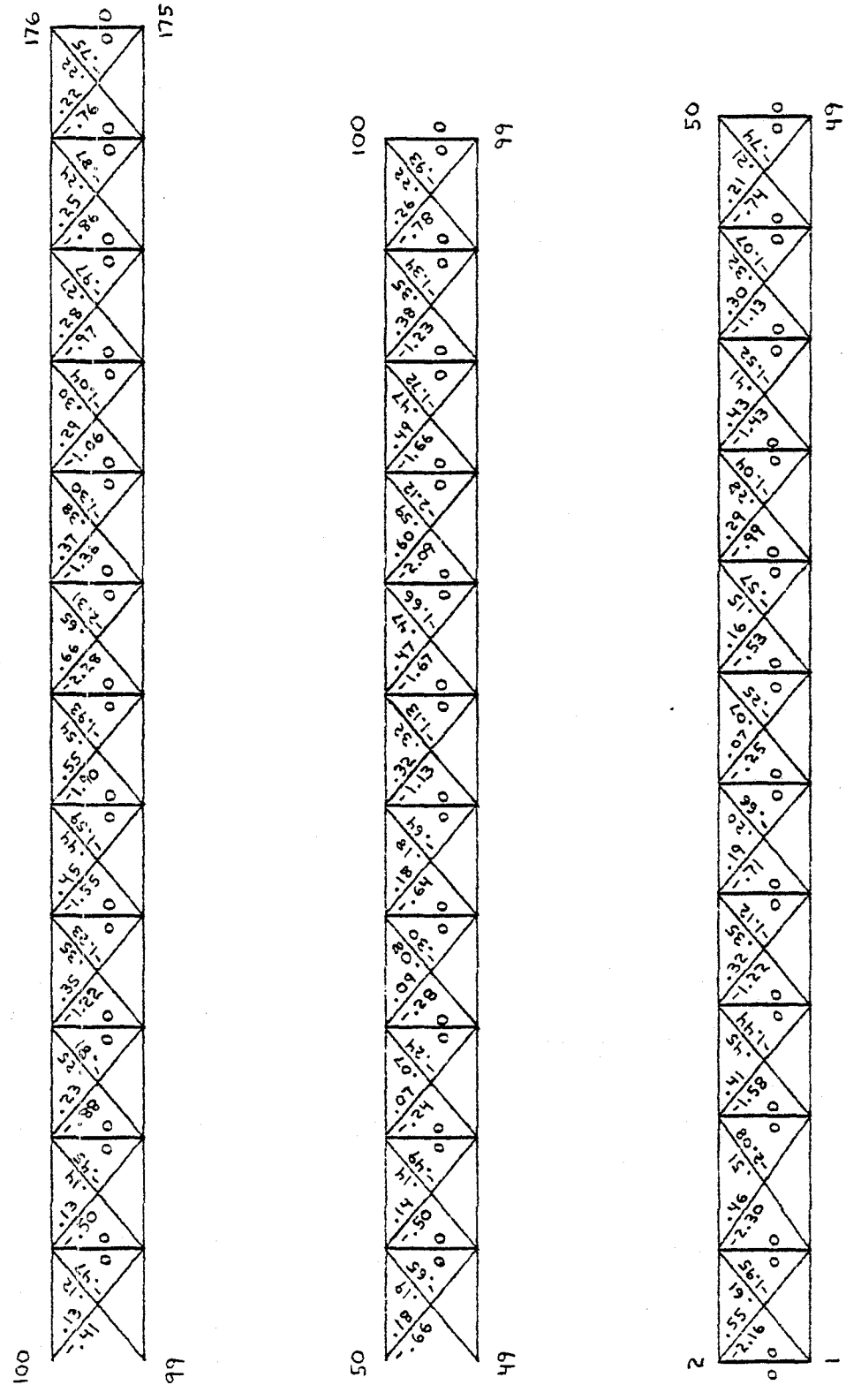

Figure 34

Buckling and yield ratios, truss system 1: floor view, undamped.

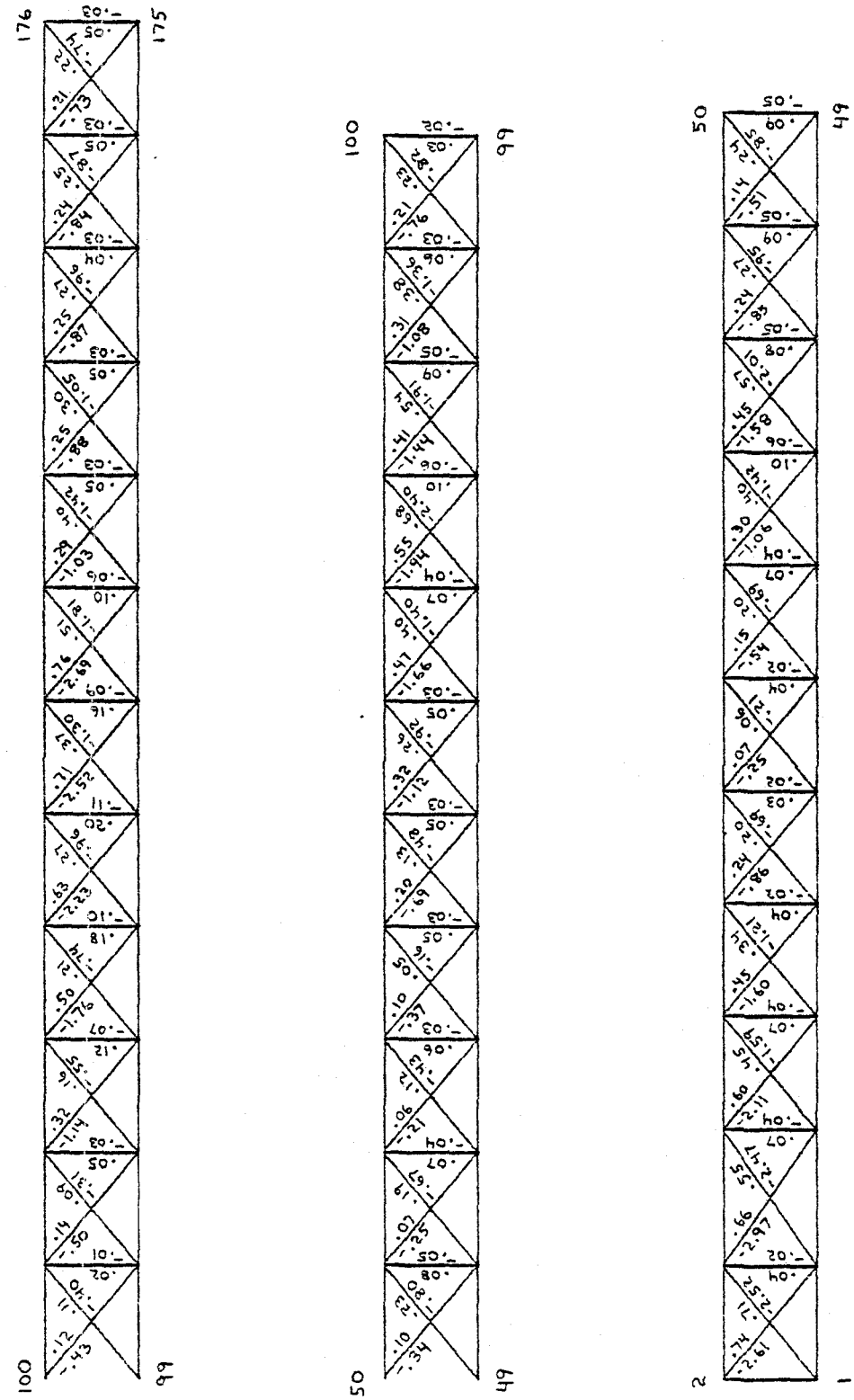

Figure 35

Buckling and yield ratios from the response spectrum analysis, truss system 1: floor view, undamped.

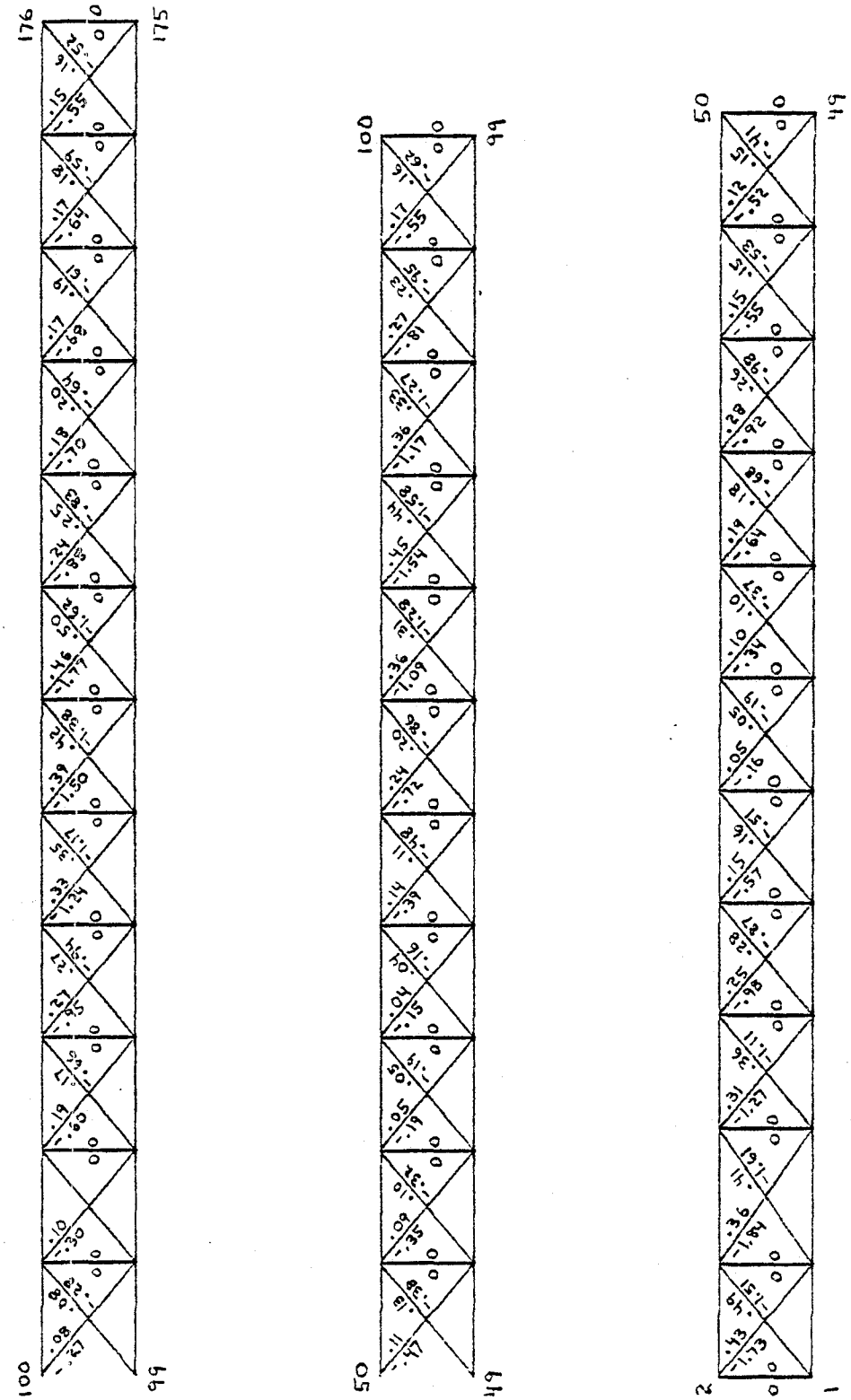

Figure 36

Buckling and yield ratios, truss system 1: floor view, fraction of critical damping = .01.

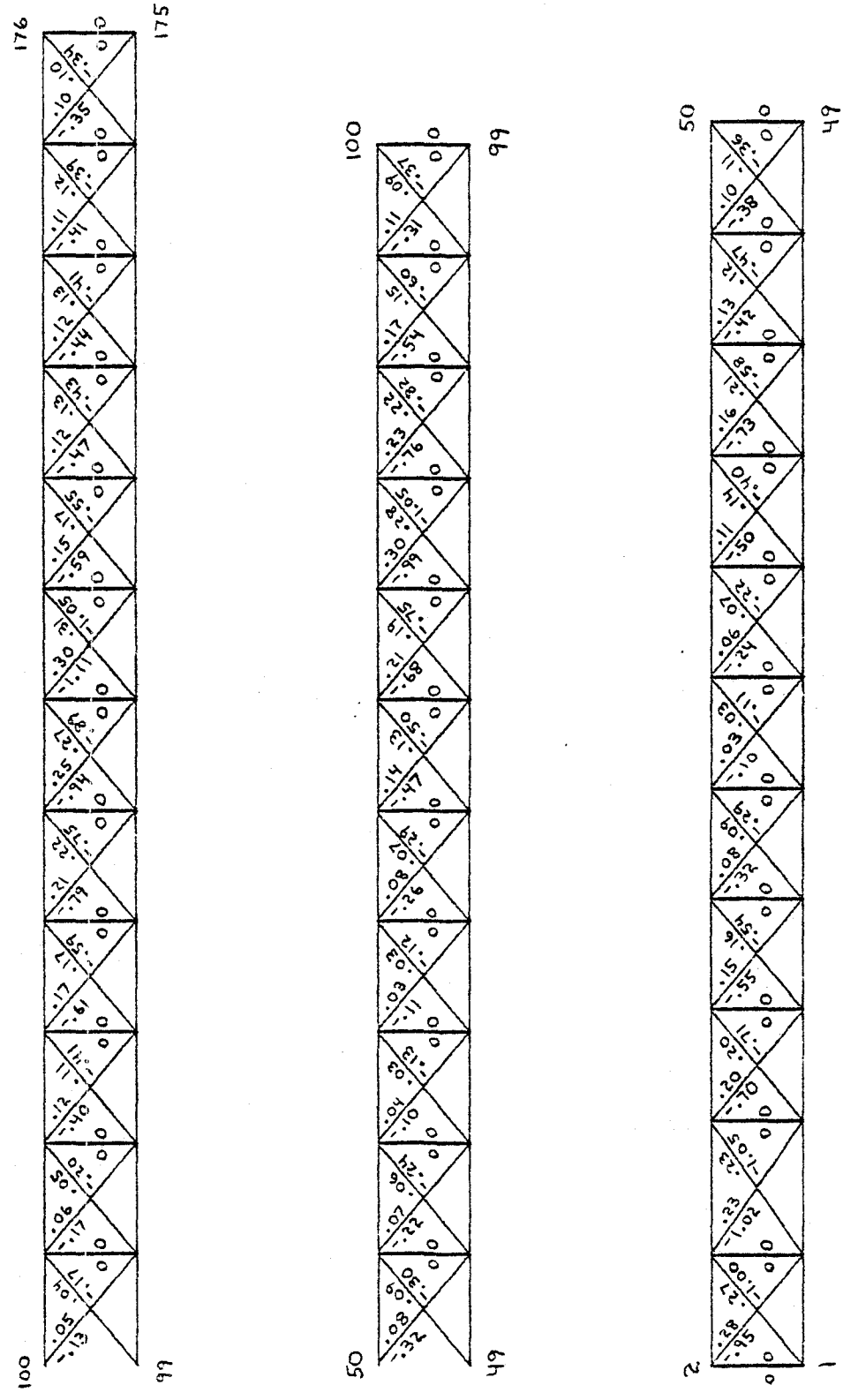

Figure 37

Buckling and yield ratios, truss system 1: floor view, fraction of critical damping = .05.

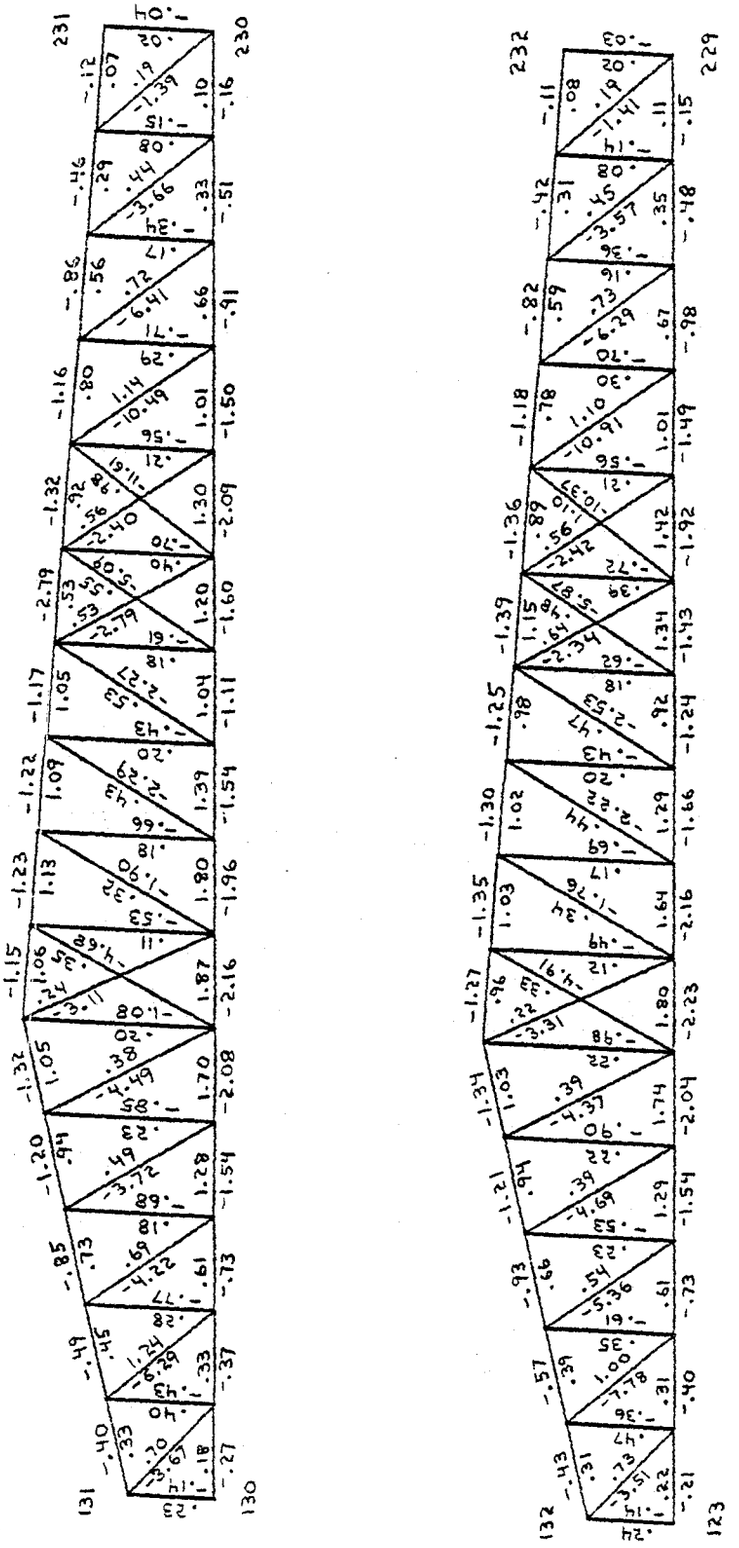

Figure 38

Buckling and yield ratios, truss system 2: back and front views, undamped.

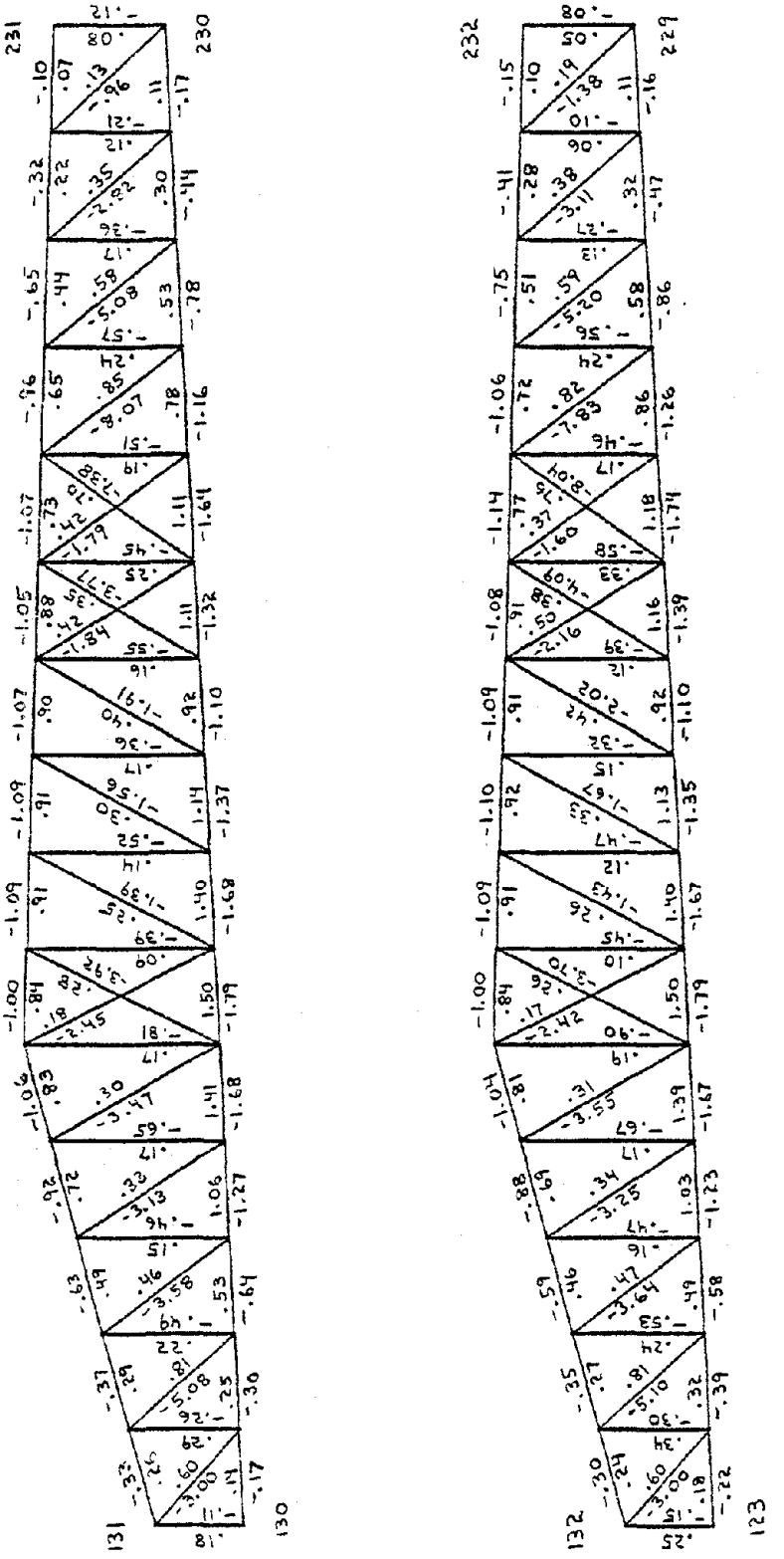

Figure 39

Buckling and yield ratios from the response spectrum analysis, truss system 2: back and front views, undamped.

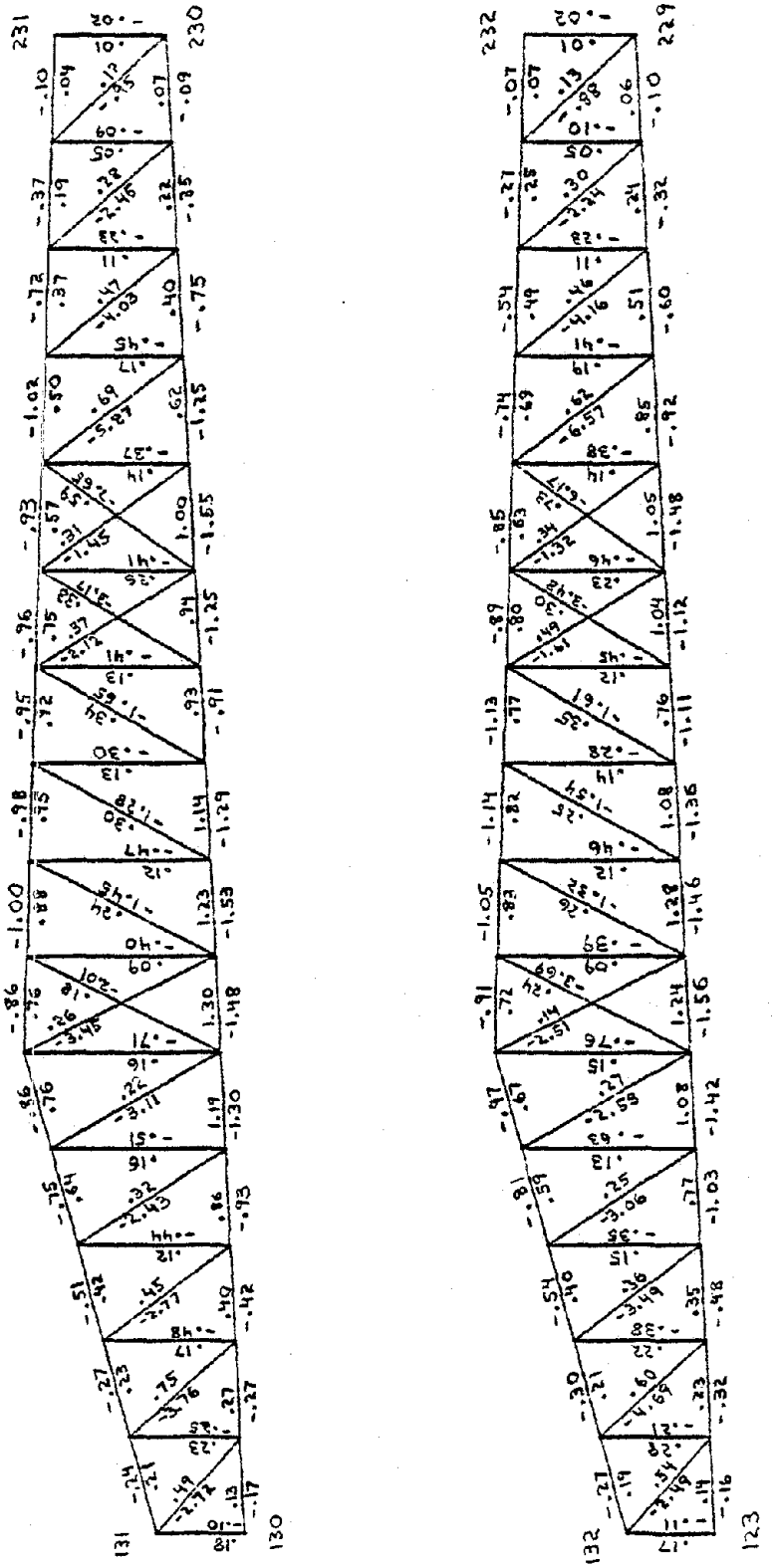

Figure 40

Buckling and yield ratios, truss system 2: back and front views, fraction of critical damping = .01.

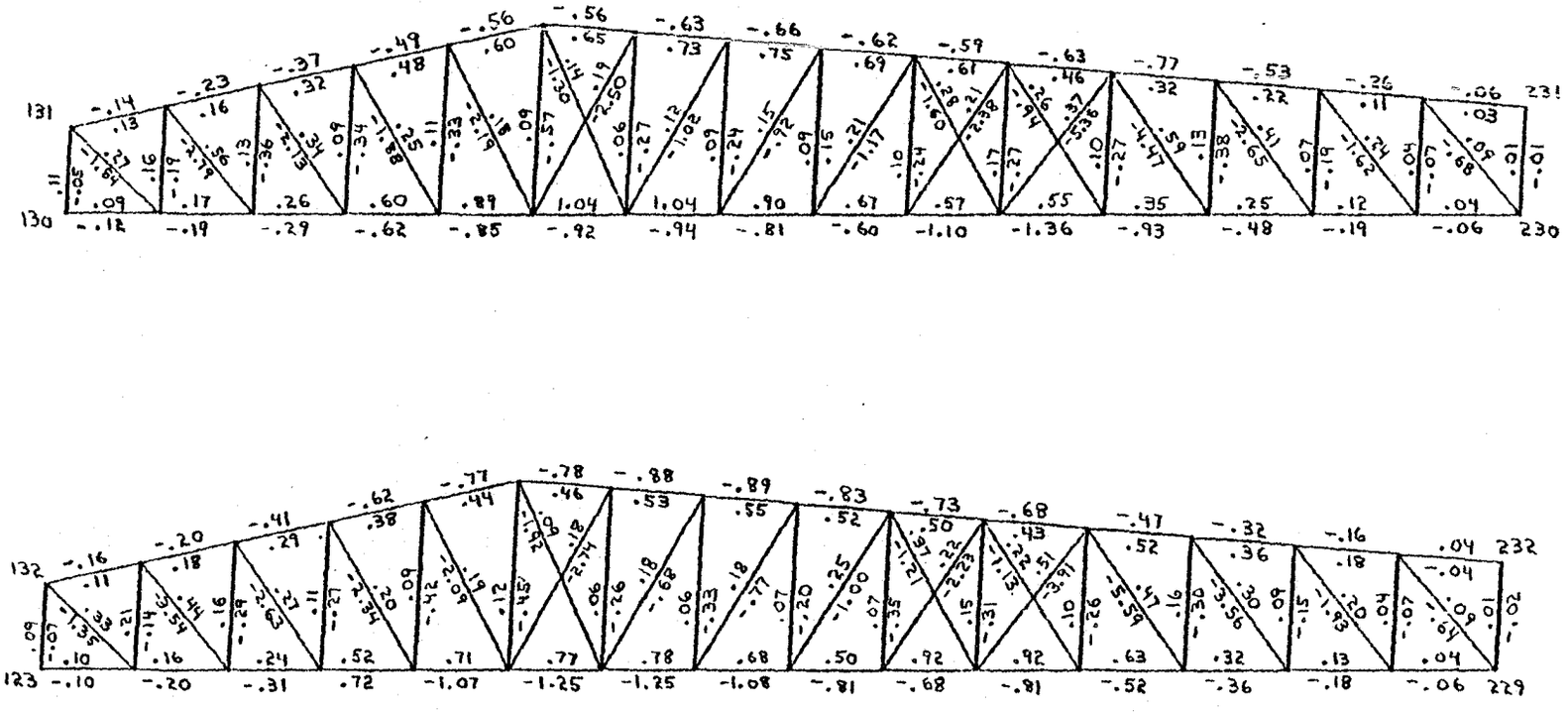

Figure 41

Buckling and yield ratios, truss system 2: back and front views, fraction of critical damping = .05.

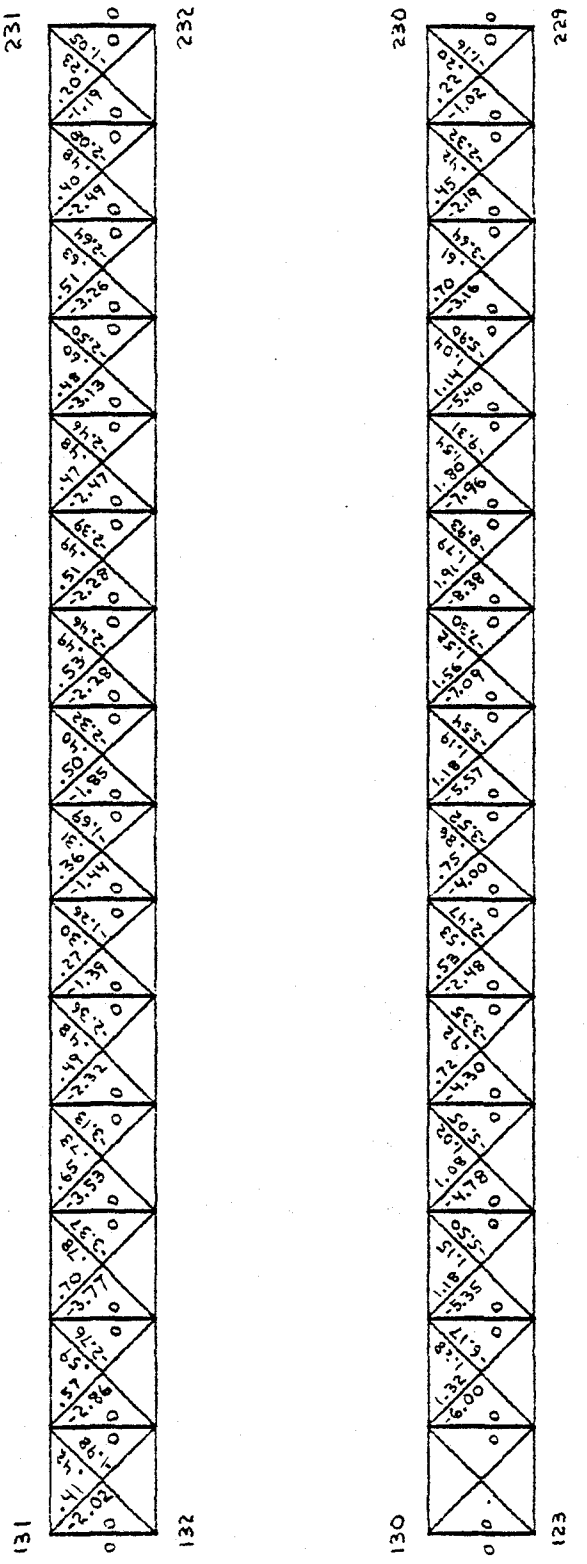

Figure 42

Buckling and yield ratios, truss system 2: roof and floor views, undamped.

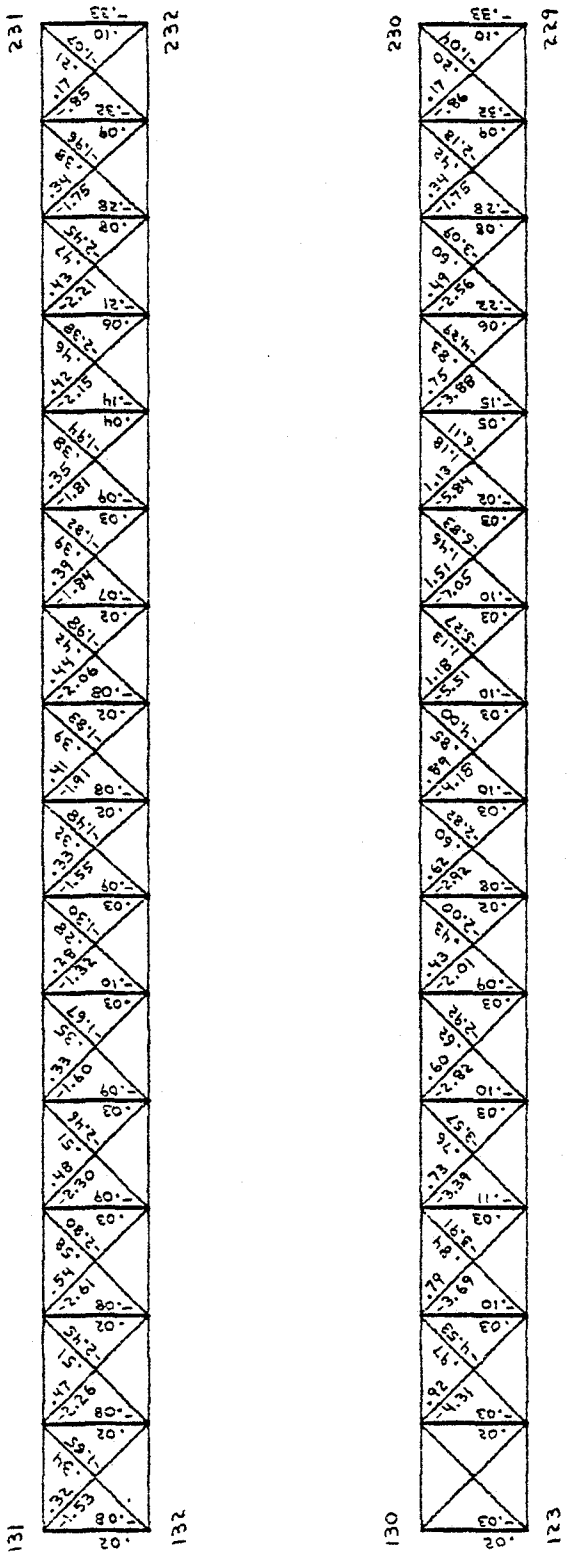

Figure 43

Buckling and yield ratios from the response spectrum analysis, truss system 2: roof and floor views, undamped.

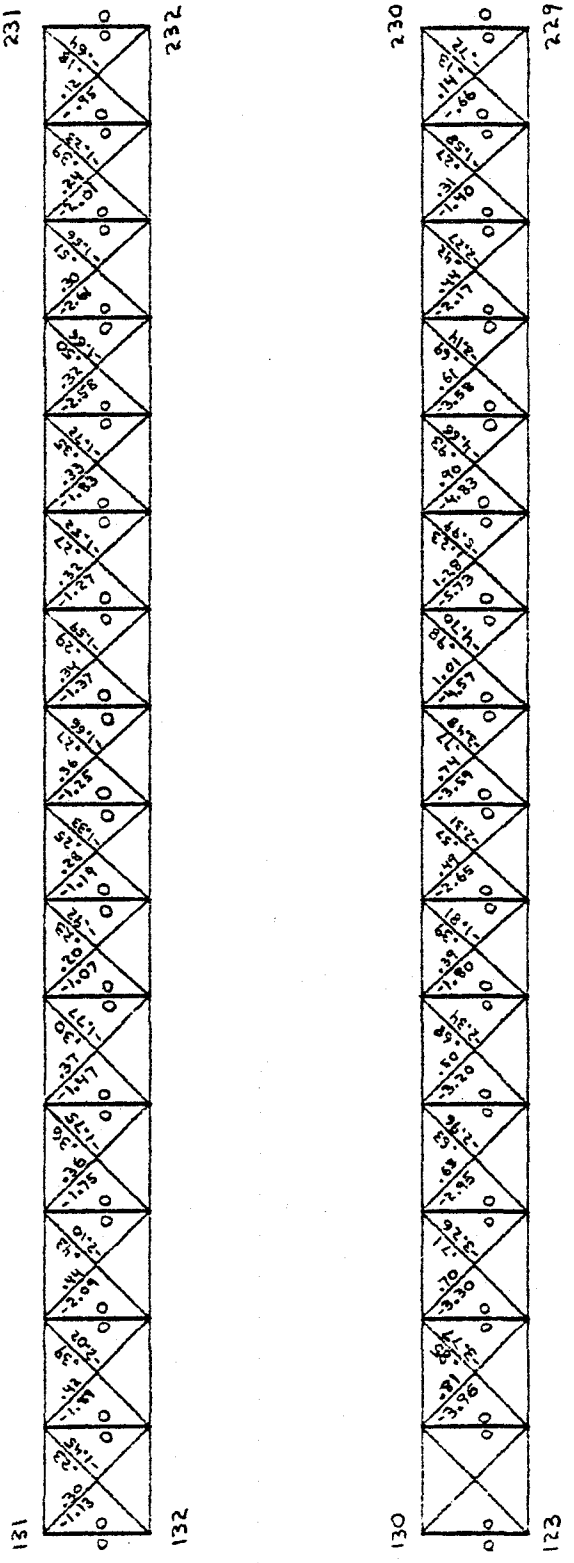

Figure 44

Buckling and yield ratios, truss system 2: roof and floor views, fraction of critical damping = .01.

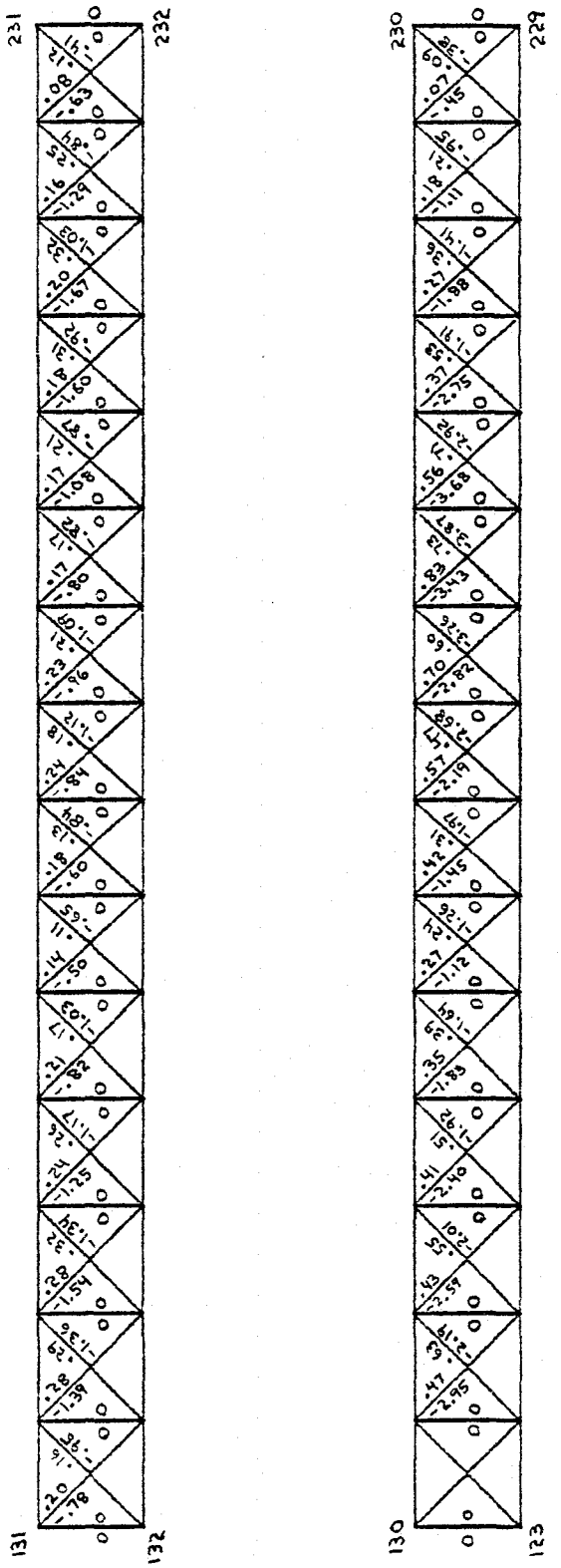

Figure 45

Buckling and yield ratios, truss system 2: roof and floor views, fraction of critical damping = .05.

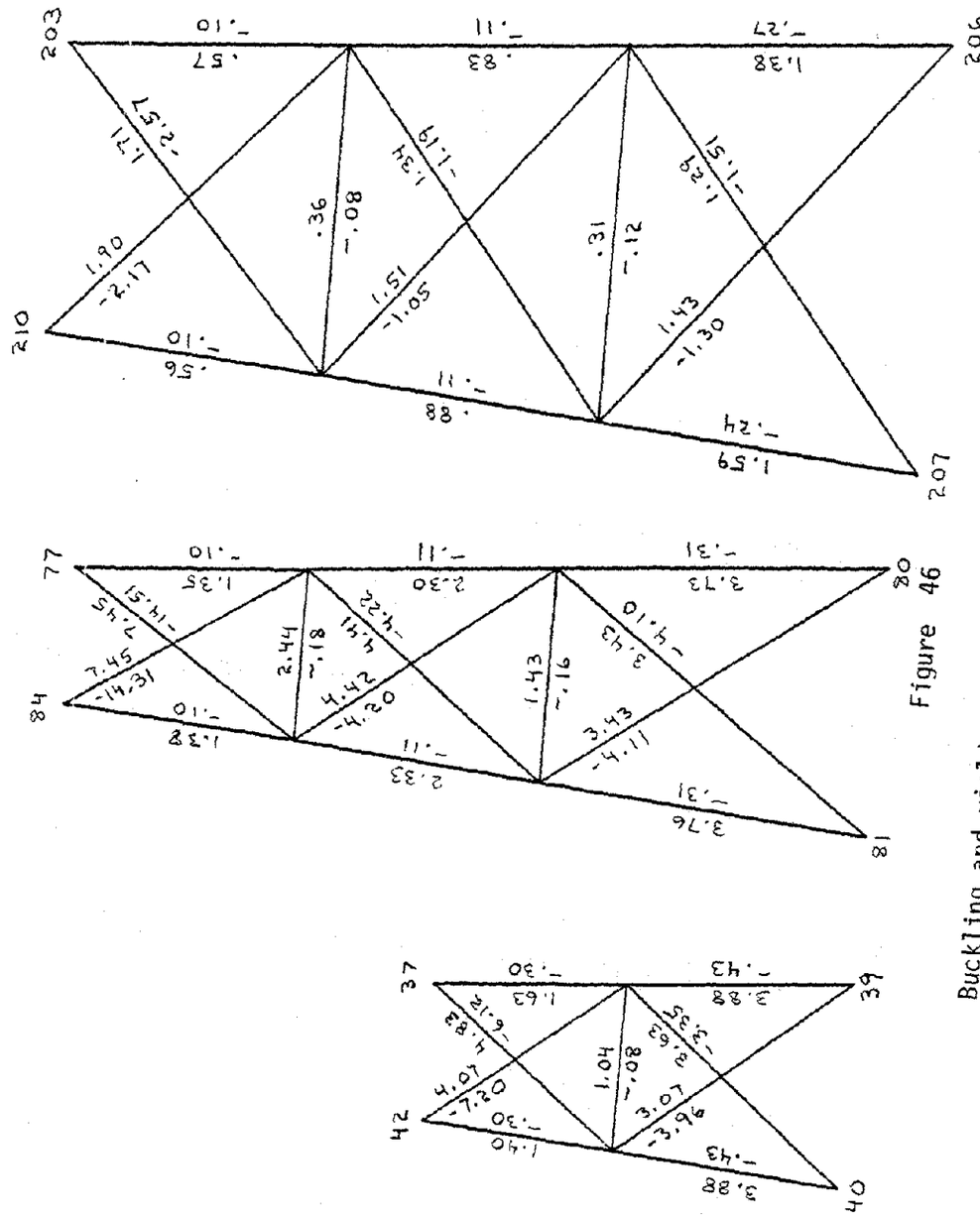

Figure 46 Buckling and yield ratios, bents 1, 2, and 3, undamped.

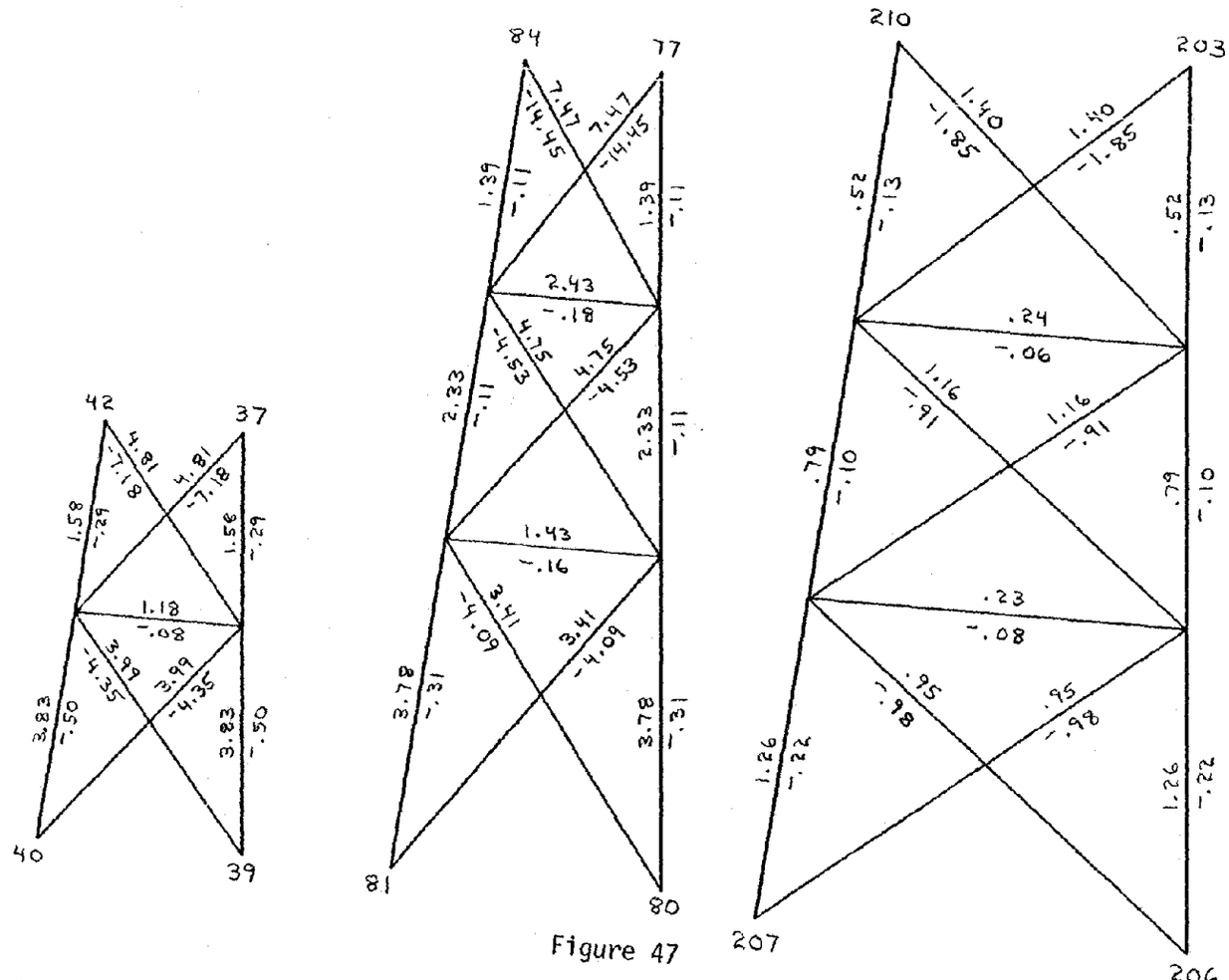

Figure 47

Buckling and yield ratios from the response spectrum analysis, bents 1, 2, and 3, undamped.

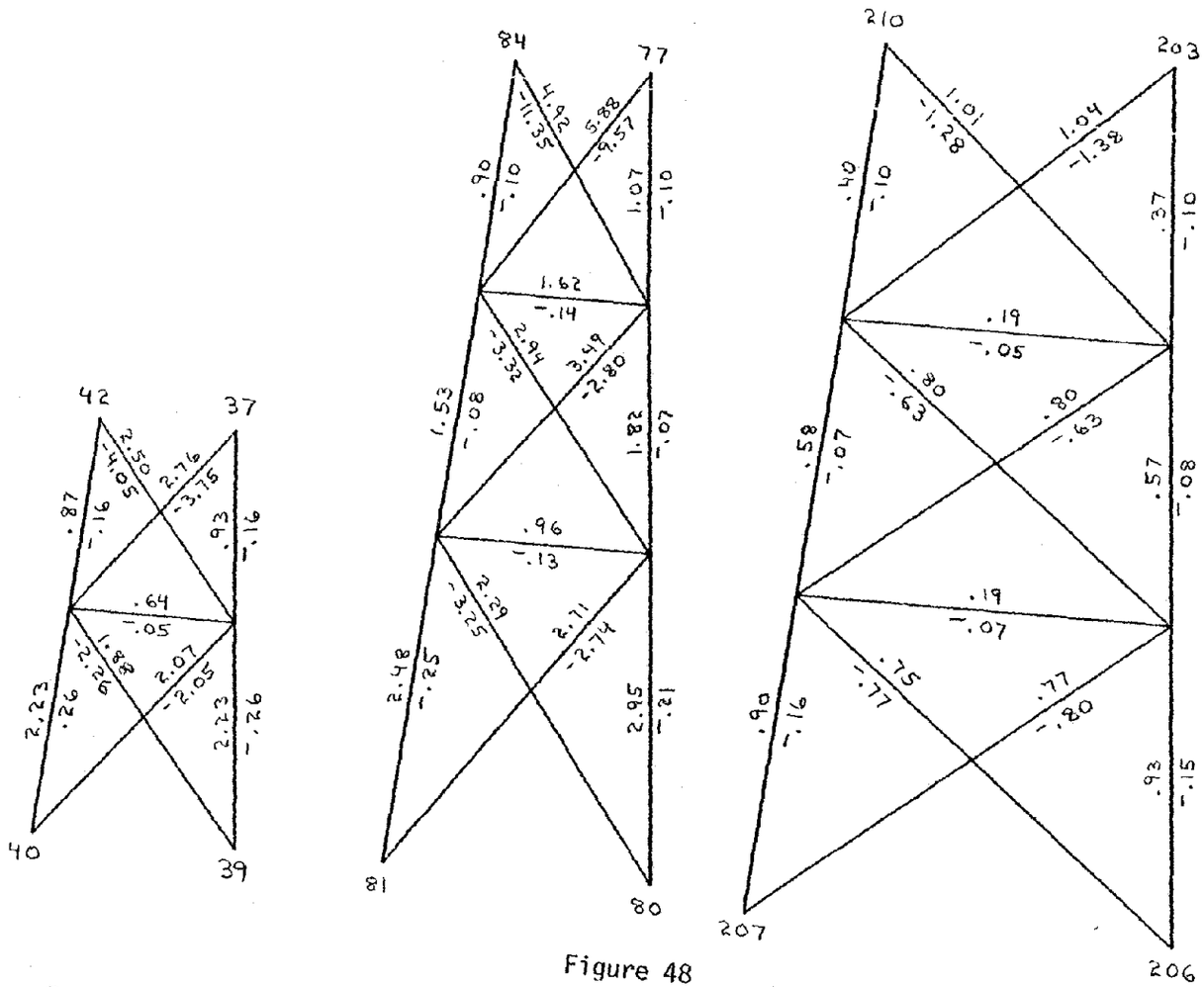

Figure 48

Buckling and yield ratios, bents 1, 2, and 3, fraction of critical damping = .01.

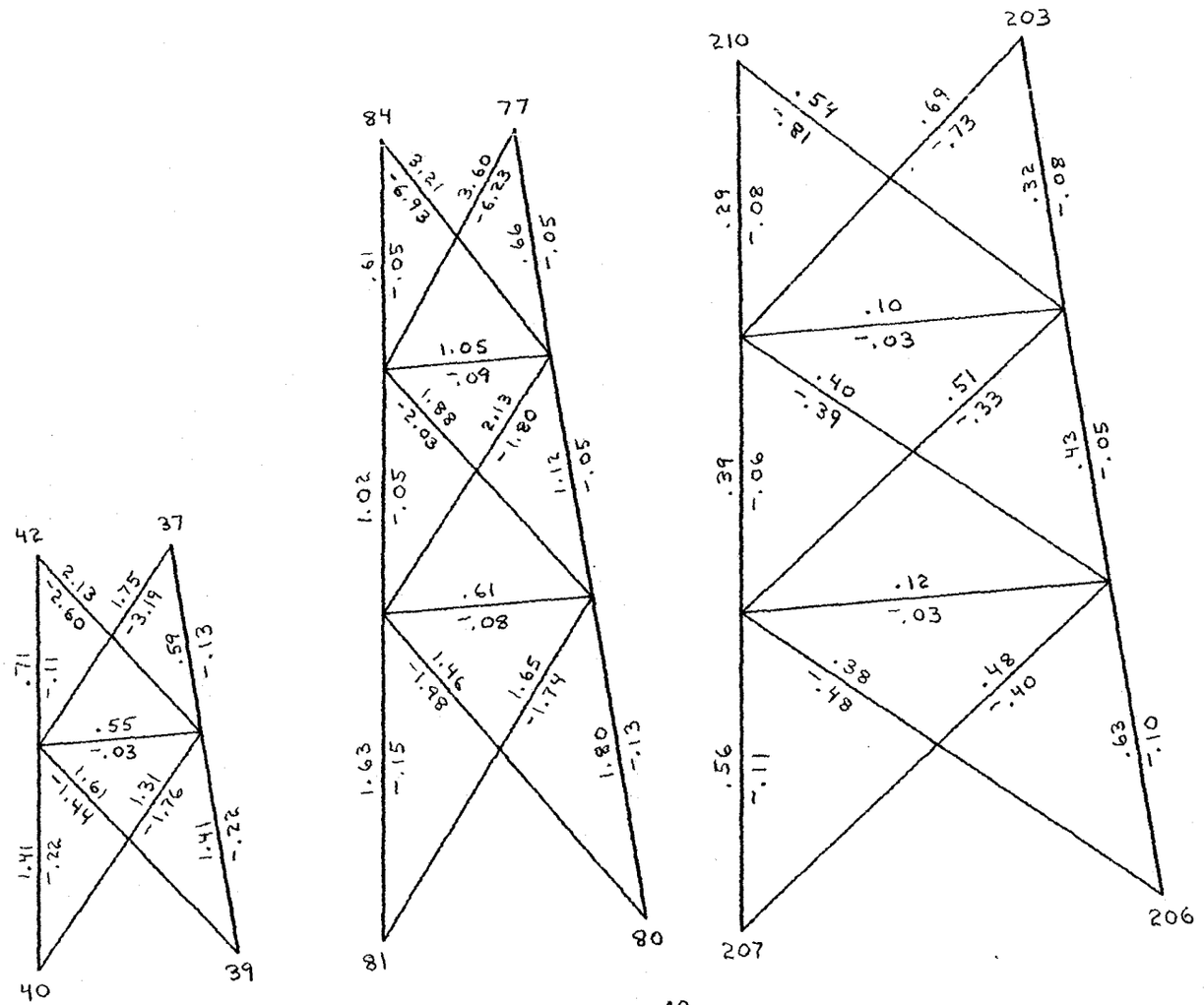

Figure 49

Buckling and yield ratios, bents 1, 2, and 3, fraction of critical damping = .05.

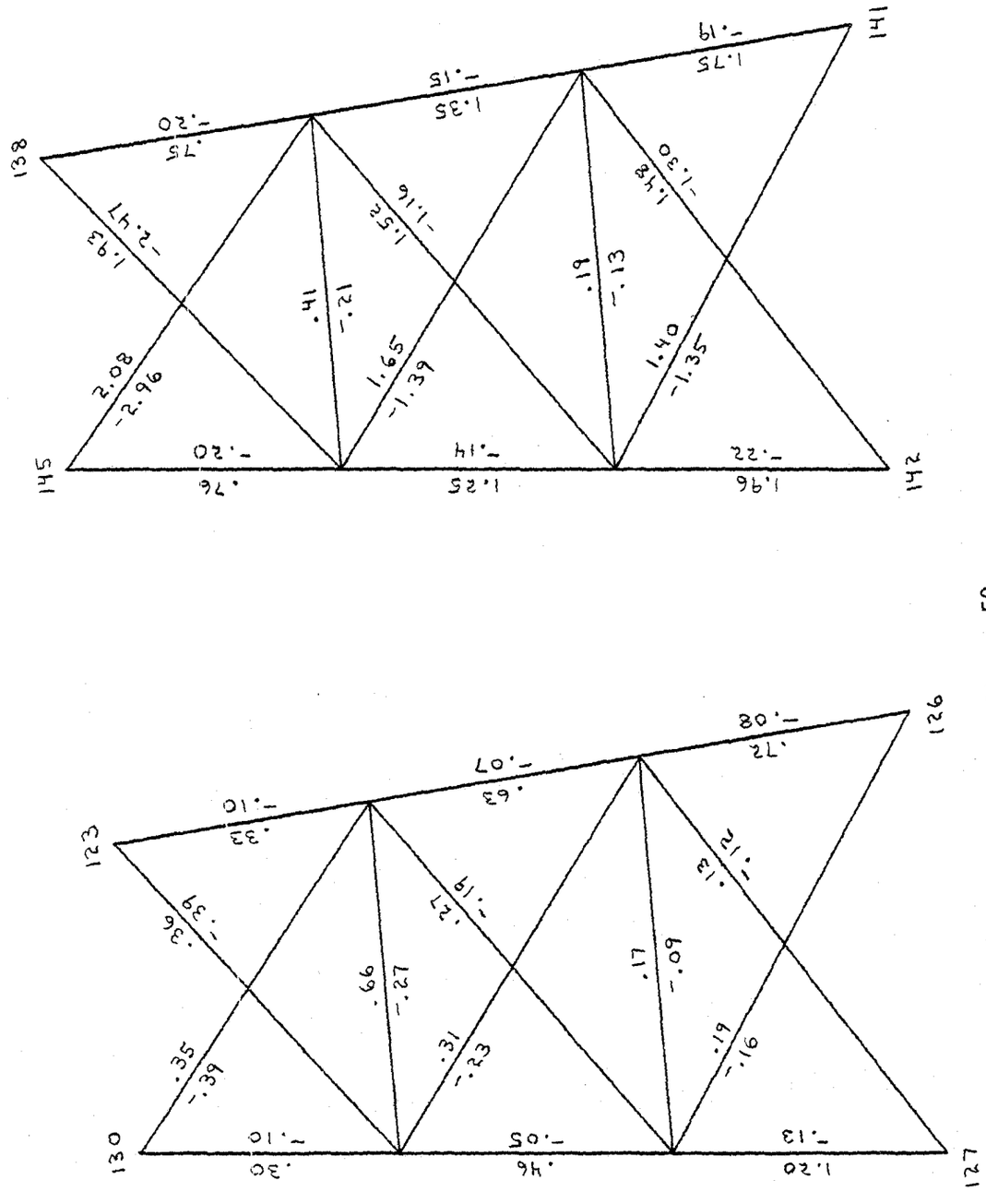

Figure 50

Buckling and yield ratios, tower: end views, undamped

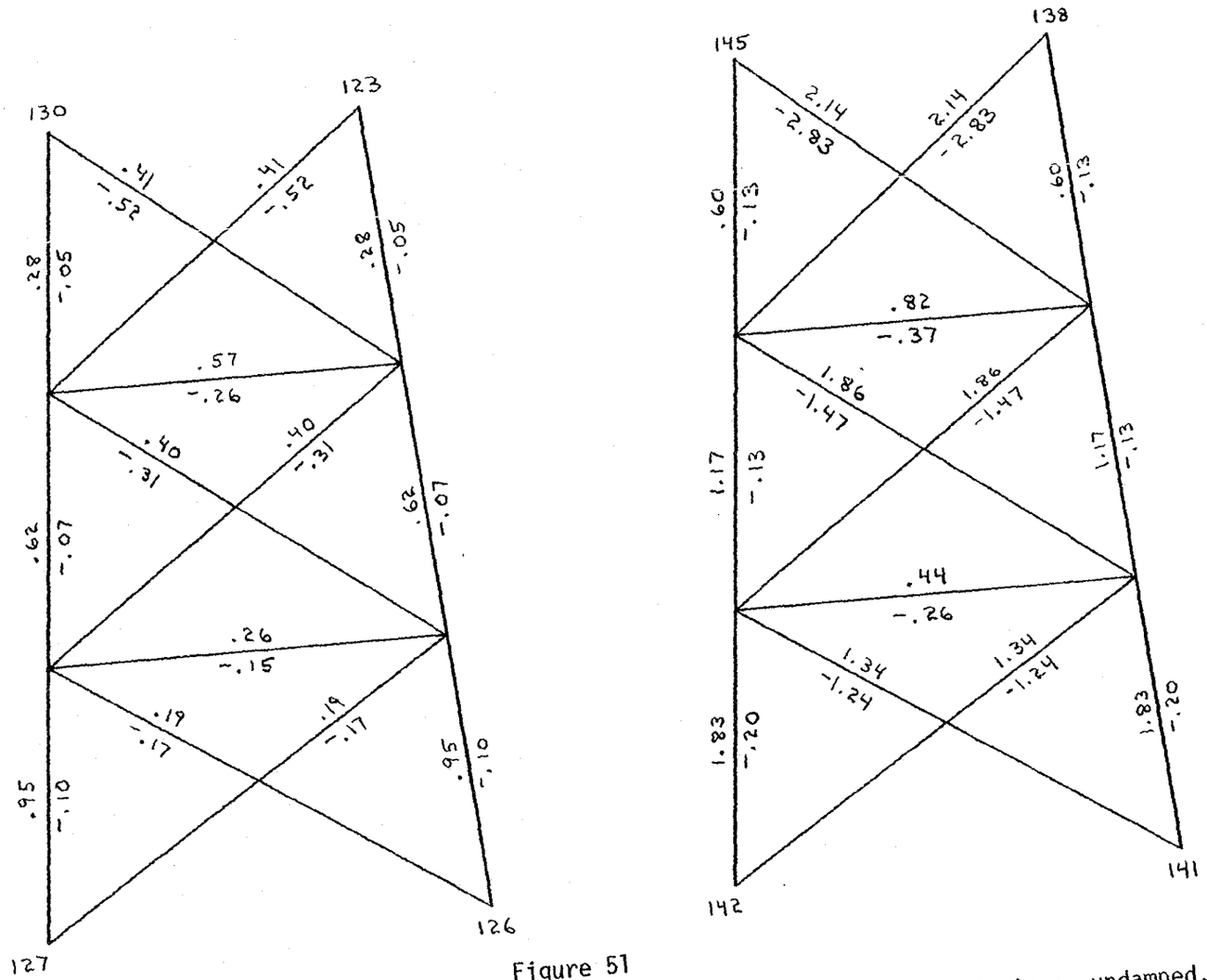

Figure 51

Buckling and yield ratios from the response spectrum analysis, tower: end views, undamped.

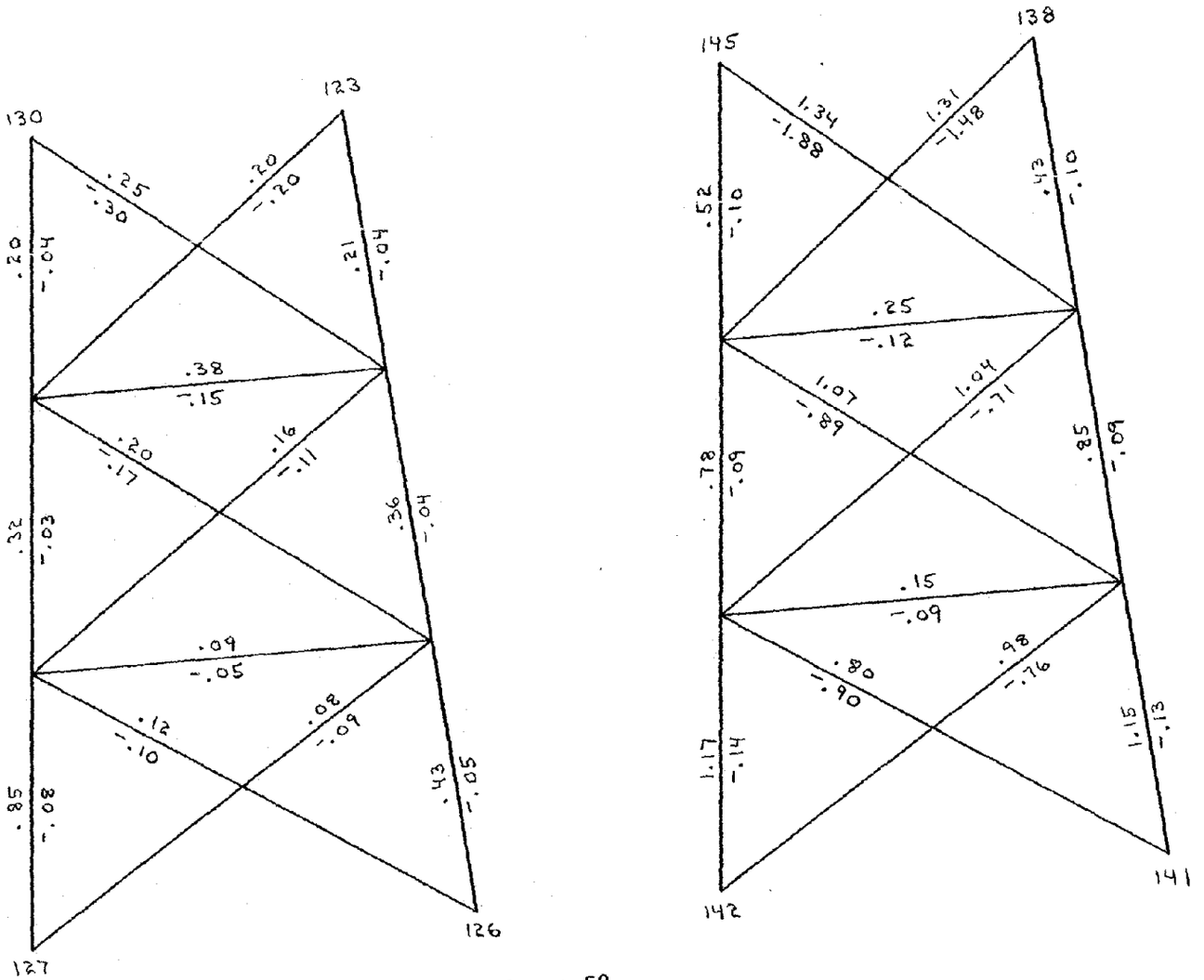

Figure 52

Buckling and yield ratios, tower: end views, fraction of critical damping = .01.

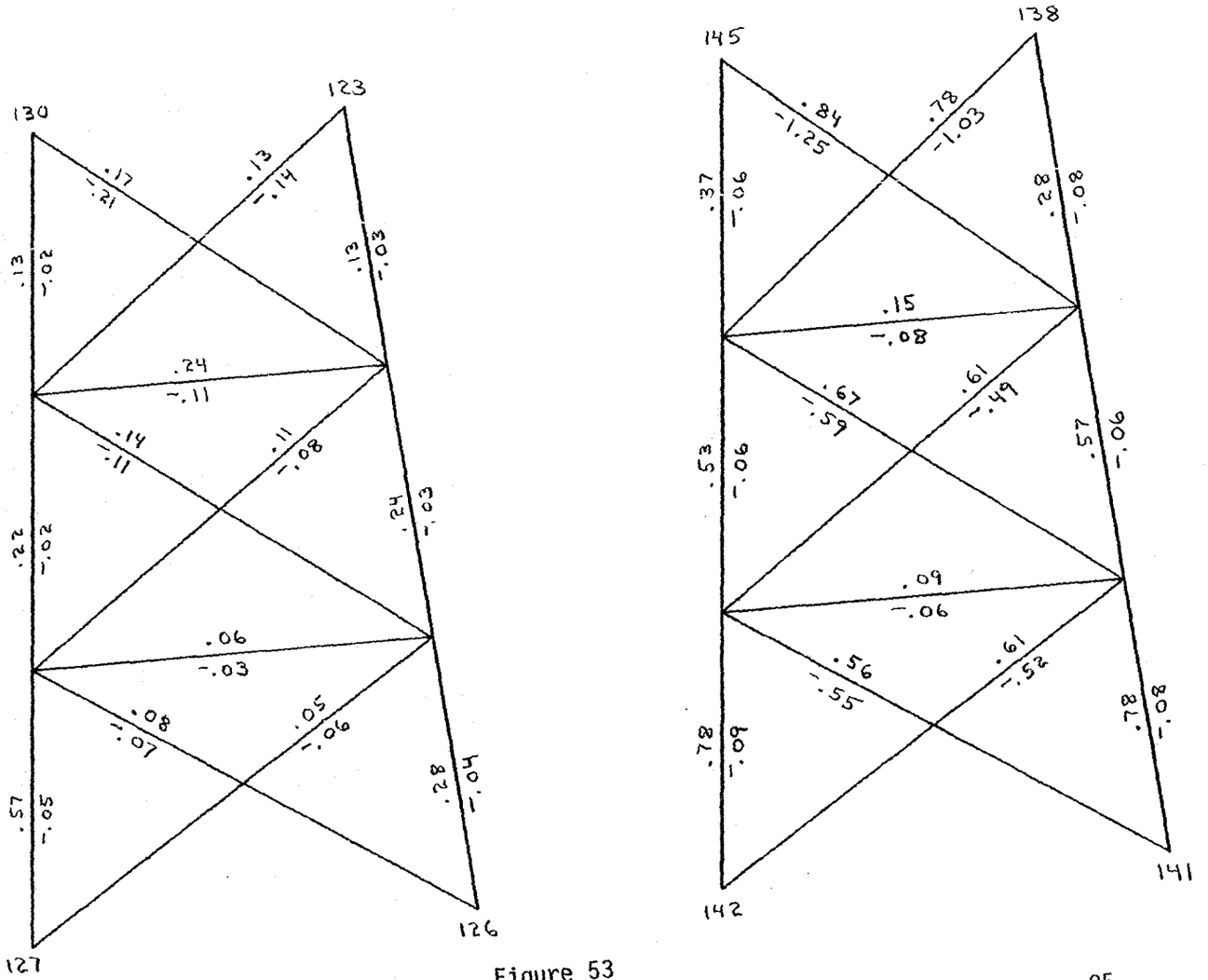

Figure 53

Buckling and yield ratios, tower: end views, fraction of critical damping = .05.

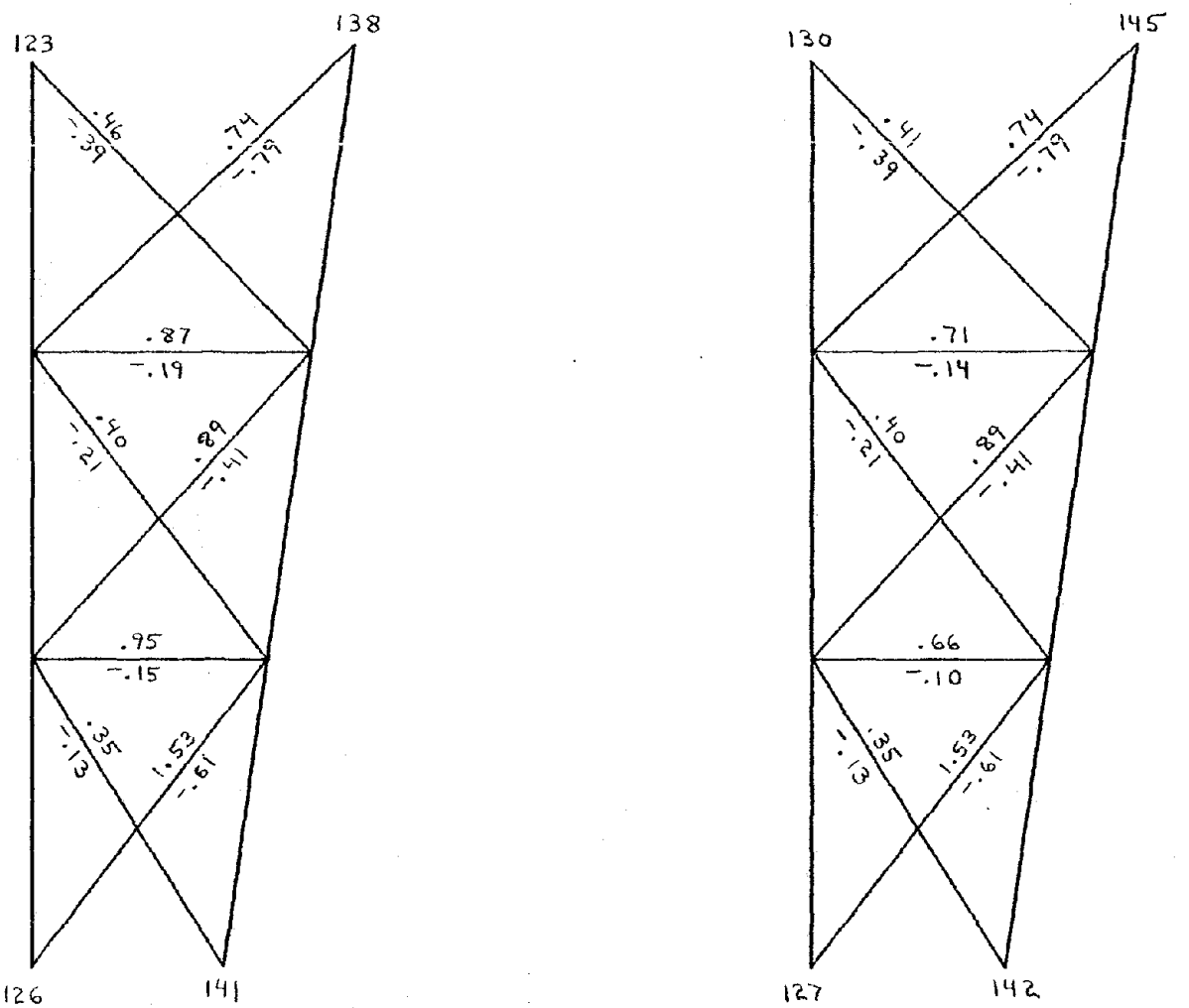

Figure 54

Buckling and yield ratios, tower: front and back views, undamped.

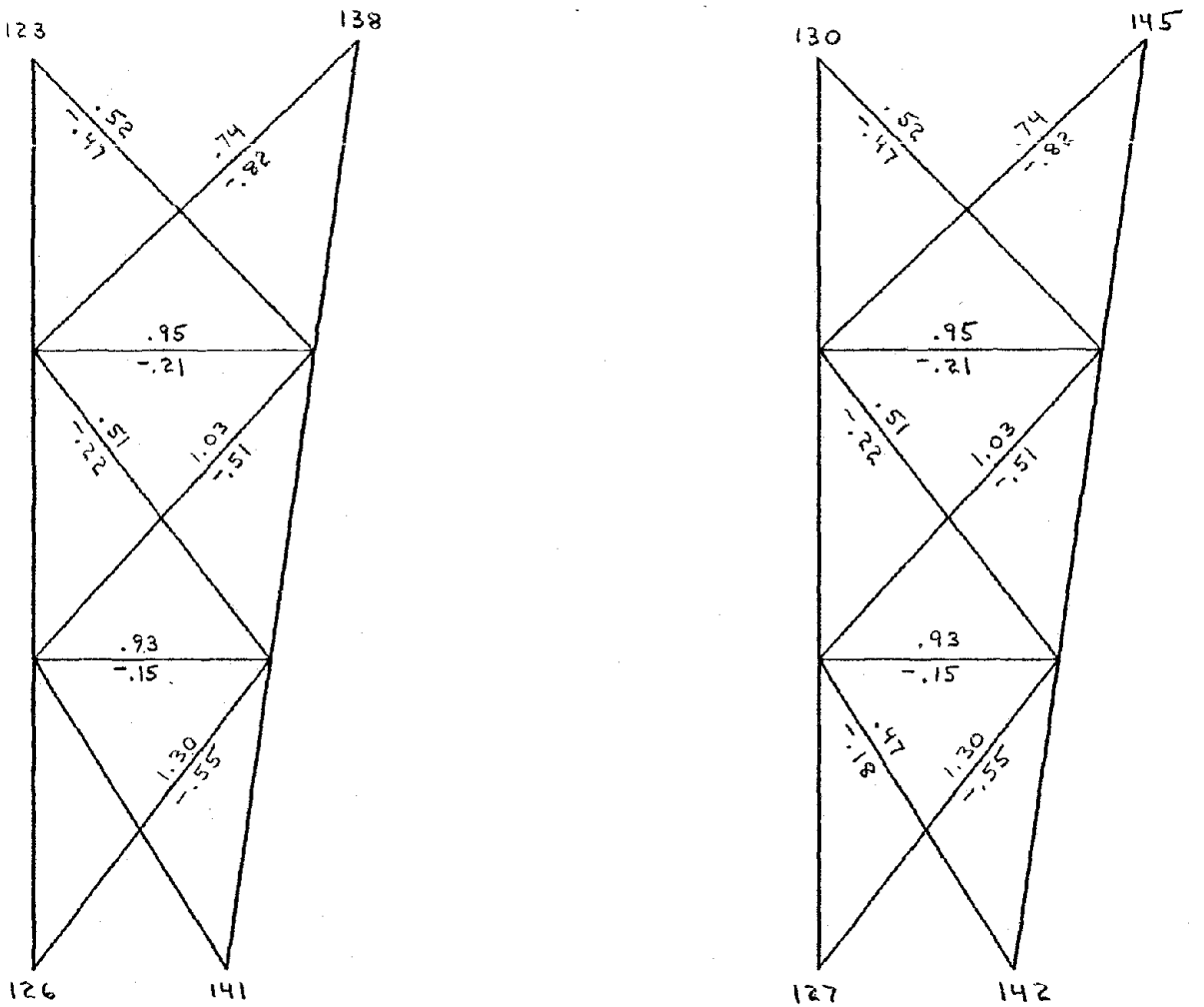

Figure 55

Buckling and yield ratios from the response spectrum analysis, tower: front and back views, undamped.

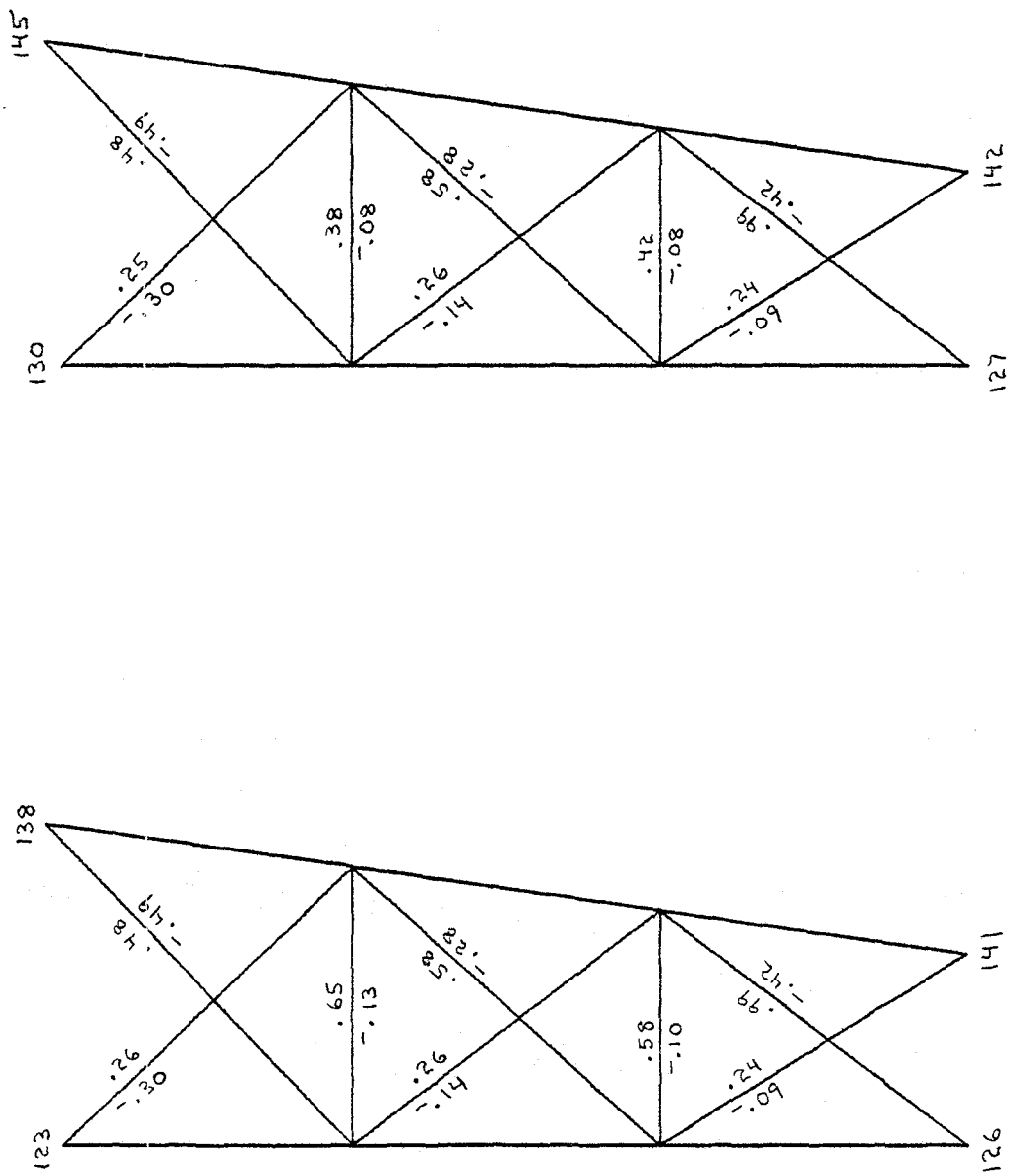

Figure 56

Buckling and yield ratios, tower: front and back views, fraction of critical damping = .01.

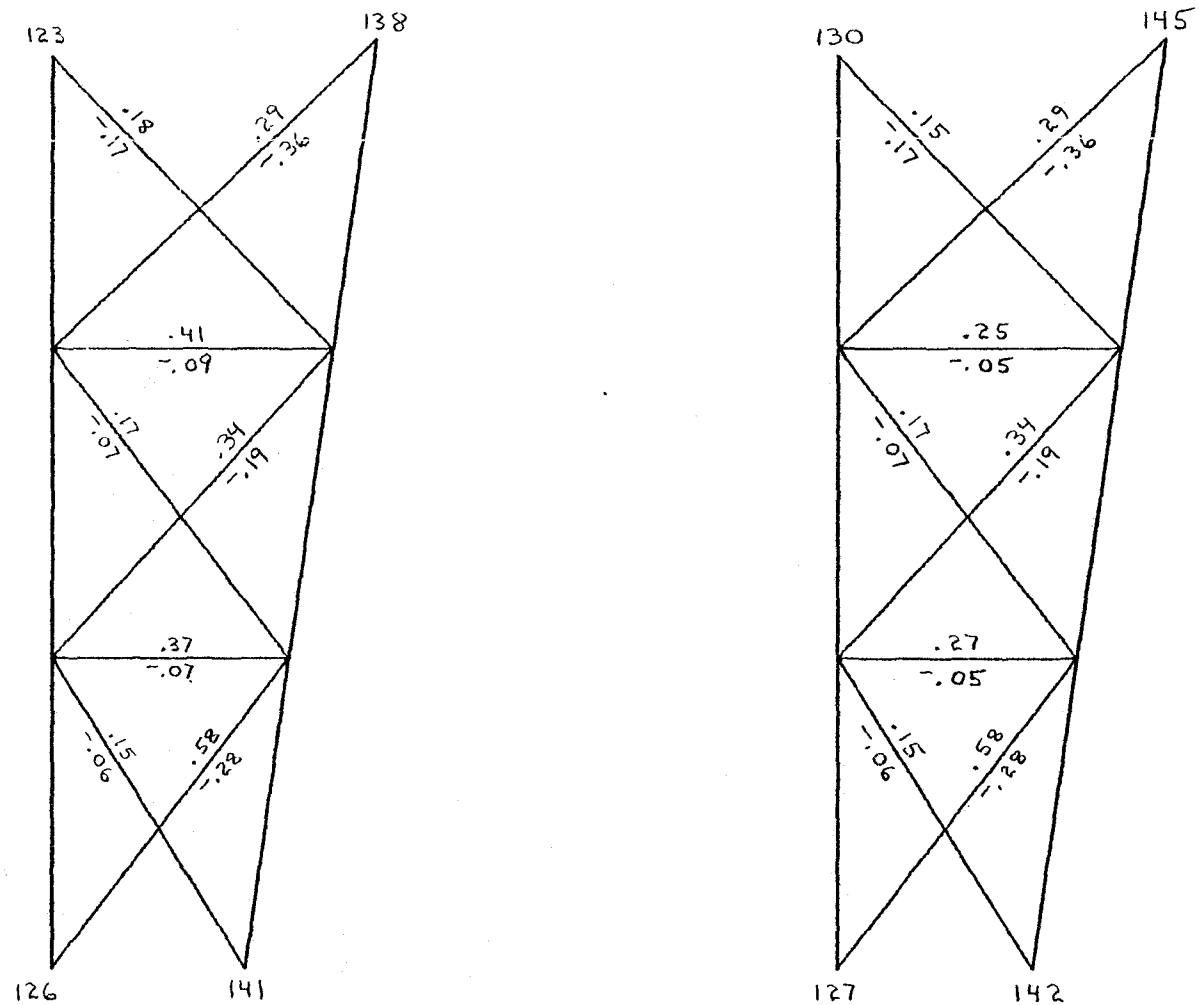

Figure 57

Buckling and yield ratios, tower: front and back views, fraction of critical damping = .05.

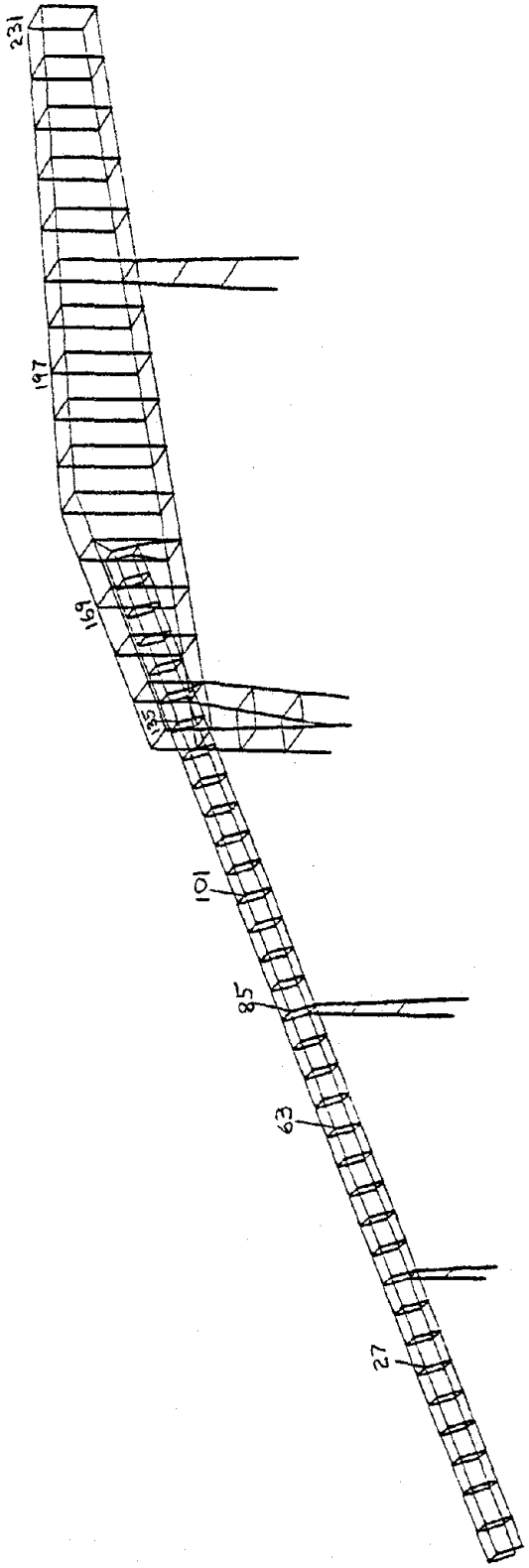

Figure 58

Key to nodal point z - displacement time-histories.

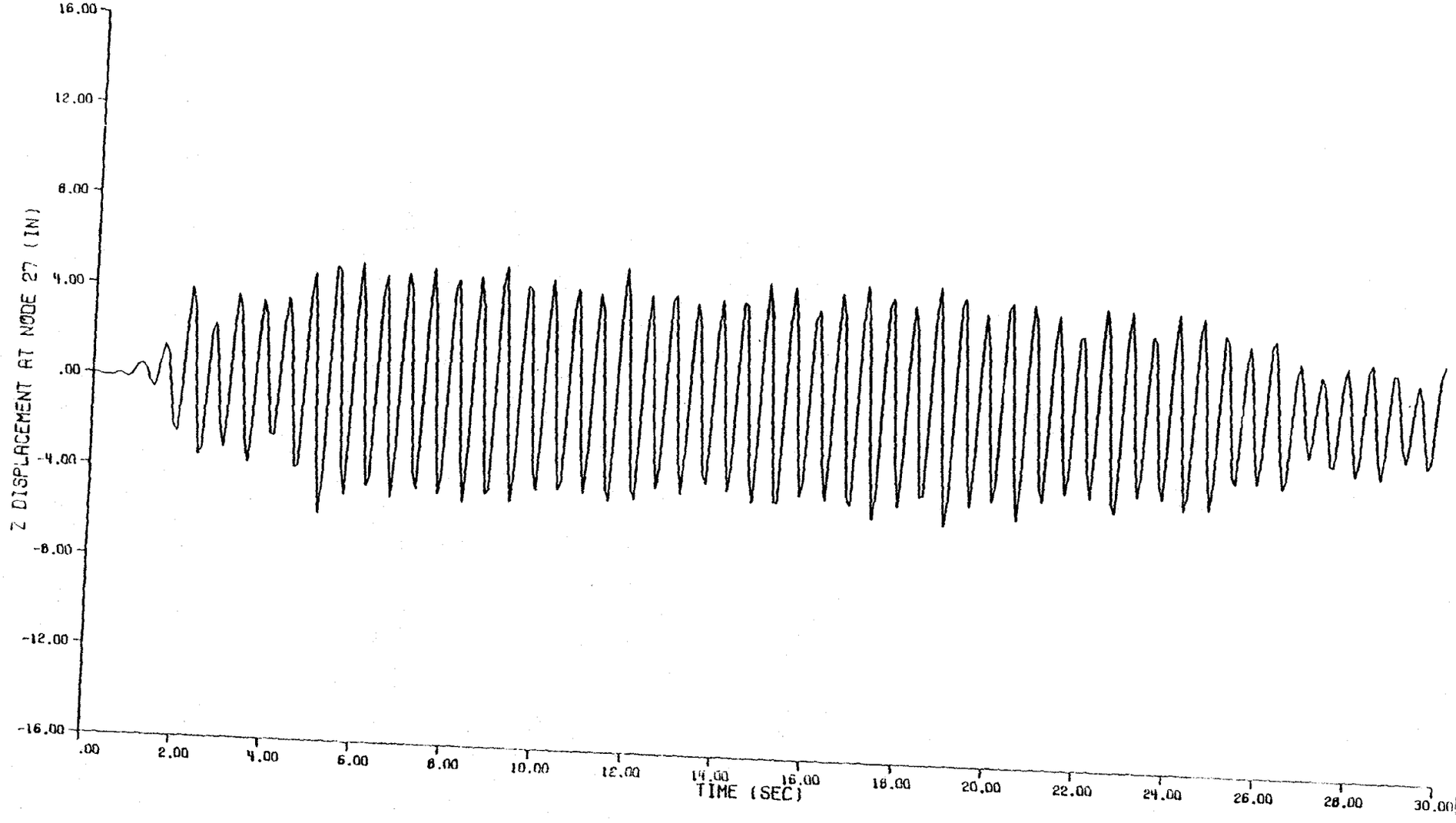

Figure 59

z - displacement time-history at node 27, undamped.

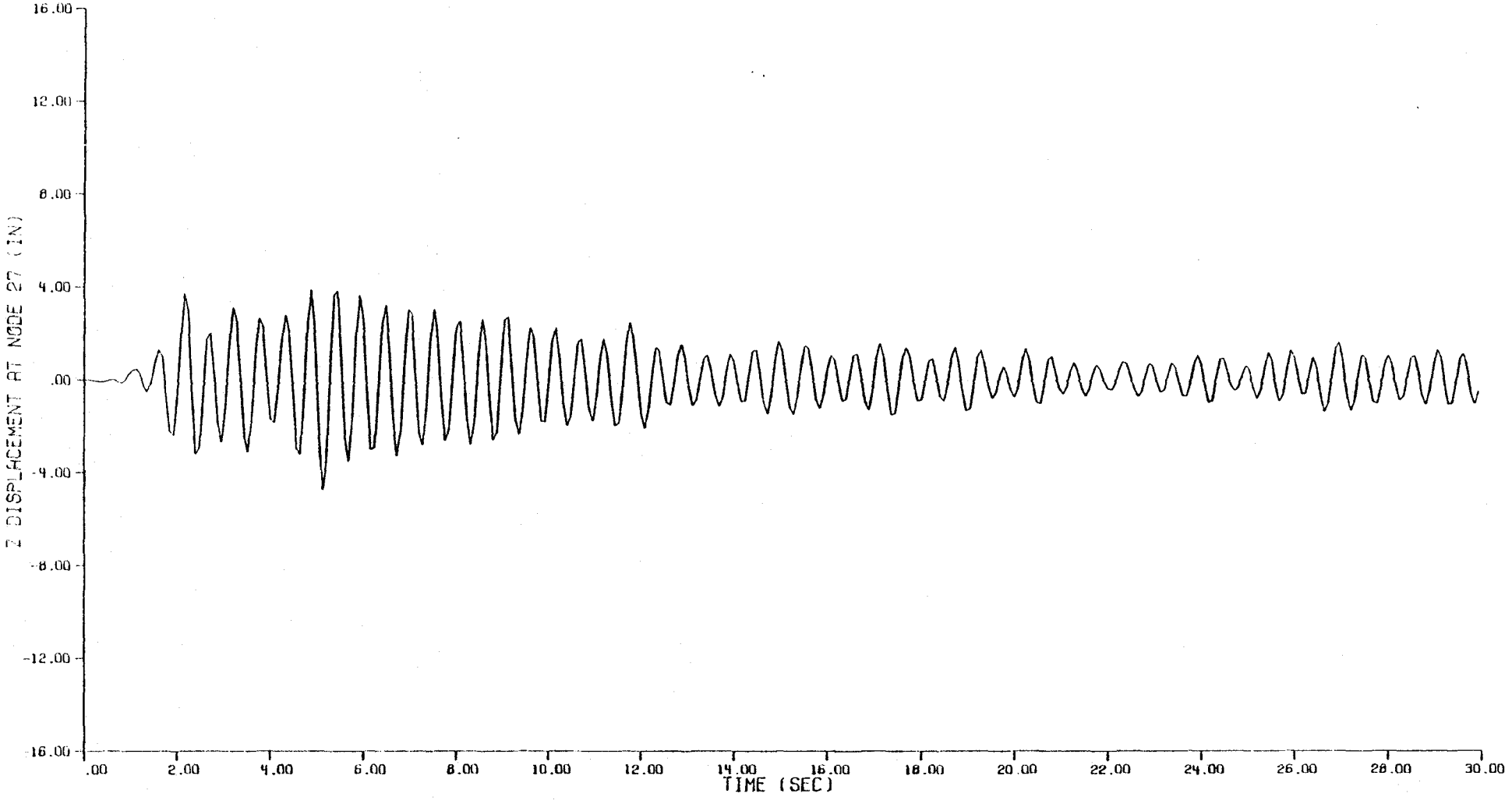

Figure 60

z - displacement time-history at node 27, fraction of critical damping = .01.

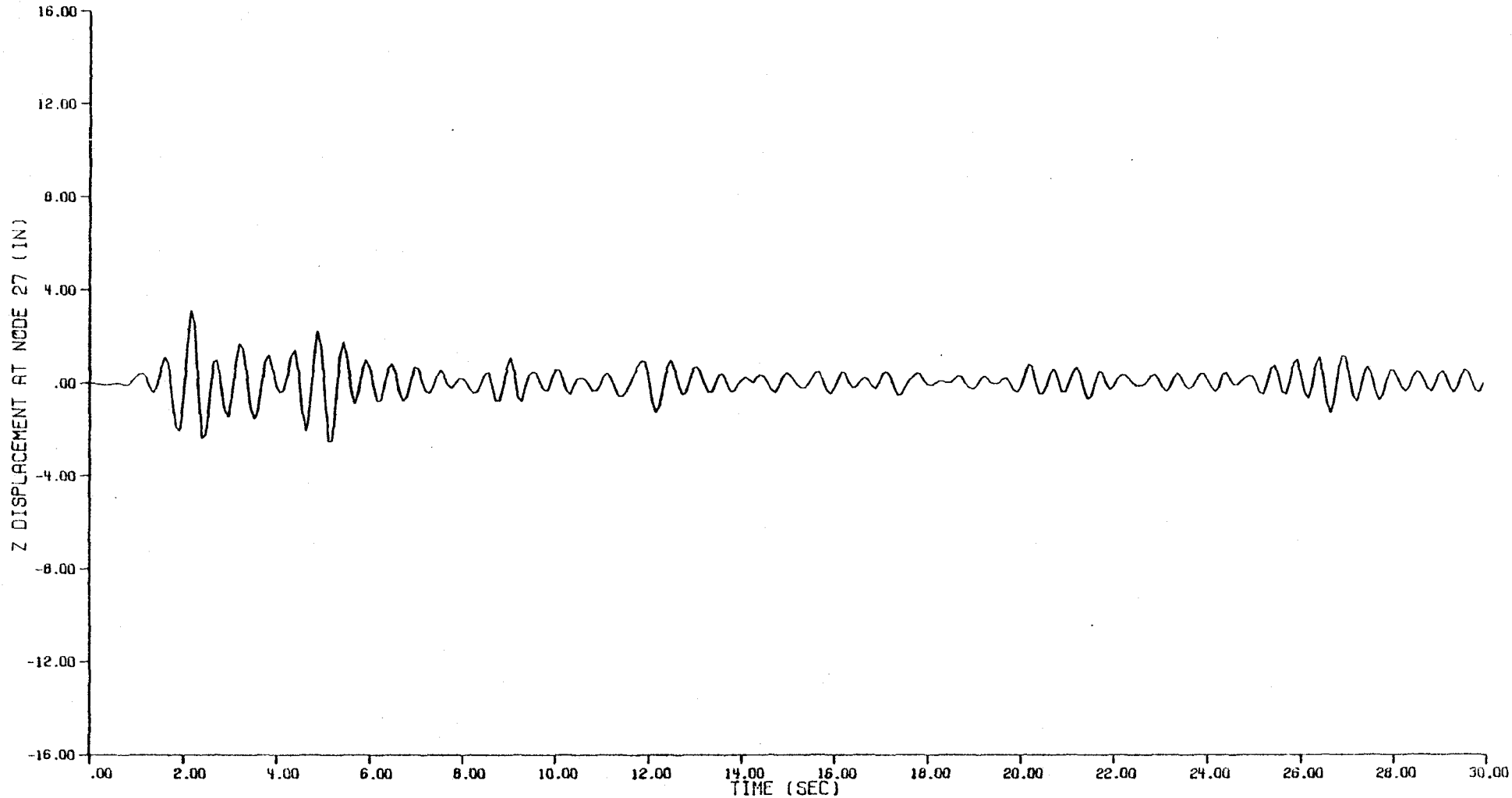

Figure 61

z - displacement time-history at node 27, fraction of critical damping = .05.

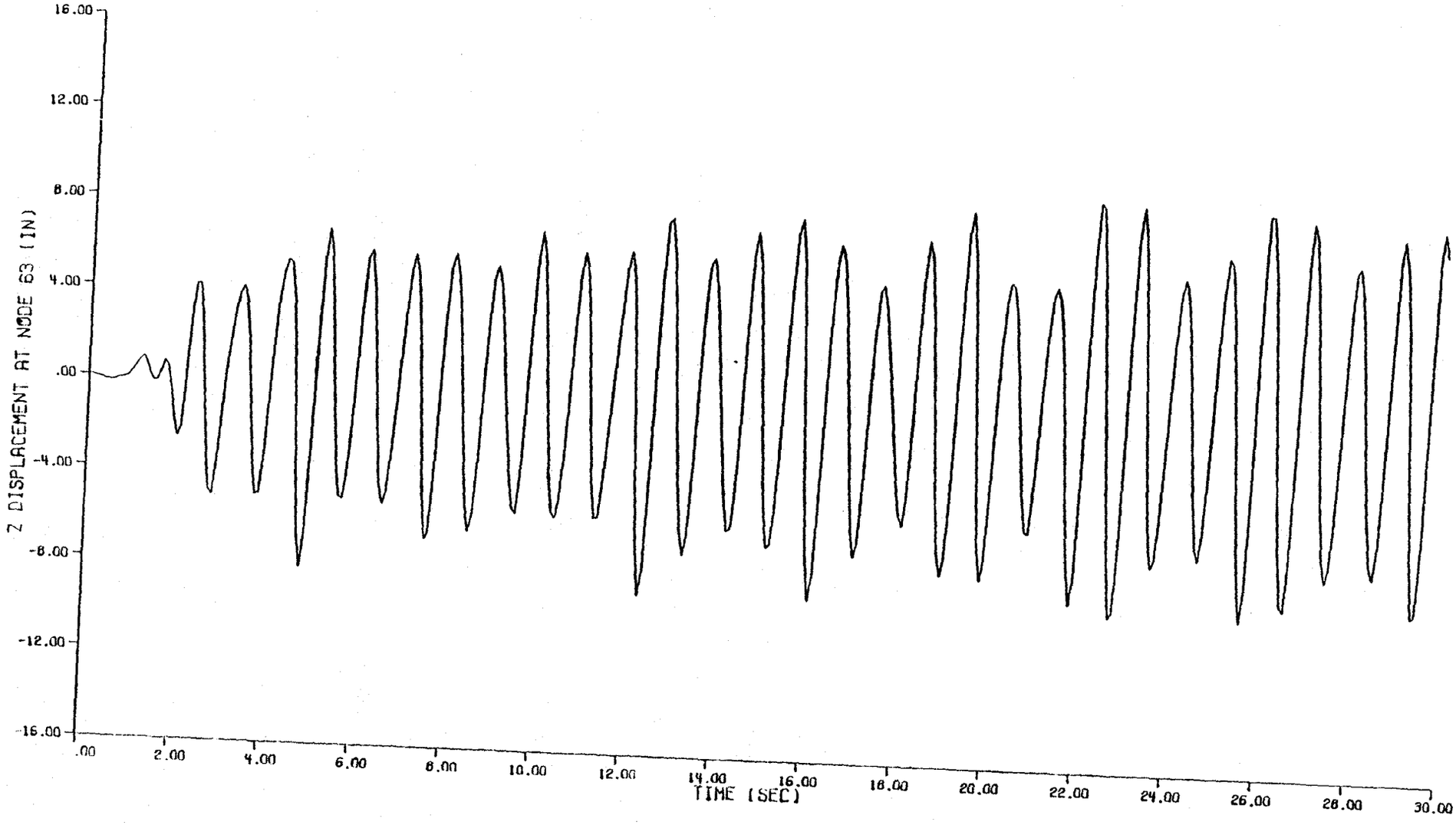

Figure 62

z - displacement time-history at node 63, undamped.

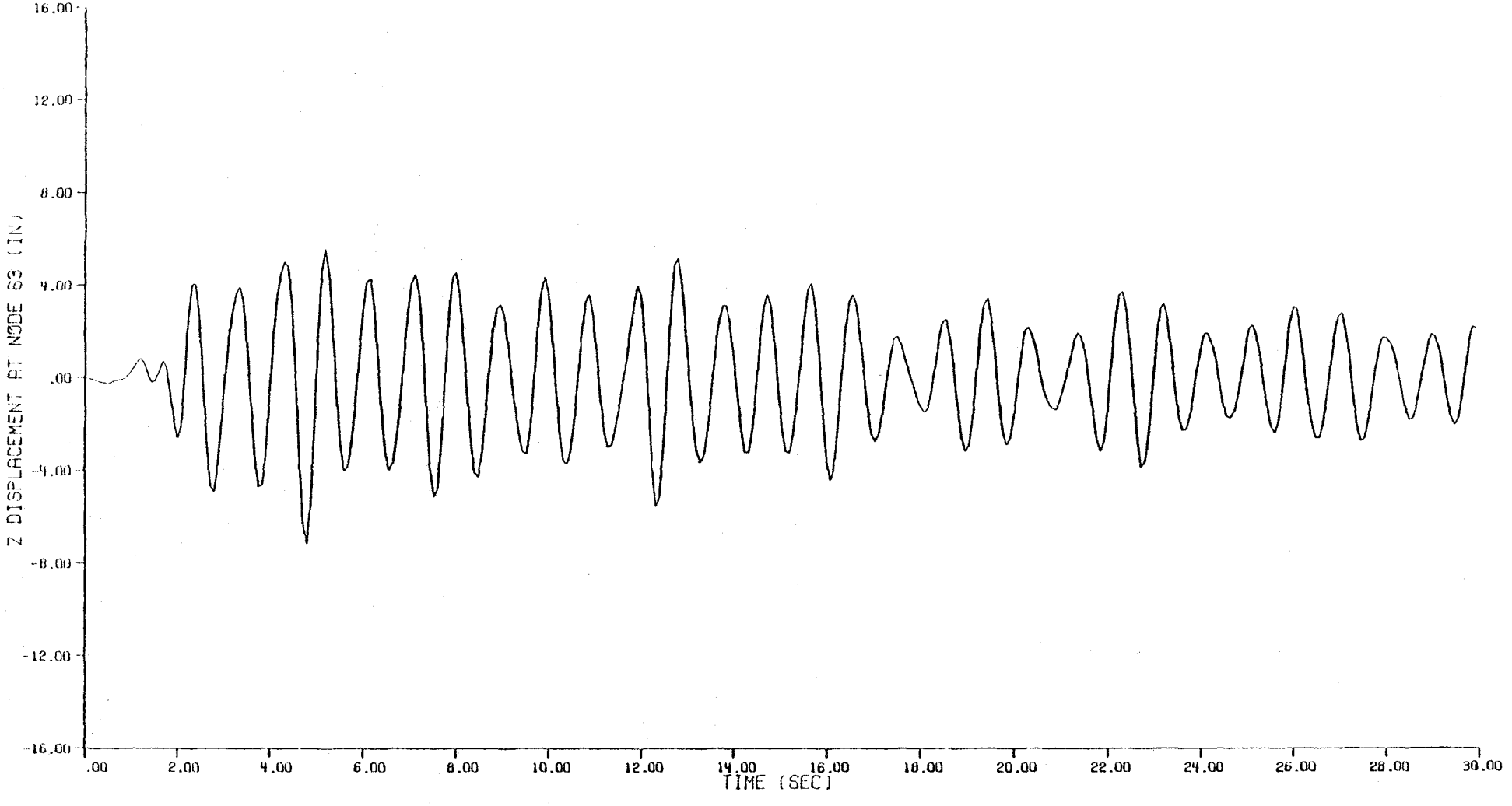

Figure 63

z - displacement time-history at node 63, fraction of critical damping = .01.

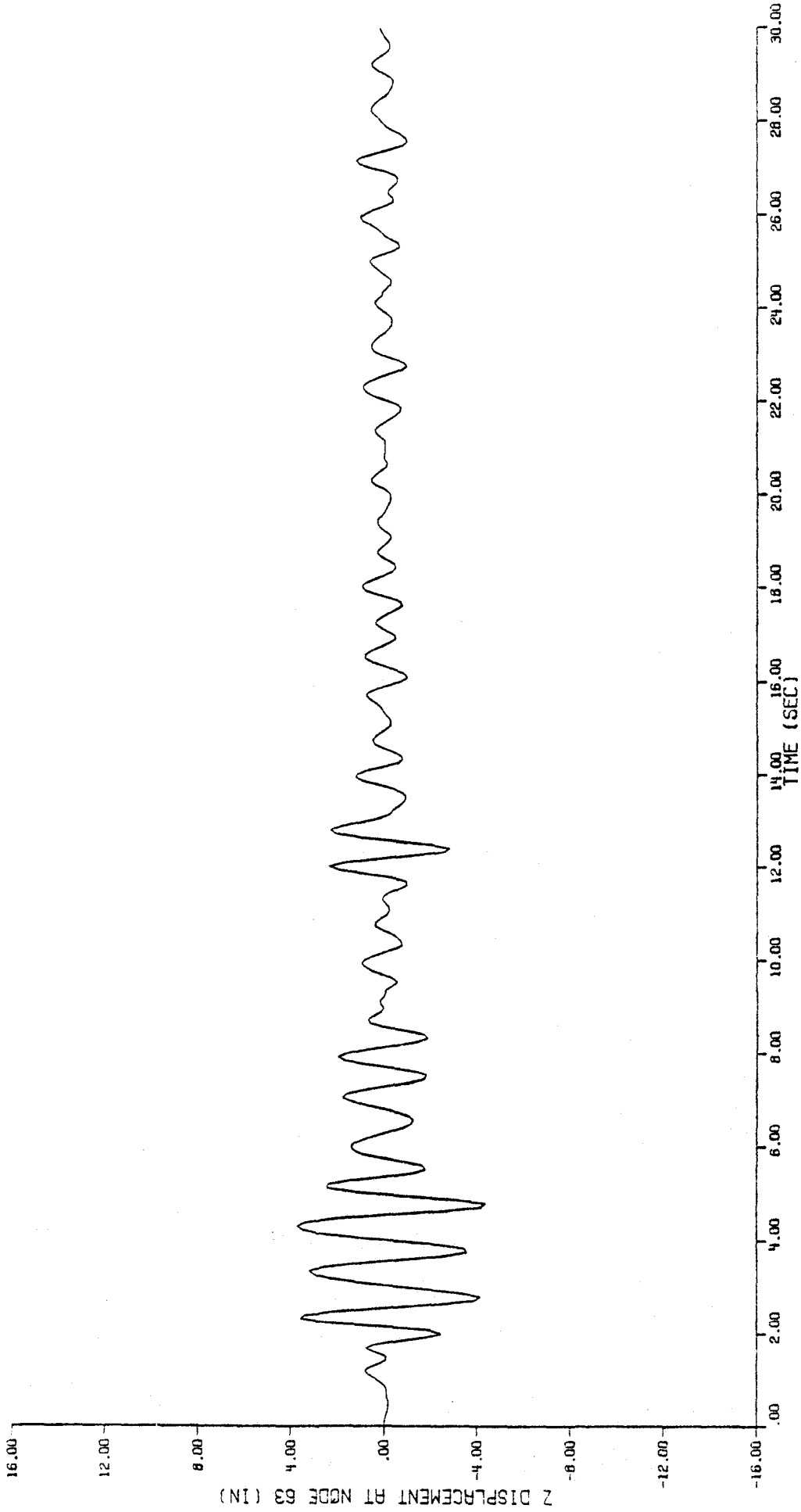

Figure 64

z - displacement time-history at node 63, fraction of critical damping = .05.

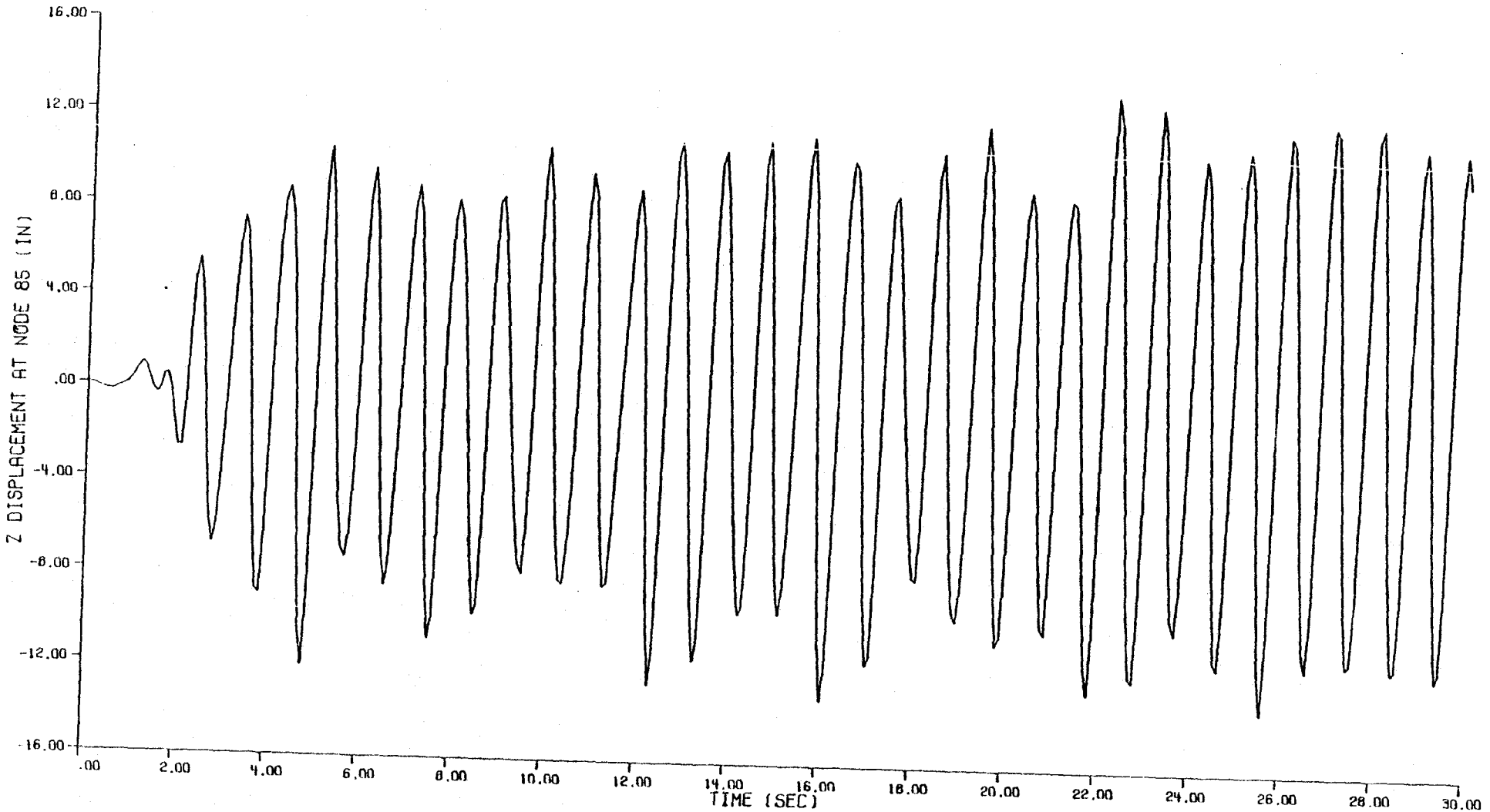

Figure 65

z - displacement time-history at node 85, undamped.

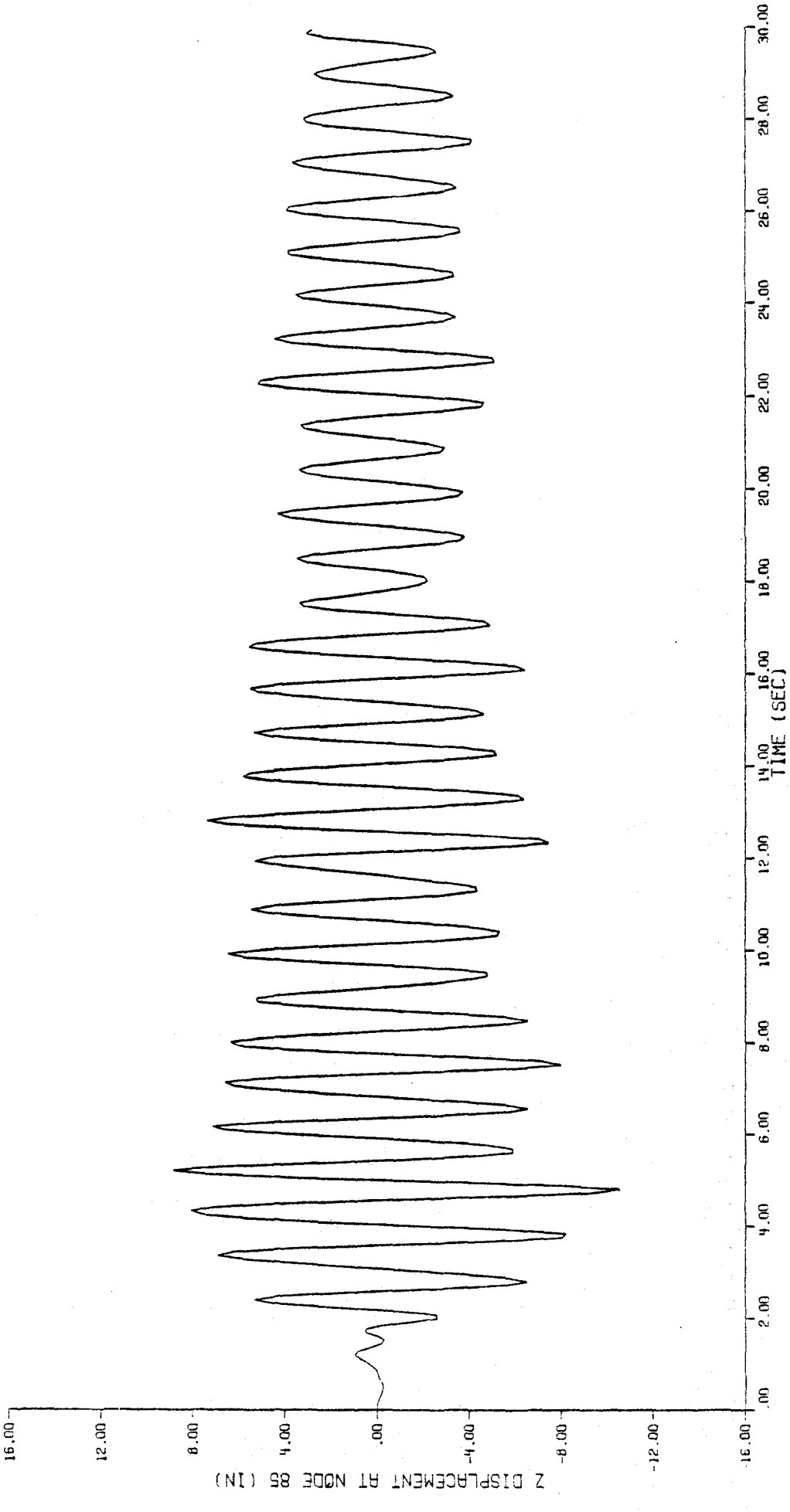

Figure 66

z - displacement time-history at node 85, fraction of critical damping = .01.

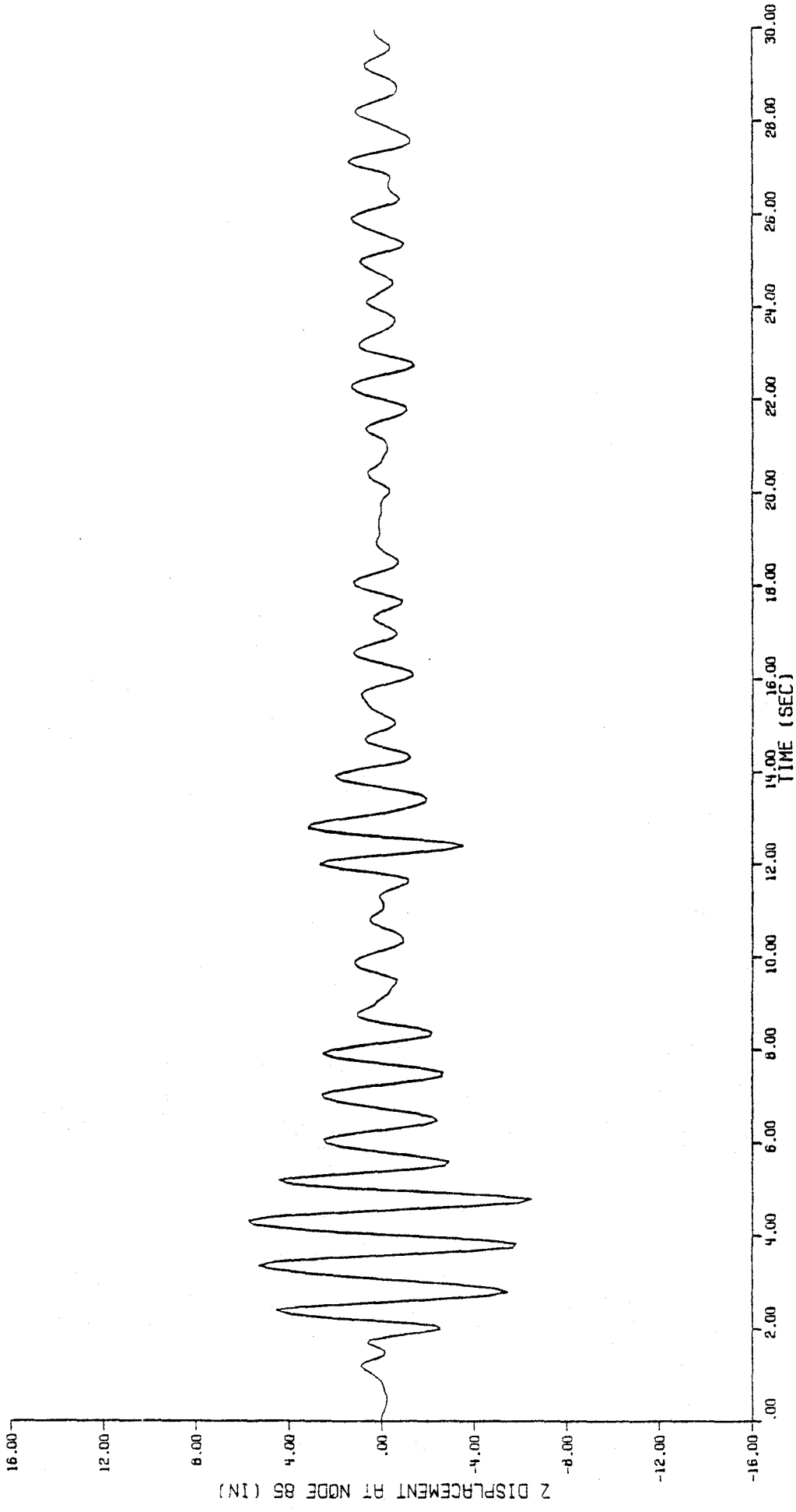

Figure 67

z - displacement time-history at node 85, fraction of critical damping = .05.

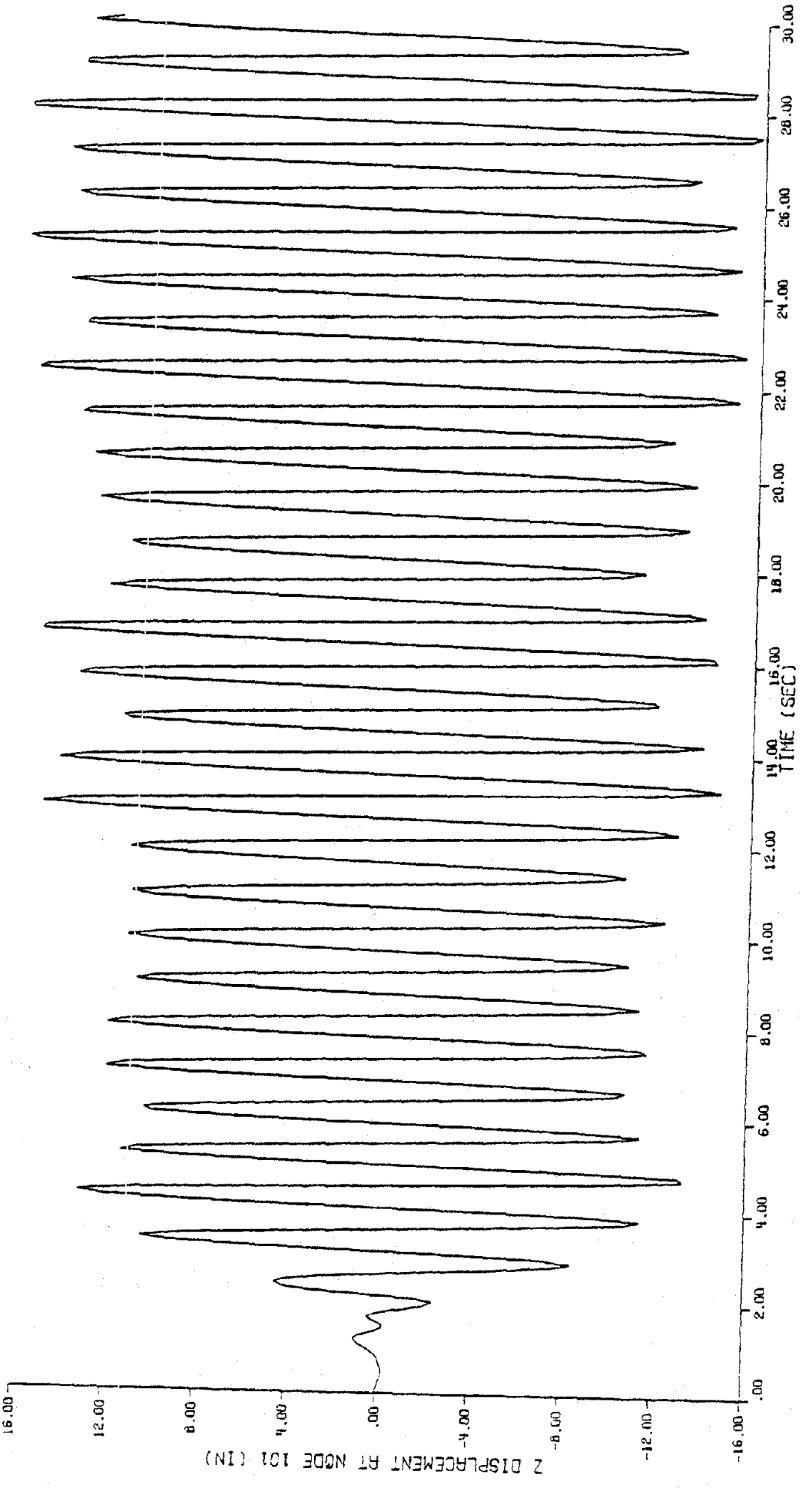

Figure 68

z - displacement time-history at node 101, undamped.

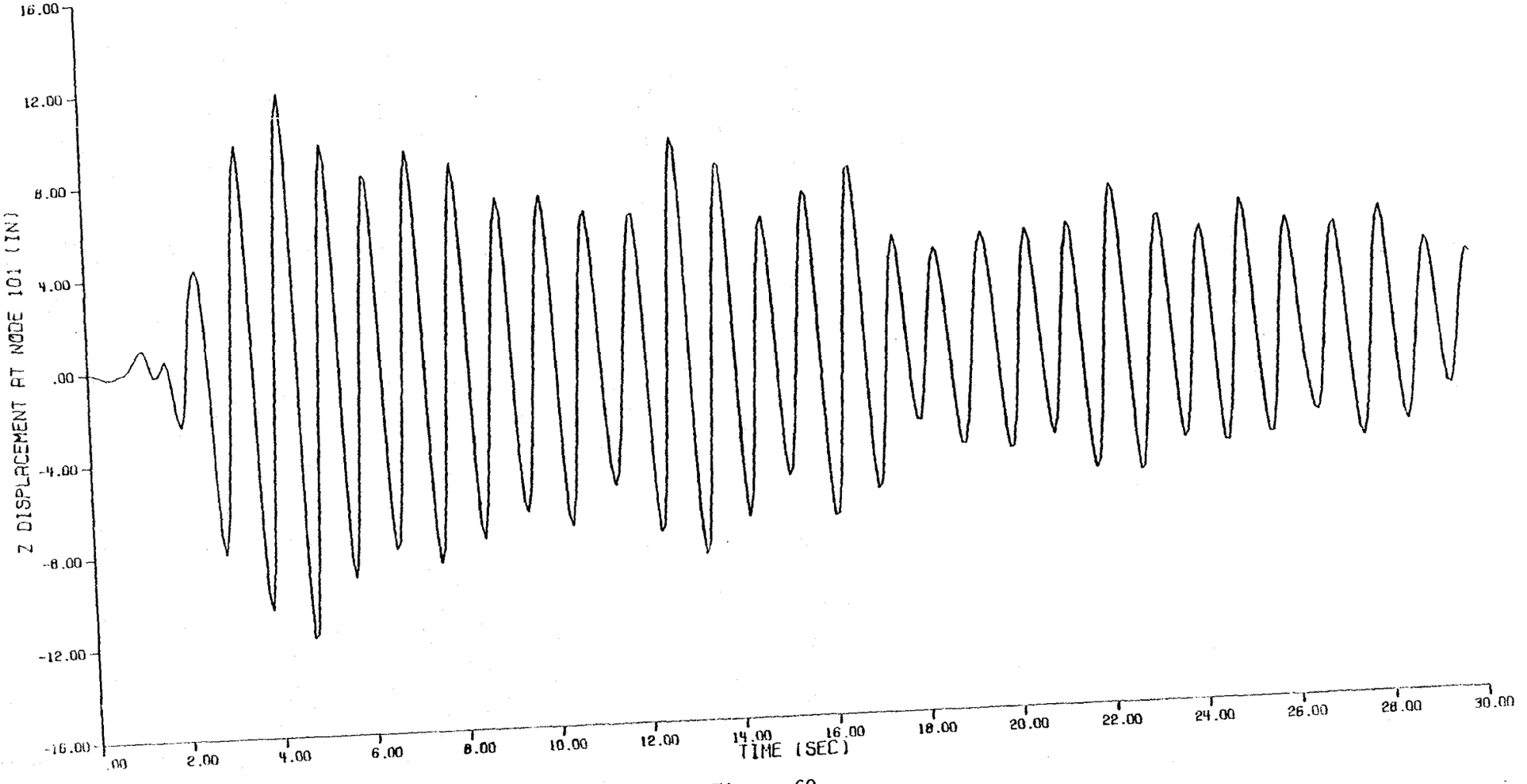

Figure 69

z - displacement time-history at node 101, fraction of critical damping = .01.

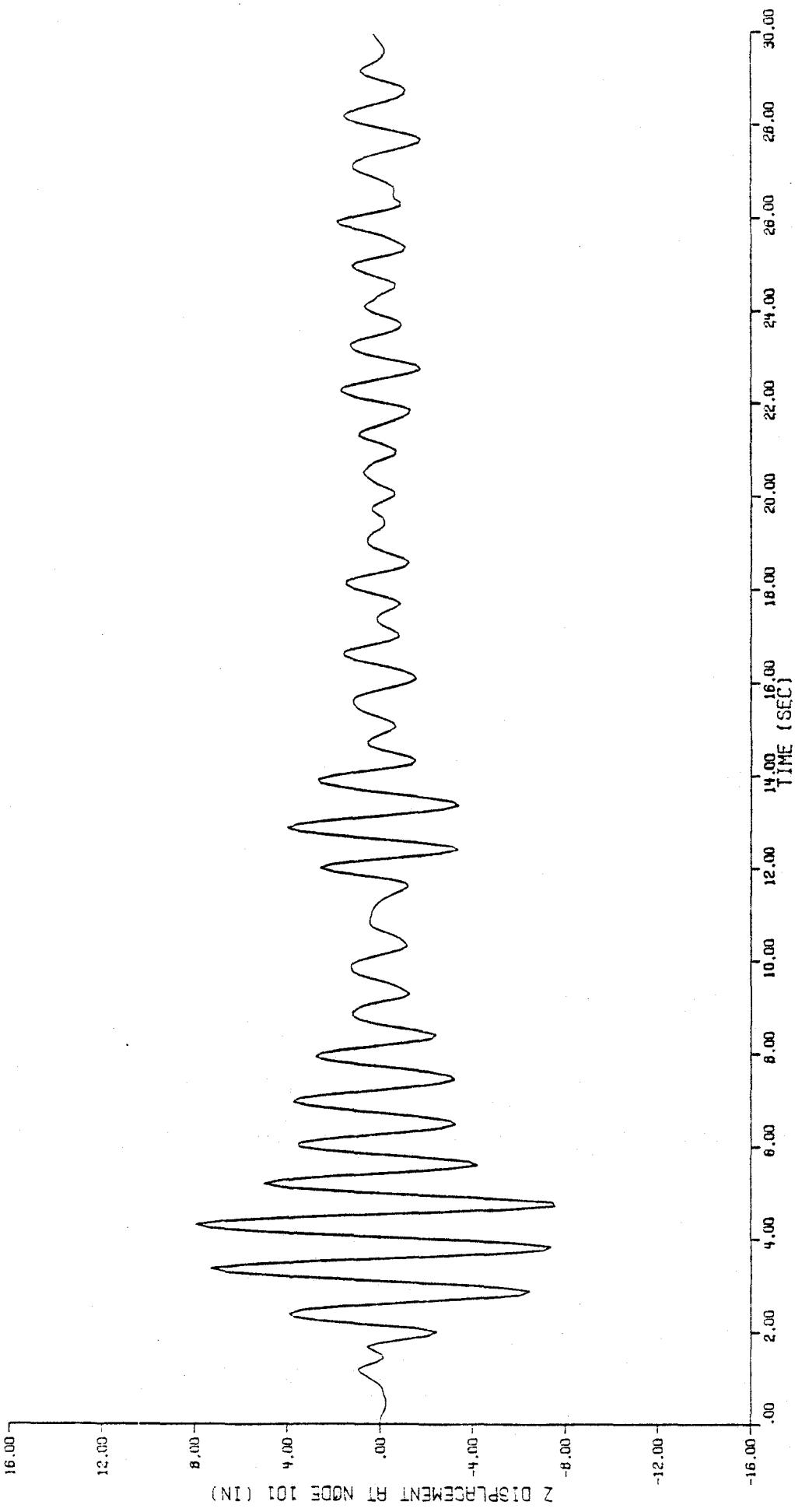

Figure 70

z - displacement time-history at node 101, fraction of critical damping = .05.

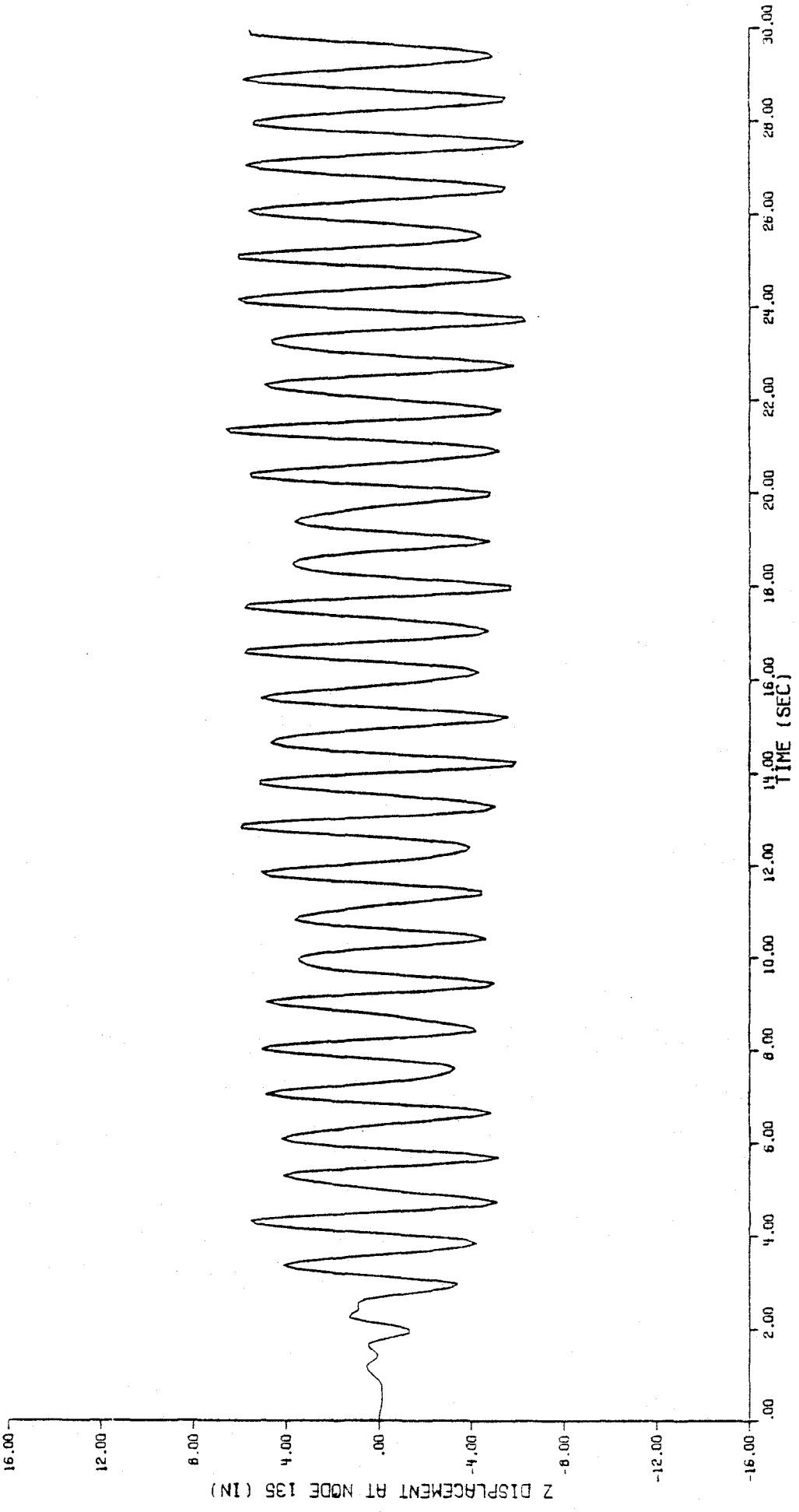

Figure 71

z - displacement time-history at node 135, undamped.

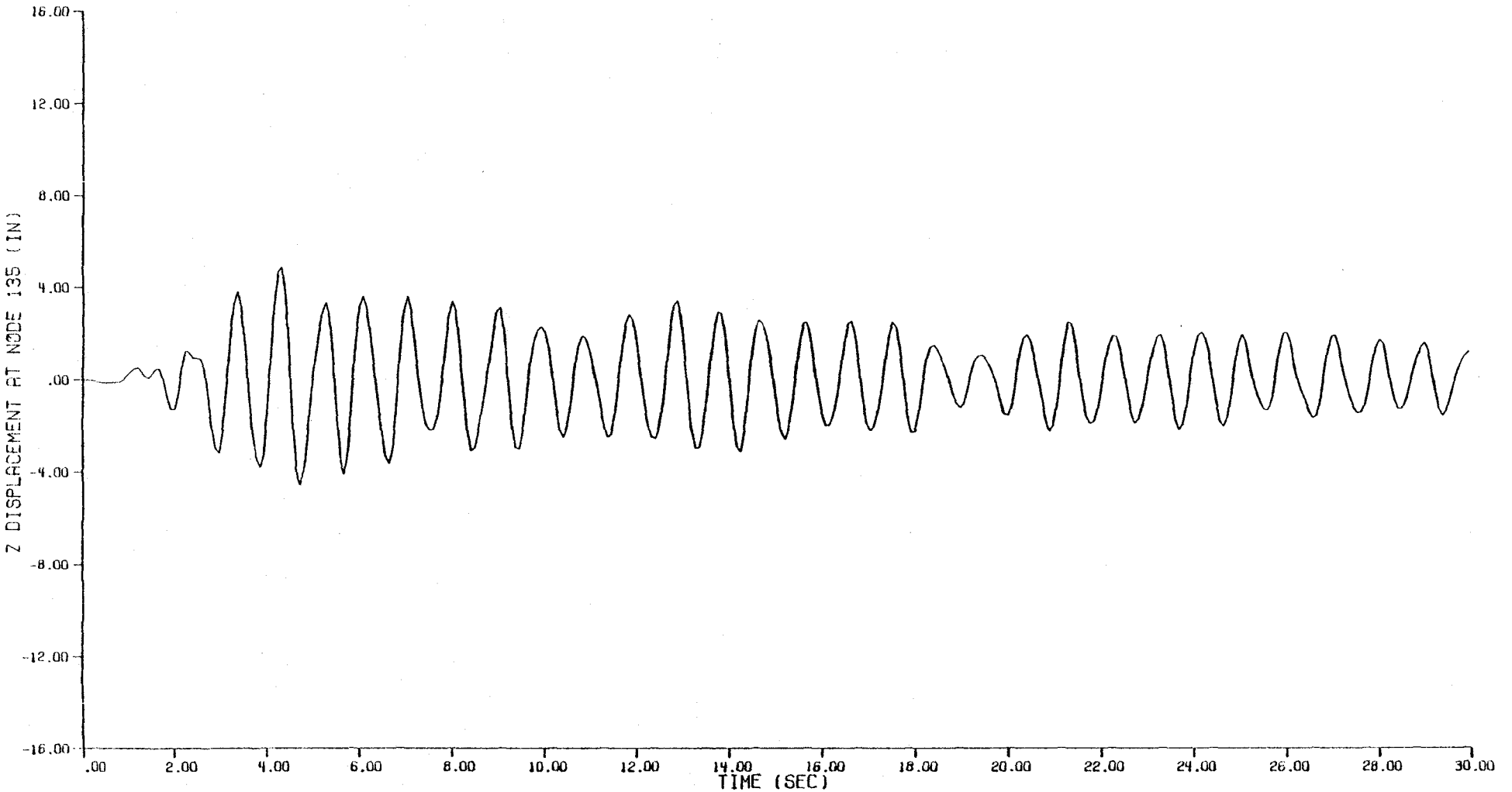

Figure 72

z - displacement time-history at node 135, fraction of critical damping = .01.

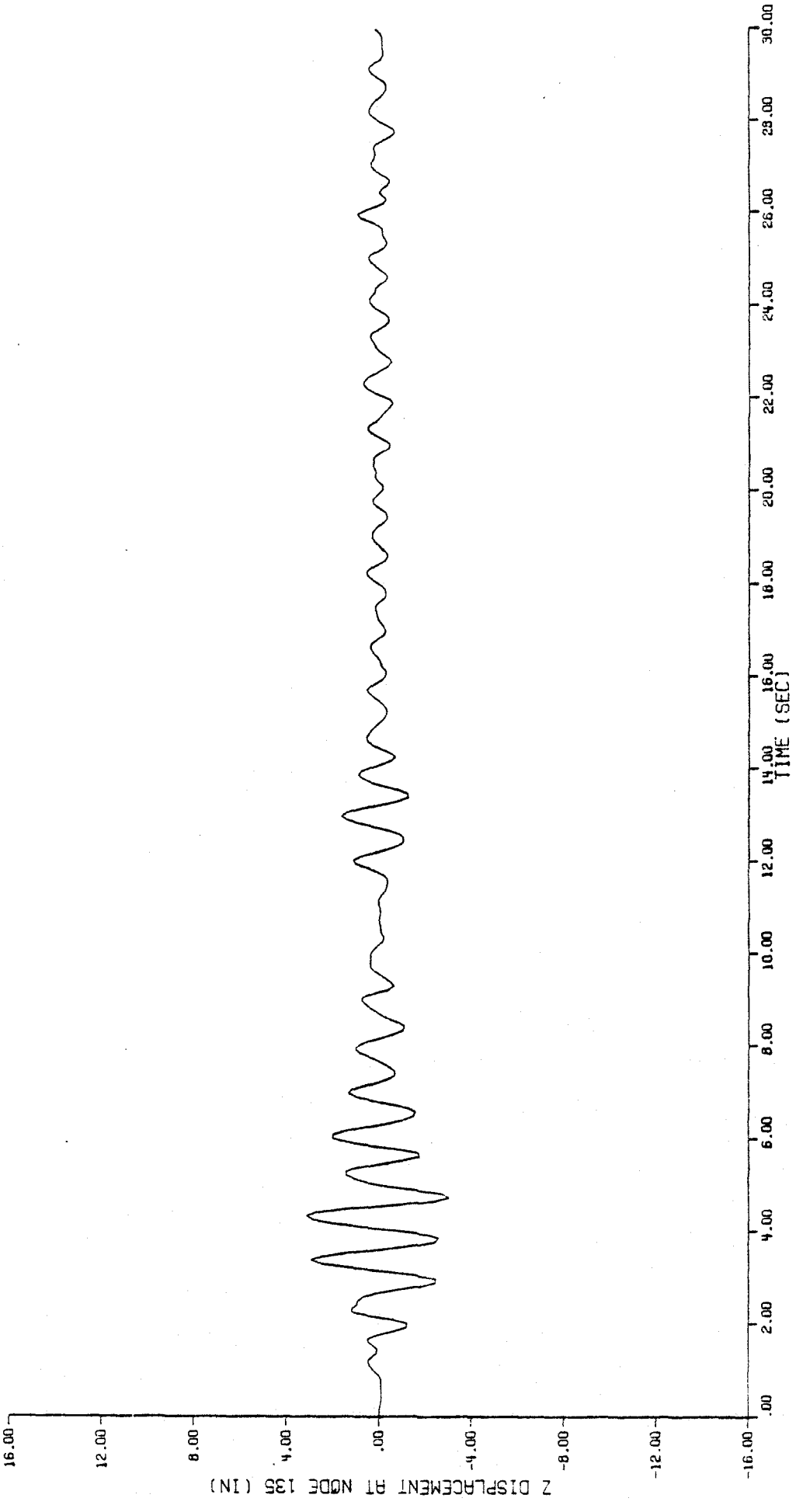

Figure 73

z - displacement time-history at node 135, fraction of critical damping = .05.

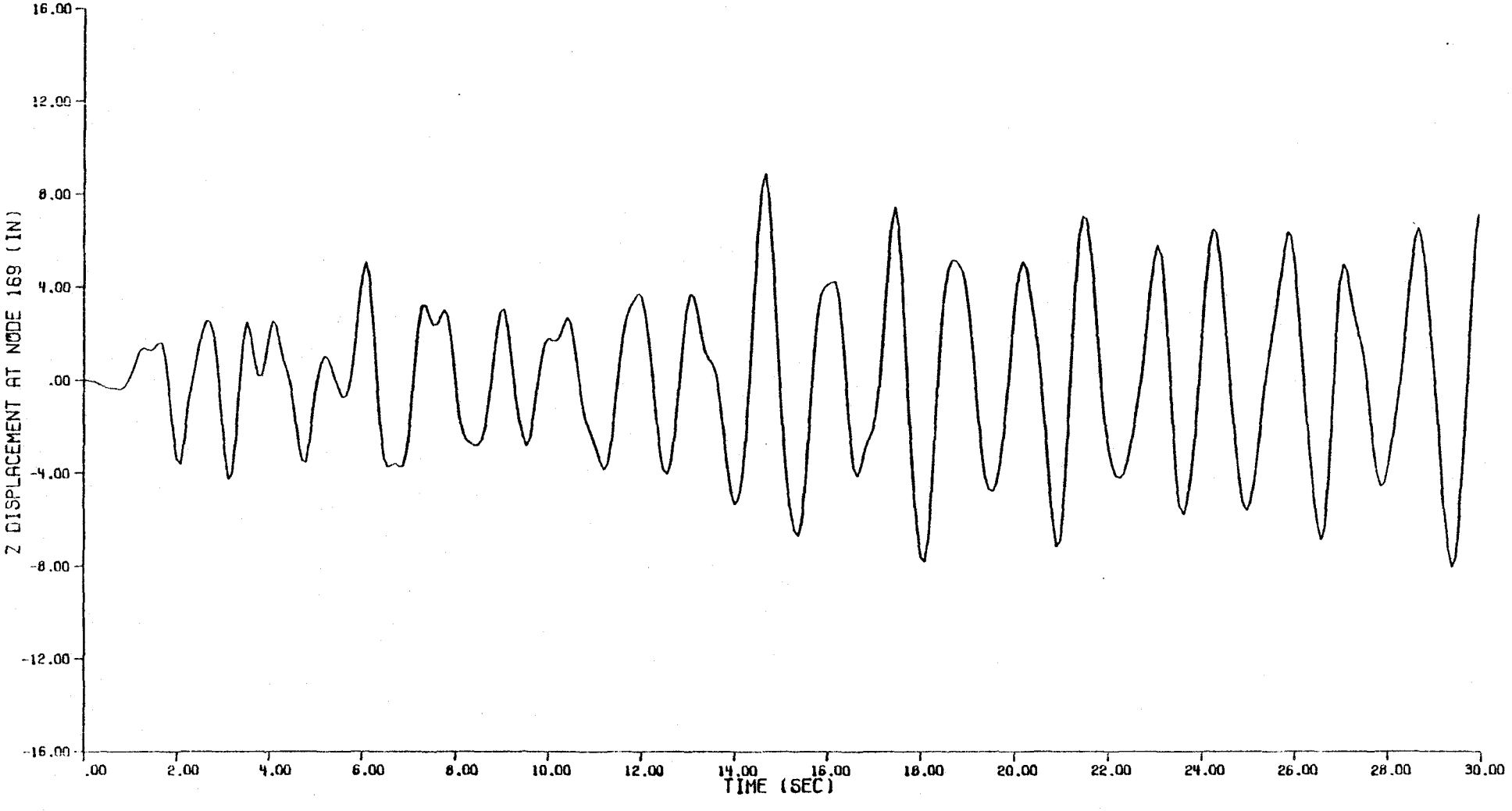

Figure 74

z - displacement time-history at node 169, undamped.

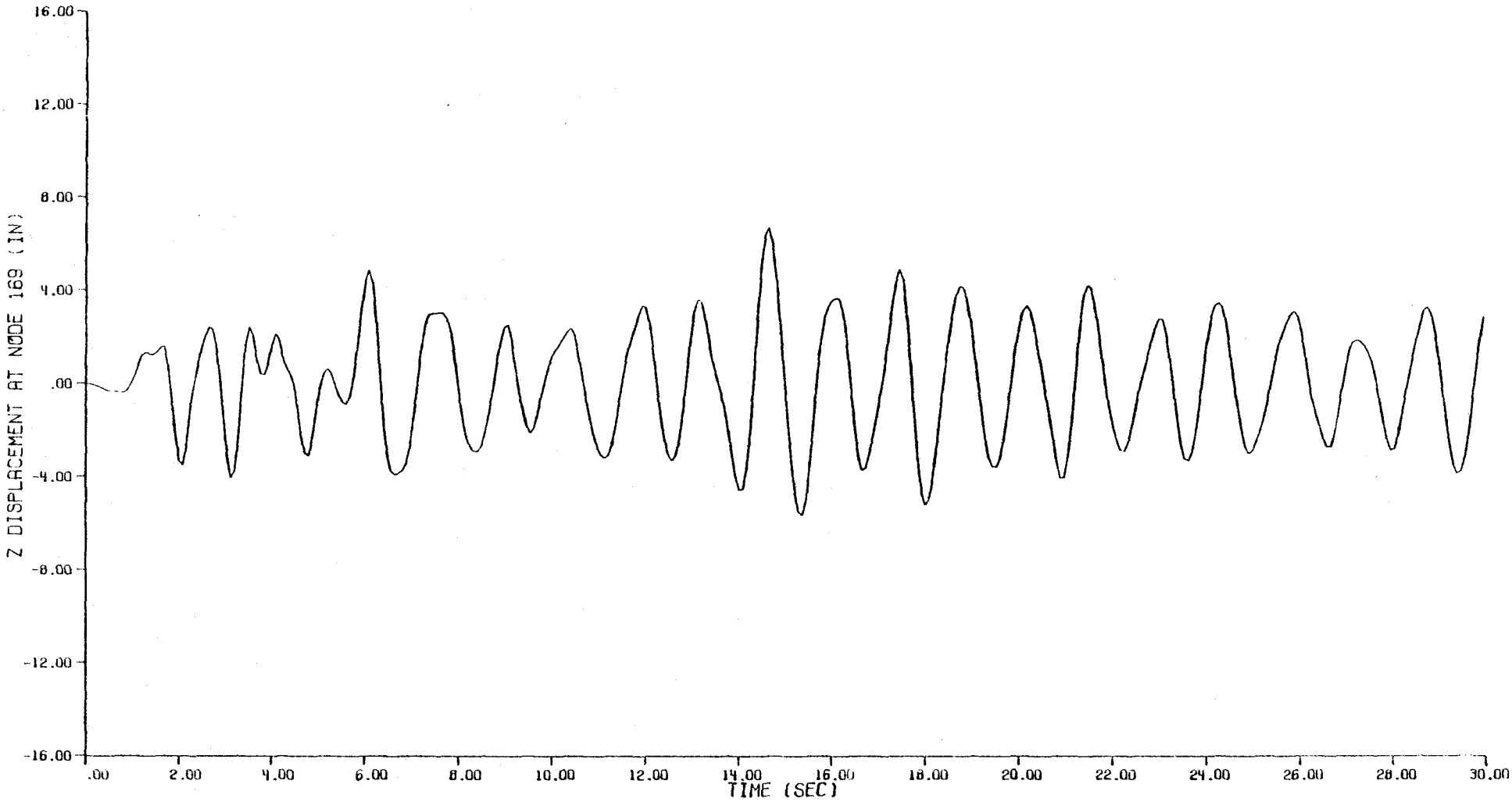

Figure 75

z - displacement time-history at node 169, fraction of critical damping - .01.

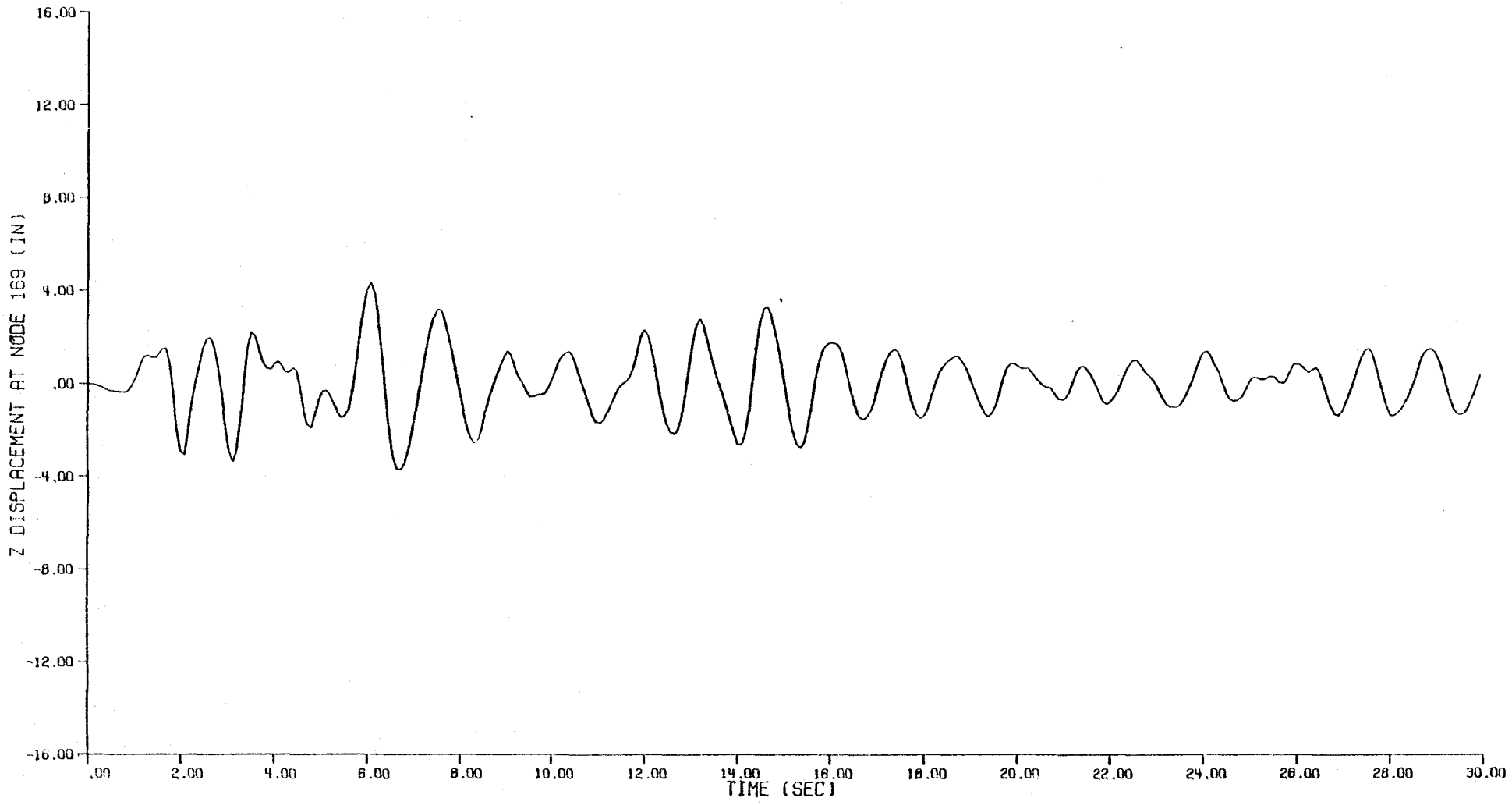

Figure 76

z - displacement time-history at node 169, fraction of critical damping = .05.

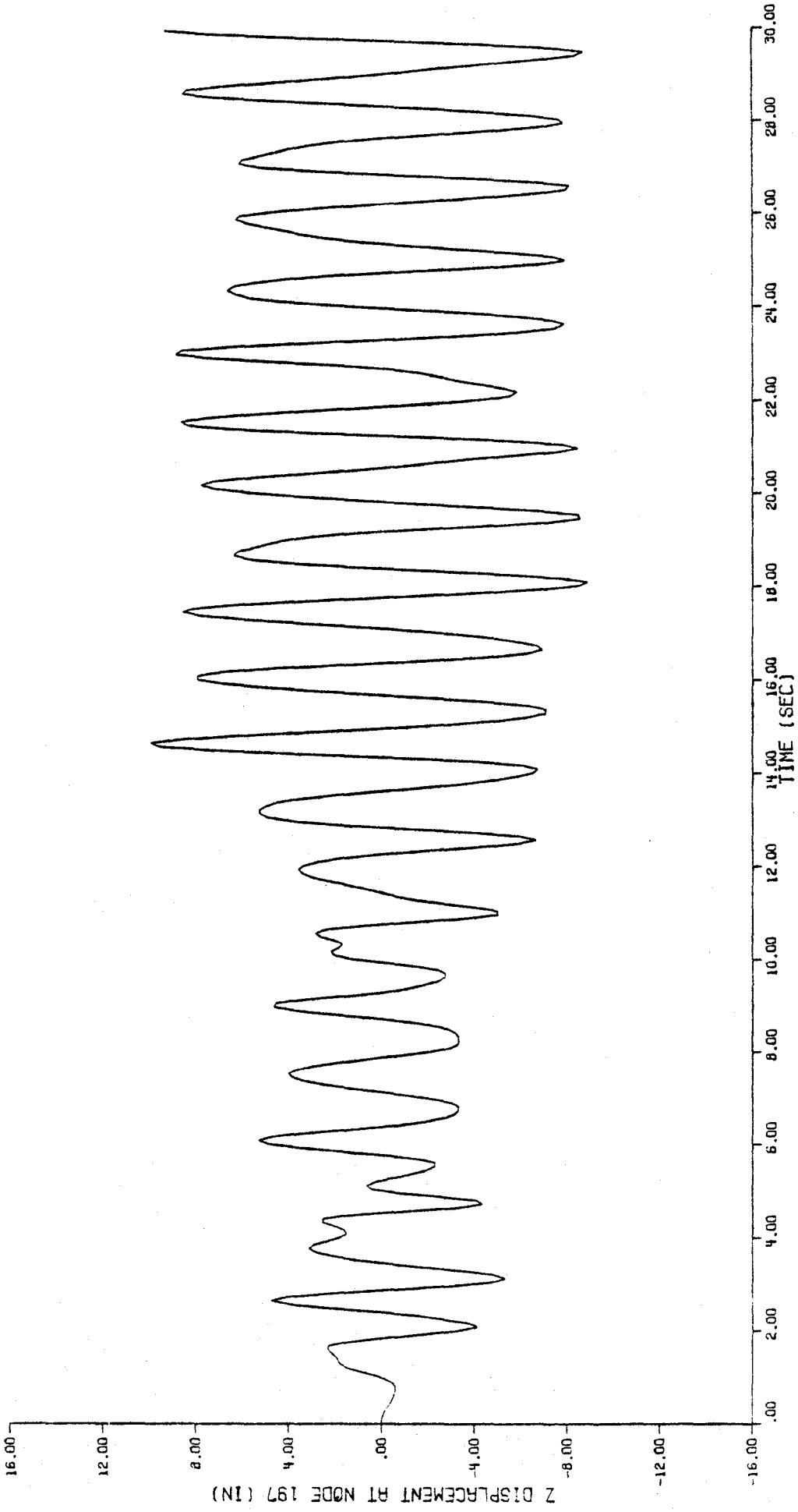

Figure 77

z - displacement time-history at node 197, undamped.

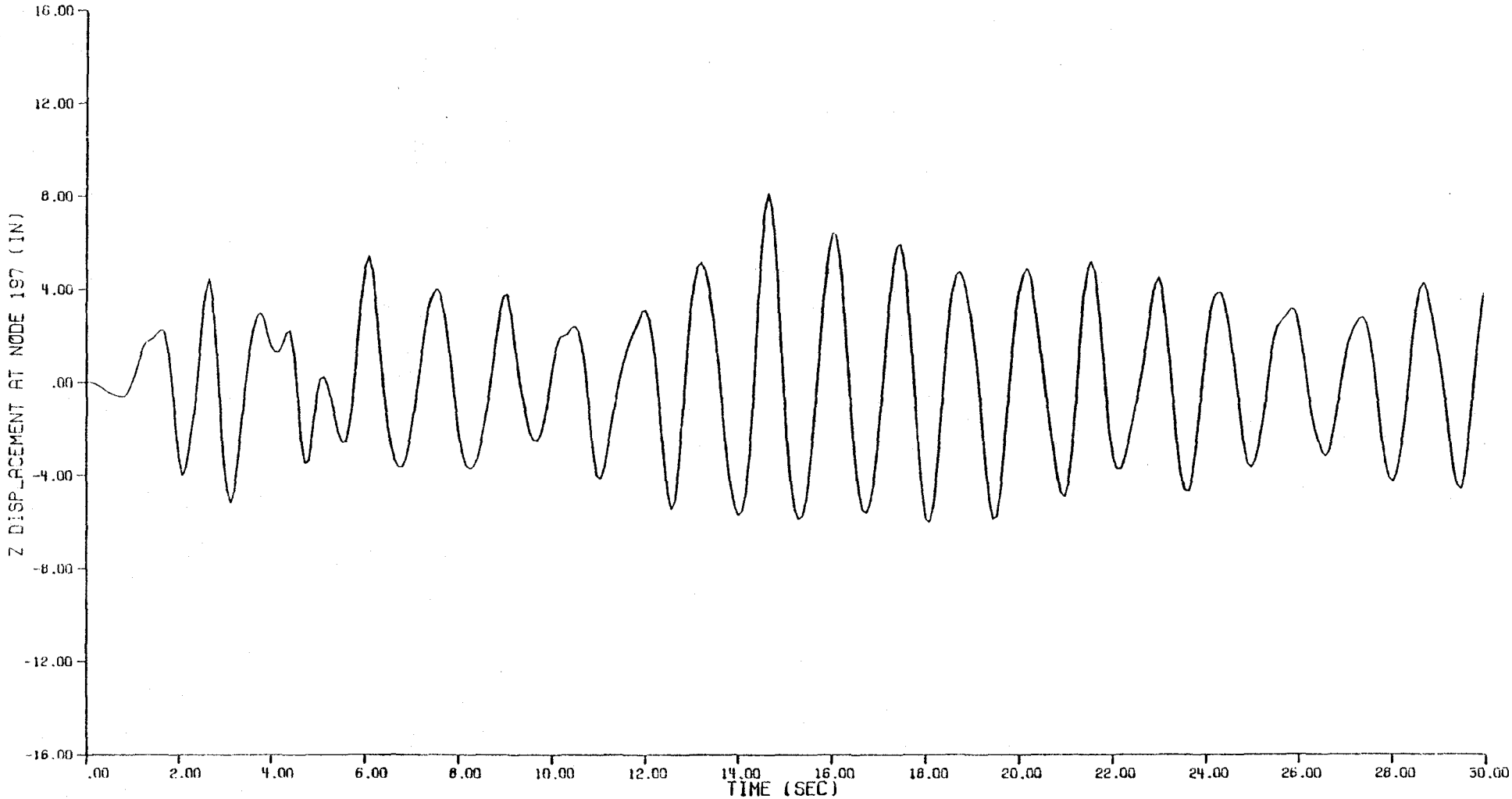

Figure 78

z - displacement time-history at node 197, fraction of critical damping = .01.

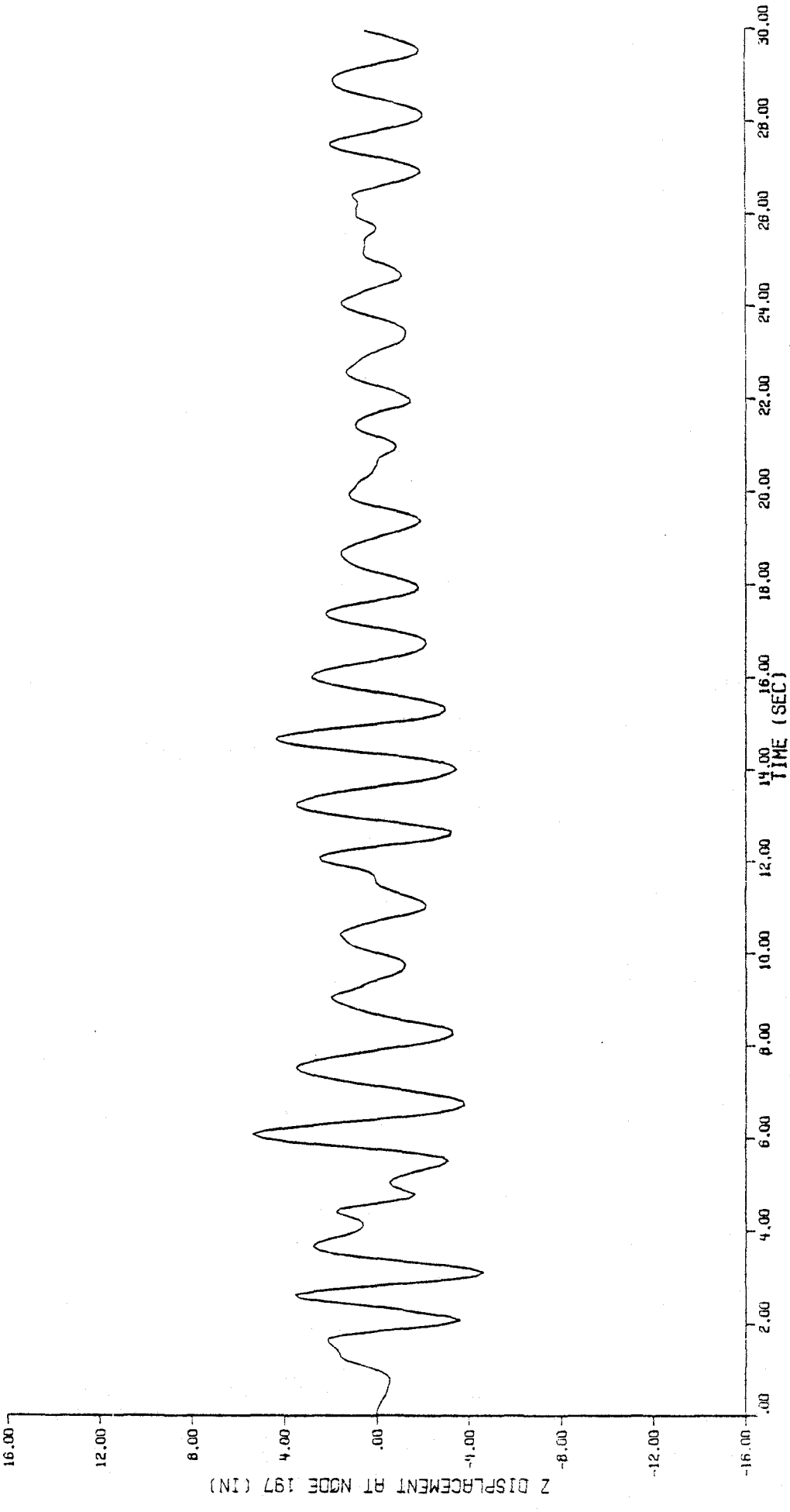

Figure 79

z - displacement time-history at node 197, fraction of critical damping = .05.

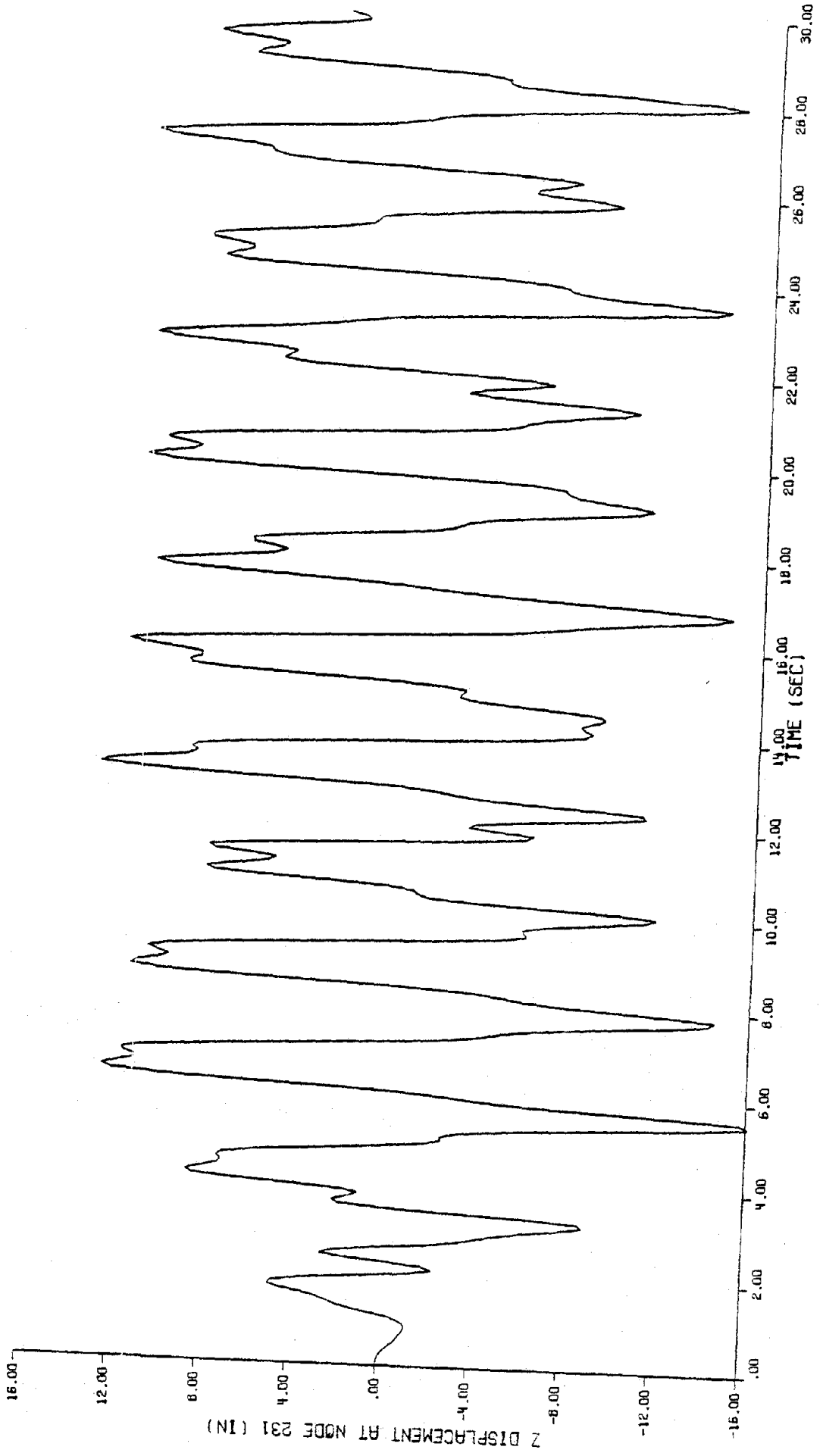

Figure 80

z - displacement time-history at node 231, undamped.

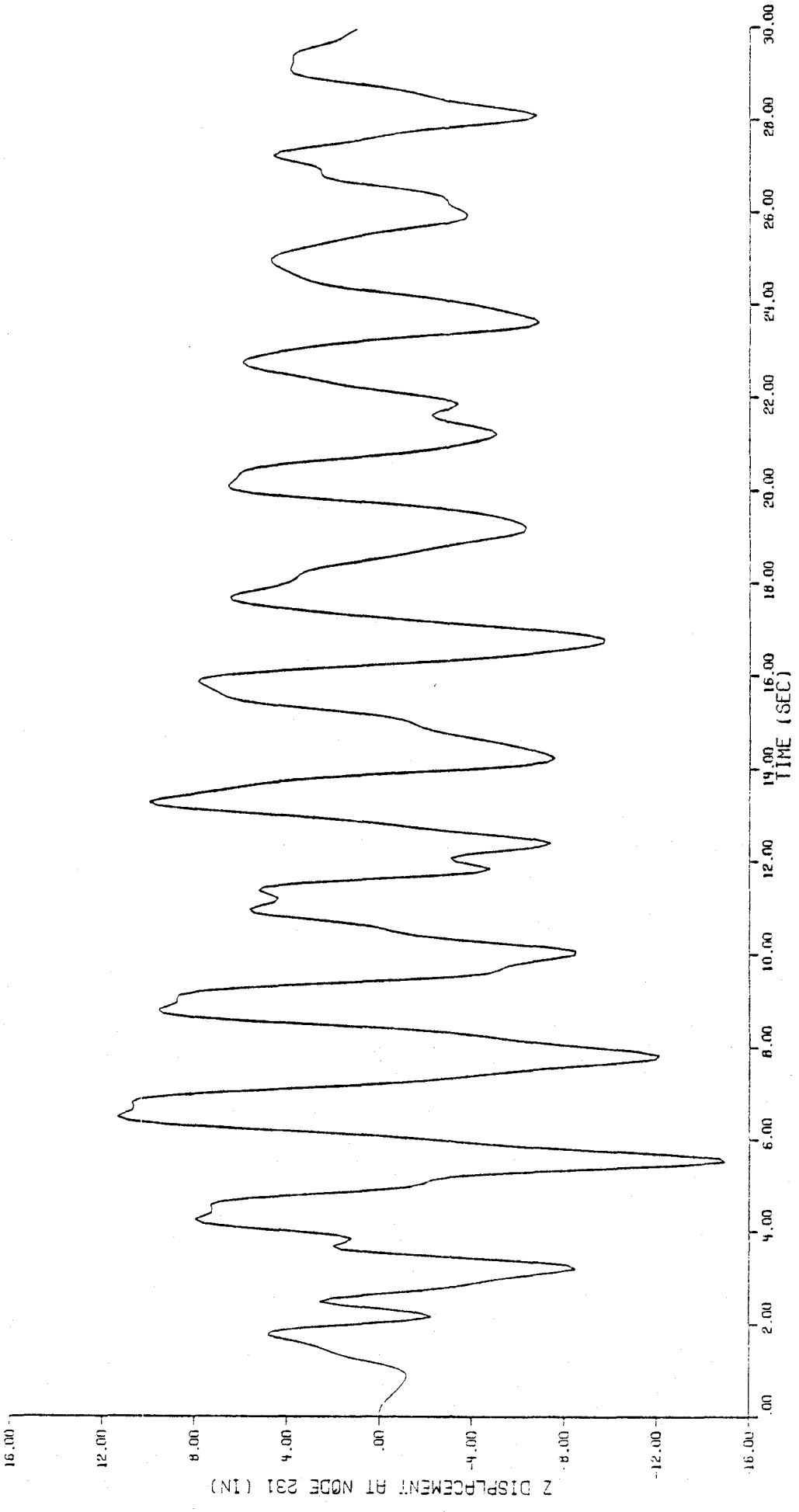

Figure 81

z - displacement time-history at node 231, fraction of critical damping = .01.

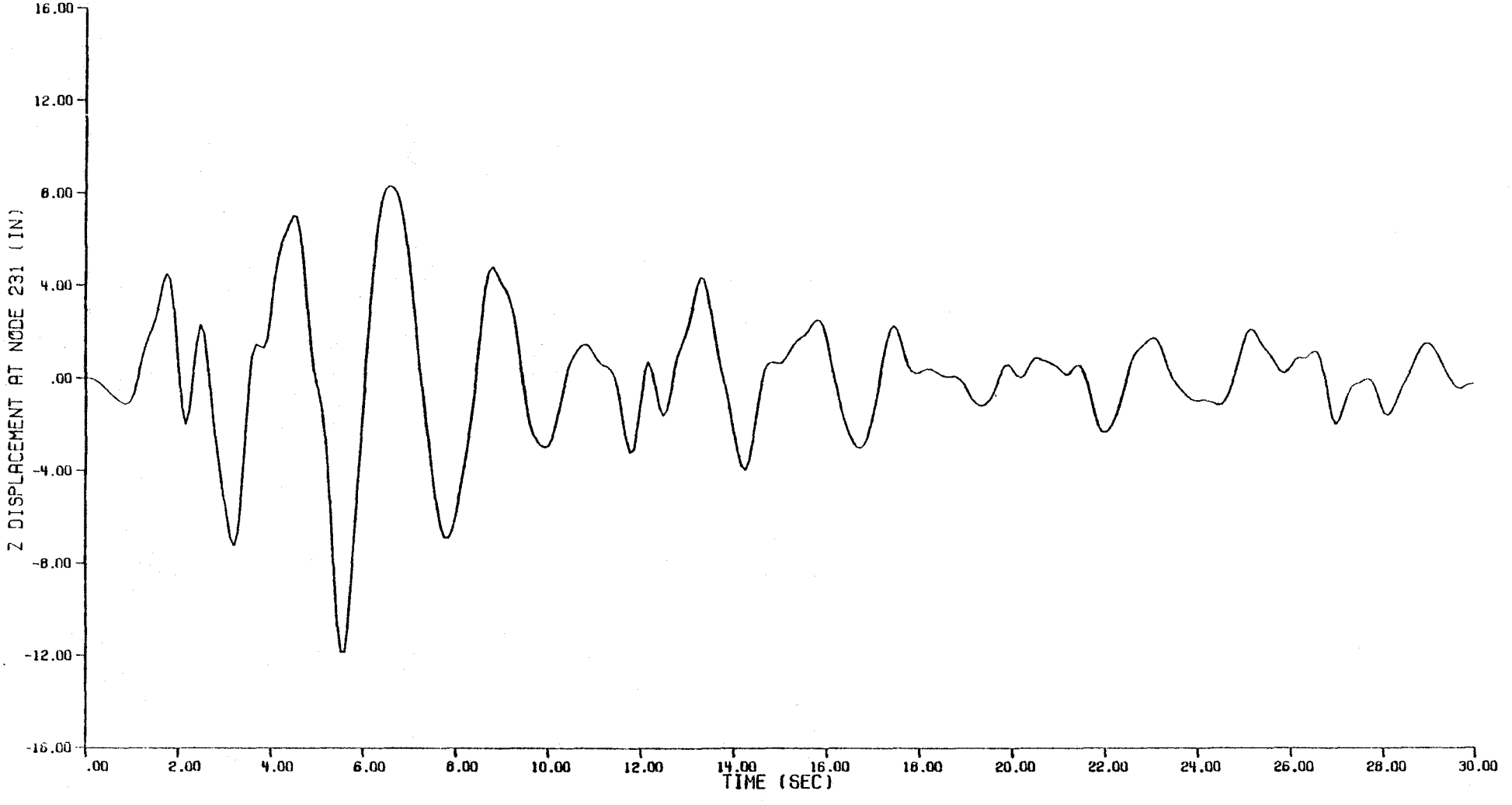

Figure 82

z - displacement time-history at node 231, fraction of critical damping = .05.

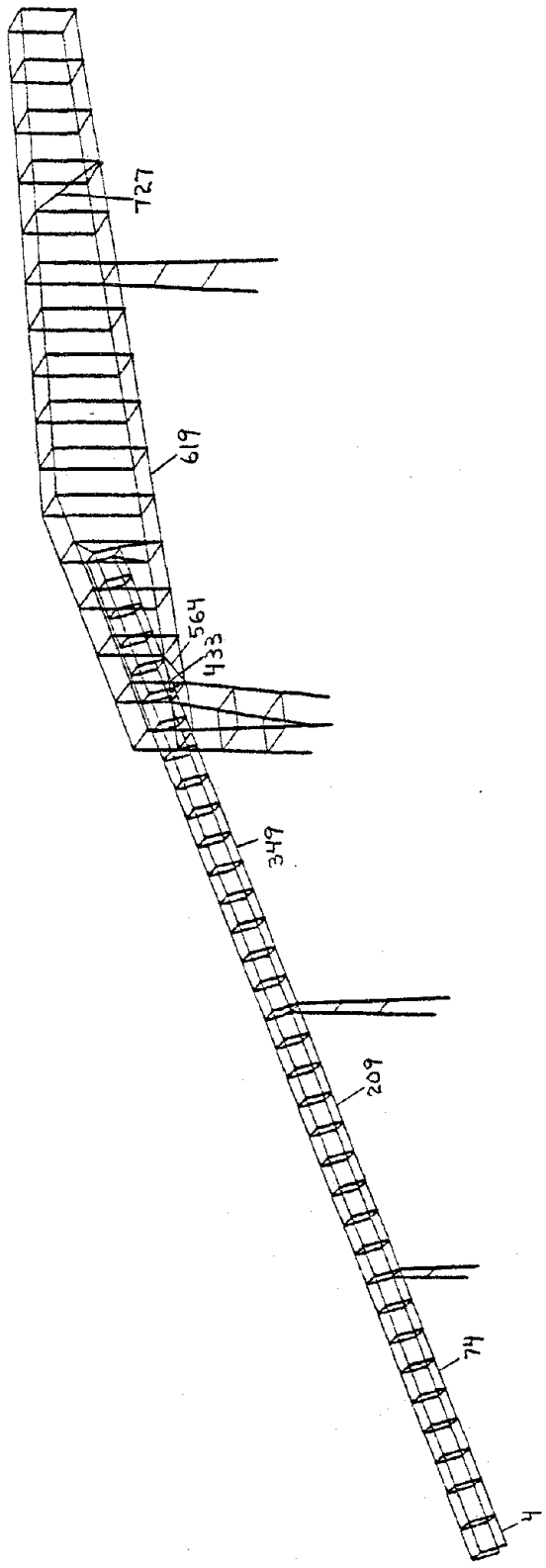

Figure 83

Key to element axial stress time-histories.

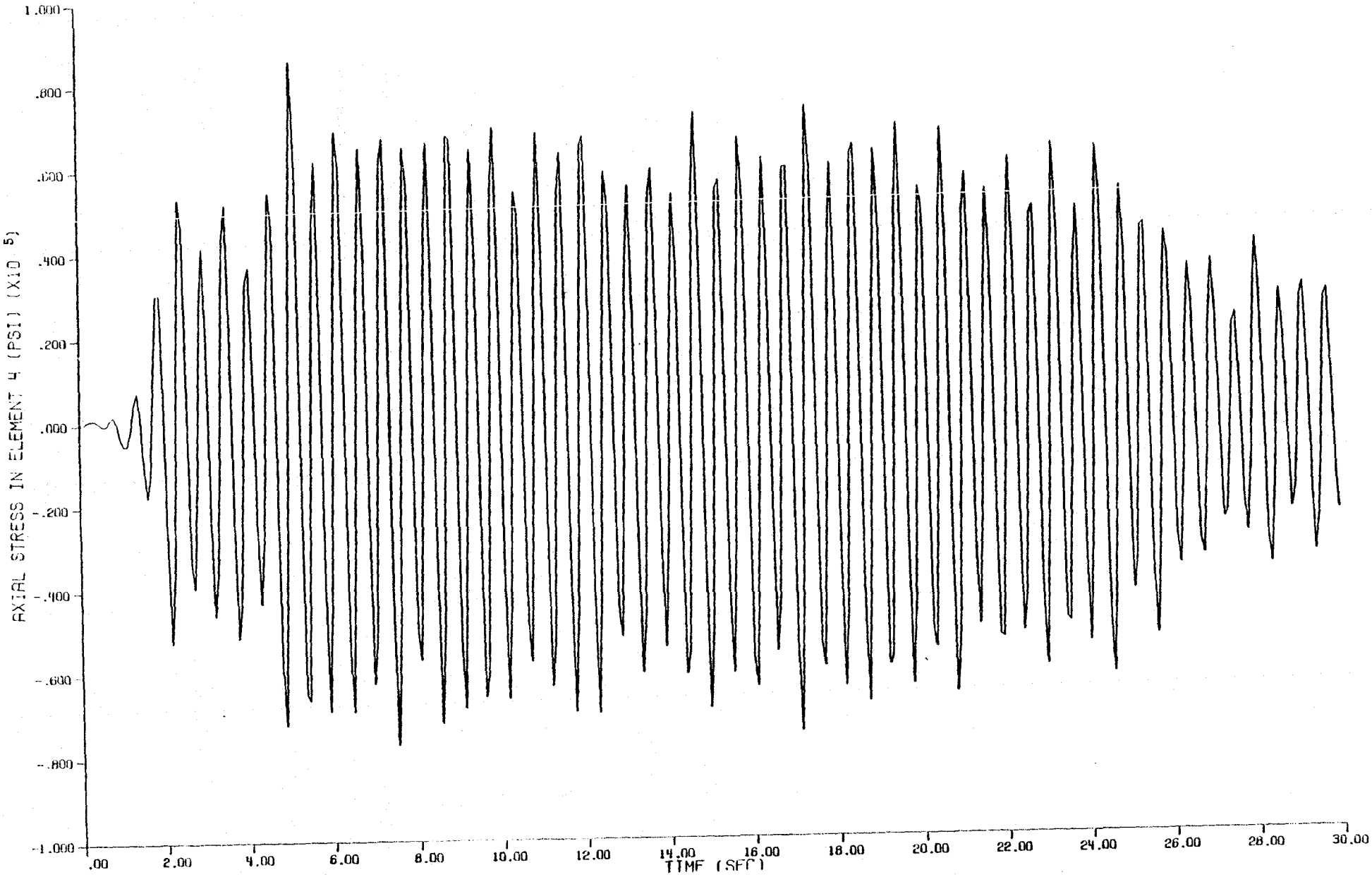

Figure 84

Axial stress time-history in element 4, undamped.

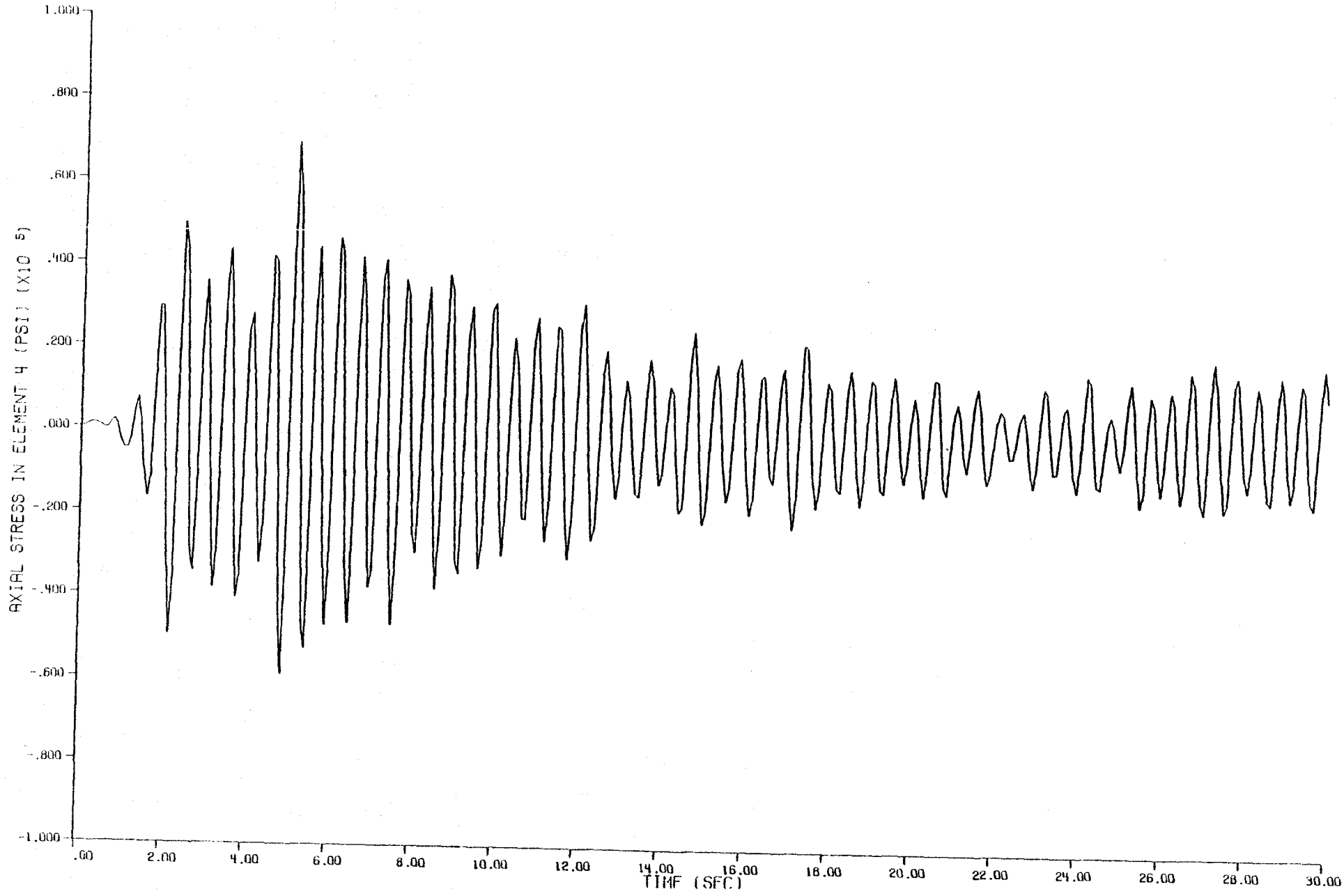

Figure 85

Axial stress time-history in element 4, fraction of critical damping = .01.

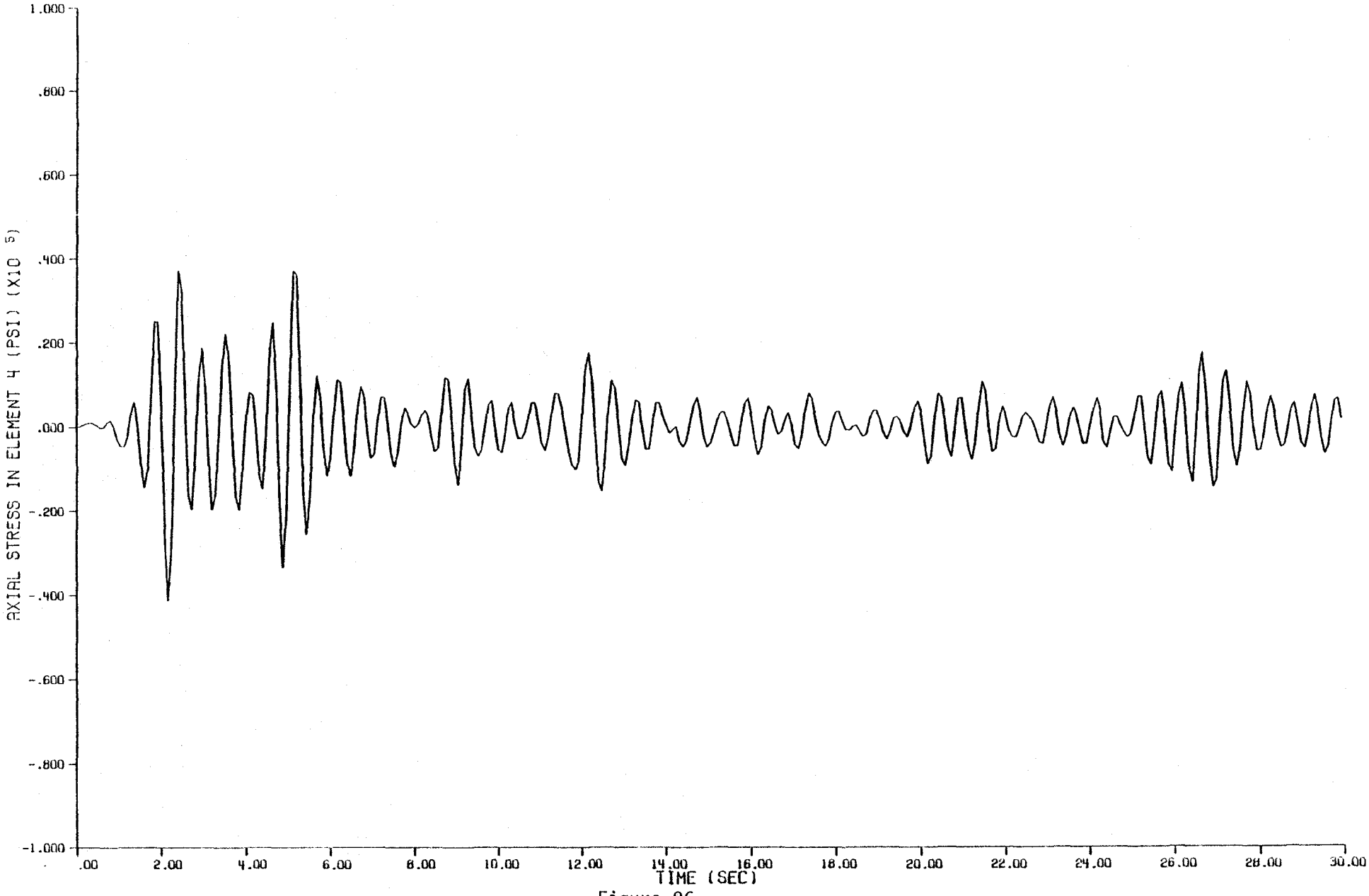

Figure 86

Axial stress time-history in element 4, fraction of critical damping = .05.

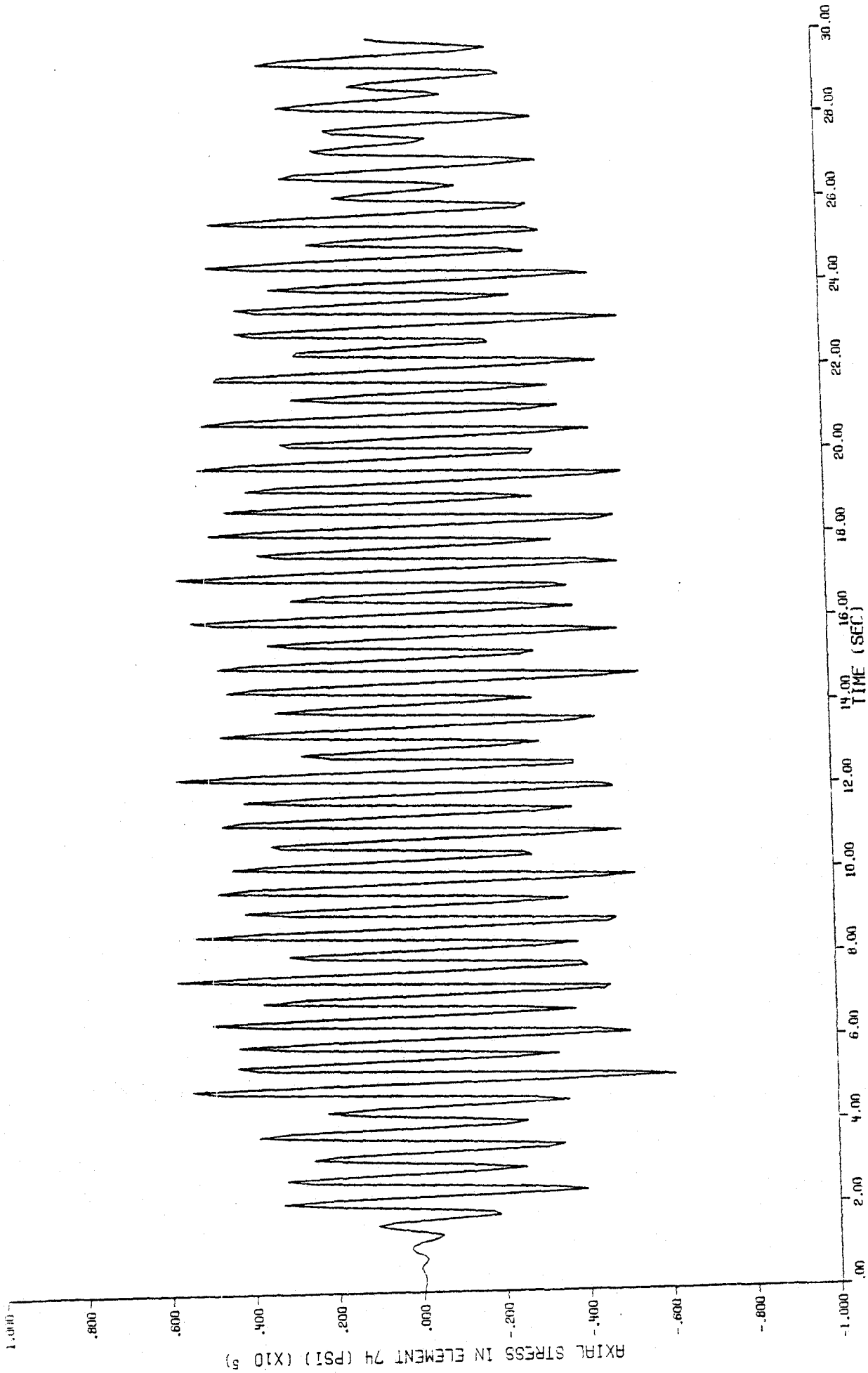

Figure 87

Axial stress time-history in element 74, undamped.

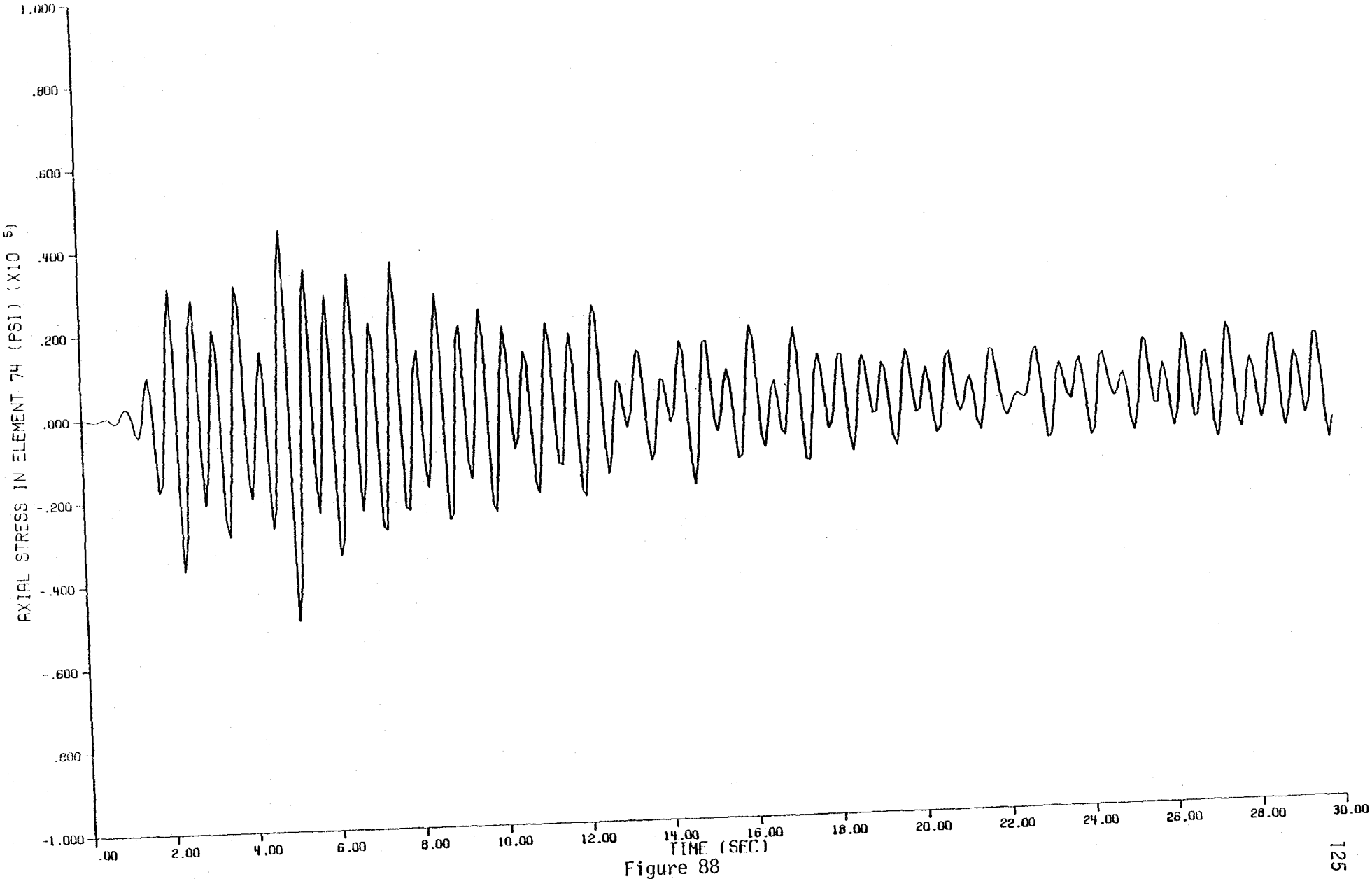

Figure 88

Axial stress time-history in element 74, fraction of critical damping = .01.

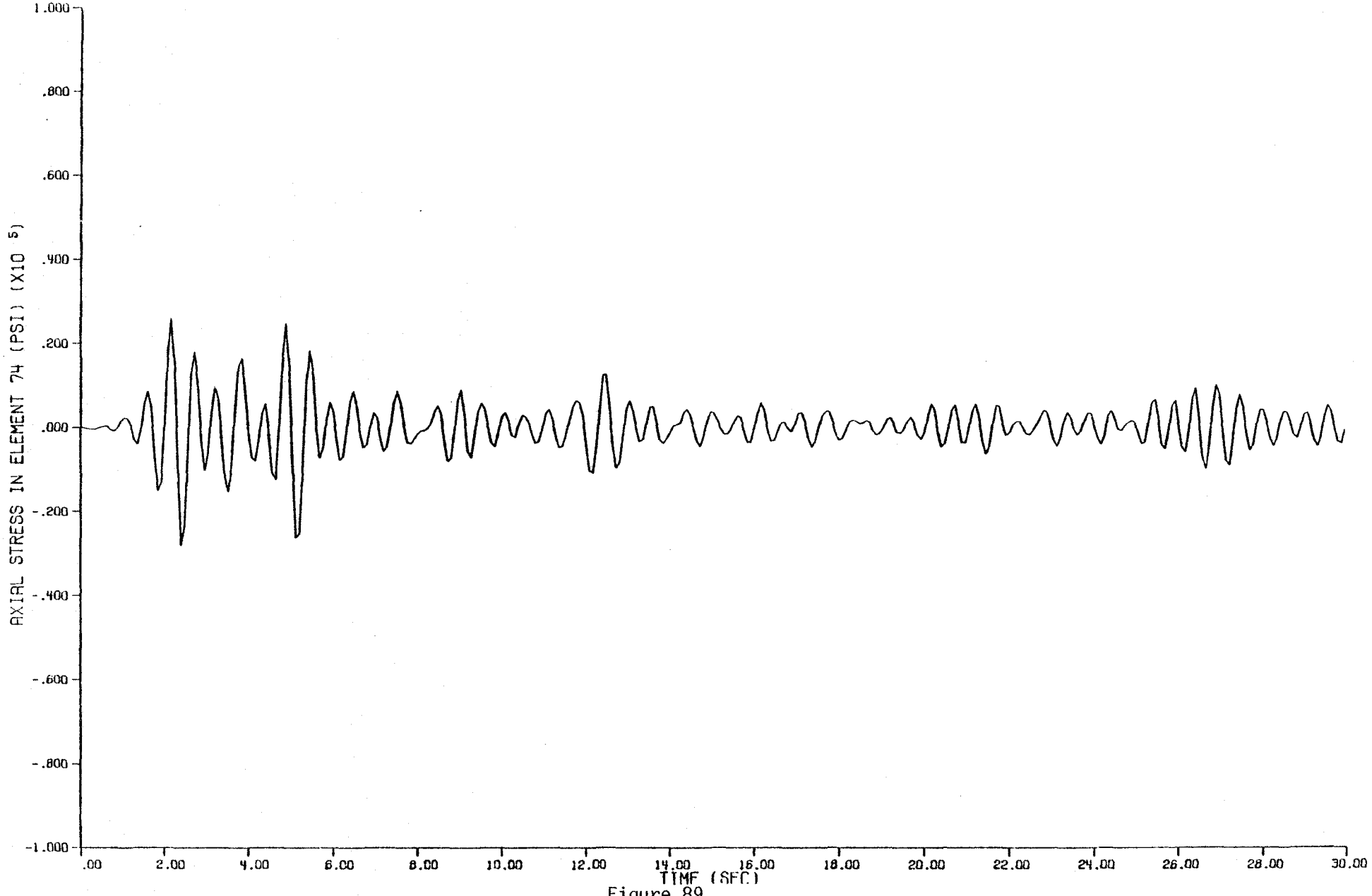

Figure 89

Axial stress time-history in element 74, fraction of critical damping = .05.

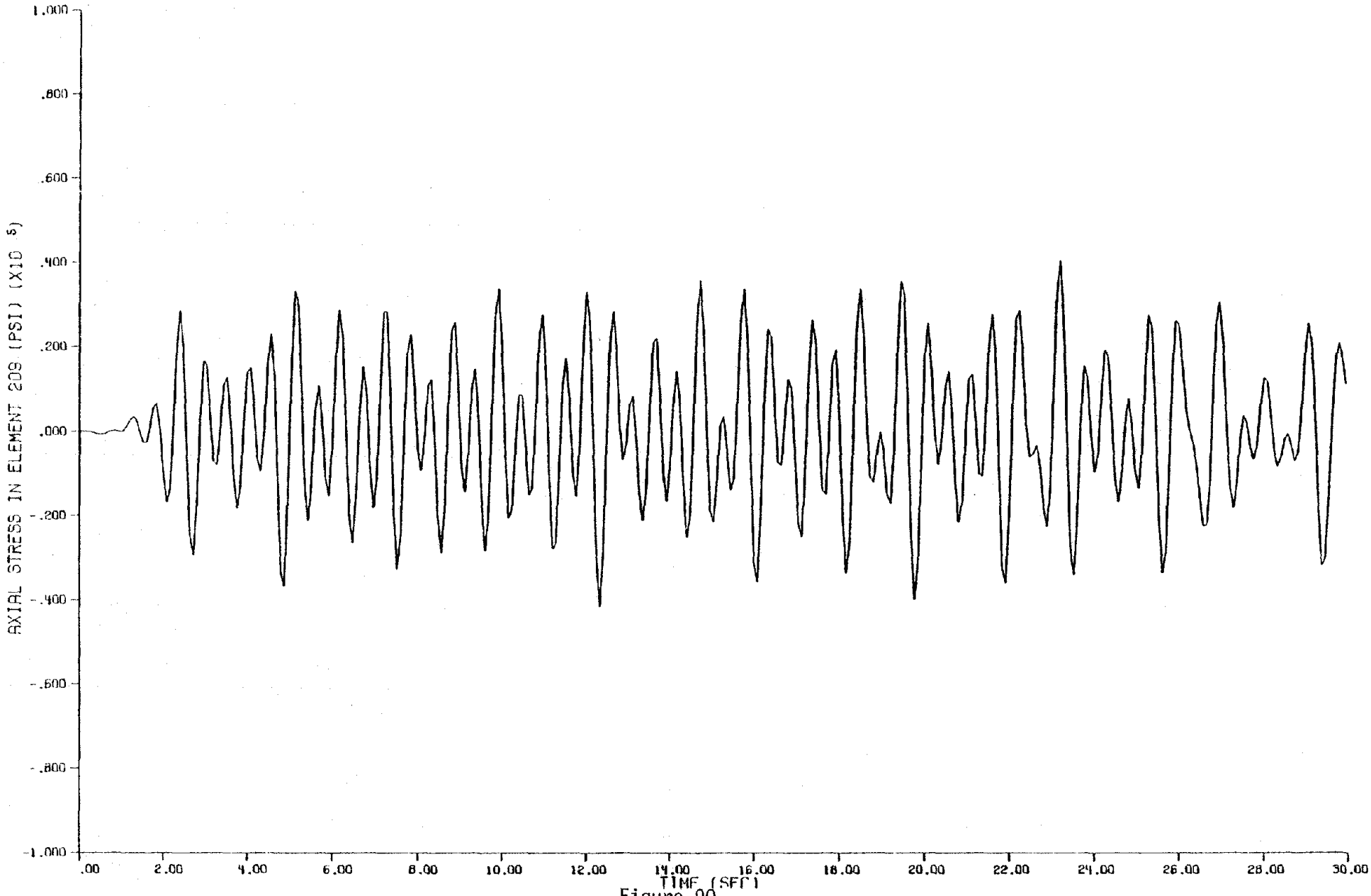

Figure 90

Axial stress time-history in element 209, undamped.

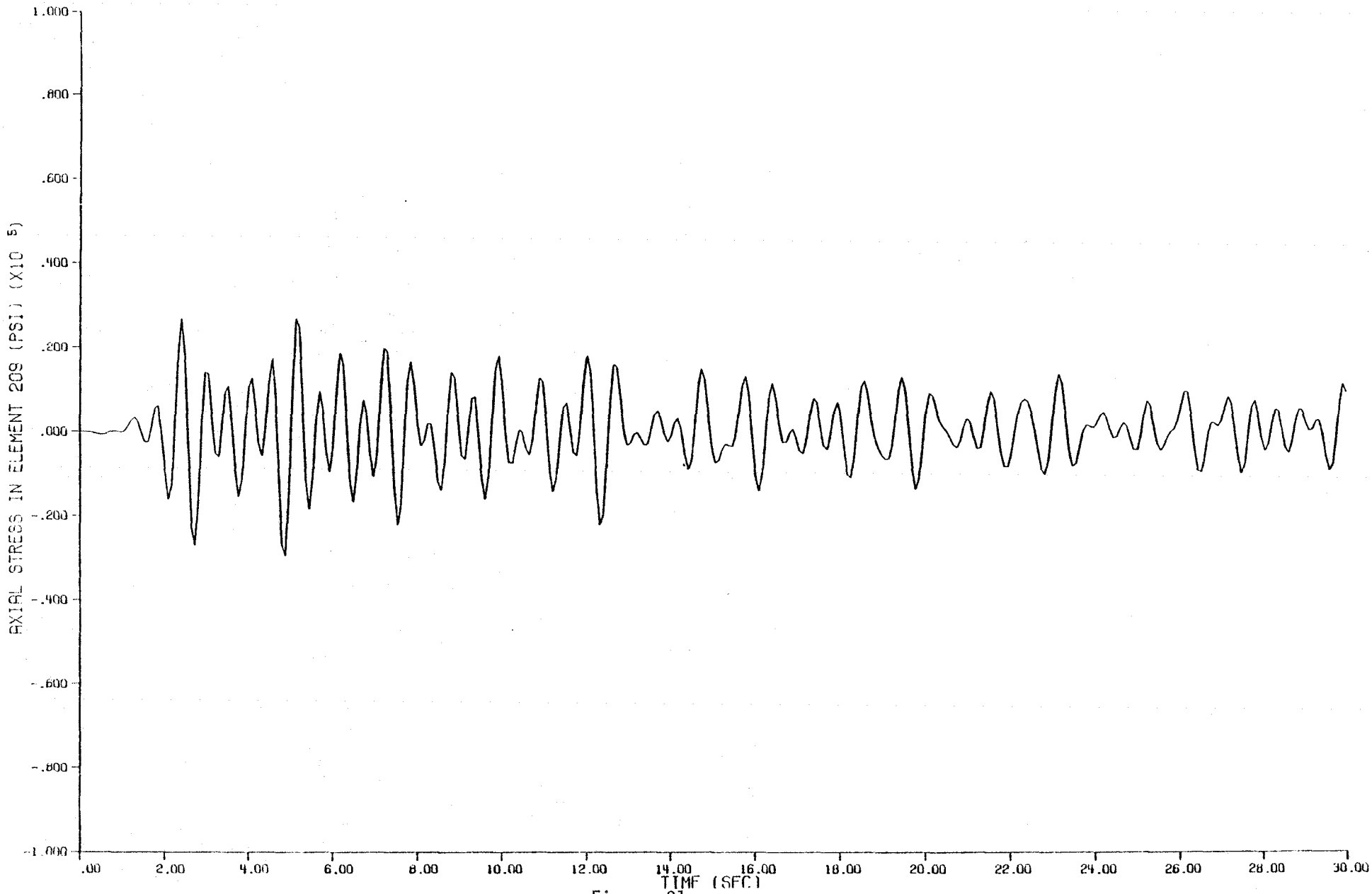

Figure 91

Axial stress time-history in element 209, fraction of critical damping = .01.

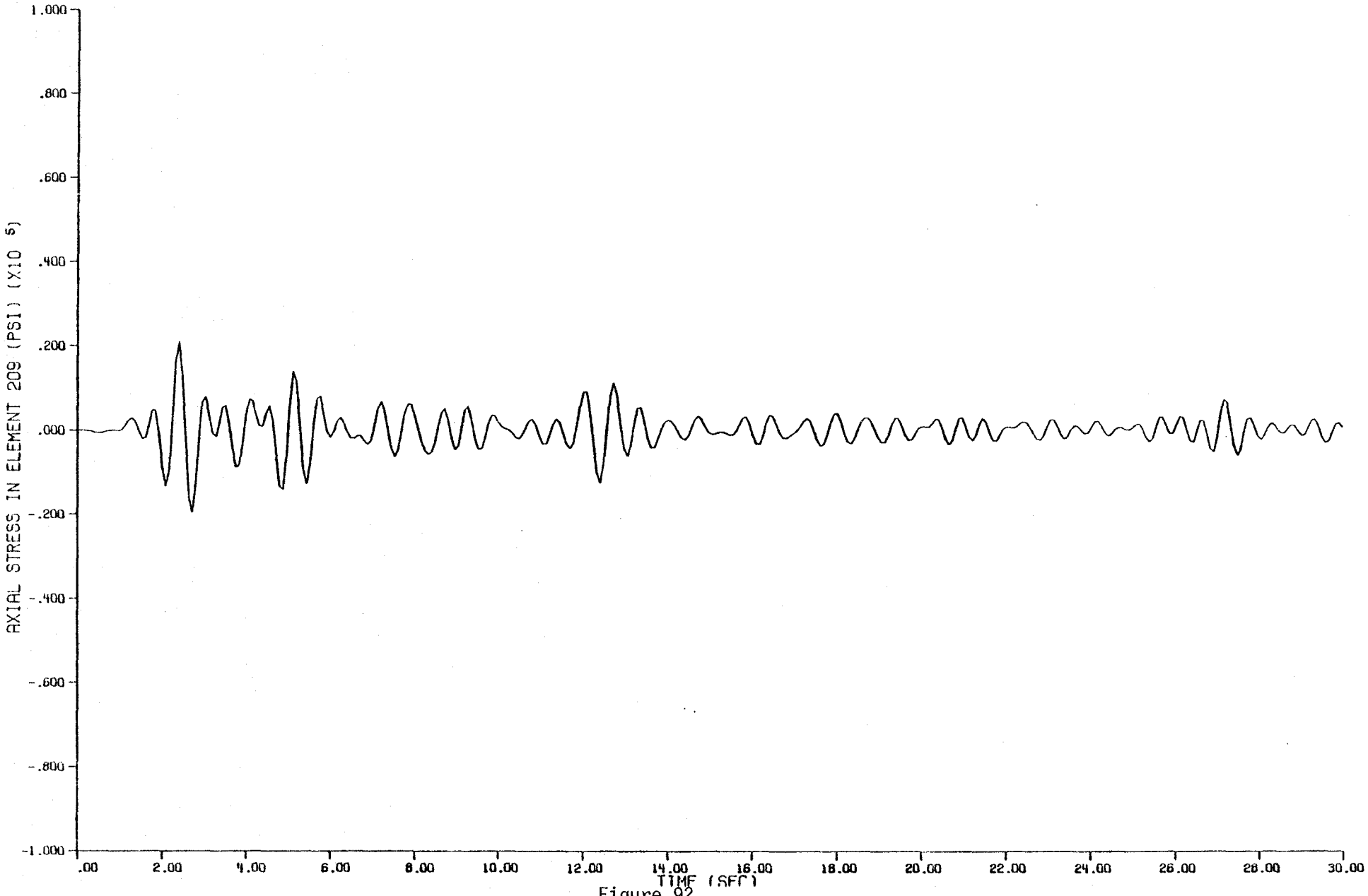

Figure 92

Axial stress time-history in element 209, fraction of critical damping = .05.

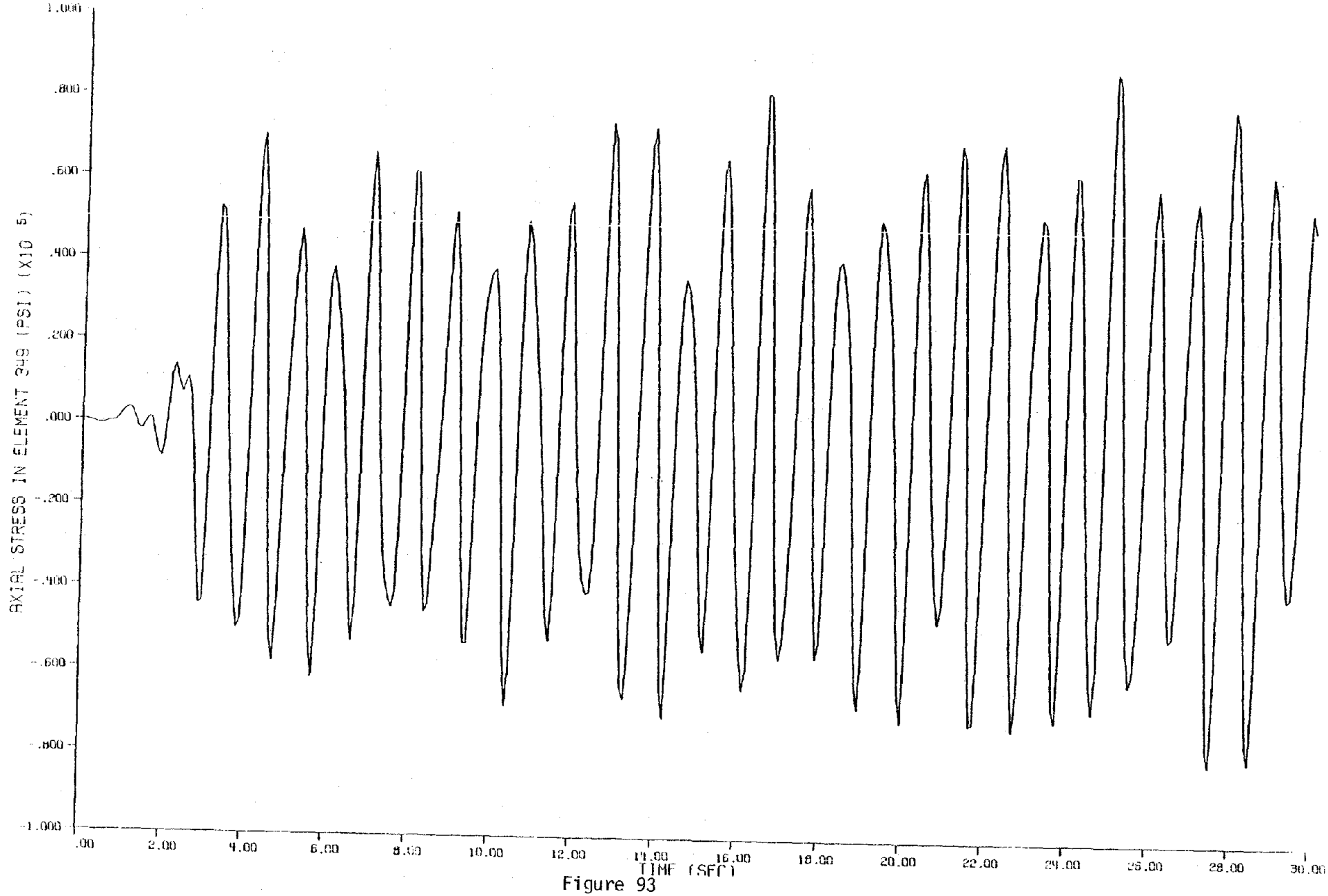

Figure 93

Axial stress time-history in element 349, undamped.

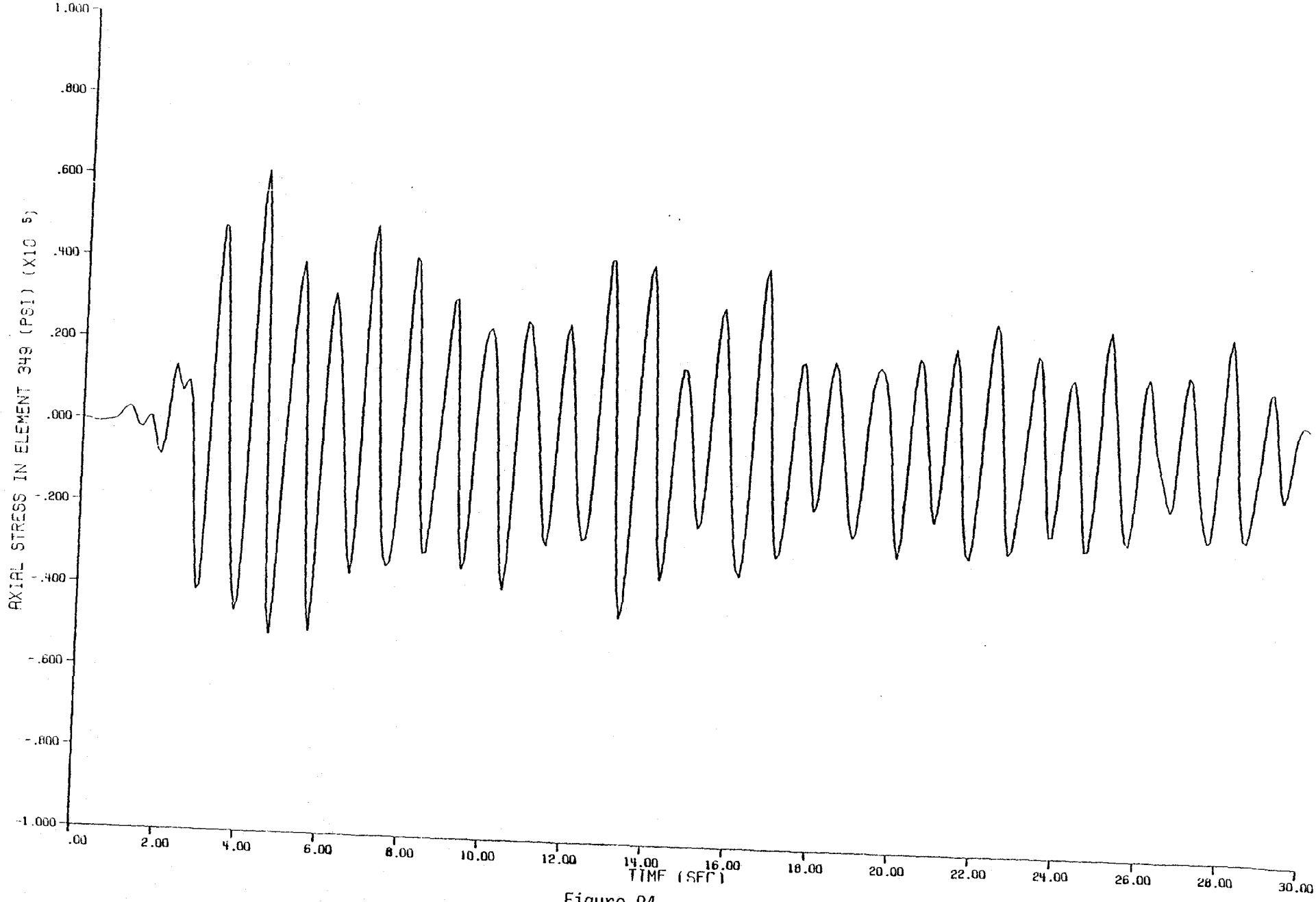

Figure 94

Axial stress time-history in element 349, fraction of critical damping = .01.

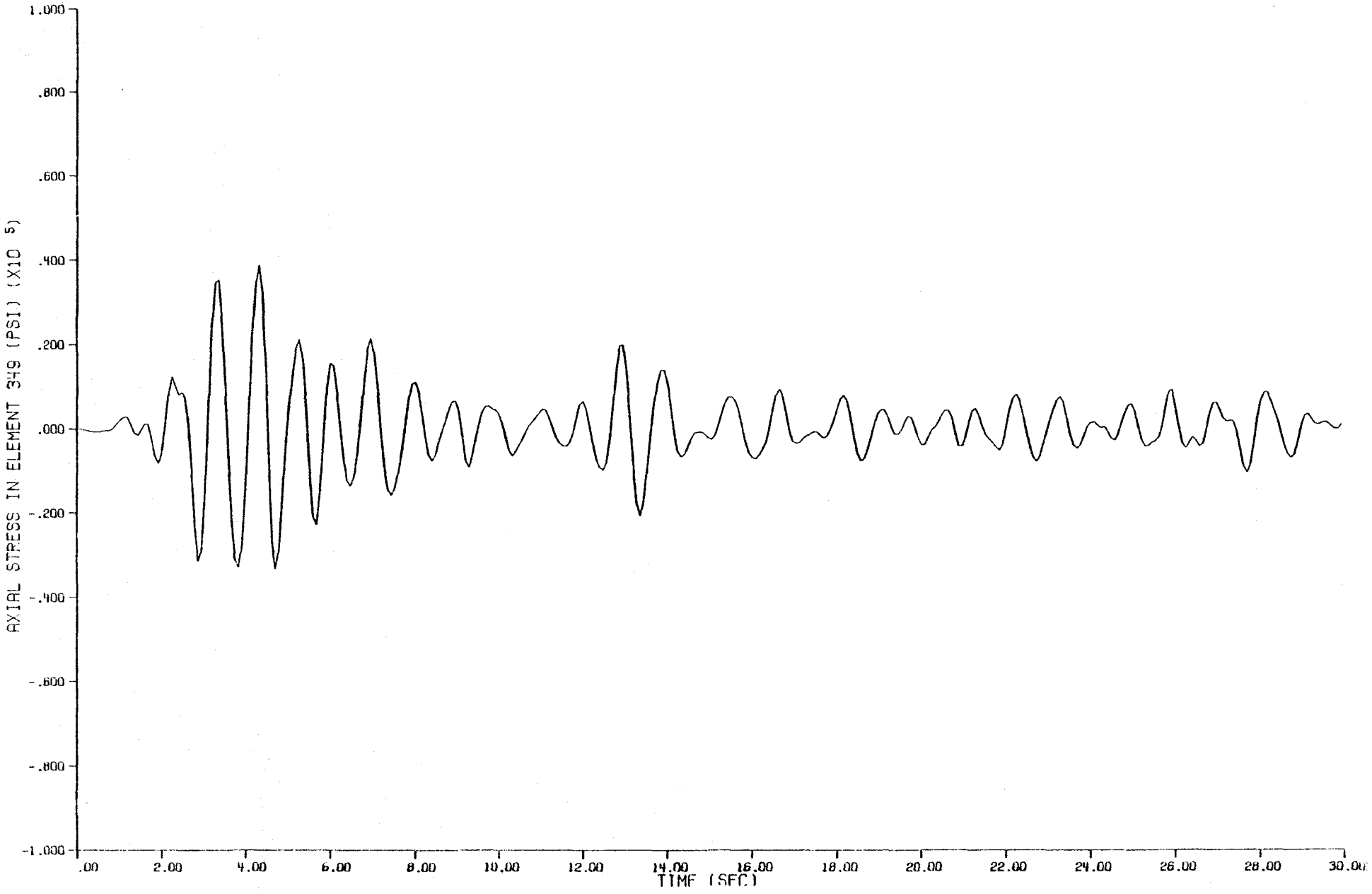

Figure 95

Axial stress time-history in element 349, fraction of critical damping = .05.

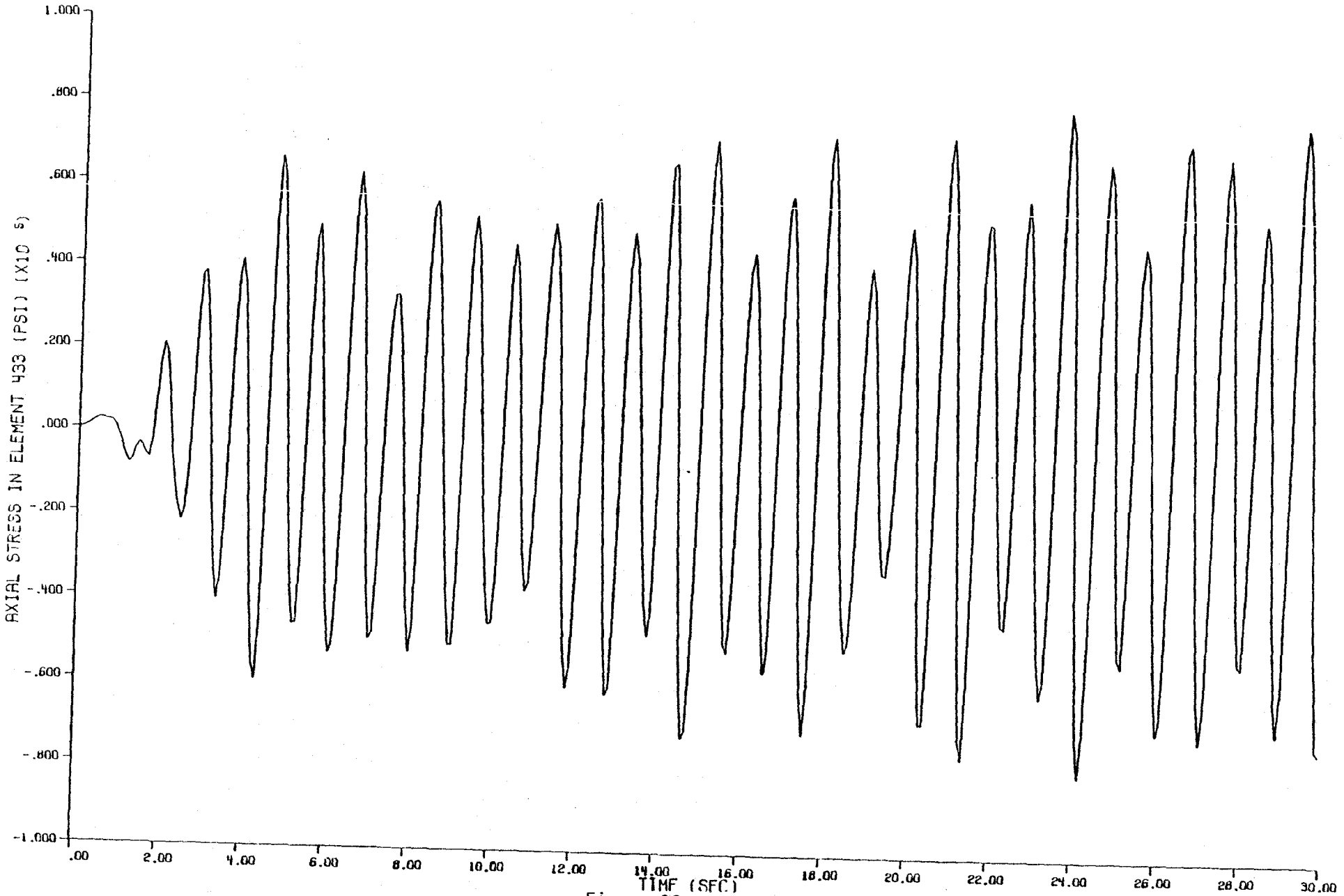

Figure 96

Axial stress time-history in element 433, undamped.

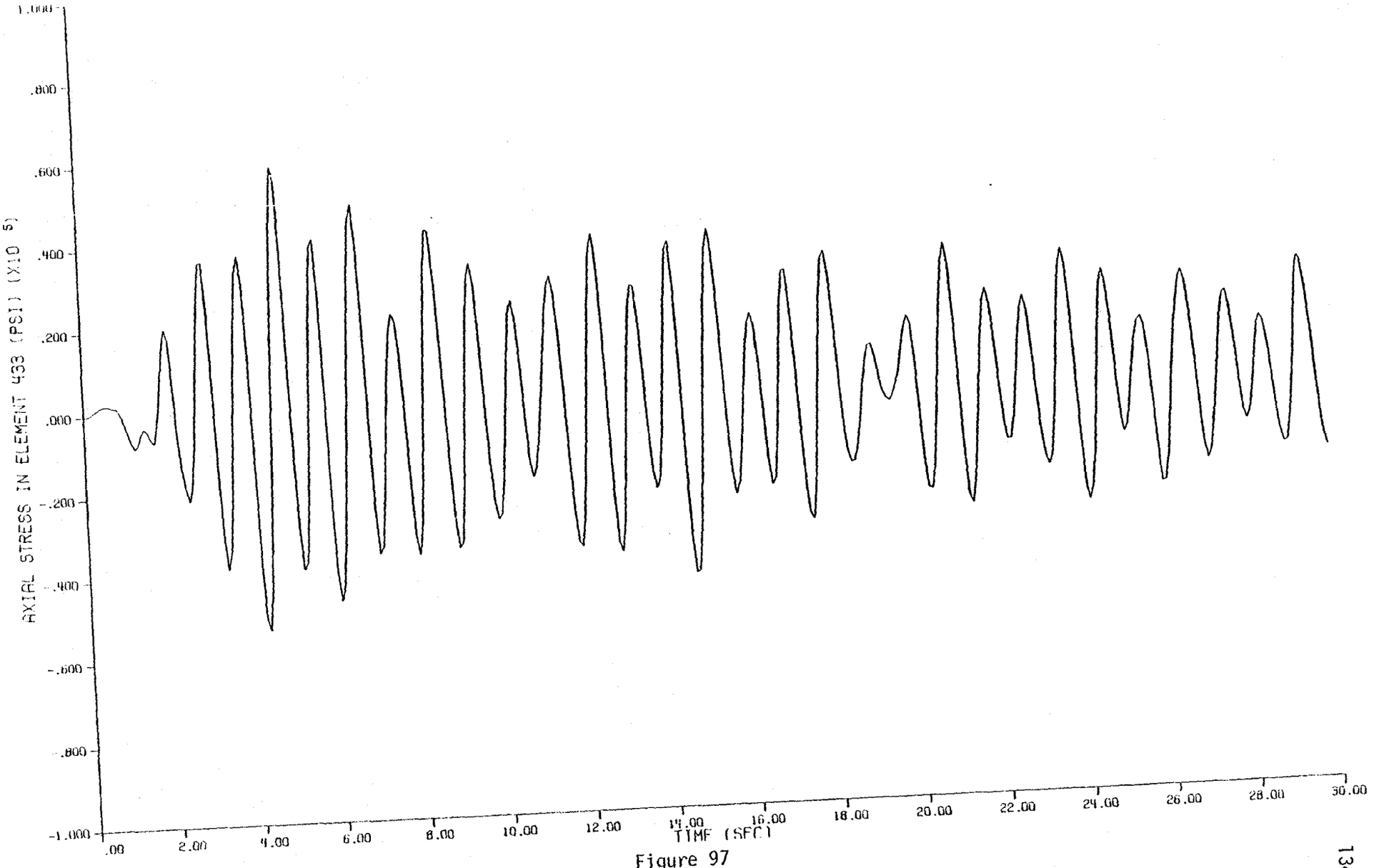

Figure 97

Axial stress time-history in elemet 433, fraction of critical damping = .01.

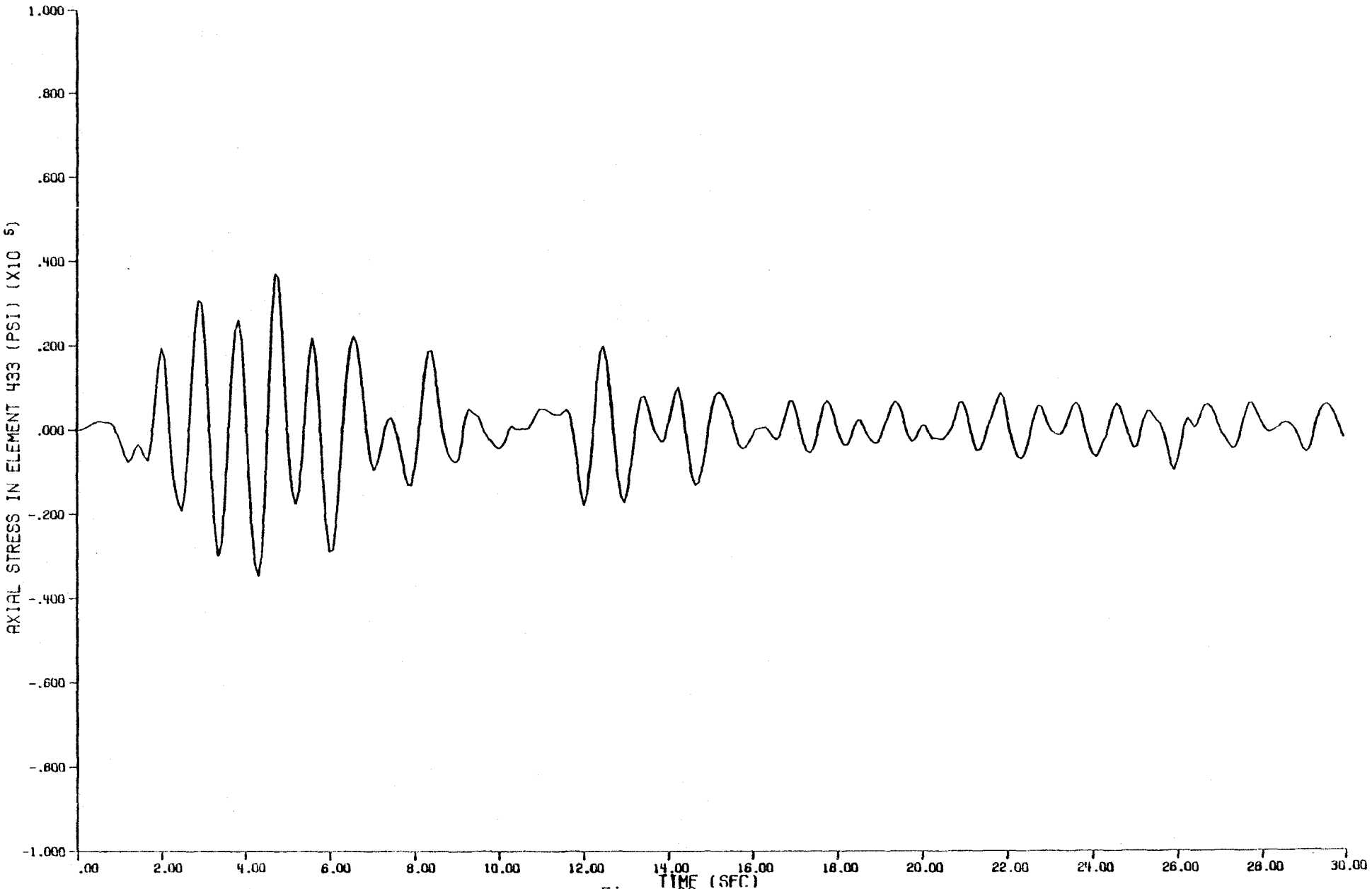

Figure 98

Axial stress time-history in element 433, fraction of critical damping = .05.

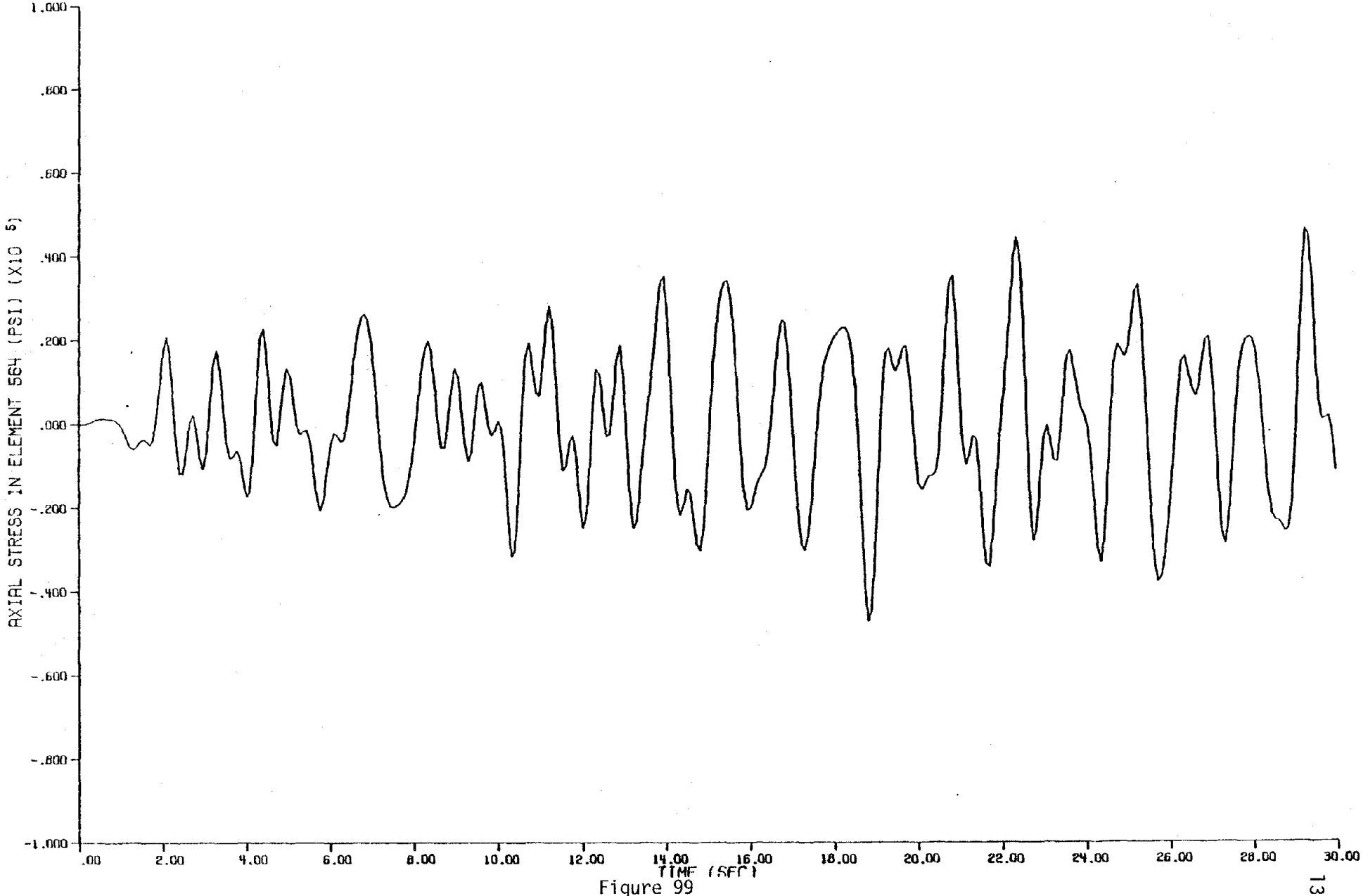

Figure 99

Axial stress time-history in element 564, undamped.

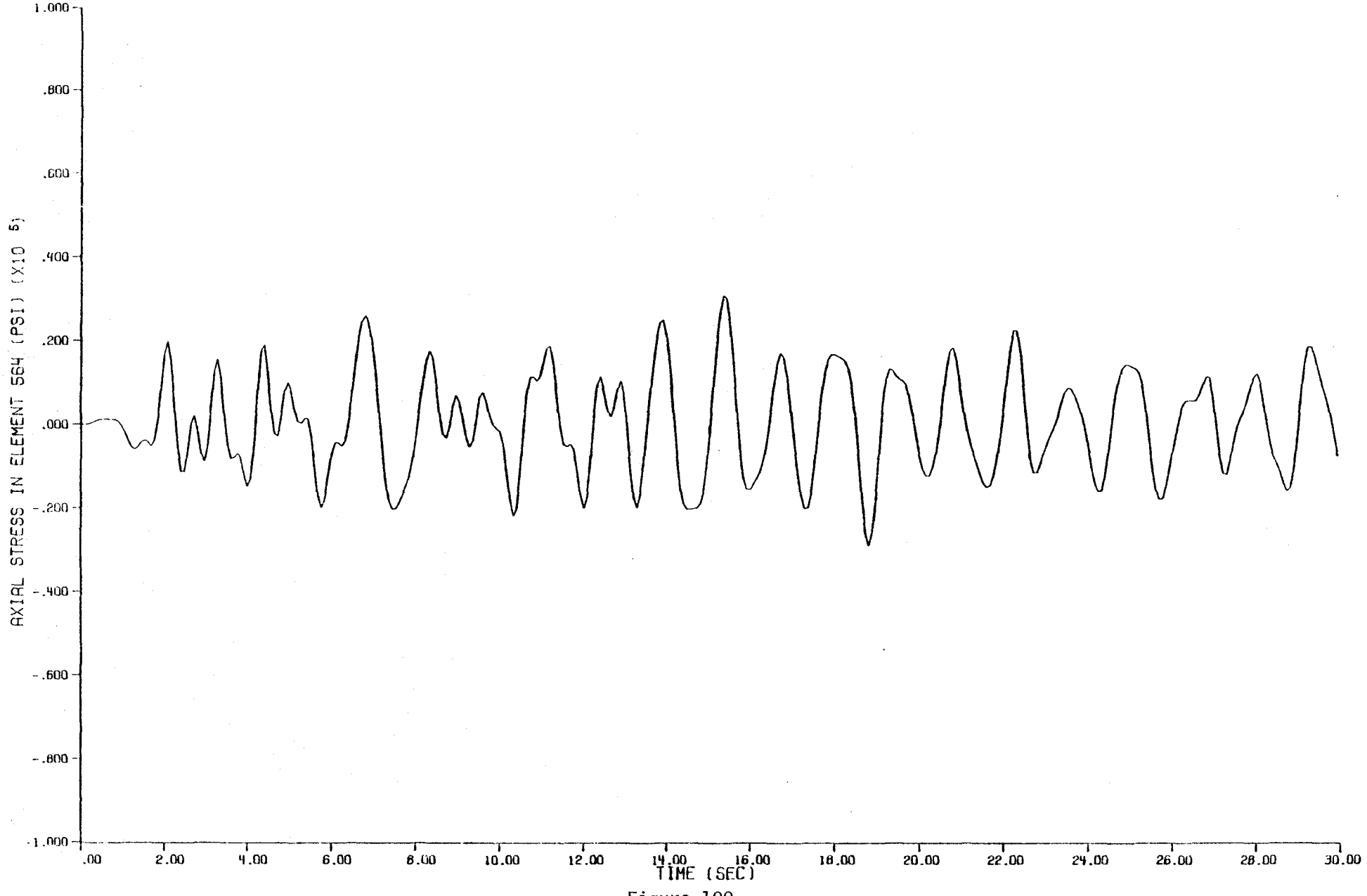

Figure 100

Axial stress time-history in element 564, fraction of critical damping = .01.

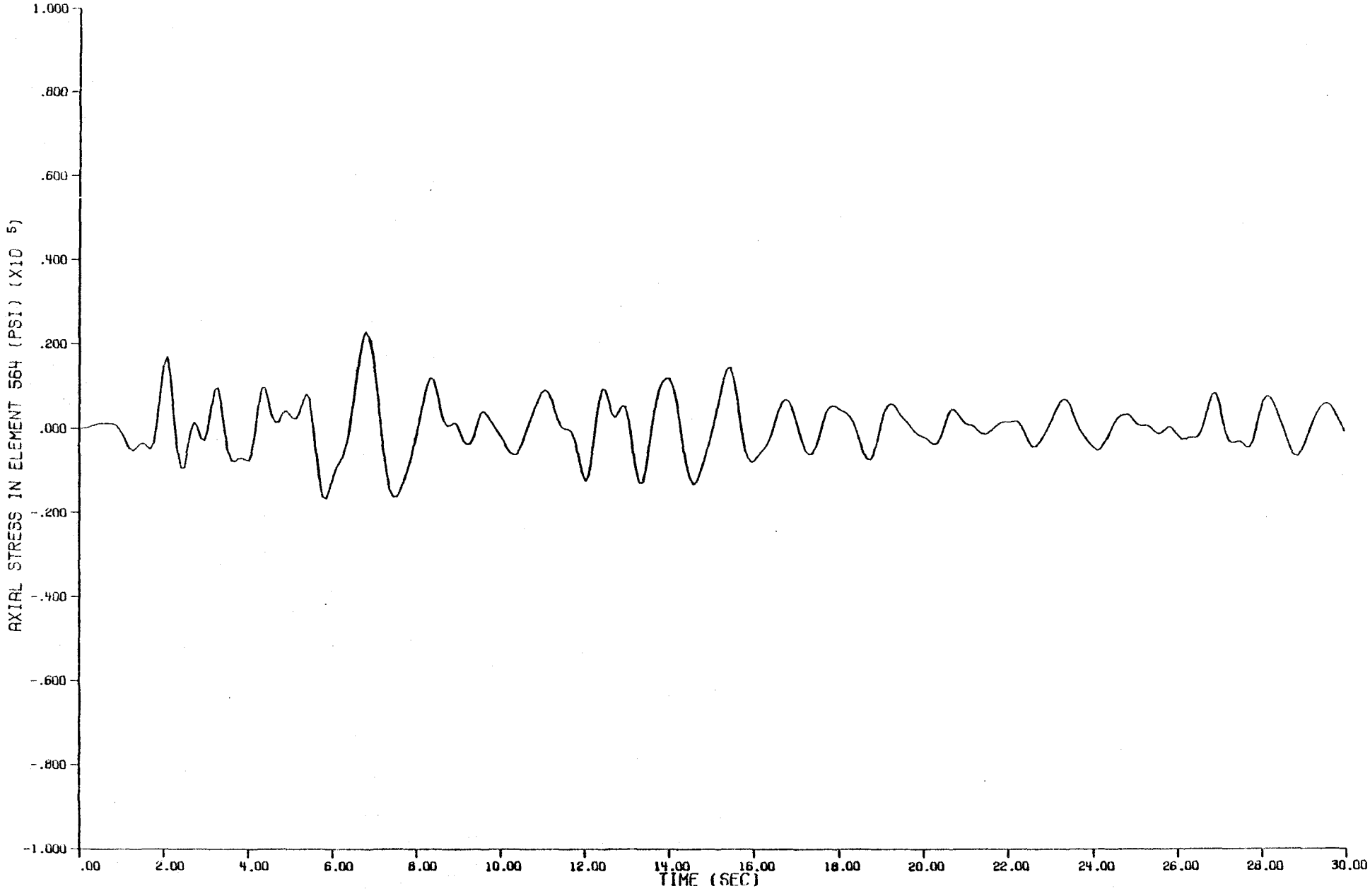

Figure 101

Axial stress time-history in element 564, fraction of critical damping = .05.

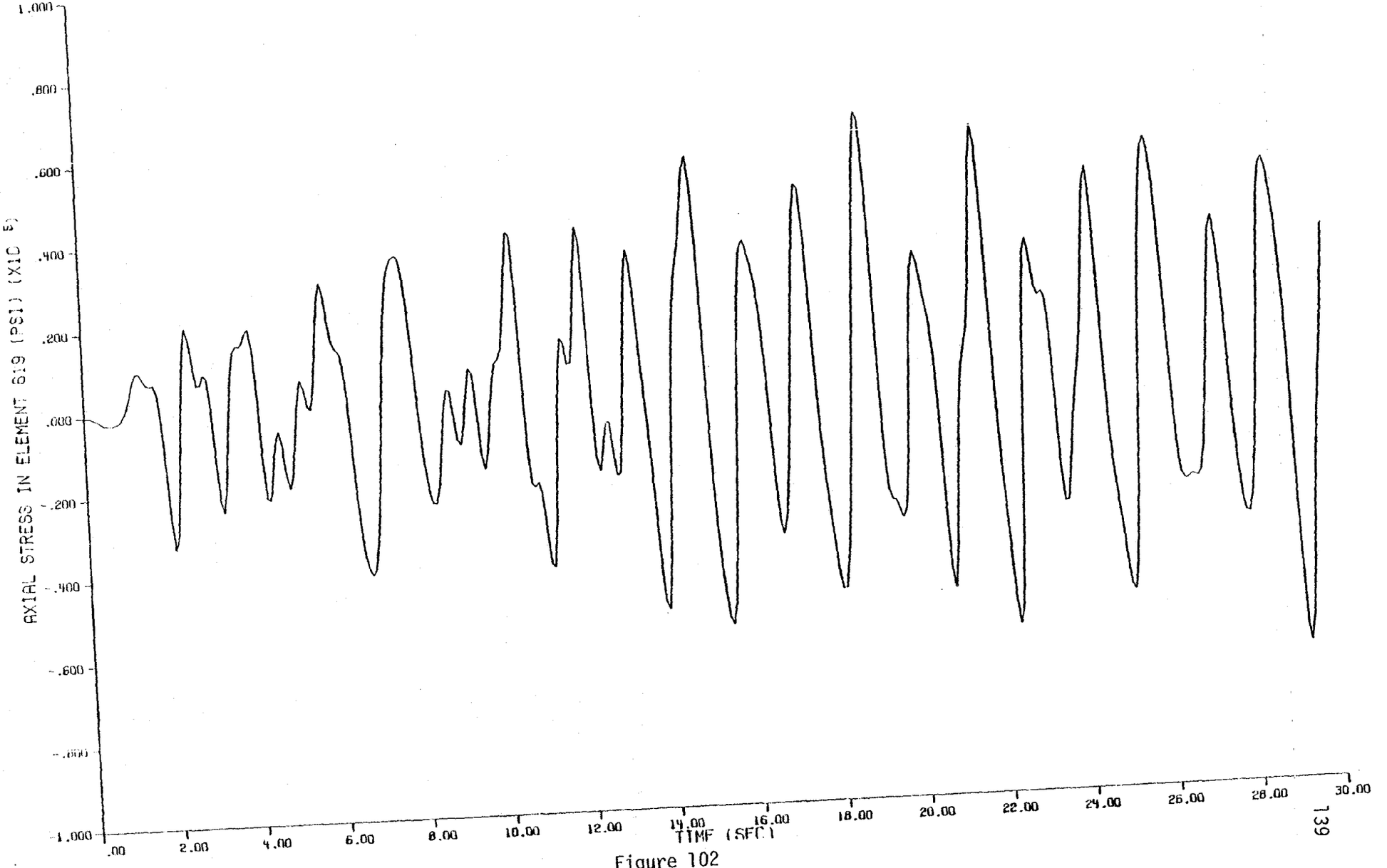

Figure 102

Axial stress time-history in element 619, undamped.

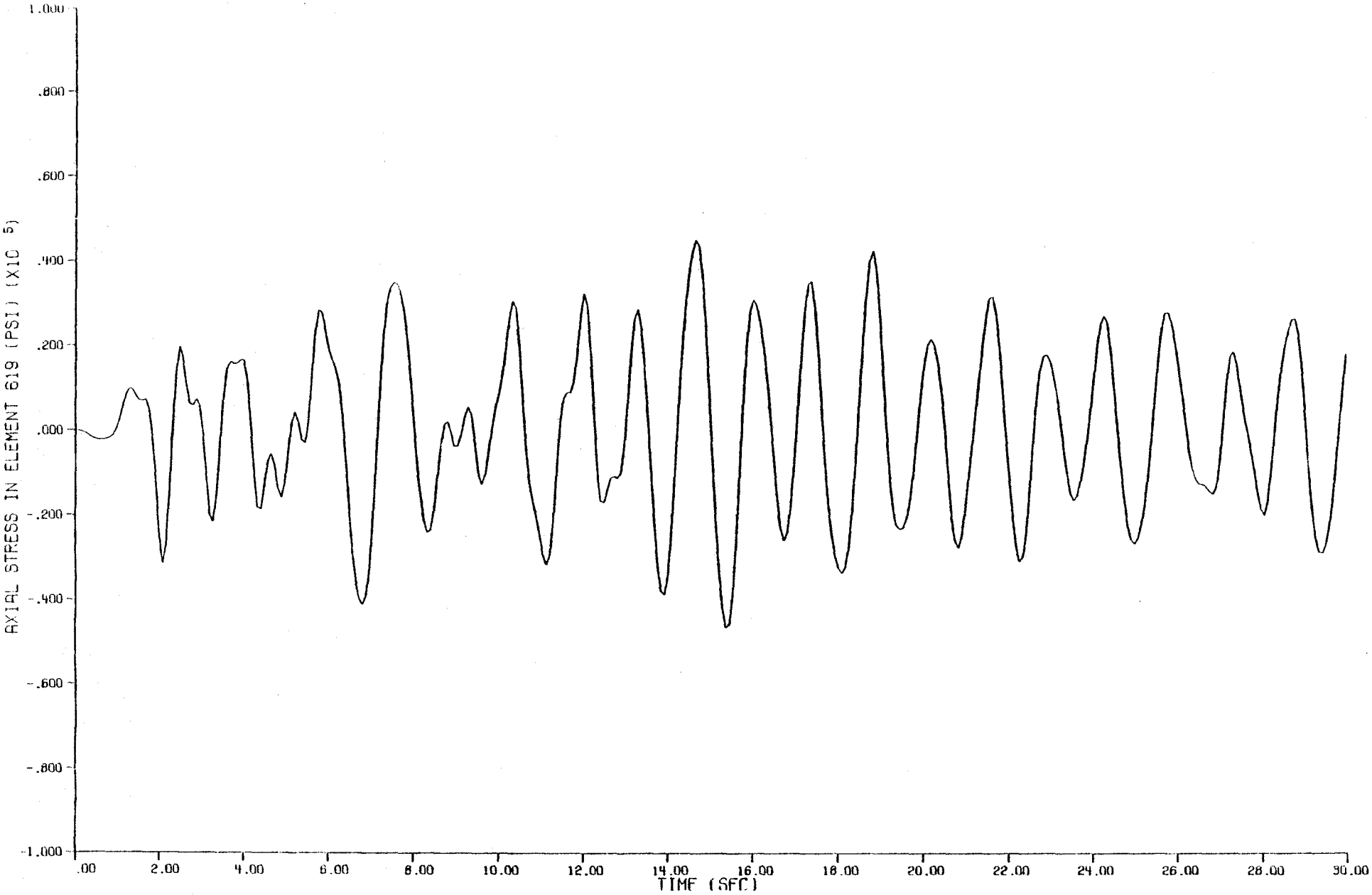

Figure 103

Axial stress time-history in element 619, fraction of critical damping = .01.

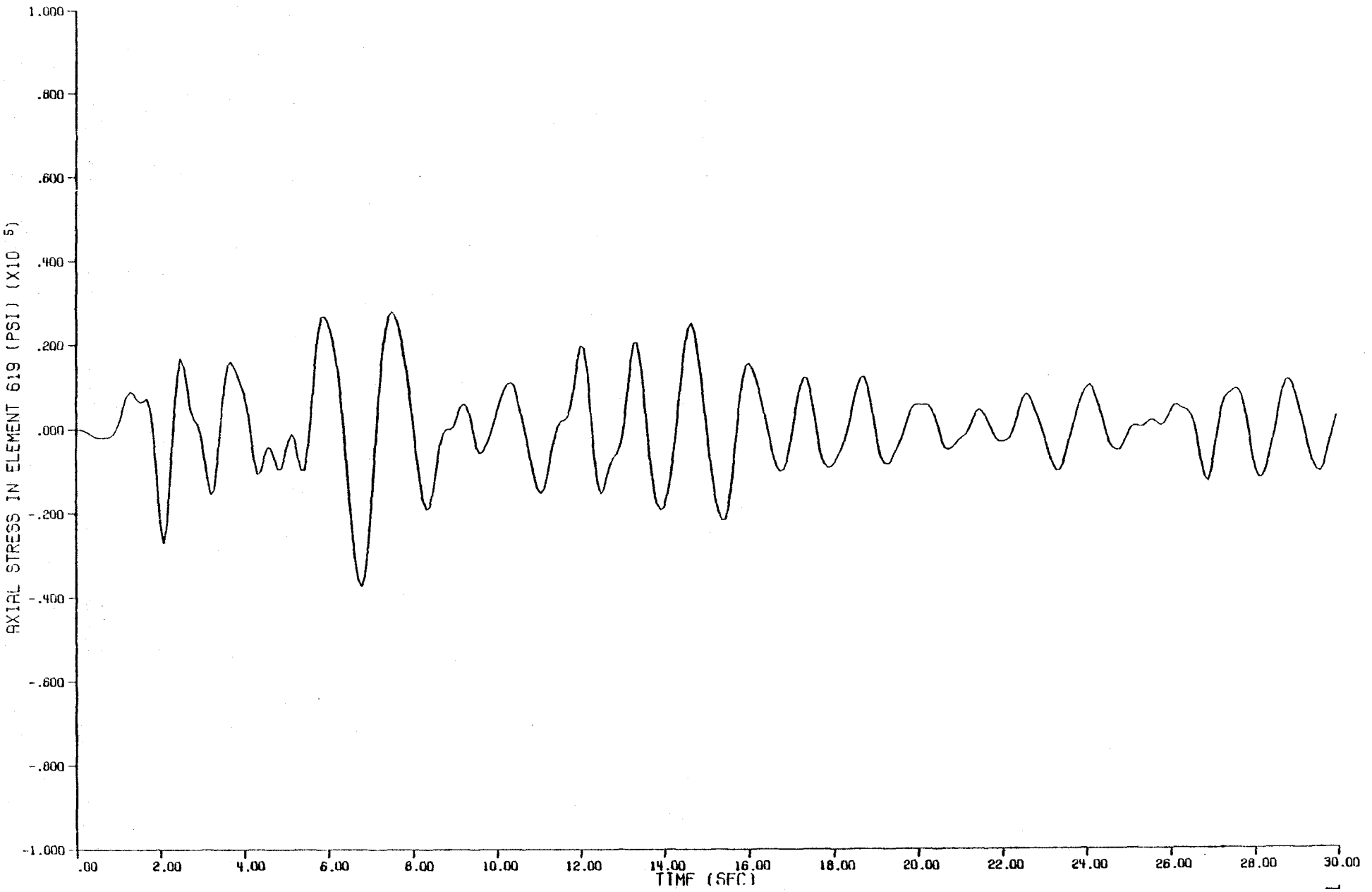

Figure 104

Axial stress time-history in element 619, fraction of critical damping = .05.

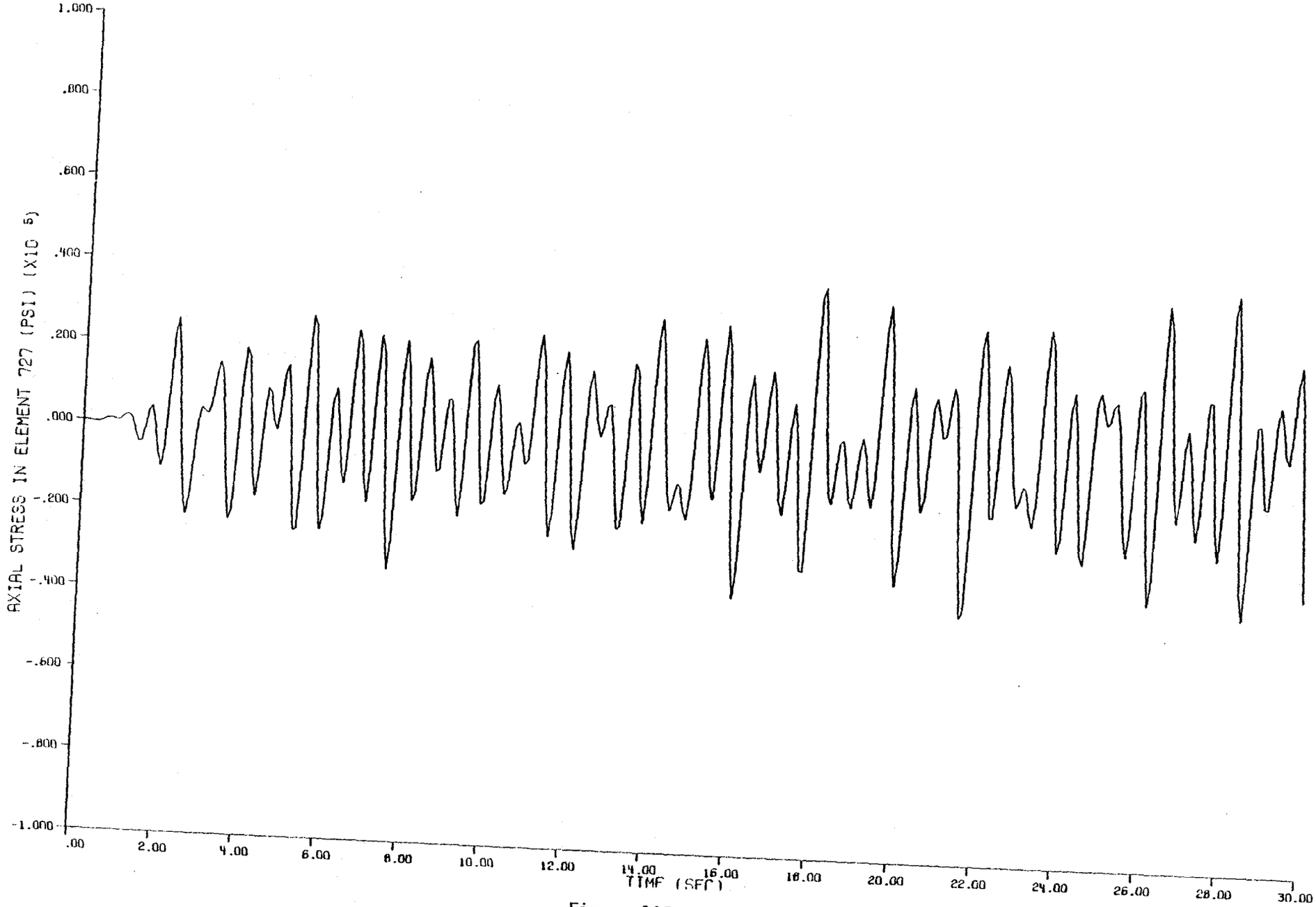

Figure 105

Axial stress time-history in element 727, undamped.

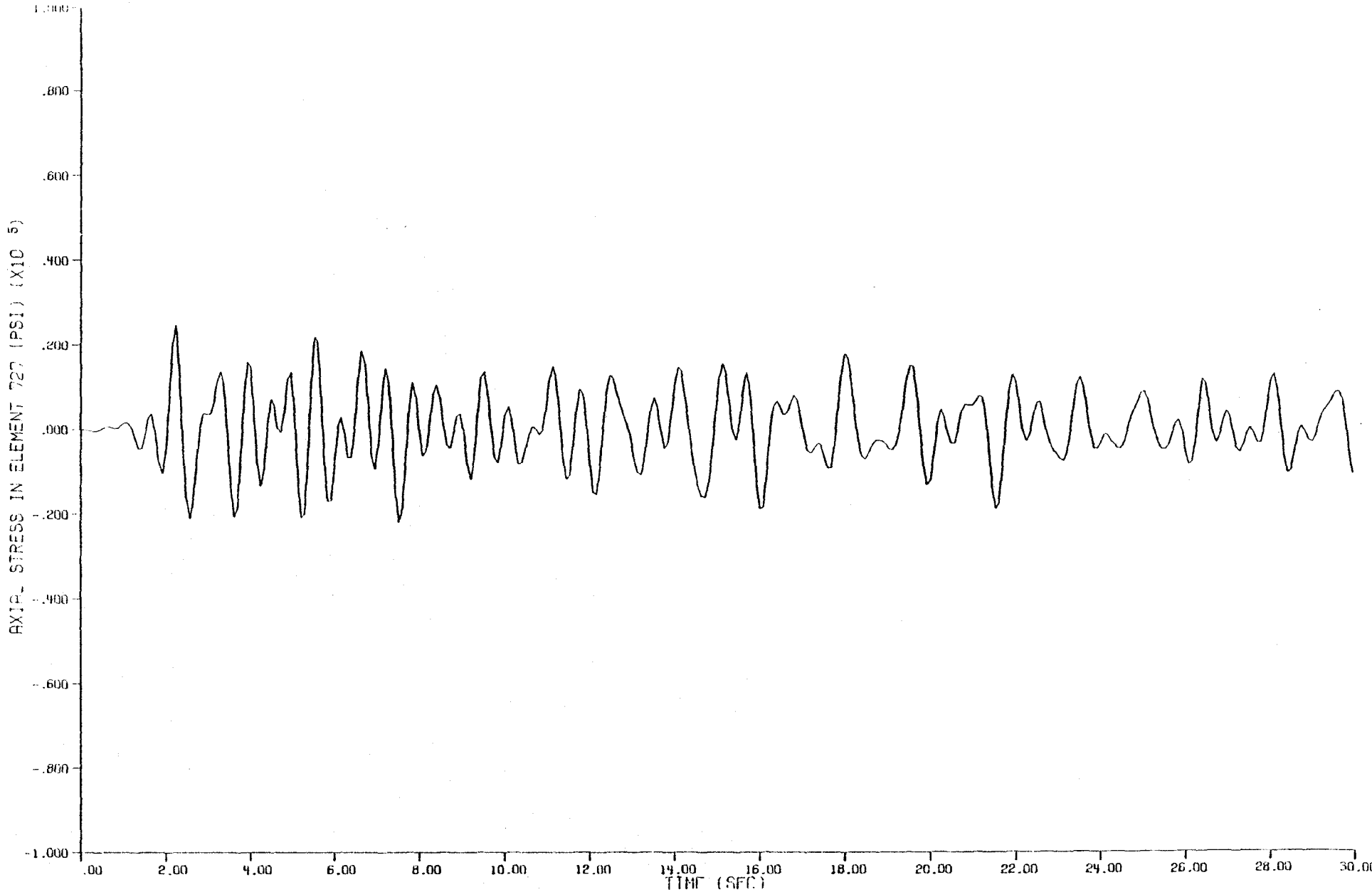

Figure 106

Axial stress time-history in element 727, fraction of critical damping = .01.

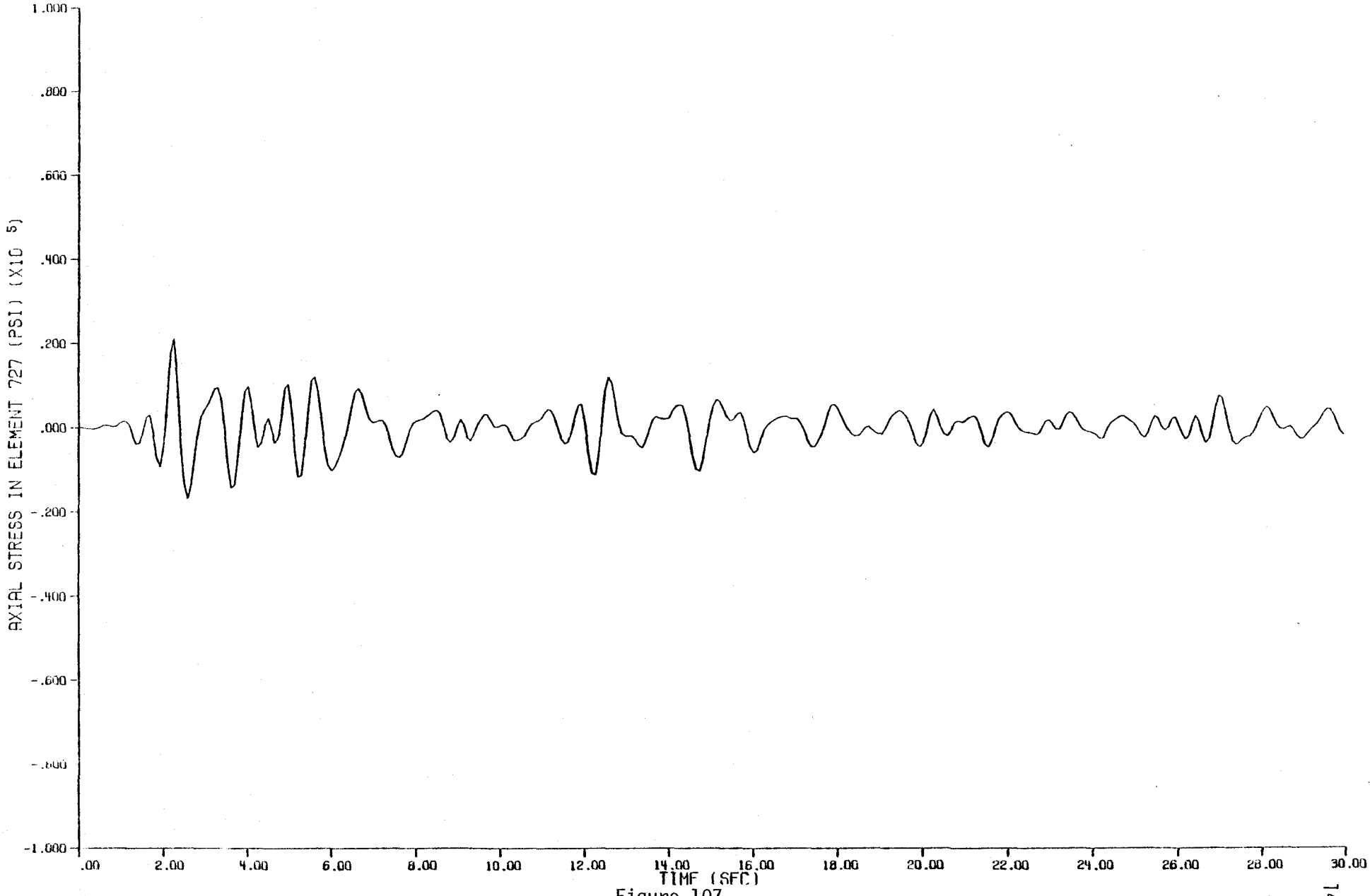

Figure 107

Axial stress time-history in element 727, fraction of critical damping = .05.

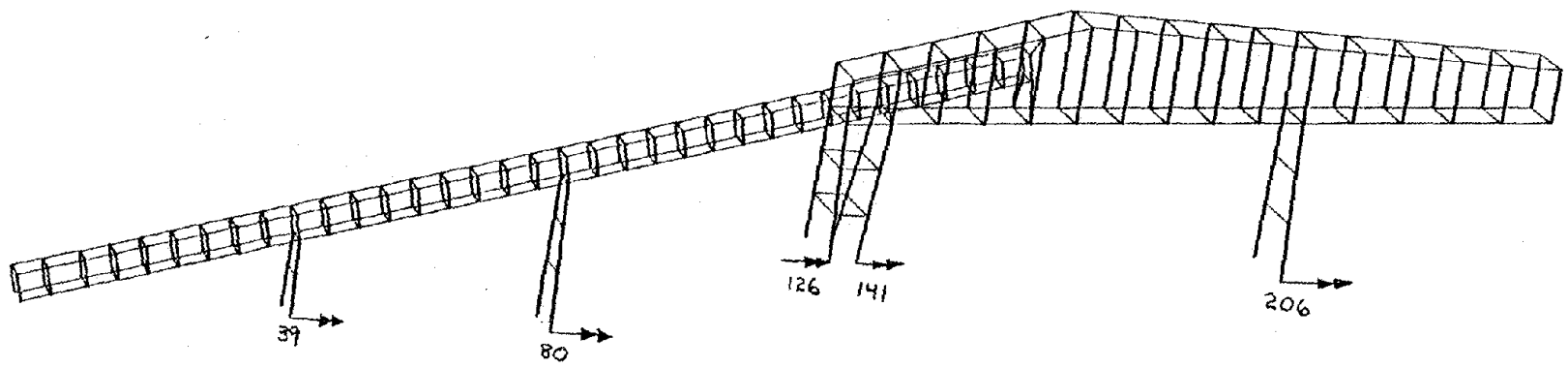

Figure 108

Key for bending moment time-histories.

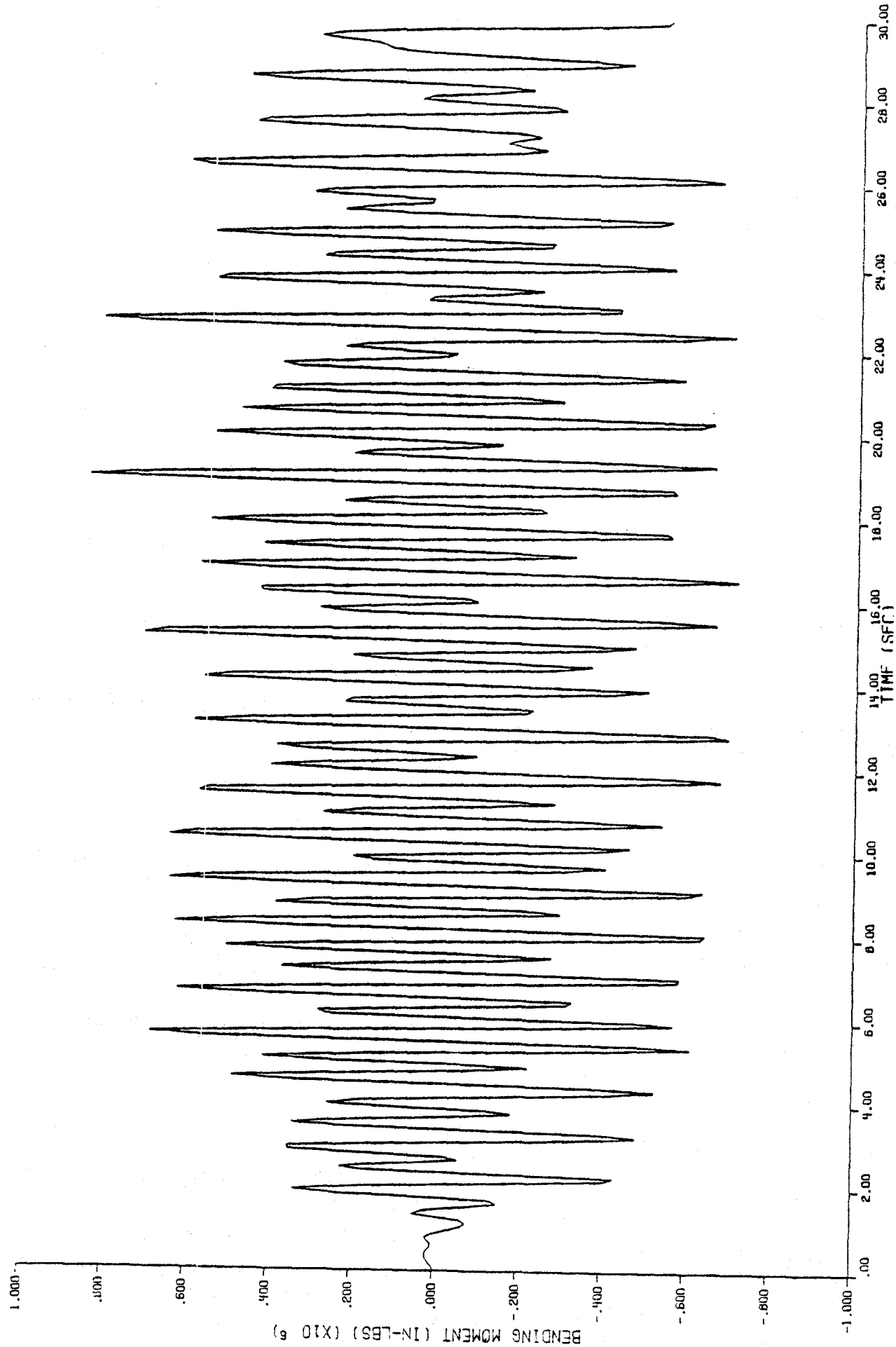

Figure 109

Bending moment time-history at node 39, undamped.

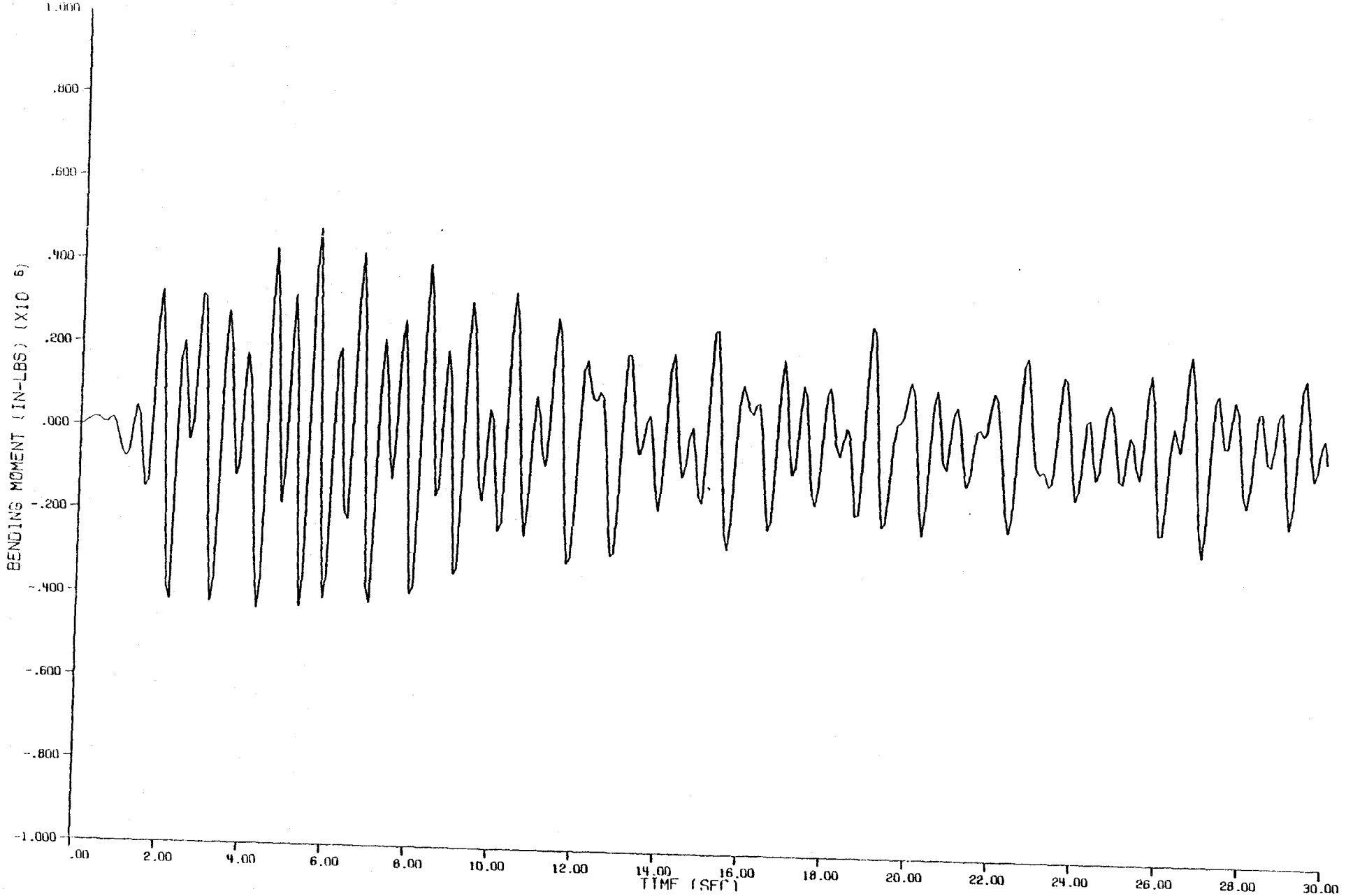

Figure 110

Bending moment time-history at node 39, fraction of critical damping = .01.

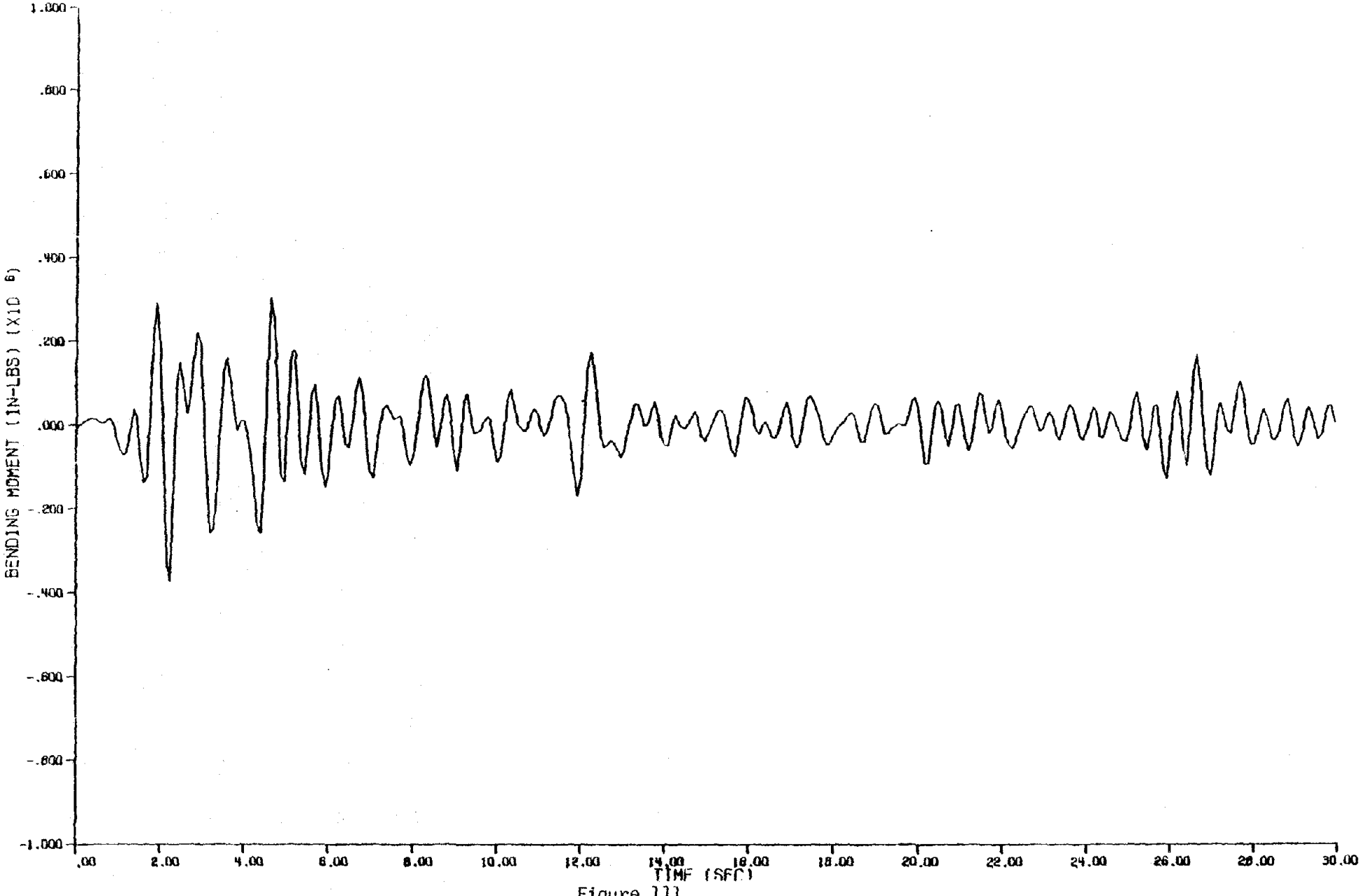

Figure 111

Bending moment time-history at node 39, fraction of critical damping = .05.

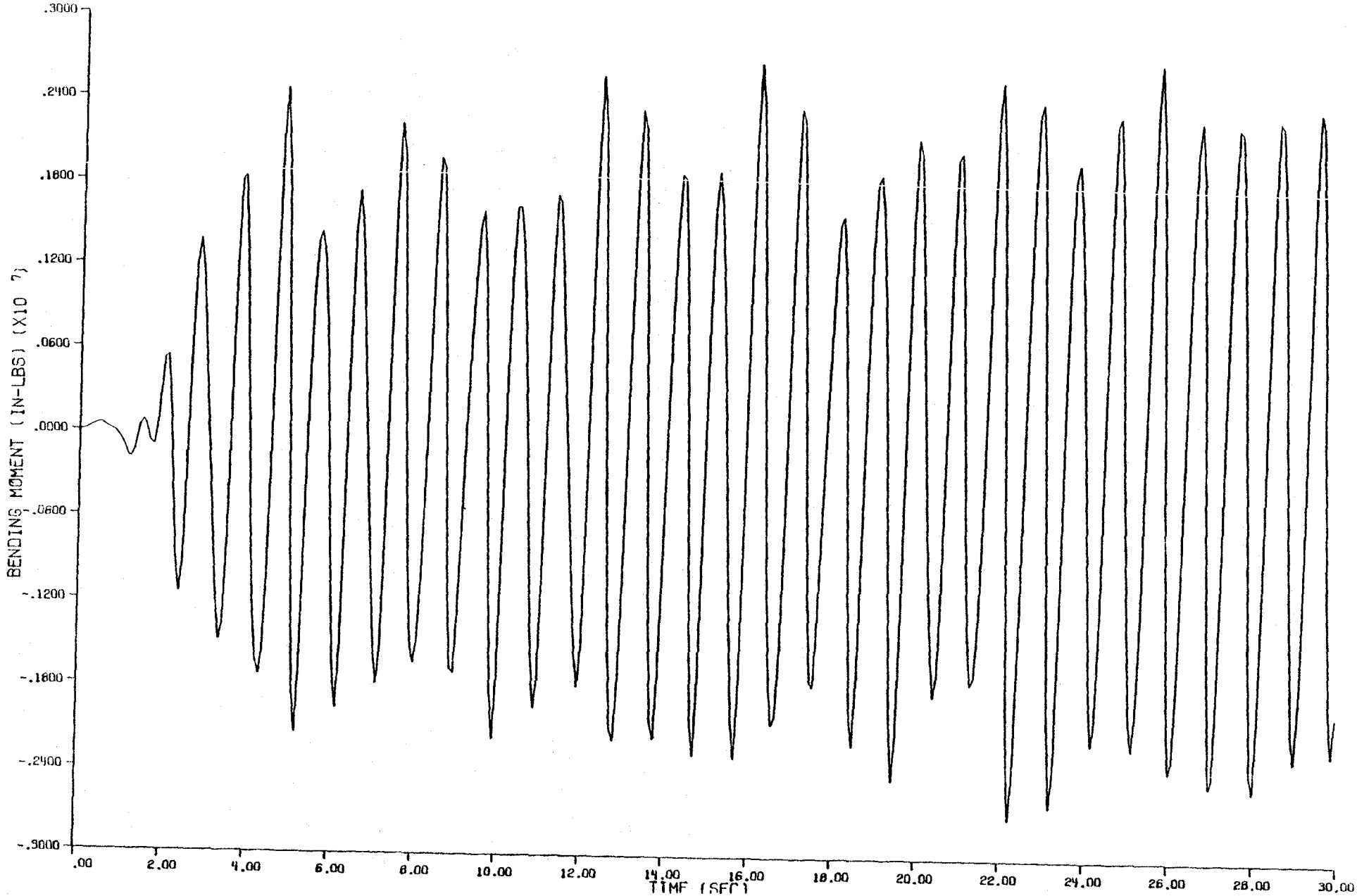

Figure 112
Bending moment time-history at node 80, undamped.

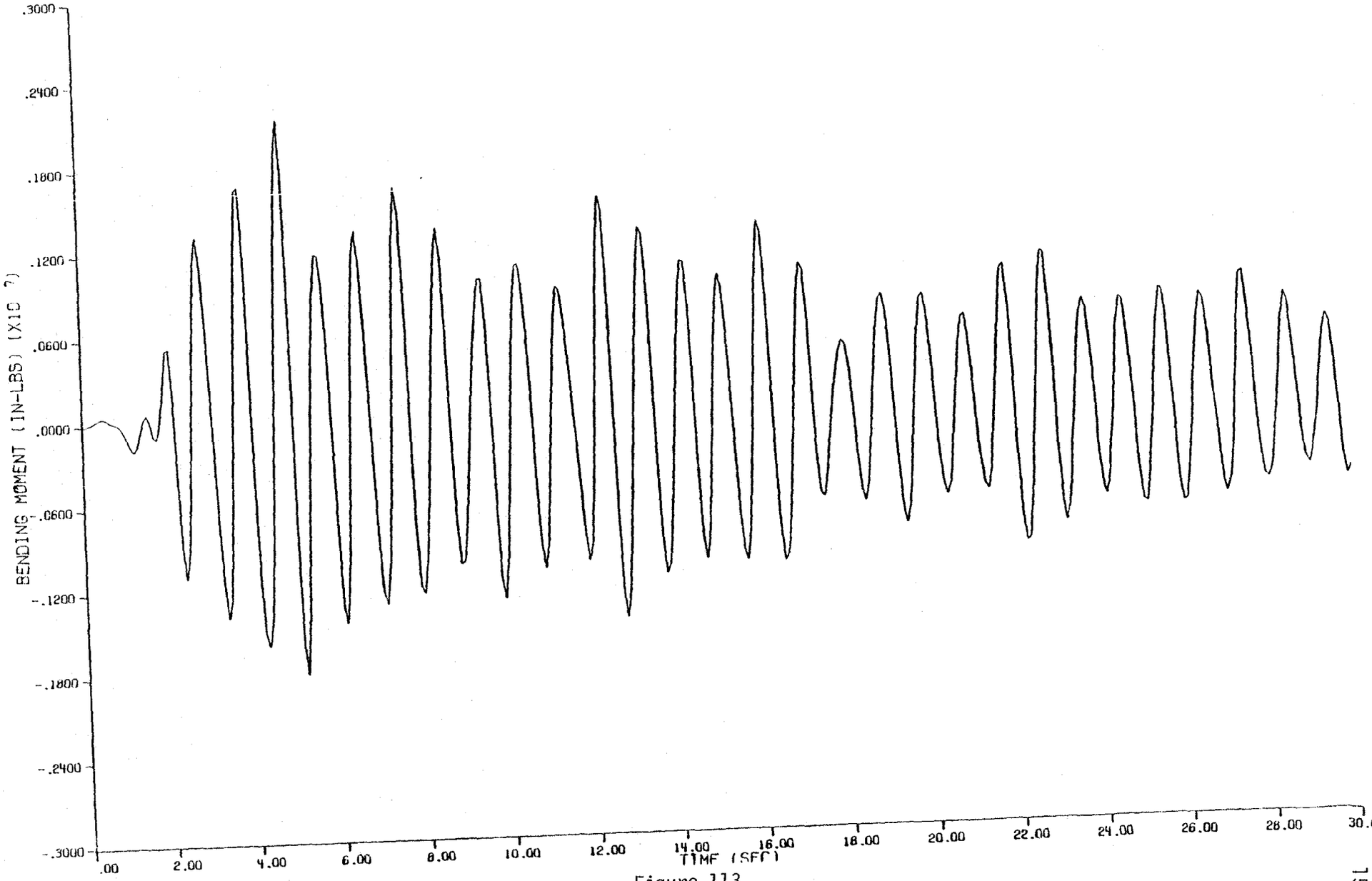

Figure 113

Bending moment time-history at node 80, fraction of critical damping = .01.

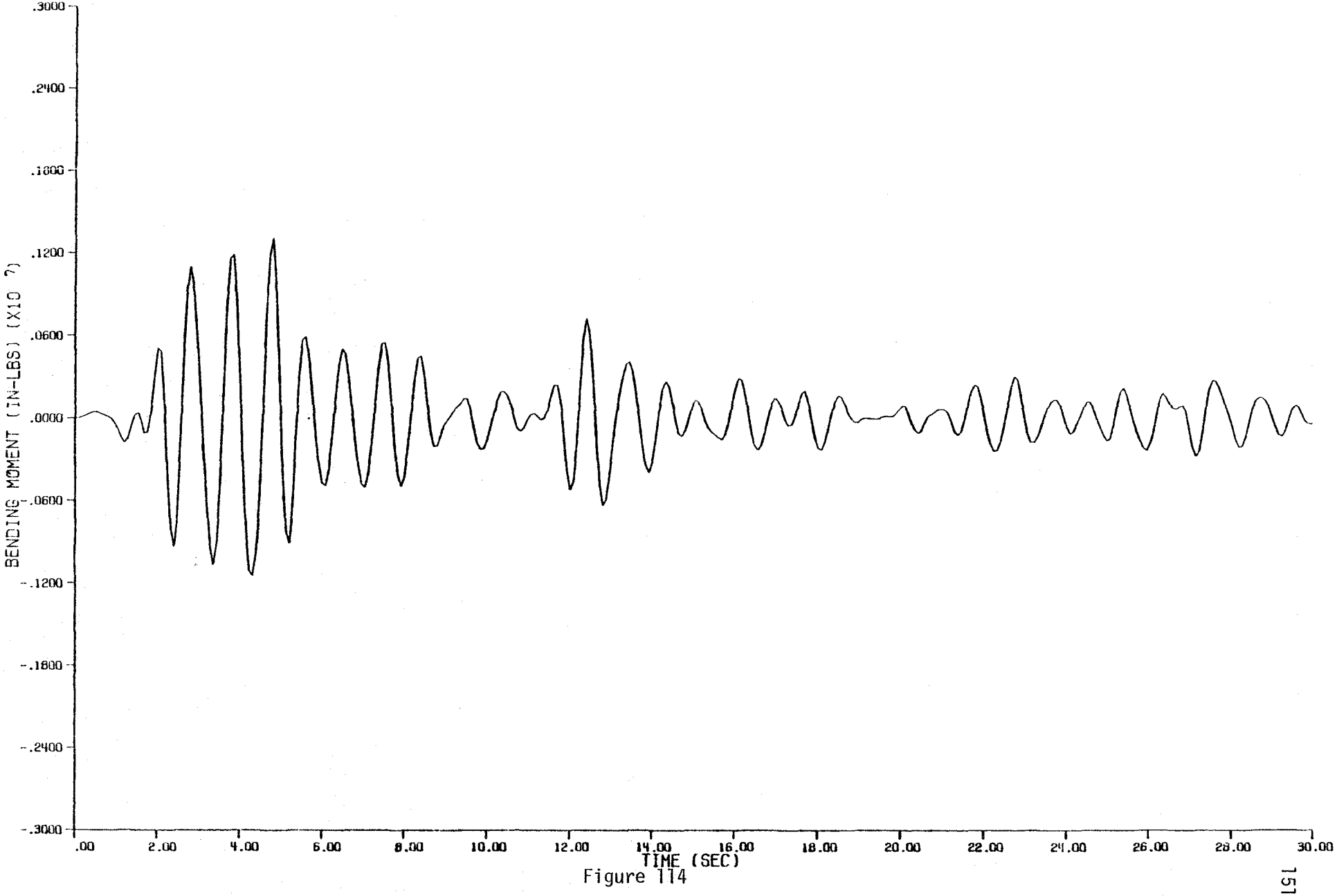

Figure 114

Bending moment time-history at node 80, fraction of critical damping = .05.

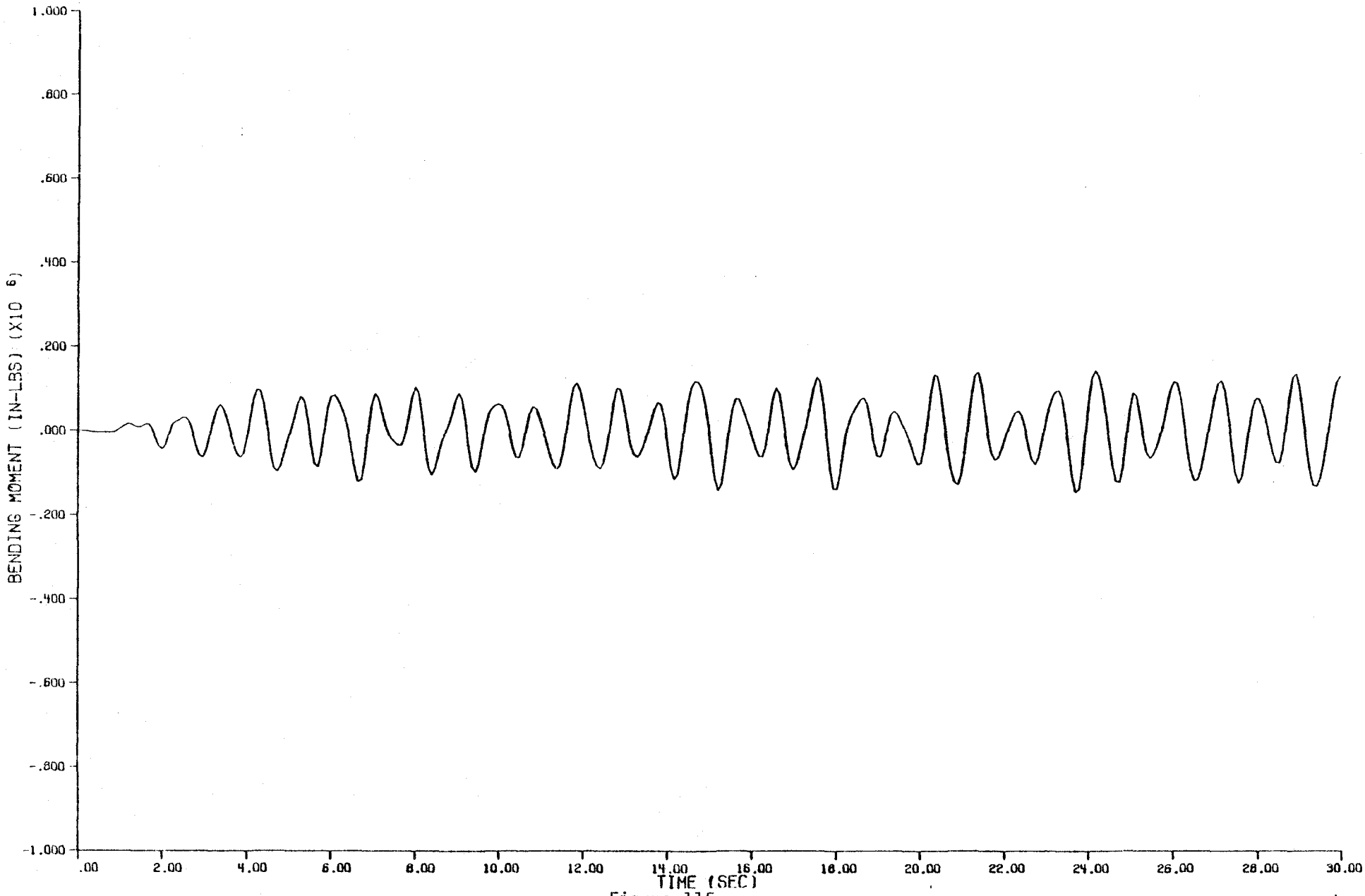

Figure 115
Bending moment time-history at node 126, undamped.

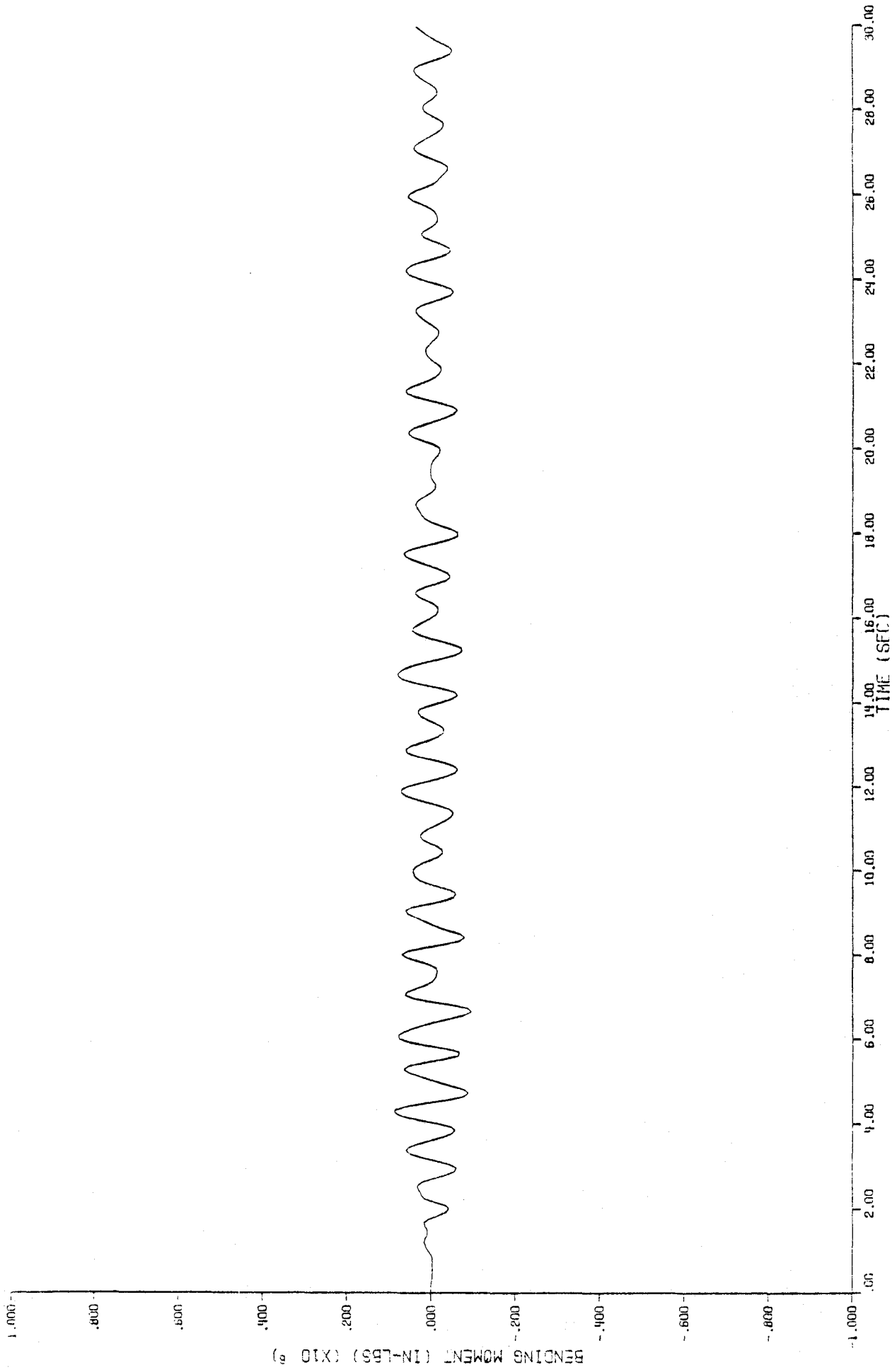

Figure 116

Bending moment time-history at node 126, fraction of critical damping = .01.

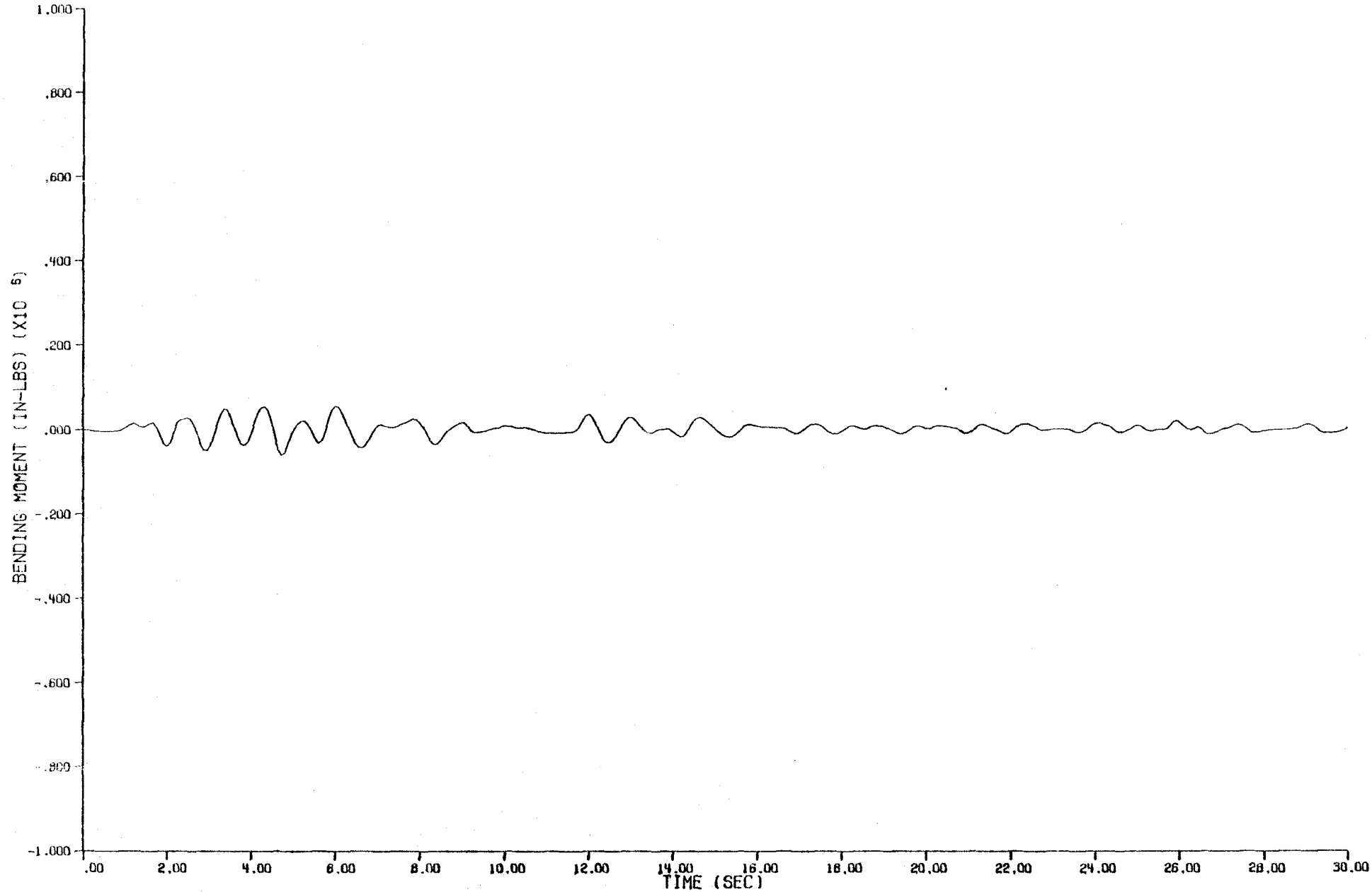

Figure 117

Bending moment time-history at node 126, fraction of critical damping = .05.

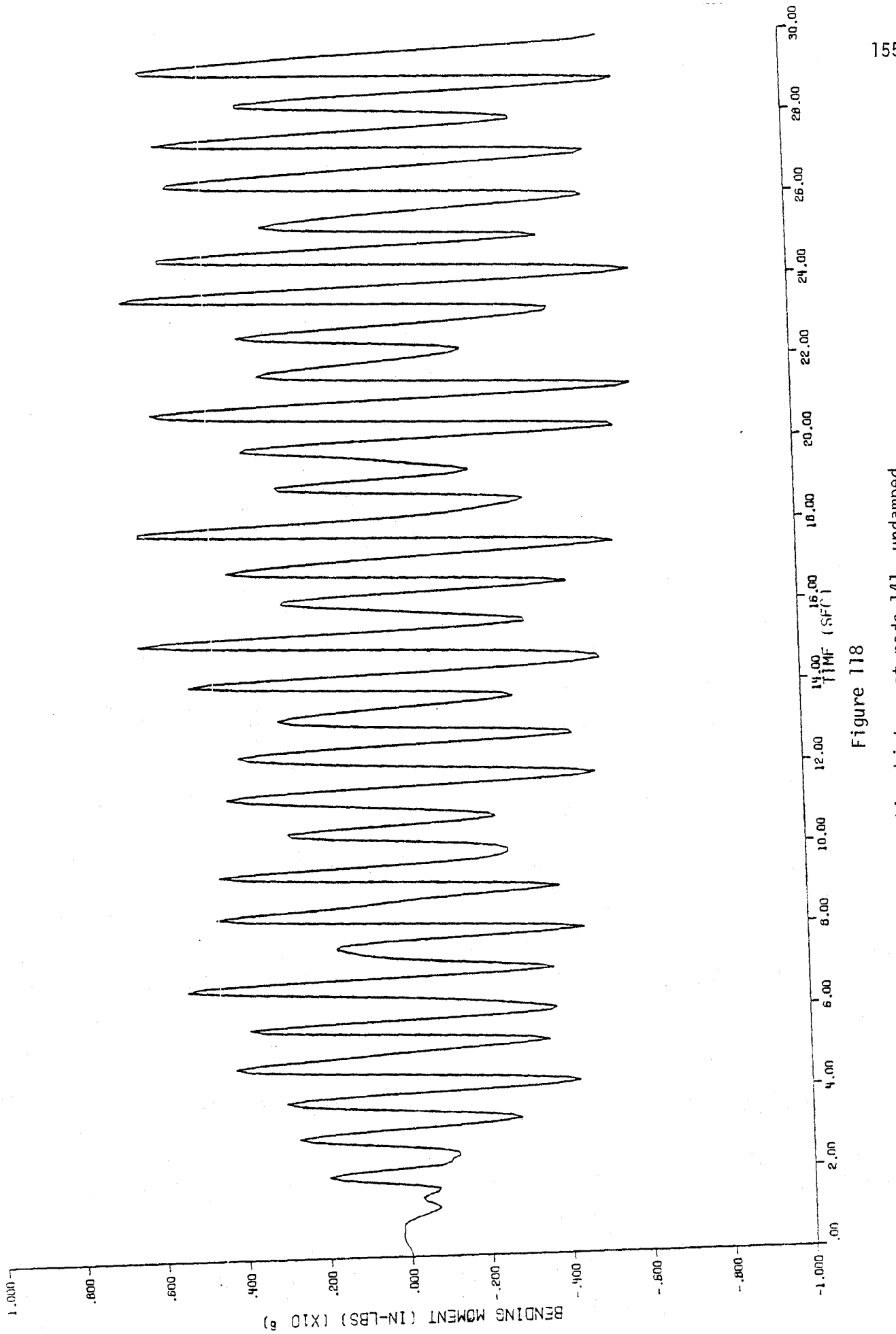

Figure 118

Bending moment time-history at node 141, undamped.

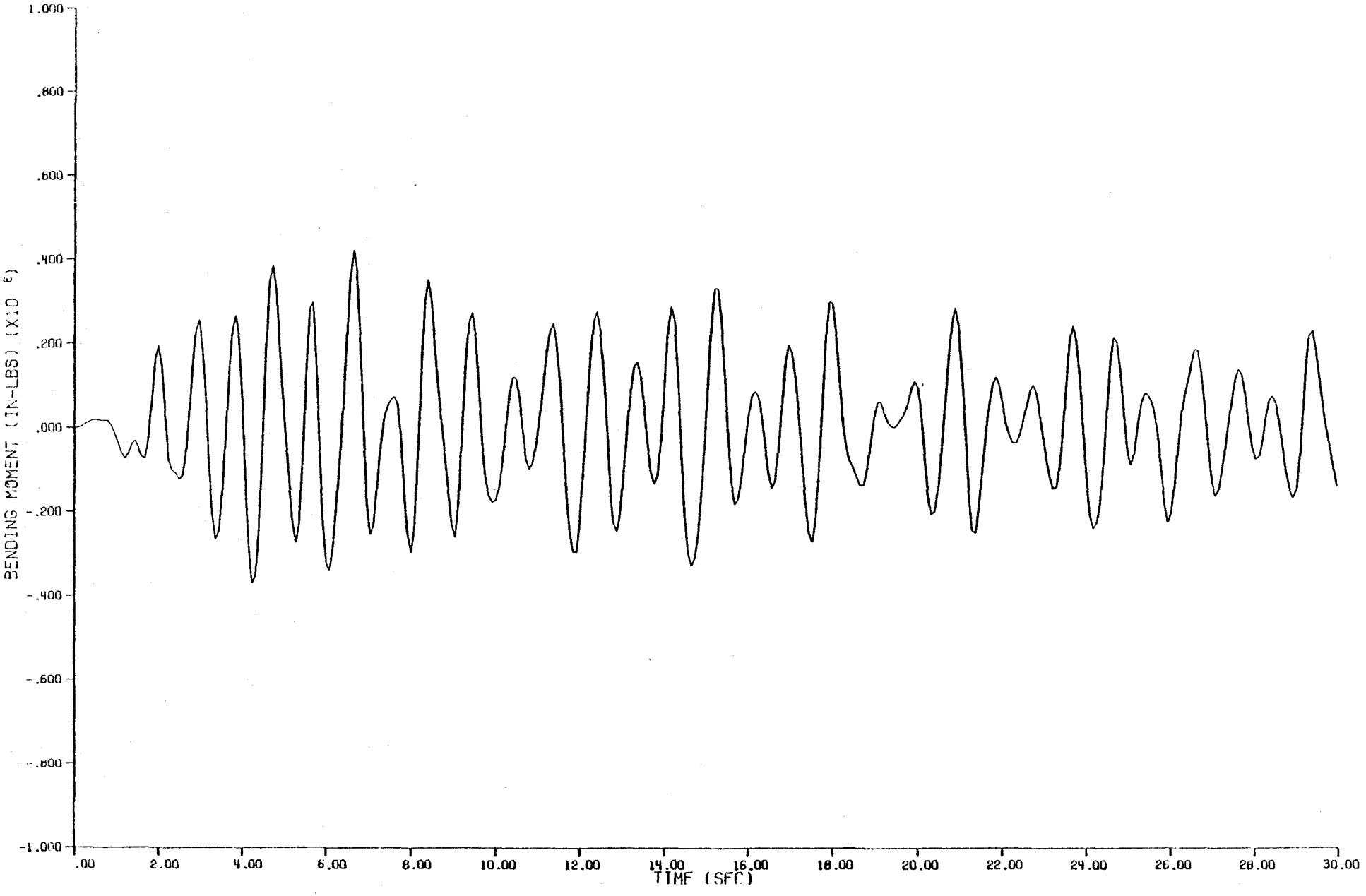

Figure 119

Bending moment time-history at node 141, fraction of critical damping = .01.

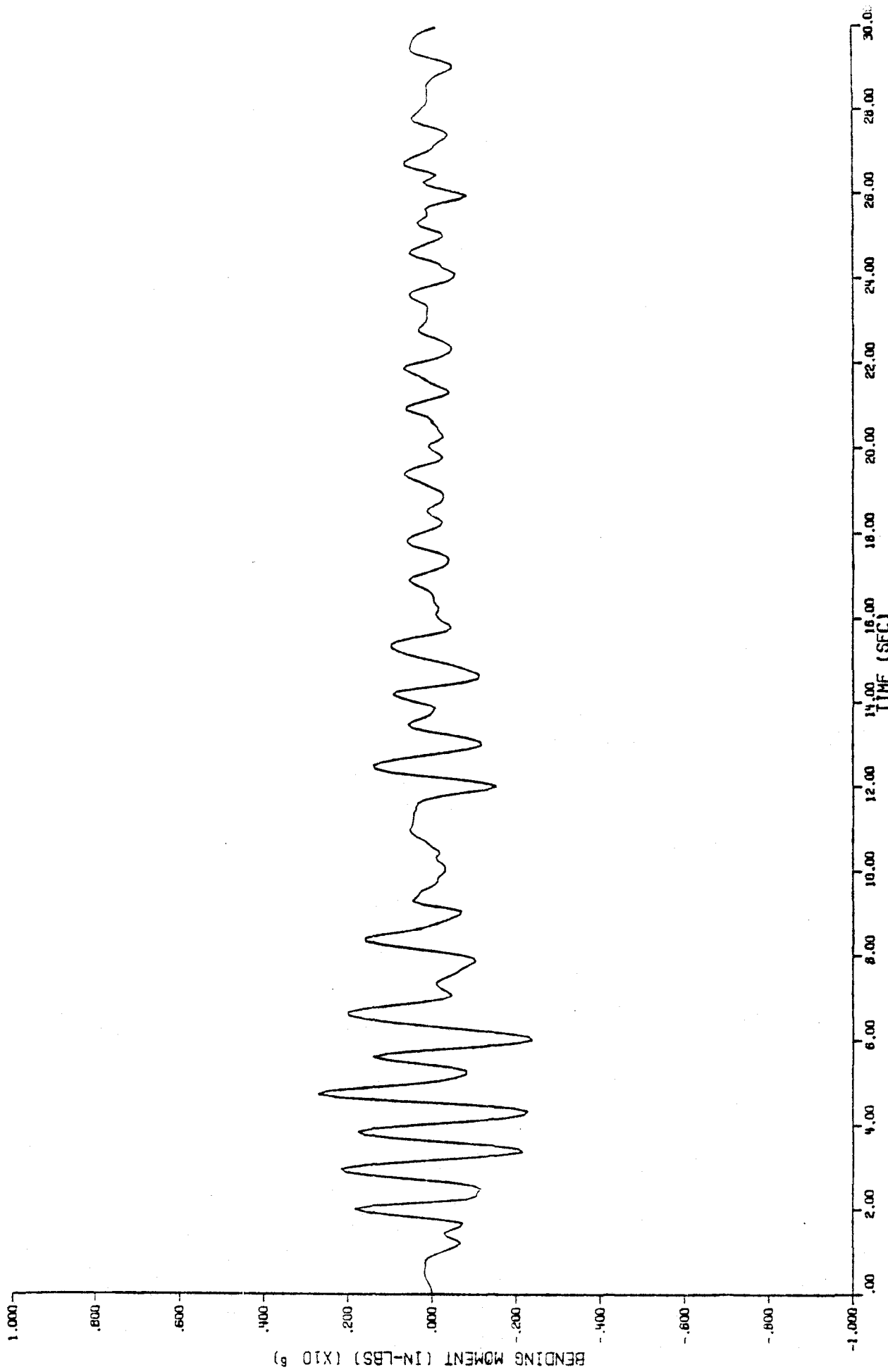

Figure 120

. Bending moment time-history at node 141, fraction of critical damping = .05.

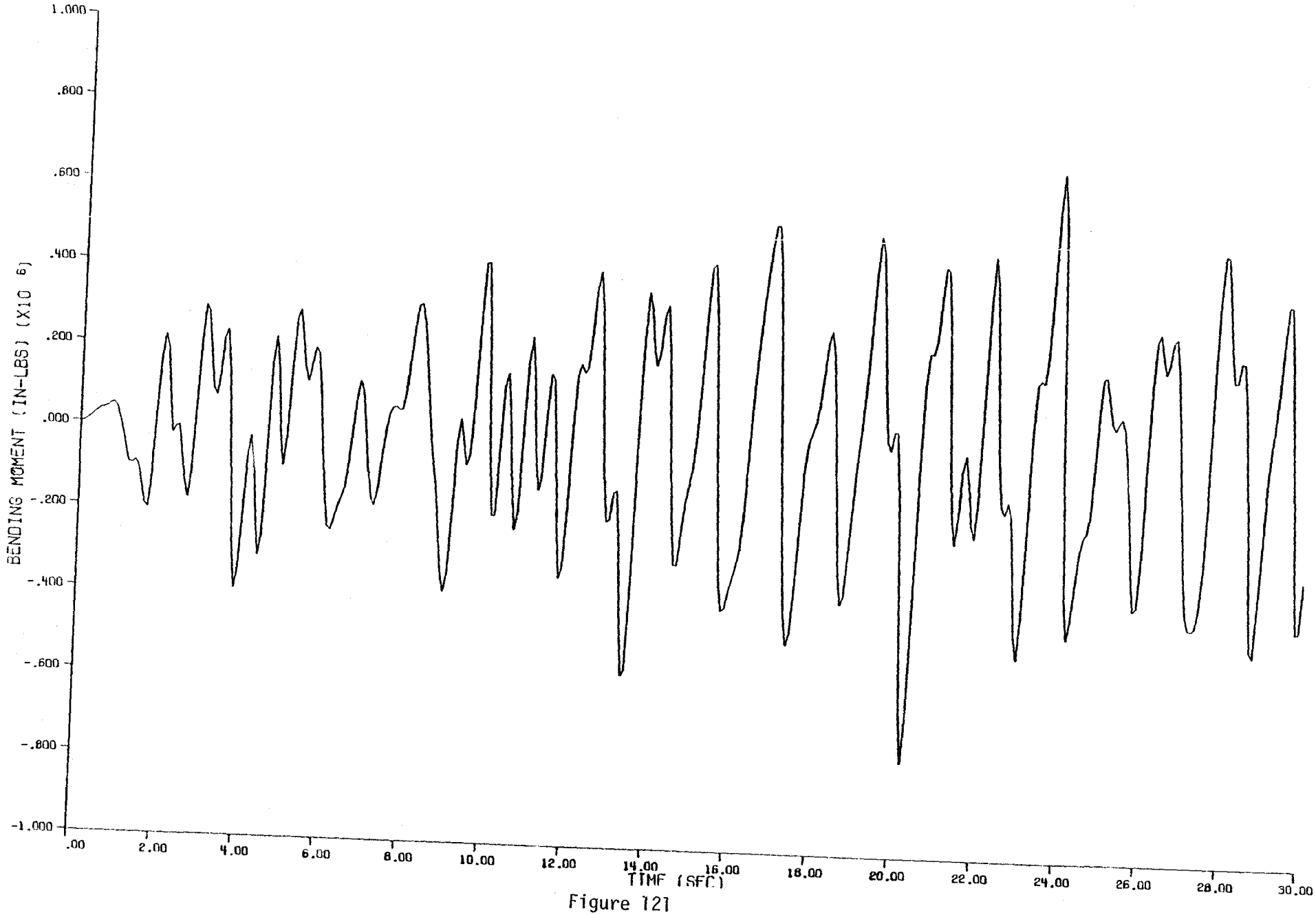

Figure 121

Bending moment time-history at node 206, undamped.

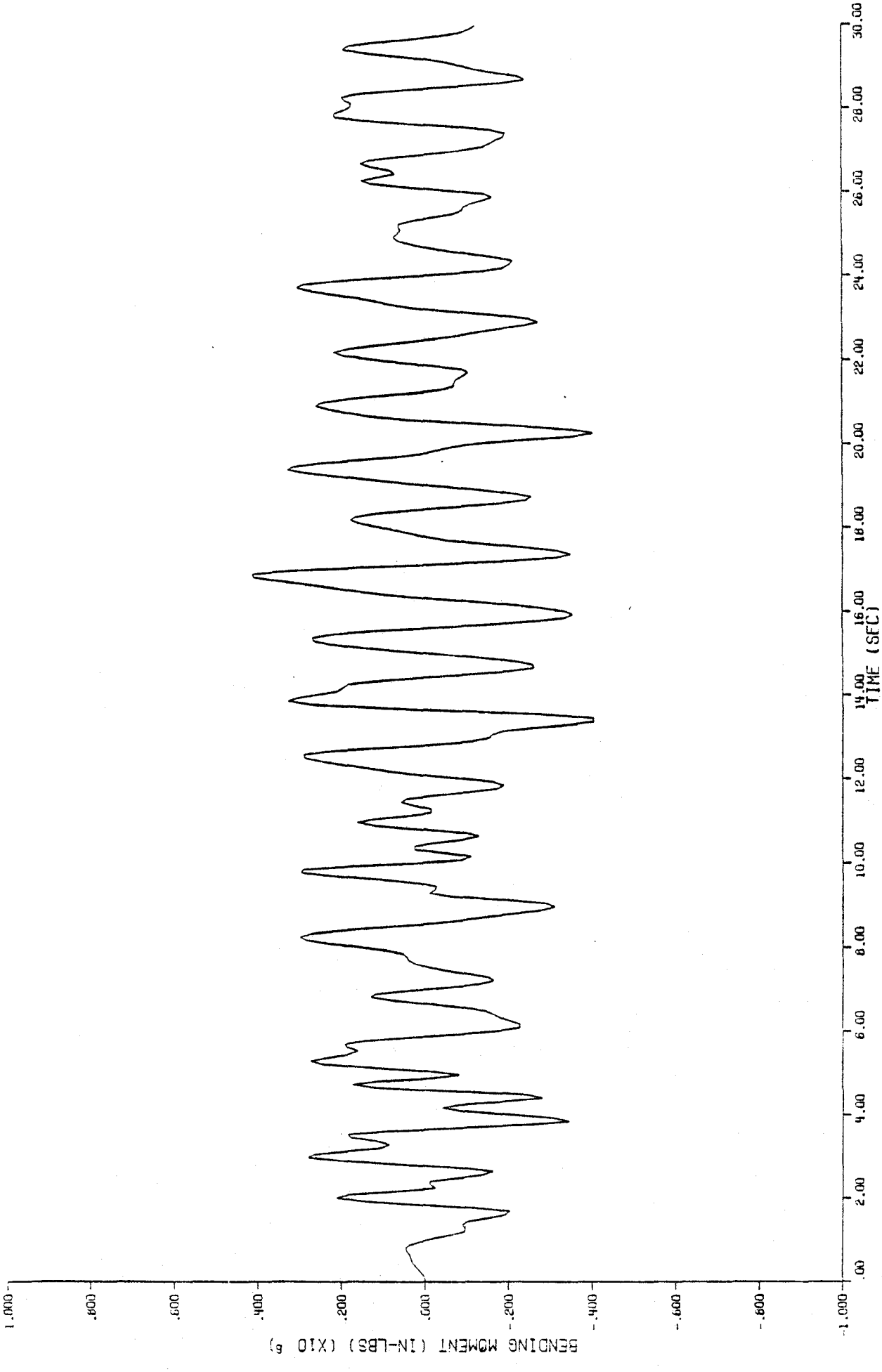

Figure 122

Bending moment time-hsitory at node 206, fraction of critical damping = .01.

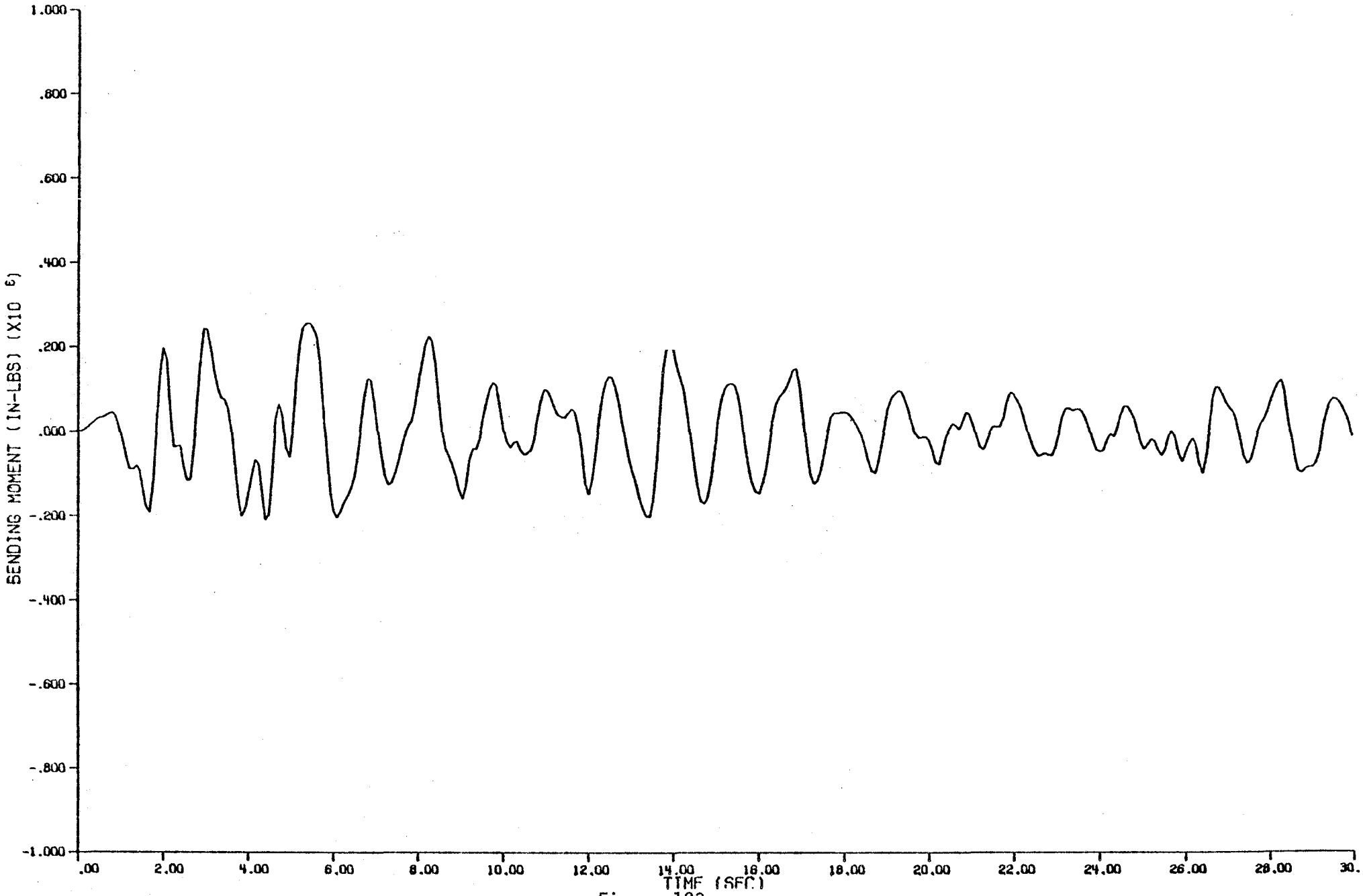

Figure 123

Bending moment time-history at node 206, fraction of critical damping = .05.